



UNIVERSITY OF
BIRMINGHAM

X-ray Absorption Spectroscopy Studies of Electrochemical Processes

by

Ornella Smila-Castro

Supervisor: Prof. Trevor Rayment

A thesis submitted to The University of Birmingham for the degree of
DOCTOR OF PHILOSOPHY

School of Chemistry
University of Birmingham
December 2010

UNIVERSITY OF
BIRMINGHAM

University of Birmingham Research Archive

e-theses repository

This unpublished thesis/dissertation is copyright of the author and/or third parties. The intellectual property rights of the author or third parties in respect of this work are as defined by The Copyright Designs and Patents Act 1988 or as modified by any successor legislation.

Any use made of information contained in this thesis/dissertation must be in accordance with that legislation and must be properly acknowledged. Further distribution or reproduction in any format is prohibited without the permission of the copyright holder.

Acknowledgements

I would like to extend my gratitude to the following people for their help, guidance and encouragement over the course of my research.

First, to Prof. Trevor Rayment for providing with the opportunity to work under his supervision, and for his constant optimism for facing the challenges of this study. Beyond this work, he has been a very caring person. I am looking forward to another debate on French vs. British puddings (although, is there any debate...). It has been a pleasure and an honour, Trevor.

Then, my gratitude goes to Prof. William Geiger from the University of Vermont. My time in his laboratory brought me knowledge and guidance in inorganic electrochemistry. I would like to thank him as well for his precious help beyond my visit.

I would also like to thank Dr. Sarah Horswell for helping me in times where I really needed it.

Members of staff of the synchrotron radiation sources that I've had the chance to work at during this work: staff at the SRS, Daresbury, Swiss Light Source and Diamond Light Source. In particular to Dr. Messaoud Harfouche (Swiss Light Source), Dr. Andy Dent (Diamond Light Source), and Dr. Giannantonio Cibin (Diamond Light Source).

This work would not have been possible without the immense efforts of the members of the Workshops. Particular appreciation is given to Tony Rothin (mechanical) and Andy Tanner (electrical) for the construction of the spectroelectrochemical cells and associated parts, often in unreasonably short timescales!

The EPSRC for financial support.

My friends that have been here all the way through, and the ones I met here in Birmingham for their support and encouragement. They'll know who they are.

I would like now to finish this page in my own mother-tongue language:

Mille mercis á mes parents Chantal et Maurice, à mes trois soeurs Audrey, Odélia, et Alexandra pour leur soutien continu durant ces quatre années d'études.

Abstract

Electron transfer is a key part of many chemical, biological and physical processes, that is commonly studied by electrochemical methods, which give insight into reaction mechanisms but no structural information. It is necessary to combine electroanalysis with another technique to gain essential knowledge of metal-ligand bond length and oxidation states. X-ray absorption spectroscopy (XAS) can provide these data for species in dilute solution and, if combined with electrochemistry, could potentially provide powerful insight into electron transfer reactions.

This dissertation describes the development and application of techniques for the study of electrochemical intermediates by XAS.

Chapters 2 and 3 introduce the theory and practice of electrochemistry and spectroscopy with emphasis on XAS. Chapter 4 describes the development of variable-temperature spectroelectrolysis cells for the study of electrochemical intermediates. In Chapter 5, the electrochemical behaviour of $\text{Cp}^*\text{Rh}(\text{CO})_2$, is investigated as an organometallic compound representative of the redox chemistry studied in this thesis. Chapter 6 describes a new approach to the study of electrochemical intermediates in which a miniature electrolysis cell is combined with a microdispenser so that electrochemical intermediates can be generated and then dispensed, quenched at low temperature prior to study by XAS. Chapter 7 contains final conclusions.

Table of Contents

Chapter 1: Introduction

Introduction	2
References	5

Chapter 2: Electrochemical theory

2.1 Introduction	8
2.2 the Electrical double Layer	8
2.3 The electrochemical cell and the three-electrode system	14
2.4 Interfacial kinetics	17
2.5 Mass transport	22
2.6 Experimental considerations	28
References	35

Chapter 3: X-ray Absorption Spectroscopy

3.1 Introduction	38
3.2 The principle of interaction of X-rays with matter	38
3.3 The EXAFS formula	43
3.4 Data analysis	53
3.5 Synchrotron Radiation Sources	56
References	65

Chapter 4: Low temperature studies of Ruthenocene

4.1 Introduction	70
4.2 Systems under study	71
4.3 Designs of X-ray spectroelectrochemical cells	81
4.4 Experiments at the SRS	94
4.5 Spectroelectrochemical cell 2	110
References	130

Chapter 5: Electrochemical behaviour of Cp*Rh(CO)₂

5.1 Introduction	134
5.2 Experimental	135
5.3 Voltammetry studies of Cp*Rh(CO) ₂	137
5.4 Conclusions for studies at 298 K	144
5.5 Voltammetry studies of Cp*Rh(CO) ₂ at low temperature	145
5.6 Exhaustive Electrolysis	150
5.7 In situ IR Spectroelectrochemistry	160
5.8 NMR Spectroscopy	164
5.9 Conclusions	167
References	168

Chapter 6: Development of a microdispenser for XAS

6.1 Introduction	171
6.2 Understanding the microdispenser	173
6.3 Electrochemical characterisation of the microdispenser	180
6.4 The cryostat	192
6.5 Optimisation of deposition parameters	195
6.6 Spectroelectrochemical characterisation of the microdispenser	199
6.7 XAS studies with a microdispenser system	202
6.8 Conclusion	223

Chapter 7: Final Conclusions

Final conclusions	227
-------------------	-----

Chapter 1: Introduction

In many chemical and biological processes, the critical step is electron transfer. While conventional electroanalytical methods provide insight into molecular energy levels and reaction mechanism, via kinetic analysis, these electroanalyses alone cannot offer structural information of species formed during redox processes, such as electrochemical intermediates. This has limited the application of electroanalysis in understanding and exploiting complex electron transfer reactions. Knowledge of the metal-ligand connectivity, such as the number and types of atoms coordinated to the metal along with their bond length and bond angle, is necessary to the design of electron transfer driven organosynthetic reactions.

In recent years, there have been continuing efforts to develop spectroelectrochemical techniques to assist electrochemical research and a wide range of techniques have been applied, such as UV/visible, infrared, Mossbauer, Raman and Electron Spin Resonance (ESR) spectroscopy for the study of both homogeneous and heterogeneous processes.¹⁻³

The simplest approach and thus mostly commonly employed approach is to combine UV/vis spectroscopy with electrochemistry. This method relies on the use of optically transparent electrodes (OTEs) and an extensive literature can be found on the subject. Spectra can be recorded at regular time intervals and both qualitative data and quantitative conversion of the starting material into products during electrolysis can be determined. In addition, with a fast UV/vis spectrometer, spectroscopic information as a function of potential can be recorded simultaneously with the voltammetric data.^{4,5}

Moreover, the products or intermediates of an electrochemical reaction may be identified by vibrational spectroscopy such as infrared spectroscopy, where species are probed at the electrode surface and in a region of the solution close to it. The excitation of the vibrational modes permits the assignment of particular moieties due to their characteristic frequency.⁶

The spectroscopic methods cited above provide valuable information about symmetry and electronic structure. However, none of these techniques provides direct information into either short range or long-range order parameters such as bond lengths.⁷

X-ray diffraction (XRD) is the most widely used technique for the determination of the structure of crystalline solids. However, it is less useful for the study of complex solutions. For non crystalline samples and materials in solution, X-ray absorption spectroscopy (XAS) is much better suited to this task. Its main advantage lies in the fact that it is a local structure probe, does not require crystalline order and is element specific. When combined with an electrochemical technique, the changes in coordination number and bond length upon a change in oxidation state may be directly determined.^{8,9} All these properties make it a very attractive tool for the study of electrogenerated species. Applications of the combination of both techniques may be found in the investigation of batteries,¹⁰ electrode materials,¹⁰⁻¹⁴ electrocatalysts,¹³⁻¹⁵ passivation and corrosion or electrode/solution interface, etc.

However, very few publications can be found on the application of XAS to electroanalysis, because of several inherent challenges. Firstly, most electroanalytical experiments are carried out at submillimolar concentrations and therefore the concentration of electrogenerated species is usually small; short-lived intermediates are likely to remain undetected. Moreover, whilst their concentration is at its maximum next to the electrode surface, this decreases as molecules diffuse away from the electrode. Depending on the lifetime of the intermediates, requirements are different. For short-lived intermediates, high temporal resolution is required in order to determine the structure of electrochemical intermediates before they have the chance to react further. For long-time life species, rapid and complete electrolysis allows the concentration of the intermediates to build up in the vicinity of the electrode, which thus facilitates its detection.¹⁶⁻¹⁸ Secondly, temporal and high spatial resolution are required to

follow these processes. Finally, in most circumstances, the outcome of these reactions yields a mixture of starting material, intermediate and final product in the XAS spectra. The difficulty lies in the fact that XAS spectra are the sum of the spectrum of every species in solution. Hence the more complex the electrochemical system is, the more difficult the interpretation of spectra is likely to be.

The interest for the electrochemistry community in the combination of both techniques depends upon the choice of systems that are amenable to study. The largest chances of success are likely where the intermediate undergoes a large change in structure compared with the reactant or final product. From a technique development standpoint ideal systems would include the class of EC reactions such as dimerisation of organometallic radicals, isomerisation, and rearrangements of polynuclear complexes.

These investigations have been greatly aided by the recent discovery of fluoro-containing aryl borates based electrolytes by Geiger *et al.*¹⁹ that can dramatically improve the conditions for anodic electrochemistry in lower-polarity solvents such as CH₂Cl₂, since they enhance the reversibility and longevity of electrochemical systems.

The objective of this work is to develop instrumentation and therefore a strategy for the determination of the structure of transient intermediates in electrochemical processes.

References

1. Gale, R. J. *Spectroelectrochemistry: Theory and Practice*; Ed. Gale, R. J., Springer, **1988**.
2. Neudeck, A.; Marken, F.; Compton, R. G. *UV/Vis/NIR Spectroelectrochemistry*, Springer, New York, **2002**.
3. Wolfgang, K.; Klein, A. *Spectroelectrochemistry*; Royal Society of Chemistry: Cambridge, U.K, **2008**.
4. Marken, F.; Neuden, A.; Bond, A.M. *Electroanalytical methods: Guide to Experiments and Applications*, Ed. F. Scholtz, Springer, Berlin, **2002**.
5. Bard, A. J.; Faulkner, L. R. *Electrochemical Methods, Fundamentals and Applications*; Second Edition; John Wiley and Sons, **2004**.
6. Christensen, P. A.; Hamnett, A. *Techniques and Mechanisms in Electrochemistry*; Chapman & Hall, **1994**.
7. Connelly, N. G. Synthetic Applications of Organotransition-Metal Redox Reactions. *Chem. Soc. Rev.* **1989**, 18 (2), 153-185.
8. Crozier, E. D. A review of the current status of XAFS spectroscopy. *Nuclear Instruments & Methods in Physics Research Section B-Beam Interactions with Materials and Atoms* **1997**, 133 (1-4), 134-144.
9. Lee, P. A.; Citrin, P. H.; Eisenberger, P.; Kincaid, B. M. Extended X-Ray Absorption Fine-Structure - Its Strengths and Limitations As A Structural Tool. *Rev. Mod. Phys.* **1981**, 53 (4), 769-806.
10. Yoon, W. S.; Grey, C. P.; Balasubramanian, M.; Yang, X. Q.; McBreen, J. In situ X-ray absorption spectroscopic study on $\text{LiNi}_{0.5}\text{Mn}_{0.5}\text{O}_2$ cathode material during electrochemical cycling. *Chem. Mater.* **2003**, 15 (16), 3161-3169.
11. Davenport, A. J.; Ryan, M. P.; Simmonds, M. C.; Ernst, P.; Newman, R. C.; Sutton, S. R.; Colligon, J. S. In-situ synchrotron X-ray microprobe studies of passivation thresholds in Fe-Cr alloys. *J. Electrochem. Soc.* **2001**, 148 (6), B217-B221.

12. Isaacs, H. S.; Virtanen, S.; Ryan, M. P.; Schmuki, P.; Oblonsky, L. J. Incorporation of Cr in the passive film on Fe from chromate solutions. *Electrochim. Acta* **2002**, *47* (19), 3127-3130.
13. Mukerjee, S.; McBreen, J. An in-situ X-ray absorption spectroscopy investigation of the effect of Sn additions to carbon-supported Pt electrocatalysts - Part I. *J. Electrochem. Soc.* **1999**, *146* (2), 600-606.
14. Russell, A. E.; Maniguet, S.; Mathew, R. J.; Yao, J.; Roberts, M. A.; Thompsett, D. In-situ X-ray absorption spectroscopy and X-ray diffraction of fuel cell electrocatalysts. *J. Power Sources* **2001**, *96* (1), 226-232.
15. Mukerjee, S.; McBreen, J. Hydrogen electrocatalysis by carbon supported Pt and Pt alloys - An in-situ X-ray absorption study. *J. Electrochem. Soc.* **1996**, *143* (7), 2285-2294.
16. Dewald, H. D.; Watkins, J. W.; Elder, R. C.; Heineman, W. R. *Anal. Chem.* **1986**, *58*, 2968.
17. Igo, D. H.; Elder, R. C.; Heineman, W. R.; Dewald, H. D. *Anal. Chem.* **1991**, *63*, 2535.
18. Smith, D. A.; Elder, R. C.; Heineman, W. R. *Anal. Chem.* **1985**, *57*, 2361.
19. Lesuer, R. J.; Buttolph, C.; Geiger, W. E. Comparison of the conductivity properties of the tetrabutylammonium salt of tetrakis(pentafluorophenyl)borate anion with those of traditional supporting electrolyte anions in nonaqueous solvents. *Anal. Chem.* **2004**, *76* (21), 6395-6401.

Chapter 2: Electrochemical theory

2.1 Introduction

Electrochemistry is concerned with the study of the interrelation of electrical and chemical processes and the exploitation of the transference of electrical charges across interfaces and through solution is its intrinsic goal. The intention of this chapter is to give an understanding of electrode reactions through several fundamental electrochemical concepts. Experimental considerations that have been coupled to XAS in this thesis such as cyclic voltammetry, chronoamperometry and flow electrolysis are also presented.

2.2 The Electrical Double Layer

In order to understand electron transfer processes, the nature of the electrode/electrolyte interface has to be explained. The distribution of charges at an electrified interface is a central factor in electrochemical activity which has been carefully studied throughout the last 100 years.

When an electrode is dipped into a solution of an electrolyte, charge separation occurs. To maintain electroneutrality, the excess of charge residing on the electrode surface must be exactly balanced by an equal charge of opposite sign on the solution side, due to electrostatic attraction: in a plane parallel to the surface of the electrode, a layer of charge exists that is situated very close to the metal. This leads to a potential difference across the interface, forming an electric field gradient across the charge separation layer. The interface between an electrode and the solution has become known as the Electrical Double Layer.

2.2.1 The Helmholtz model

The interface behaves like a capacitor in its ability to store charge, which leads to the first, simplest double layer model,¹⁻⁴ due to Helmholtz: the charges are fixed at the interface. The model takes the form of a parallel plate capacitor where the charge at the surface of the metal acts as the first plate and a layer of ions is defined as the second plate. The distance at which the ion can approach the surface of the electrode is limited by a monolayer of solvent molecules, which is assumed to exist between the ion and the electrode. This configuration is known as the “Helmholtz Plane” (HP). This model contains two principal defects related to the fact that it predicts the capacitance C_d as constant, which is not true in practice:⁵

- it neglects interactions that occur further from the electrode than the first layer of adsorbed species.
- it does not take into account any structural dependence on the potential applied and the electrolyte concentration.

The expression of the capacitance in the Helmholtz model is defined by analogy with a capacitor in equation 2.1:

$$C_d = \frac{\varepsilon\varepsilon_0}{d} \quad (2.1)$$

where ε is the dielectric constant of the medium, ε_0 is the permittivity of the free space and d the distance between the two charged plates.

The arrangement of ions in the double layer in the Helmholtz model and the variation of the electrostatic potential ϕ as a function of the distance x from the electrode are shown in Figure 2.1. One can observe that in this model, with x_H being the distance of closest approach of the

charges from the electrode surface, the decay of the electrostatic potential is linear from ϕ_M to ϕ_S (where ϕ_M is the potential of the metal and ϕ_S the potential at the Helmholtz plane).

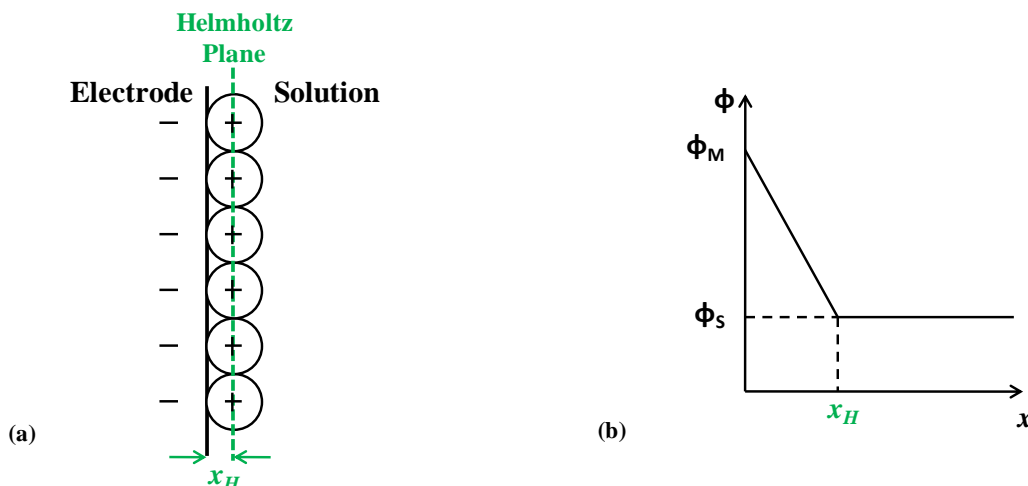


Figure 2.1: Schematic representation of the Helmholtz model of the electrical double layer (a) and variation of the electrostatic potential ϕ as a function of the distance x from the electrode (b). Adapted from Brett.⁶

Therefore, an alternative model of the interfacial region is needed.

2.2.2 The Gouy-Chapman model

Gouy and Chapman⁷⁻⁹ developed a “double layer” model in which they considered that the applied potential and the electrolyte concentration both influenced the value of the double layer capacity. The double layer would not be compact as in Helmholtz’s description, i.e. charges are not fixed anymore, but of variable thickness, the ions being free to move: this is called the *Diffuse Double Layer*. In this model, the electrical potential decreases exponentially away from the surface to the bulk solution, and the distribution of species with distance from the electrode obeys Boltzmann’s law. In practice, the capacity-potential curves were incorrect in this model and the predicted dependence on concentration was not observed. In

experimental terms, the two models above represent the two possible extremes of behaviour of an electrochemical interface in terms of electrolyte concentration. Modern interpretations are based on the model proposed by Stern¹⁰ that combines the key features of the Helmholtz and Gouy-Chapman models.

2.2.3 The Stern model

Stern considered that the double layer was formed by a compact layer of ions next to the electrode followed by a diffuse layer extending into the bulk solution. From an electrical stand point, it is equivalent to two capacitors in series, where the interfacial capacitance C_d is given by the following equation:

$$\frac{1}{C_d} = \frac{1}{C_H} + \frac{1}{C_{GC}} \quad (2.2)$$

where C_H and C_{GC} are respectively the contributions of the differential capacity of the interface due to the Helmholtz layer and to the diffuse layer.

As shown in Figure 2.2, the potential distribution across the interface drops sharply between the electrode and the Outer Helmholtz Plane, beyond which the potential falls gradually. However, parameters such as interaction of ions with solvent molecules are not taken into account in Stern's model, which is an experimental contradiction.

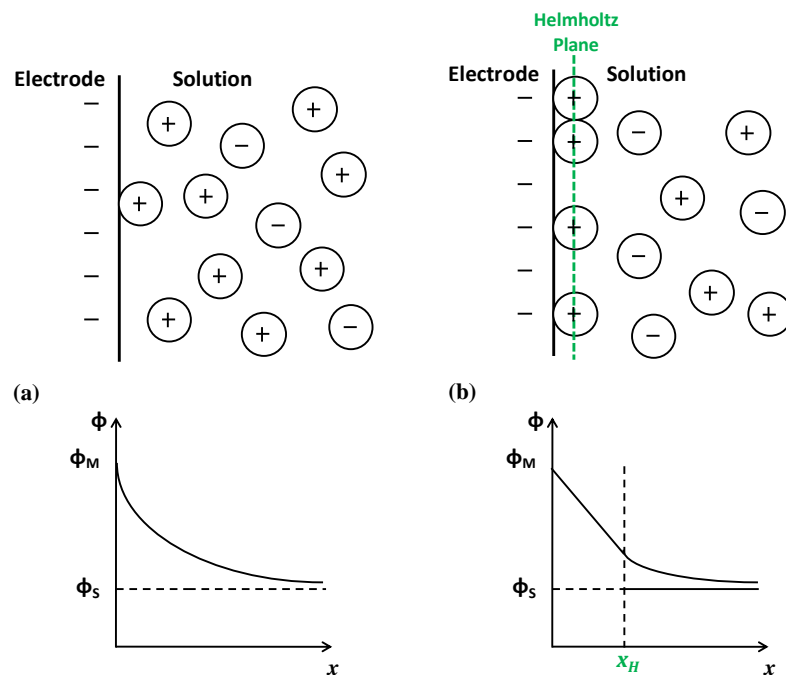


Figure 2.2: (a) the Gouy-Chapman model of the double layer and (b) the Stern model of the double layer. The variation of the electrostatic potential ϕ as a function of the distance x from the electrode is given below each diagram.

2.2.4 The Grahame model

Later, Grahame^{11,12} extended the Stern model by presenting a triple layer model. The difference between his model and Stern's model is the inclusion of specific adsorption: a specifically adsorbed ion loses its solvation, approaching closer to the electrode surface. Besides this, it can have the same charge as the electrode or the opposite charge but the bonding is stronger.⁵ The first layer extends from the electrode to the axis through the centre of the specifically adsorbed ions, and is called the Inner Helmholtz Plane (IHP). The second layer is defined by the plane drawn through the centre of ions, at a distance limited by the solvation shell of the ion: it is termed the Outer Helmholtz Plane (OHP). Finally, the third layer consists of the diffuse layer, that is to say the region that lies beyond the OHP.

Moreover, in Grahame's model, the potential changes linearly with distance up to the OHP and then exponentially through the diffuse double layer from which the effect decreases with increasing concentration in solution. The model of the electrode/electrolyte interface was therefore modified and a new (closer) plane of minimum approach identified.

2.2.5 The Bockris *et al.* model

The later model was proposed by Bockris *et al.*¹³ where the predominant role of solvent at the interface was taken into account: the solvent dipoles are oriented according to the charge on the electrode where they form a layer with the specifically adsorbed ions. They defined a plane where the ions are no longer influenced by the charge on the electrode. In addition, the triple layer model consisting of the IHP, the OHP and the diffuse layer presented in the previous section, remains valid here. In the Bockris *et al.* model, the variation of the electrostatic potential with distance is qualitatively similar to that of the Grahame model and it appears to be the best one to explain the role of the solvent in the double layer. Figure 2.3 gives a schematic diagram of this electrified interface's model. However, the electronic distribution of charges has not been fully characterised and requires further analysis by surface analytic tools.

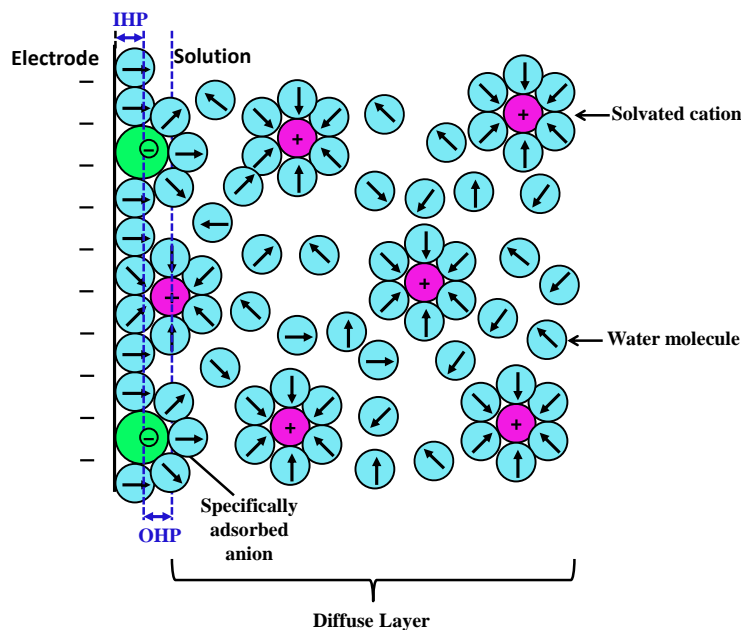


Figure 2.3: Schematic of the electrode/solution interface structure proposed by the Bockris *et al.*¹³ electrified interface model.

2.3 The electrochemical cell and the three-electrode system

The investigation of electrochemical systems is concerned with the processes and factors that affect the transport of charge across the interface between an electrode and a solution.⁵ To do so, one must understand the events that occur in this interfacial region when a potential is applied and current passes.

An electrode at which no charge transfer occurs, regardless of the potential imposed by an external source of voltage, is called an Ideal Polarizable Electrode, IPE.^{5,14,15} Although no real electrode is capable of behaving as an IPE over the whole range available in solution, over limited potential ranges several systems can approach ideal polarisability. The behaviour of the electrode-solution interface, shown to act like a capacitor, is such that when an electrode in solution is polarised, the charge on the metal q^M is compensated by an excess of cations or

anions q^S around the electrode surface in the solution. As developed in the previous section, the whole set of charges and dipoles at the solution interface are called the “Electrical Double Layer”.^{5,14,15} When the potential is changed, the sole effect is to transfer charge to the double layer.

In most experiments, only the reactions occurring at a single electrode are of interest, which is called the working electrode (WE), but it is not possible to measure a single electrode potential difference. In order to measure a potential difference two electrodes are required, which implies the presence of two electrochemical interfaces.¹⁴ One calls such an assembly of interfaces an electrochemical cell and the potential difference measured is actually the sum of two separate interfaces. The absolute contribution from each electrode remains unknown. However, the electrochemical investigation of a single electrode-solution interface is still possible.

In order to focus on the working electrode, the other electrode is chosen to be non-polarisable, i.e. possessing a constant potential. This is called the reference electrode (RE), and any changes in the cell are therefore assigned to the WE. When measuring the potential of the latter against a RE during the passage of current through the system, an ohmic drop equal to iR_s will be included in the measured potential, where R_s is the solution resistance. In that case, the potential of the working electrode is:

$$E = E_{appl} - iR_s \quad (2.3)$$

where E is the potential measured at the WE, E_{appl} is the potential applied and iR_s is the ohmic potential drop in the solution.

As an absolute value of the electrode potential cannot be obtained for any specific electrode, relative scales are used that permit the measurement of electrodes against the same standard. The Standard Hydrogen Electrode (SHE) is often used as the reference and is assigned the standard electrode potential of $E^0 = 0 \text{ V}$.¹⁴

When iR_s is small ($<1\text{-}2 \text{ mV}$), this two-electrode configuration may be used to determine the i - E curve. However, when iR_s is high, that is to say when currents that passes across the RE-solution interface or when solutions' resistances are higher (such as those based on many nonaqueous solvents), the ideal non-polarisability criterion of the RE is not true anymore.

This drawback can be prevented by the addition of a third electrode called the counter or auxiliary electrode (CE or AE). In this configuration, the current is passed between the WE and the CE, and the RE acts solely to measure the potential difference across the electrode-solution interface. In addition, the criteria for choosing a CE are different. Firstly, the CE is chosen to be an electrode that does not produce substances by electrolysis that will reach the electrode surface and cause interfering reactions.⁵ Secondly, the size of the CE must be large enough to provide current at a sufficient rate so that it does not become the limiting factor in the cell response. Finally, in order to have a uniform electric field generated with the WE, its shape and position within the cell must be chosen carefully.

On the other hand, the RE should be placed in close proximity to the WE, and should be chosen with a minimal surface area in order to keep its non-polarisability characteristic, to reduce as much as possible the iR drop and therefore to get an accurate measured potential difference.

However, even with the three-electrode configuration, not all of the iR_s is removed but modern electrochemical instrumentation frequently includes circuitry to suppress the iR_u term, where R_u is the uncompensated fraction of iR_s .

2.4. Interfacial kinetics

Electrode reactions are heterogeneous chemical processes that may involve one or more electron transfer steps across the electrical double layer.⁵ The distinctive feature of reactions at an electrode is the strong dependence of both the surface concentrations and the rate of reactions on the electrode potential. To show why this is the case, consider a metal in contact with a solution: controlling the potential applied at the working electrode controls the energy of the electrons within the WE. For electron transfer to take place, the electron energy in both the electrode and the molecule in solution have to correspond. For soluble species, it is the Lowest Unoccupied Molecular Orbital (LUMO), and for the metal it is the Highest Occupied Molecular Orbital (HOMO) (which is called the Fermi level). Illustrations of both reduction and oxidation processes are presented below in Figure 2.4:

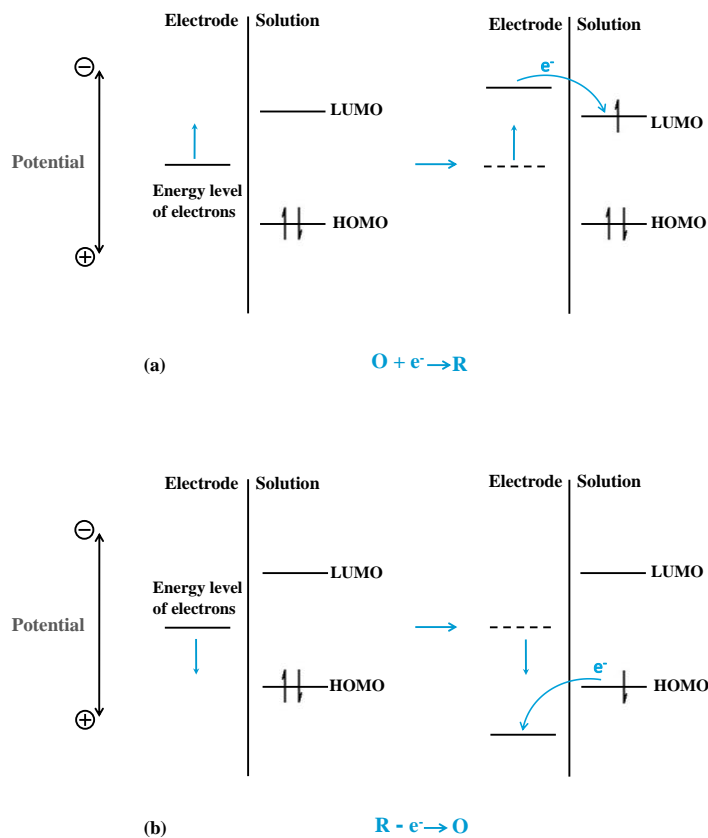
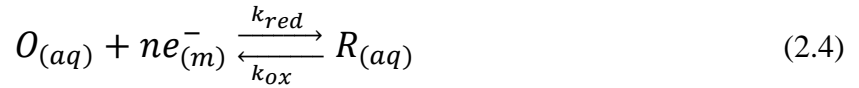


Figure 2.4: Illustration of the Reduction (a) and Oxidation (b) processes (where O the oxidised species and R is the reduced species)

By driving the electrode to more negative potential (Figure 2.4.(a)), the energy of the electron is raised until transfer from the metal into a vacant orbital takes place, and the rate of reduction of O increases. Likewise, by imposing a more positive potential (Figure 2.4.(b)), electron transfer from the solution to the electrode becomes thermodynamically favourable and an oxidation current is passed.

For a quantitative description of interfacial charge transfer dynamics, the determination of the potential-dependent rate constants is required. If we consider a simple electrode process where O and R are engaged in electron transfer, one has:



where k_{red} and k_{ox} are the heterogeneous rate constants of the reductive and oxidative electron transfer reactions, respectively and ne^- is the number of transferred electrons from the electrode.

Assuming it is a first order reaction where both forward (reduction) and backward (oxidation) reactions take place, the net reaction rate, and therefore also the current measured in the external circuit, is given by the difference between the forward and backward rates such as:

$$v = v_{red} - v_{ox} = k_{red}C_0^* - k_{ox}C_R^* = \frac{i}{nFA} \quad (2.5)$$

and,

$$i = i_c - i_a \quad \text{with} \quad i_c = nFAk_{red}C_0 \quad (2.6) \text{ and } (2.7)$$

$$\text{and} \quad i_a = nFAk_{red}C_R \quad (2.8)$$

where i is the net current flowing for the reaction, i_c and i_a are the currents that pass during the reductive and oxidative processes, respectively.

In activated complex theory or transition state theory, the reaction between O and R (considered as reaction coordinates) is represented as passing along a reaction coordinate through an activated complex barrier: the reaction can be seen as occurring via a path that involves the reactants $[O_{(aq)} + e_{(m)}^-]$ overcoming an energy barrier to becoming products $R_{(aq)}$ (see Figure 2.5). The barrier corresponds to the standard free energy of activation ΔG^\ddagger and, by analogy with the Arrhenius equation, one can write:

$$k_{red} = Ae^{\frac{-\Delta G_{red}^\ddagger}{RT}} \text{ and } k_{ox} = Ae^{\frac{-\Delta G_{ox}^\ddagger}{RT}} \quad (2.9)$$

where ΔG_{red}^\ddagger is the standard free energy and A is a frequency factor which accounts for the rate of collision of the electroactive molecule with the electrode surface.

The model shown in Figure 2.5 illustrates the way that the potential affects the net rates and directions of electrode reactions: if the potential changes from its equilibrium value E_0 by ΔE to a new value of the applied potential to the cell E_{appl} , then the relative energy of the electron in the electrode becomes: $-F\Delta E = -F(E_{appl} - E^0)$.

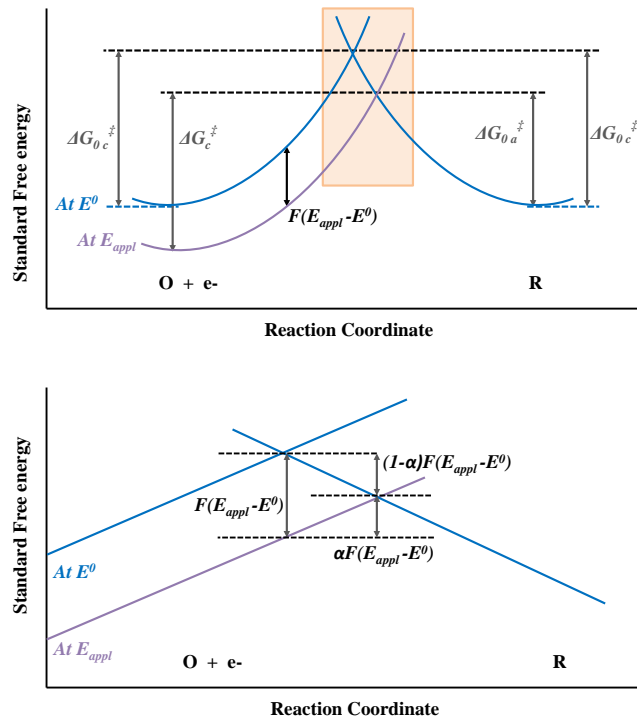


Figure 2.5: Schematic of the effects of a potential change on the standard free energies of activation for reduction and oxidation. The lower figure is a magnification of the boxed area in the upper figure.

By introducing the transfer coefficient α as the fraction of applied potential that drives the reaction, which is a measure of the symmetry of the energy barrier, and with $0 \leq \alpha \leq 1$, the activation free energies may be defined as:

$$\Delta G_{red}^{\ddagger} = \Delta G_{0\ red}^{\ddagger} + \alpha F(E_{appl} - E^0) \quad (2.10)$$

$$\Delta G_{ox}^{\ddagger} = \Delta G_{0\ ox}^{\ddagger} - (1 - \alpha)F(E_{appl} - E^0) \quad (2.11)$$

By combining equations (2.9), (2.10) and (2.11), one obtains:

$$k_{red} = A e^{\left(\frac{-\Delta G_{red}^{\ddagger}}{RT}\right)} e^{\left(\frac{-\alpha F(E_{appl} - E^0)}{RT}\right)} \quad (2.12)$$

$$k_{ox} = A e^{\left(\frac{-\Delta G_{ox}^{\ddagger}}{RT}\right)} e^{\left(\frac{(1-\alpha)F(E_{appl} - E^0)}{RT}\right)} \quad (2.13)$$

In addition, the product of the first two factors in each of these above equations is independent of the potential and is equal to the rate constant when $E_{appl} = E^0$. In fact, reduction and oxidation rates being equivalent at equilibrium, a standard rate constant k_0 can be introduced in those expressions, and one has:

$$k_{red} = k_0 e^{\left(\frac{-\alpha F(E_{appl} - E^0)}{RT}\right)} \quad (2.14)$$

$$k_{ox} = k_0 e^{\left(\frac{(1-\alpha)F(E_{appl} - E^0)}{RT}\right)} \quad (2.15)$$

Finally, if one introduces the term η , known as the overpotential such as $\eta = (E_{appl} - E^0)$, the Butler-Volmer equation can be written. It expresses the current density that flows through

the electrode/solution interface due to the overpotential in terms of two kinetics parameters: the exchange current density and the transfer coefficient α .

$$i = nFAk_0[e^{(1-\alpha)\eta F/RT} - e^{-\alpha\eta F/RT}] \quad (2.16)$$

When changing the electrode potential or the solution potential, not only the absolute value of the free energies of the reactants, products and transition state changes but also their relative values via α . The potential dependence of the electrode reaction kinetics shows that the free energy barriers to reduction and oxidation are changed as well.

2.5 Mass transport

The rate of an electrode reaction v is not only determined by the rate of electron transfer at the electrode but also by the concentration of species at the electrode. Therefore, the rate of a reaction is influenced by the transport of the species to and from the electrode. An overall electrochemical reaction can be decomposed as shown in Figure 2.6. Besides charge transfer, mass transport has to be considered in order to establish a relationship between the current i , the potential E and the concentrations of O and R .

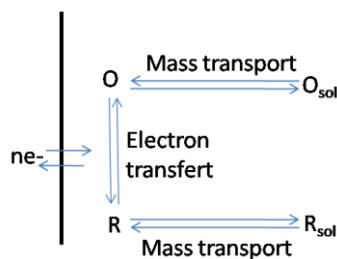


Figure 2.6: The different steps of an electrochemical reaction.

Transport can occur by diffusion, convection or migration.

Diffusion is the movement of a species due to a concentration gradient caused by oxidation or reduction of species at the electrode surface. Migration is the movement of a charged species under the influence of an electric field caused by a potential gradient applied between the electrodes. Normally, conditions are chosen such that migration effects can be neglected. These conditions correspond to the presence of a large quantity of supporting electrolyte which does not interfere in the electrode reaction. The purpose of the background electrolyte is to carry the current in the bulk solution, and thereby remove the dependence of the current upon the migration of the reactants in solution. Its concentration is generally set to 50 to 100 times that of the electroactive species under investigation.¹⁶ The addition of a high concentration of supporting electrolyte also removes problems of solution resistance and thereby unwanted contributions to the total cell potential.

Convection (forced) is the movement of species under the influence of a flow speed gradient caused by stirring of the solution or hydrodynamic transport. Natural convection, due to thermal gradient also exists. However, under most commonly used conditions this movement is negligible; the use of sufficiently high potential scan rate permits the neglect of species flow induced by natural convection. We will consider situations where pure diffusion and convective diffusion are important.

The particular case of a planar electrode will now be considered in order to study the diffusion phenomena in a one-dimensional axis, along (0x). The flux J expressed in $\text{mol s}^{-1} \text{cm}^{-2}$ is the number of moles of electroactive species O that pass a given location x per time unit per cm^2 of area normal to the axis of diffusion. In accordance with Fick's first law, the flux of a species O is directly proportional to its concentration gradient:

$$J_O(x, t) = -D_O \frac{\partial C_O(x, t)}{\partial x} \quad (2.17)$$

where D_O is the diffusion coefficient of the species O (in $\text{cm}^2 \text{s}^{-1}$) and $\frac{\partial C_O}{\partial x}$ the concentration gradient.

According to the law of conservation of matter, for each O that undergoes electron transfer at the electrode, a molecule of R must be produced. By equating the current to the flux, one has:

$$\frac{i}{nFA} = D_R \left(\frac{\partial C_R}{\partial x} \right)_{x=0} = -D_O \left(\frac{\partial C_O}{\partial x} \right)_{x=0} \quad (2.18)$$

Fick's second law relates the change in concentration with time and distance and is written as:

$$\frac{\partial C_O(x, t)}{\partial t} = D_O \frac{\partial^2 C_O(x, t)}{\partial x^2} \quad (2.19)$$

In order to solve this equation, it is necessary to define the semi-infinite and electrode surface boundary conditions.

2.5.1 Transport by diffusion control

In the case of an electrolytic solution where no stirring occurs, mass transport is dominated by diffusion. Figure 2.7 gives the evolution of the concentration profiles with time, for a system under diffusion control, as a function of the distance x from the electrode.

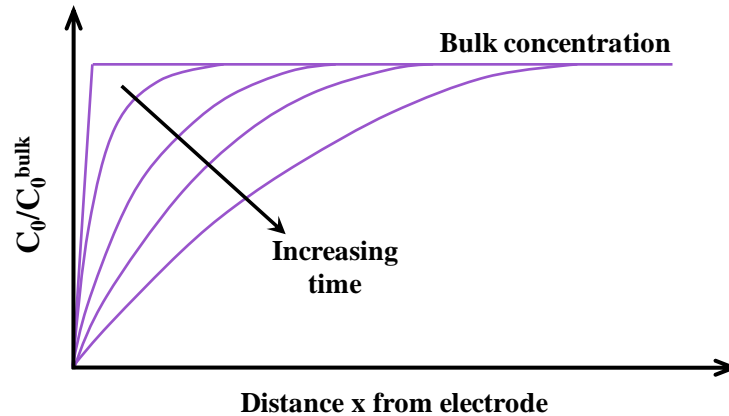


Figure 2.7: Concentration profiles as a function of distance from the electrode under diffusion control.

To solve the linear diffusion equation, the three boundary conditions are:

$$\text{Initial condition: } C_o(x, t) = C_o^{bulk}$$

$$\text{Semi-finite condition: } C_o(\infty, t) = C_o^{bulk}$$

$$\text{Condition at the surface of the electrode: } C_o(0, t) = 0 \text{ (for } t > 0 \text{)}$$

The initial condition states that the solution concentration is uniform throughout the solution before the experiment starts ($t=0$). Then, the semi-infinite condition expresses that regions distant from the electrode are unperturbed by the experiment. Finally, the third condition corresponds to the condition at the surface of the electrode ($x=0$), after applying a potential at

the electrode. Those boundary conditions, combined with a Laplace transformation of Fick's second law gives the equation of the concentration profile:

$$C_0(x, t) = C_0^{bulk} \operatorname{erf} \left[\frac{x}{2\sqrt{D_0 t}} \right] \quad (2.20)$$

from this the Cottrell equation is derived:

$$i(t) = i_d(t) = \frac{nFAD_0^{1/2}C_0^{bulk}}{\pi^{1/2}t^{1/2}} \quad (2.21)$$

where i_d is the diffusion-limited current and the suffix indicates that the current is determined entirely by diffusion.

2.5.2 Transport by convective diffusion

In the case of forced convection, for example stirring, the transport of species to and from the electrode is much faster than via diffusion. For a system under conditions of a convective diffusion regime, the following considerations hold. A simplified theoretical approach considers that a stagnant layer exists close to the electrode within which transport is dominated by diffusion, the stagnant layer being the diffusion layer. Two different places in solution have to be considered:

- For $x < \delta$: mass transport is diffusion-controlled. This region is the diffusion layer.
- For $x > \delta$: the efficiency of stirring of the solution is good enough to maintain the concentration of species uniform and equal to the bulk value, here C_0^{bulk} .

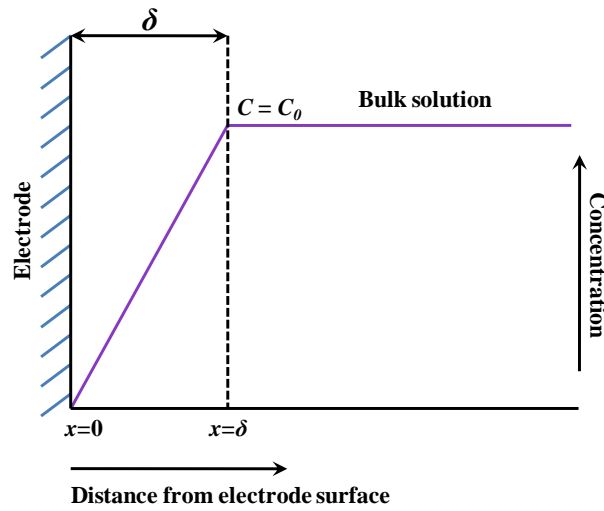


Figure 2.8: Schematic of the evolution of concentration throughout the solution as a function of the distance from the electrode surface.

The system is considered as following a steady state regime, it is independent of time and the diffusion flux can be expressed as follows:

$$J_i = D_i \frac{1}{\delta} (C_i^* - C_i^{El}) \quad (2.22)$$

where C_i^* is the bulk concentration of species i and C_i^{El} is the concentration of species i at the electrode.

The current density is thus a function of the difference between the concentration of a species (O or R) in the bulk solution and its concentration at the electrode surface. The anodic and cathodic current density can be written as:

$$j_a = \frac{nFD_R}{\delta} (C_R^* - C_R^{El}) \quad (2.23)$$

$$j_c = \frac{nFD_O}{\delta} (C_O^* - C_O^{El}) \quad (2.24)$$

When the diffusion rate is much smaller than the charge transfer rate at the electrode surface then $C_i^{El} = 0$. The electroactive species is consumed as it approaches the electrode surface and the limiting current density is proportional to the concentration of species in the bulk solution. It is defined by the following values:

$$j_{lim,a} = \frac{nFD_R C_R^*}{\delta} \quad (2.25)$$

$$j_{lim,c} = \frac{nFD_O C_O^*}{\delta} \quad (2.26)$$

2.6 Experimental considerations

To study electrode processes, potential sweep methods are the most widely used and are based on the concept of continuously varying the potential that is applied across the electrode-solution interface and measuring the resulting current. Cyclic voltammetry is one of those methods and will be presented in the first part of this section.

The second part of this section is concerned with chronoamperometry, a potential step experimental method, where the electrode potential is controlled and the current is measured as a function of time.

Among voltammetric methods, both techniques cited above are categorised as transient techniques which give a current response that is time-dependent. The other category is concerned with time-independent techniques, called steady-state techniques.

2.6.1 Cyclic Voltammetry

Cyclic voltammetry is a very popular technique for initial electrochemical studies of new systems and for the study of complex electrode reactions. In a cyclic voltammetry experiment,

the triangular potential excitation signal (see Figure 2.9) causes the potential of the working electrode to be swept back and forth between two chosen limits (the switching potentials) at a steady rate, ν , and the current is monitored continuously. The current-potential curves obtained give information about the nature and concentration of species O and R , and the data may be used to evaluate electrochemical kinetics parameters or reaction mechanism in the case of reactions coupled to electron transfer.

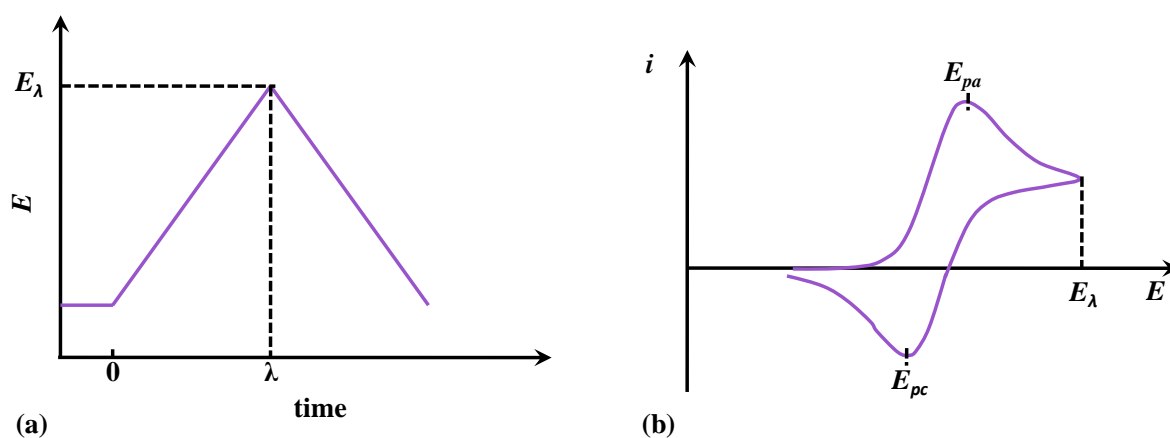


Figure 2.9: Variation of the applied potential in a cyclic voltammetry experiment. (a) Cyclic potential sweep. (b) Resulting cyclic voltammogram.

For the following treatments, we will consider the reaction $O + ne^- \rightleftharpoons R$, assuming semi-infinite linear diffusion and a solution initially containing only species O .

Let us assume that diffusion is the main mode of transport under semi-infinite linear diffusion conditions. During the relatively short time of measurement, it is assumed that natural convection is not significant.

If the applied potential E is such that the electroactive species present at the electrode surface are oxidised (or reduced), then the anodic current (or cathodic) increases during the potential

step until it reaches a maximum, as shown in Figure 2.9. Then, the concentration of species consumed at the electrode/solution interface decreases and, under conditions of semi-infinite linear diffusion, the “after-peak” current then decreases following $1/(\pi t)^{1/2}$ (Cottrell law). The current maximum obtained is proportional to the concentration of the corresponding species.

The behaviour of electrodes can be classified according to the speed of the electrode processes that take place. One can distinguish three types of systems: reversible, irreversible, and quasi-reversible.

Reversible system

A so-called reversible system or Nernstian system is a system where charge transfer is fast. The concentrations of electroactive species at the electrode surface are therefore given by the Nernst equation which, when combined with the Butler-Volmer equation, gives the following expression for the peak current, i_p :

$$i_p = 0.4463 \left(\frac{F^3}{RT}\right)^{1/2} n^{3/2} A D_0^{1/2} C_0^* \nu^{1/2} \quad (2.27)$$

At 25°C, for A in cm^2 , D_0 in $\text{cm}^2 \text{ s}^{-1}$, C_0^* in mol cm^{-3} , and ν in V s^{-1} , this results in the so-called Randles-Sevcik equation where i_p , in ampere, is given by:

$$i_p = (2.69 \times 10^5) n^{3/2} A D_0^{1/2} C_0^* \nu^{1/2} \quad (2.28)$$

This equation permits calculation of the diffusion coefficient of the species O.

From the peak potential, E_p , and the half-peak potential, $E_{p/2}$, the number of electrons transferred, n , can be determined via the following equation:

$$|E_p - E_{p/2}| = 2.20 \frac{RT}{nF} = \frac{5.65}{n} \text{ mV at } 25^\circ\text{C} \quad (2.29)$$

The potential midway between the two peak potentials is called the formal potential and can be calculated as follows:

$$E^{0'} = \frac{E_{pa} + E_{pc}}{2} \quad (2.30)$$

Finally, if the product formed is stable and the scan rate is sufficiently high to allow neglect of the retro-diffusion of the species from the interface to the bulk solution, then the peak current ratio, for a reversible couple with no kinetics complications, gives:

$$\frac{i_{pa}}{i_{pc}} = 1 \quad (2.31)$$

Irreversible system

An irreversible system is a system for which the electron transfer is slow. The Nernst relationship is not applicable, and the reverse reaction can be neglected. In that case, the peak current is given by:

$$i_p = 0.4968nFAC_0^*D_0^{1/2}v^{1/2} \left(\frac{\alpha n_a F}{RT} \right)^{1/2} \quad (2.32)$$

$$\text{Thus at } 25^\circ\text{C:} \quad i_p = (2.99 \times 10^5)n(n_a\alpha)^{1/2}AD_0^{1/2}C_0^*v^{1/2} \quad (2.33)$$

where α is the transfer coefficient and its value lies between 0 and 1.

Under those conditions, the peak potential varies with the scan rate according to the Nicholson and Shain relationship:

$$E_p = E^{0'} + \frac{RT}{\alpha n_a F} \left[0.780 + \ln \left(\frac{D_0^{1/2}}{k^0} \right) + \ln \left(\frac{\alpha n_a F v}{RT} \right)^{1/2} \right] \quad (2.34)$$

where

$$|E_p - E_{p/2}| = 1.857 \frac{RT}{\alpha n_a F} = \frac{47.7}{\alpha n_a} \text{ mV at } 25^\circ\text{C} \quad (2.35)$$

Experimentally speaking, cyclic voltammograms, for irreversible systems, are identified by the presence of a unique peak (no reverse peak) or by an oxidation peak and a reduction peak that are highly separated from one another.

Quasi-reversible system

For a quasi-reversible system, even though characterised by a slow electron transfer rate, the reverse reaction cannot be ignored. The peak shape then depends on α and on a dimensionless parameter Λ as follows:

$$\Lambda = \frac{k^0}{(D_O^{(1-\alpha)} D_R^{\alpha} \frac{F n_a}{RT} v)^{1/2}} \quad (2.36)$$

The value of Λ is determined from the difference between the anodic peak and cathodic peak. For values of Λ greater than 15, the system has to be considered as fast and in that case, the equations describing a reversible system are applicable. The system is thus diffusion-limited. For values of Λ between 15 and $10^{-2(1+\alpha)}$, the system is so called quasi-reversible and the reaction rate at the electrode is controlled by charge transfer but as well by diffusion. Finally, if Λ is less than $10^{-2(1+\alpha)}$, the system is said to be irreversible and the reaction rate at the electrode is only limited by charge transfer. In that case, the equations that describe totally irreversible systems can be used.

6.2 Chronoamperometry

In a chronoamperometry experiment, the current is monitored after a potential step at $t=0$ to an electrode, in a solution containing either oxidised or reduced species, from a value where there is no electrode reaction to the value where the electroactive species that reach the electrode reacts. Immediately following this step, a large current is detected and falls steadily with time, as electrolysis proceeds, as shown in Figure 2.10:

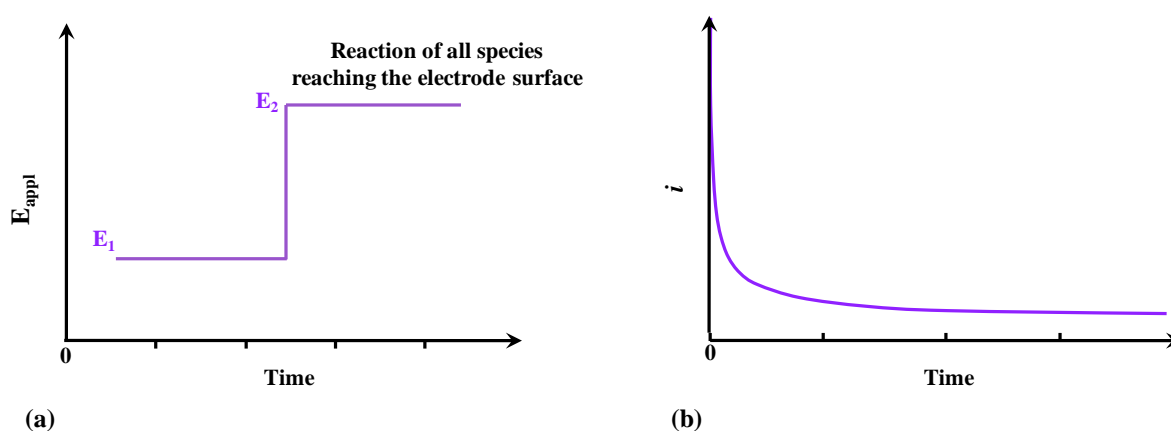


Figure 2.10: Variation of the applied potential in a chronoamperometry experiment. (a) Waveform for a potential step experiment. (b) Resulting chronoamperogram.

The area under the $i = f(t)$ curve represents the total quantity of electricity $Q(t)$ that passes through the interface and is defined as follows:

$$Q(t) = \int_0^t I(t) dt \quad (2.37)$$

Q is related to the amount of material that has been converted and i to the instantaneous rate at which conversion occurs. Q can be defined by Faraday's law such as :

$$Q = nFe \quad (2.38)$$

where n is the number of moles converted and e the number of electrons transferred.

By considering Fick's first law of diffusion introduced earlier (Equation 2.17) and by assuming that the concentration of O varies uniformly over a distance δ from the electrode surface, one has:

$$\frac{i}{nFA} = D_O \frac{c_O - c_O^*}{\delta} \quad (2.39)$$

Recalling Cottrell's equation (Equation 2.21), one finally obtains an expression for the diffusion layer, δ , and of the mass transfer coefficient, k_d , which shows that the diffusion layer thickness δ increases with time at a fixed potential:

$$\delta = D_O^{1/2} \pi^{1/2} t^{1/2} \left(\frac{1 - c_O}{c_O^*} \right) \quad \text{and} \quad k_d = \left(\frac{D_O}{\pi t} \right)^{1/2} \quad (2.40) \text{ and } (2.41)$$

References

1. Von Helmholtz, H. L. F.; Abhandl. W. *Physik. Tech. Reichsanstalt* **1879**, *1*, 925.
2. Quincke, G. *Pogg. Ann.* **1861**, *113*, 513.
3. Von Helmholtz, H. L. F. Some laws concerning the distribution of electrical currents in conductors with applications to experiments on animal electricity. *Ann. Physik* **1853**, *89* (6), 221-233.
4. Von Helmholtz, H. L. F. *Ann. Physik* **1879**, *7*, 337.
5. Bard, A. J.; Faulkner, L. R. *Electrochemical Methods, Fundamentals and Applications*; Second Edition, John Wiley and Sons, **2004**.
6. Brett, C. M. A.; Brett, A. M. O. *Electrochemistry: Principles, Methods, and Applications*; Oxford University Press Inc., New York, **1993**.
7. Chapman, D. L. *Phil. Mag.* **1913**, *25*, 475.
8. Gouy, G. *J. Phys. Radium* **191**, *9*, 457.
9. Gouy, G. *Compt. Rend.* **1910**, *149*, 654.
10. Stern, O. The theory of the electrolytic double shift. *Z. Elektrochem.* **1924**, *30*, 508-516.
11. Grahame, D. C. The Electrical Double Layer and the Theory of Electrocapillarity. *Chem. Rev.* **1947**, *41* (3), 441-501.
12. Grahame, D. C. Electrode Processes and the Electrical Double Layer. *Ann. Rev. Phys. Chem.* **1956**, *6*, 337-358.
13. Bockris, J. O.; Devanathan, M. A. V.; Muller, K. On Structure of Charged Interfaces. *Proc. R. Soc. London Ser. A* **1963**, *274* (1356), 55-79.

14. Bockris, J. O.; Reddy, A. K. N.; Gamboa-Aldeco, M. *Modern Electrochemistry, Volume 2A*; Plenum Publishers, **2000**.
15. Southampton Electrochemistry Group *Instrumental Methods in Electrochemistry*; Ellis Horwood Ltd Publisher, **1985**.
16. Sawyer, D. T.; Roberts JR, J. L. *Experimental Electrochemistry for Chemists*; New York: Wiley, **2010**.

Chapter 3: X-ray Absorption Spectroscopy

3.1 Introduction

X-ray Absorption Spectroscopy (XAS) has been known since the early 1920s, but its use as an analytical tool has been possible since the 1970s with the availability of Synchrotron radiation sources. It permits the characterisation of local atomic order in any material, irrespective of its chemical state, and it does not require long range order. X-ray Absorption Spectroscopy gives information on interatomic distances (up to a range of 5 Å from the element of interest^{1,2}), oxidation states and the nature and number of neighbours surrounding the absorbing atom. In addition, it distinguishes itself by its selectivity since it allows study of each element in turn of a material under study. Finally, it permits the study of samples at low concentration.

In XAS, broadly speaking, two types of analyses are possible: EXAFS (Extended X-ray Absorption Fine Structure) and XANES (X-ray Absorption Near Edge Structure).

In this chapter, after describing the principle of the interaction of X-rays with matter, and the different physical phenomena that it leads to, the attention will be focused on EXAFS by recalling its historical development and by establishing the EXAFS formula at the K-edge under the single-scattering approximation. Then, multiple scattering theory will be briefly evoked. To conclude this chapter, the IFFEFIT software that has been used to extract the structural information of our EXAFS measurements, has been developed as the data analysis tool.

3.2 The principle of interaction of X-rays with matter

X-rays are electromagnetic radiation with energies that range from 1 to 200 keV. When X-rays interact with matter, three types of interactions may be distinguished: scattering, elastic and inelastic, and the photoelectric effect. XAS relies on the photoelectric effect in which absorption of

a photon leads to the ejection of an electron from a bound level (K, L, etc. shell) of the absorbing atom, and followed by the emission of a photoelectron. The level to which the electron is promoted may be a bound state within the same atom or an unbound state, determined by the energy of the incoming photon, $h\nu$, and the binding energy of the electron E_b . The final energy of the ejected photoelectron E_f is given by:

$$E_f = h\nu - E_b \quad (3.1)$$

The absorbing atom can then relax through several mechanisms, giving rise to fluorescence X-rays, Auger electrons or secondary electrons as shown schematically in Figure 3.1:

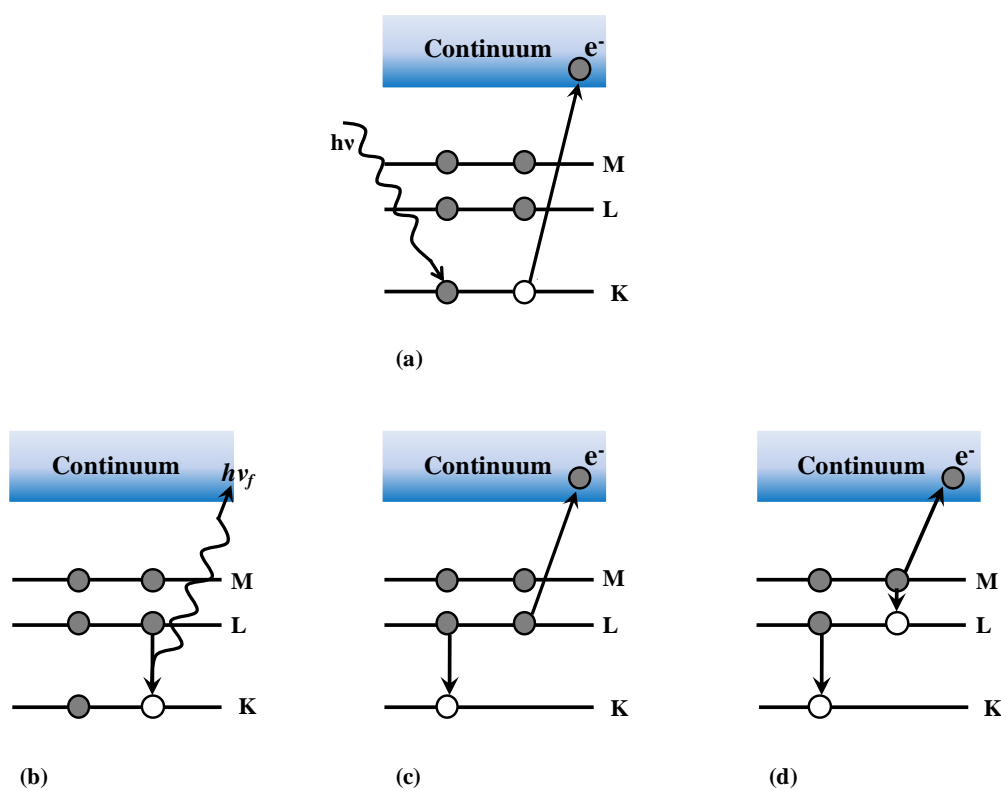


Figure 3.1: Schematic representation of X-ray photoionisation and subsequent ejection of a photoelectron (a) and the different relaxation processes of the excited atom: fluorescence (b), Auger electrons (c) or secondary electrons (d).

In the case of X-ray fluorescence, which is the phenomenon of particular interest for this study, an electron from an outer shell fills the hole created in the inner shell, yielding X-ray fluorescence characteristic of the absorbing material. The minimum photon energy required to eject an electron out of a specific atomic state is called the threshold energy, $E_0 = h\nu_0$, which corresponds to the binding energy of the electron.

From an experimental point of view, the measurement of the absorption consists of irradiating the medium of interest over a range of energies that includes the binding energy of core electrons of a selected element. The absorption of X-rays may be described by the Beer-Lambert law, and for a transmission experiment, one has:

$$\mu(E)x = \ln I_0/I_t \quad (3.2)$$

where I_0 and I_t are the intensities of the incoming and outgoing beams respectively. E is the photon energy, $\mu(E)$ is the absorption coefficient of the sample and x is the sample thickness.

The X-ray absorption coefficient depends on the incident beam energy in the following manner: as the energy of the photon increases, μ generally decreases until it reaches a certain critical energy called the absorption edge. At this point, the absorption coefficient increases sharply due to the ejection of a core electron of an atom and then decreases as the energy of the photon is further increased.

The absorption spectrum can be divided into three main regions: the pre-edge, the X-Ray Absorption Near Edge Structure (XANES) and the Extended X-ray Absorption Fine structure (EXAFS), as shown on a typical XAS spectrum in Figure 3.2. They correspond to the different physical processes that are taking place throughout the absorption and define themselves regarding the binding energy of the core electrons of the atom considered:

-in the pre-edge region, the incoming photon energy is below the ionisation energy E_0 (or threshold energy) but corresponds to a sufficient energy range to cause the excitation of an electron 1s of the absorbing atom, from the core level to higher vacant orbitals. This region gives information about the local electronic structure at short distances ($< 3 \text{ \AA}$) from the excited atom.

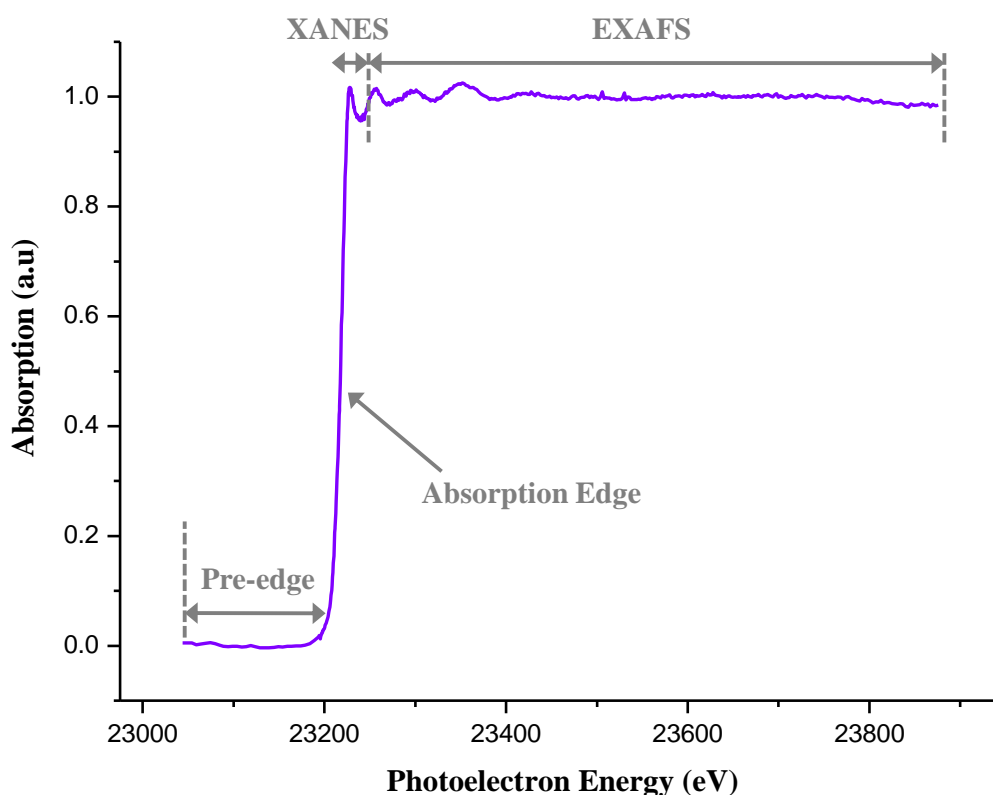


Figure 3.2: Typical EXAFS spectrum at the Rhodium edge.

-the XANES region corresponds to the part of the spectrum where the energy is close to the absorption edge: whilst the energy is below the threshold energy E_0 , the core electron is excited but is not ejected from the atom. This region gives information on the coordination number, the electronic configuration, and the oxidation state of the absorbing atom. Once the incoming photon energy exceeds E_0 , and up to 50 eV above E_0 , the core electron is then ejected from the atom into

the continuum. However, the energy of the emitted photoelectron has a low kinetic energy: its wavelength is comparable with interatomic distances and its mean free path is quite high. Therefore, there is a high probability that the photoelectron will scatter from more than one atom in the surroundings of the absorber, making the XANES region complex to analyse. In some cases, it is possible to theoretically interpret a XANES spectrum by use of ab initio calculation codes such as the FEFF code.³ However, this approach remains difficult.

-EXAFS generally refers to the region 40 to 1000 eV above the absorption edge. The ejected photoelectron to the continuum, having a high kinetic energy and a low free mean path, is essentially implicated in single scattering paths. The photoelectron can be viewed as a spherical wavefunction that is backscattered by neighbouring atoms. The incoming and outgoing wavefunctions give rise to constructive and destructive interferences, resulting in the oscillatory behaviour of the absorption coefficient (see Figure 3.3). The frequency of the oscillations is correlated to the interatomic distances between the neighbouring atoms and the absorber, whereas the amplitude of the sinusoidal modulation of μ vs E depends on the type and number of surrounding atoms but describes as well the thermal and structural disorder of the system. Therefore, simulation of EXAFS spectra can, in principle, give a full structural assignment on the local environment of the studied material.

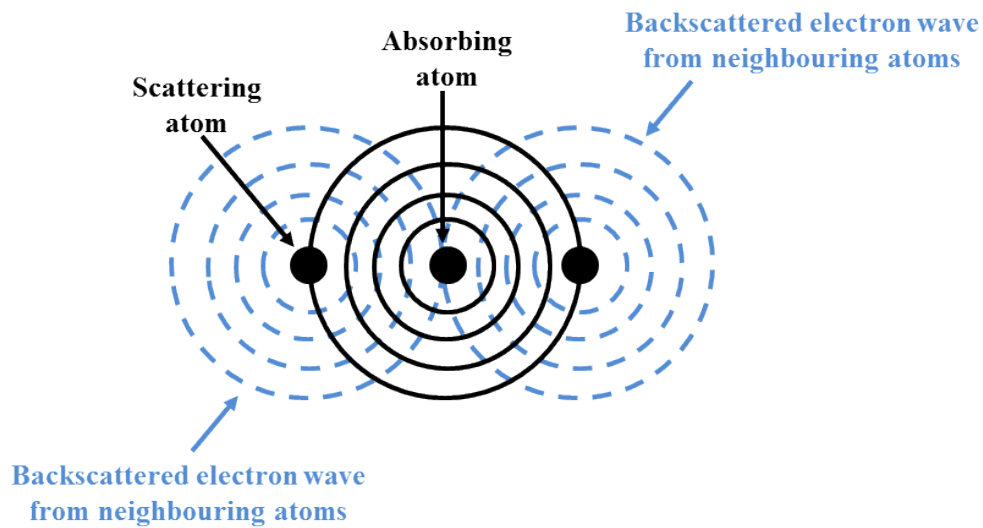


Figure 3.3: Schematic of the propagation and diffusion of the photoelectron wave.

Since EXAFS has been the technique mostly used in this work, it will be described in detail in the following section.

3.3 The EXAFS formula

3.3.1 Treatment of experimental spectra

The phenomenon of Extended X-ray Absorption fine structure was first observed in 1920 by Fricke and Hertz.^{4,5} They noticed that there was an oscillatory variation of the absorption coefficient for solid samples whereas in monoatomic gases the absorption coefficient decreases monotonically as a function of energy beyond the edge. It seemed therefore obvious at this time that those oscillations were linked to the environment of the atom that absorbs the radiation. However, it took a long time to establish a coherent physical explanation of EXAFS, which was first treated theoretically in the early 1930s.^{6,7} R.D. Kronig proposed a short range order (SRO) approach according to which oscillations were due to the modification of the final state wave function of the photoelectron caused by backscattering from neighbouring atoms.

It was not until the 1970s that three fundamental publications by Stern, Sayers, and Lytle produced the breakthrough for the modern EXAFS theory.⁸⁻¹⁰ These authors established the possibility of extracting structural information from the technique, such as bond distances and coordination numbers, by pointing out that a Fourier Transform (FT) of EXAFS with respect to the photoelectron wave number should peak at distances related to the atomic neighbours of the absorbing atom. In addition, they showed that the FT only revealed the first few shells of neighbouring atoms, making the SRO approach a valid theory. However, before the fine structure beyond the absorption edge became well understood as it is nowadays,¹¹⁻¹³ several approximations, modifications, and theoretical advances had to be realised (for full historical development of these advances, see Rehr and Albers¹⁴).

At the same time, the availability of Synchrotron radiation sources¹⁵⁻¹⁸ permitted the rapid development of the EXAFS technique. The high intensity (10^6 times over characteristic lines of conventional X-ray tubes), the broad spectral distribution, high collimation and variable polarisation make Synchrotron radiation sources an invaluable tool for structural analyses of chemical and biological systems where conventional diffraction methods are not applicable.

3.3.2 Single scattering EXAFS formula at the K edge

In this section, the classic EXAFS formula at the K-edge will be derived. Several approximations are required. The principal approximation is the single scattering approximation, which is to say that only the interaction of the photoelectron between two atoms is taken into account: the absorbing atom and a unique neighbouring atom. Such an approximation can be justified by the fact that in the EXAFS region, the photoelectron has a high kinetic energy and thus its scattering is principally back and forward, from 0 to π . This approximation only makes it possible to consider the first shell of neighbours, which has the shortest scattering pathlength. As it will be shown later,

this hypothesis leads to errors in the treatment and multiple scattering must be taken into account to make a quantitative treatment of the EXAFS spectrum.

The following derivation comprises four steps. Firstly, the absorption coefficient is expressed as a function of the transition probability of the electron of the absorbing atom to the photoelectron that propagates in the material. Secondly, the hypothesis and approximations are described. Then, the phaseshift experienced by the photoelectron is taken into account for the derivation. Finally, consideration of two physical factors: the core hole lifetime effects and the Debye-Waller factor leads to the establishment of the EXAFS formula at the K-edge, and therefore, only the transition from a symmetry s state to a symmetry p state will be considered.

3.3.2.a The transition probability and the absorption coefficient

The EXAFS function $\chi(E)$ is defined as the relative absorption coefficient, which is the absorption of the crystal or liquid μ compared to the free atom-like absorption μ_0 :

$$\chi(E) = \frac{[\mu(E) - \mu_0(E)]}{\mu_0(E)} \quad (3.3)$$

This allows neglect of the absorption edge of the free-atom like absorbing atom (gas phase) and therefore consideration of only the oscillations.

In order to calculate μ , it is necessary to relate μ to the probability that an atom will absorb a photon. Thus, μ is written as:

$$\mu = \rho \sigma \frac{N_a}{M} \quad (3.4)$$

where ρ is the mass density of the material (in kg m^{-3}), N_a the Avogadro number and M the molar mass. σ is characteristic of the electronic transitions induced by the incoming radiation. It can be

defined as the number of excited transitions, normalised to the flux of incoming photons that would be capable of inducing them. If we call j the flux of incoming photons, ρ the density of photons and V the elementary volume for one photon (considered as an harmonic oscillator in quantum theory of light), the total absorption may be expressed as follows:

$$\sigma = \frac{W_{i \rightarrow f}}{j} \quad (3.5)$$

with
$$j = \rho c = \frac{c}{V} \quad (3.6)$$

where $W_{i \rightarrow f}$ is the transition probability, and c the speed of light.

3.3.2.b Fermi's golden rule

Under the dipole approximation, where the electric field of the electromagnetic wave is assumed to be constant over the dimension of the K shell, and where one assumes that the wavelength of the photons must be much greater than the size of the initial state, the transition probability from a discrete initial state to a continuum of final states, of state density ρ_f , is given by Fermi's golden rule:

$$W_{i \rightarrow f} = \frac{2\pi}{\hbar} \rho_f \quad (3.7)$$

By combining equations (3.5) and (3.7), the absorption cross section can be written as follows:

$$\sigma = \frac{2\pi V}{\hbar c} \sum_f \rho(E_f) \langle f | H_{int} | i \rangle^2 \quad (3.8)$$

with
$$H_{int} = e\vec{r} \cdot \vec{E}(0, t) \quad (3.9)$$

Or, in the case of absorption only, that is to say with a particular component of H_{int} , one has:

$$\sigma = 4\pi^2 \alpha \hbar \omega \sum_f \rho(E_f) |\langle f | \vec{d} \cdot \vec{\epsilon} | i \rangle|^2 \quad (3.10)$$

where α is the fine structure constant and $\vec{\epsilon}$ the electric field polarisation vector.

3.3.2.c Calculation of transition matrix elements

The single scattering EXAFS equation, that will now be established, is based on the Stern hypothesis where absorption phenomena are essentially due to the emission of a photoelectron that is scattered. The final state is therefore characterised by the overlapping of the emitted wave and the same backscattered wave from the neighbouring atom, and can be expressed as follows:

$$|f\rangle = |f_0\rangle + |\delta f\rangle \quad (3.11)$$

where $|f_0\rangle$ is the outgoing photoelectron wave and reflects the free atom's final state and $|\delta f\rangle$ the wave backscattered by the neighbouring atom and thus reflects the effect of placing the atom in its local environment. One thus has:

$$\langle f | H_{int} | i \rangle = \langle f_0(\vec{r}) | H_{int} | i \rangle + \langle \delta f | H_{int} | i \rangle \quad (3.12)$$

$\langle f_0(\vec{r}) | H_{int} | i \rangle$ represents the absorption without a backscattered wave and without surrounding atoms, and is therefore proportional to μ_0 . Considering a unique final state and a unique initial state, $\chi(E)$ can be expressed as follows:

$$\chi(E) = \frac{[\mu - \mu_0]}{\mu_0} = \frac{|\langle f_0 | H_{int} | i \rangle + \langle \delta f | H_{int} | i \rangle|^2 - |\langle f_0 | H_{int} | i \rangle|^2}{|\langle f_0 | H_{int} | i \rangle|^2} \quad (3.13)$$

In order to resolve this equation, one has to determine the possible final state wavefunctions f_0 and $f_0 + \delta f$, with and without neighbours, respectively.

To do so, we will consider several approximations:

- The dipole approximation selection rules give: $\Delta l = \pm 1$; $\Delta s = 0$; $\Delta j = \pm 1, 0$; $\Delta m = 0$. Therefore, if the transition involves only one electron, the rules imply that in the case of symmetry s (i.e. $l = 0$) for the initial state, the final state has a p symmetry (i.e. $l = 1$). This is the case for the K-edge.
- The muffin-tin approximation assumes the atomic potentials to be spherically symmetric and centered on the diffusing or absorbing atom. The span length of the potential is limited and is regarded as constant beyond the so-called “muffin-tin radius” R_{MT} . In addition, the muffin-tin radius is assumed non-overlapping muffin-tin potential. Therefore, for $r > R_{MT}$, the electron is “free”.
- Under the small-atom approximation, also called the plane-wave approximation, the atomic radius of the diffusing atom is small compared to the distance between the absorbing atom and the neighbour. In that case, the outgoing photoelectron wave is approximated to a plane wave when interfering with the scatterer.

3.3.2.d Phase shifts

The final step for the determination of the absorption coefficient is to determine the phase shift undergone by the electron. The photoelectron wave experiences three phase shifts. Firstly, due to the distance between the absorbing atom and the scatterer j , the photoelectron will be phase shifted by the time it travels from the former to the latter and back. Secondly, the photoelectron first has to exit the absorbing atom’s potential ($2\delta_1$) that is counted twice since the shift is experienced once going out and once coming back. The third phaseshift $\phi(\pi)$ occurs when the photoelectron is backscattered towards the absorbing atom, with an angle π . The total phase shift is therefore:

$$\varphi_i(k) = 2kR_i + 2\delta_1 + \phi(\pi) \quad (3.14)$$

Given the number of atoms, the relative absorption is thus a sum of sinusoids of phase $\varphi_i(k)$.

Finally, since to extract the structural parameters from the $\chi(E)$ function, one has to convert the energy E into the photoelectron wavevector, the EXAFS will be described from now on in k space, with:

$$k = \sqrt{\frac{2m}{\hbar^2}(E - E_0)} \quad (3.15)$$

The EXAFS oscillations created by a unique scattering atom can thus be expressed as follows:

$$\begin{aligned} \chi(k) &= \frac{[\mu(k) - \mu_0(k)]}{\mu_0(k)} \\ &= -\frac{3 \cos^2 \theta_i |f_i(\pi)|}{kR_i^2} \sin[2kR_i + 2\delta_1 + \phi(\pi)] \text{ with } \phi(\pi) = \arg(f_i(\pi)) \end{aligned} \quad (3.16)$$

Therefore, under the single-scattering approximation, EXAFS oscillations correspond to the sum, over all the i shell, of the contributions of each scatterers j constituting the i^{th} shell. One obtains:

$$\chi(k) = \sum_i \sum_{j=1}^{j=N_i} -\frac{3 \cos^2 \theta_j^i |f_i(\pi)|}{kR_i^2} \sin[2kR_i + 2\delta_1 + \phi(\pi)] \quad (3.17)$$

N_i is the number of atom constituting the i^{th} shell, j describes the atoms of the same shell and θ_j^i is the angle between the polarisation and the absorbing atom- j atom of the i^{th} shell binding.

Finally, to fully explain the oscillatory behaviour of the absorption coefficient, there are three other physical factors that have to be taken into account: the intrinsic loss parameter, the core hole lifetime effects (inelastic losses) and the thermal and structural disorders (Debye-Waller).

The intrinsic loss parameter

The process of multi-electron excitation¹⁹⁻²¹ introduces the necessity of accounting for the intrinsic loss parameter. During this process, the ejected photoelectrons have a lower kinetic energy than the principal photoelectrons and this leads to different interference effects. Therefore, the term S_0^2 has to be included in the expression of $\chi(k)$.

Core hole lifetime effects and inelastic losses.

The intensity of the photoelectron's flux decreases exponentially as a function of the travelled distance. Electron-electron collisions lead to inelastic losses and therefore limit the number of photoelectrons that are coming back toward the absorbing atom and contributing to the EXAFS oscillations.

Moreover, the core hole, created in the excited atom by the ejection of a photoelectron, must last long enough for the backscattered electron to interfere with the direct beam (ca. 7×10^{-6} s), otherwise its contribution would be equal to zero.

These two phenomena are accounted in the EXAFS formula by a damping factor $e^{-2R_i/\lambda(k)}$ with $\lambda(k)$ being the electron mean free path.

The Debye-Waller factor

Equation 3.17 assumes that in each shell of first neighbours there is one and only one distance between the absorbing atom and the atom from the i^{th} shell, that is to say that the system is perfectly rigid and ordered. This is never the case and atoms from the same shell are organised around an average position according to a distribution function, $g_i(r)$. There are two factors to account for this distribution and which weaken the EXAFS oscillations: the thermal vibrations and the structural disorder. The thermal vibration is characterised by a so-called dynamic distribution where the atom vibrates around its equilibrium position and can be damped when working at low

temperature. The structural disorder weakens as well interferences and damps the amplitudes of EXAFS oscillations.

Therefore, $g_i(r)$ can be regarded as the probability of finding an atom from the i^{th} shell at a distance r from the central atom. It is here supposed that $g_i(r)$ is Gaussian type distribution function and that the damping factor caused by the thermal vibration and structural disorder is defined as $(e^{-2k^2\sigma_i^2})$. σ_i is characteristic of the dispersion of the distances in the i^{th} shell. In some cases where the sample is very disordered, a Gaussian type distribution is not valid. One can then utilise some other models such as the *cumulant method*.²²

At last, the modern EXAFS equation at the K edge under the single-scattering approximation defines itself by:

$$\chi(k) = -S_0^2(k) \sum_i \frac{N_i^*}{kR_i^2} |f_i(\pi)| e^{-2k^2\sigma_i^2} e^{-2R_i/\lambda_i(k)} \sin[2kR_i + 2\delta_1(k) + \phi_i(k)] \quad (3.18)$$

where $N_i^* = \sum_{j=1}^{j=N_i} 3\cos^2 \theta_j^i$ and is called the effective number of atoms in the i^{th} shell.

3.3.3 Multiple Scattering

In the previous paragraph, it has been established that the main approximation used for the determination of the EXAFS formula is the single scattering approach. The single-scattering short-range order theory, even though valid to analyse the first neighbour shell, is not valid when there are different neighbours, and multiple shells. Multiple scattering cannot be ignored, in particular, triangular paths involving a first and a second neighbouring atom, or atoms arranged in a long collinear paths where amplitude and phase of the EXAFS signal are significantly affected by the intermediate atom. This phenomenon is called the focusing or shadowing effect²³ (See Figure 3.4).

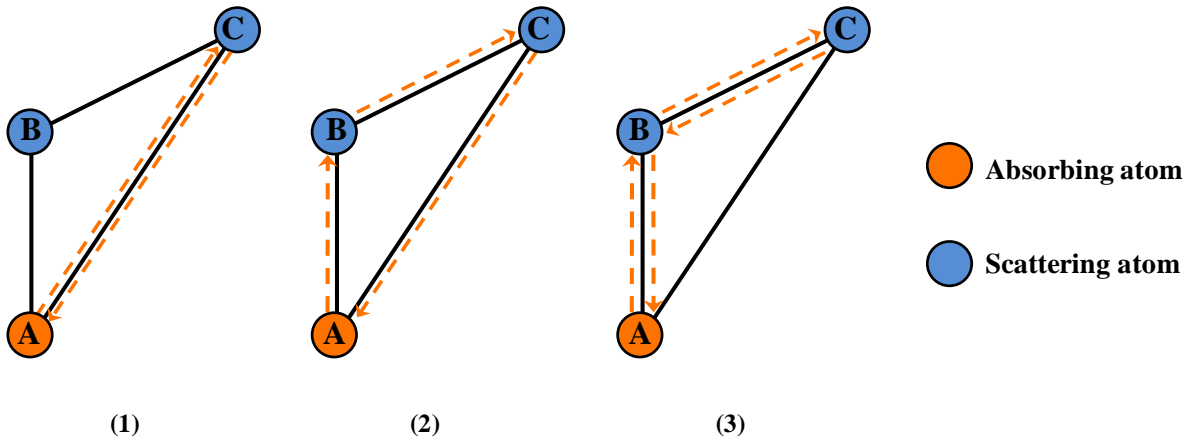


Figure 3.4: Schematic of three different multiple scattering paths for a triatomic system,²⁴ with A the absorbing atom, B the nearest neighbour, and C the next nearest neighbour. Path (1) shows the direct backscattering from A to C and back. Path (2) illustrates the multiple scattering in a triangular way from A to C but with B as an intermediate atom. Path (3) shows the multiple scattering via B in both outgoing and incoming trajectories.

Consider now that the EXAFS function can be expanded in a series of sums where each of them accounts for all contributions of multiple scattering involving a definite number of atoms:¹¹

$$\chi = \sum_{j \neq 0} \chi_2^{0i0} + \sum_{i \neq j; i, j \neq 0} \chi_3^{0ij0} + \sum_{i \neq j \neq k; i, k \neq 0} \chi_4^{0ijk0} + \dots \quad (3.19)$$

where $\chi_{\Gamma}^{0ijk\dots 0}$ is the contribution to the EXAFS of the multiple scattering involving $\Gamma - 1$ scatterers (i, j, k, ...) and the first term of the sum represents the single scattering contribution.

The EXAFS equation can thus be written as follows if one associates to each path Γ scattering amplitude f_{Γ} and a Debye-Waller factor:

$$\chi_{\Gamma}(k) = S_0^2 \frac{N_{\Gamma}}{kR_{\Gamma}^2} |f_{\Gamma}(k)| \sin(2kR_{\Gamma} + 2\delta + \phi_{\Gamma}) e^{-2k^2\sigma_{\Gamma}^2} \quad (3.20)$$

The series expansion of equation 3.19 will not be treated here but for a more complete derivation of the general multiple scattering EXAFS formula see Filipponi *et al.*,¹¹ and Ankudinov *et al.*³

Most of these paths usually have a negligible amplitude and a filtering process is necessary in order to selectively remove those paths.¹³ The FEFF code was developed,³ making nowadays MS paths calculation a routine procedure.

3.4 Data analysis

An experimental XAS spectrum containing the XANES and EXAFS signals is not directly interpretable. A series of numerical treatments has to be performed in order to extract the information that they contain. In the frame of this work, experimental EXAFS spectra have been treated with the IFFEFIT software package containing different programs for XAS analyses. Among them, we will focus on its main components of interest for us: ATHENA, a program for XAS data processing and ARTEMIS, a program for EXAFS data analysis using theoretical standards from FEFF.^{3,25,26}

3.4.1 Data processing

The first step in EXAFS analysis is to process the experimentally measured raw data. It includes the conversion of raw data to $\mu(E)$ spectra, the normalisation of the data, background subtraction and Fourier transformation.

Normalisation of the data:

Normalisation of the data permits to make the measurement independent of the details of the sample or the detector set-up. The method used in ATHENA consists of subtracting a linear contribution

before the edge, called the “pre-edge line” (see Figure 3.5.a) and then to determine, via a regression analysis, a quadratic polynomial beyond the edge, called the “post-edge line”²⁵ (see Figure 3.5.b).

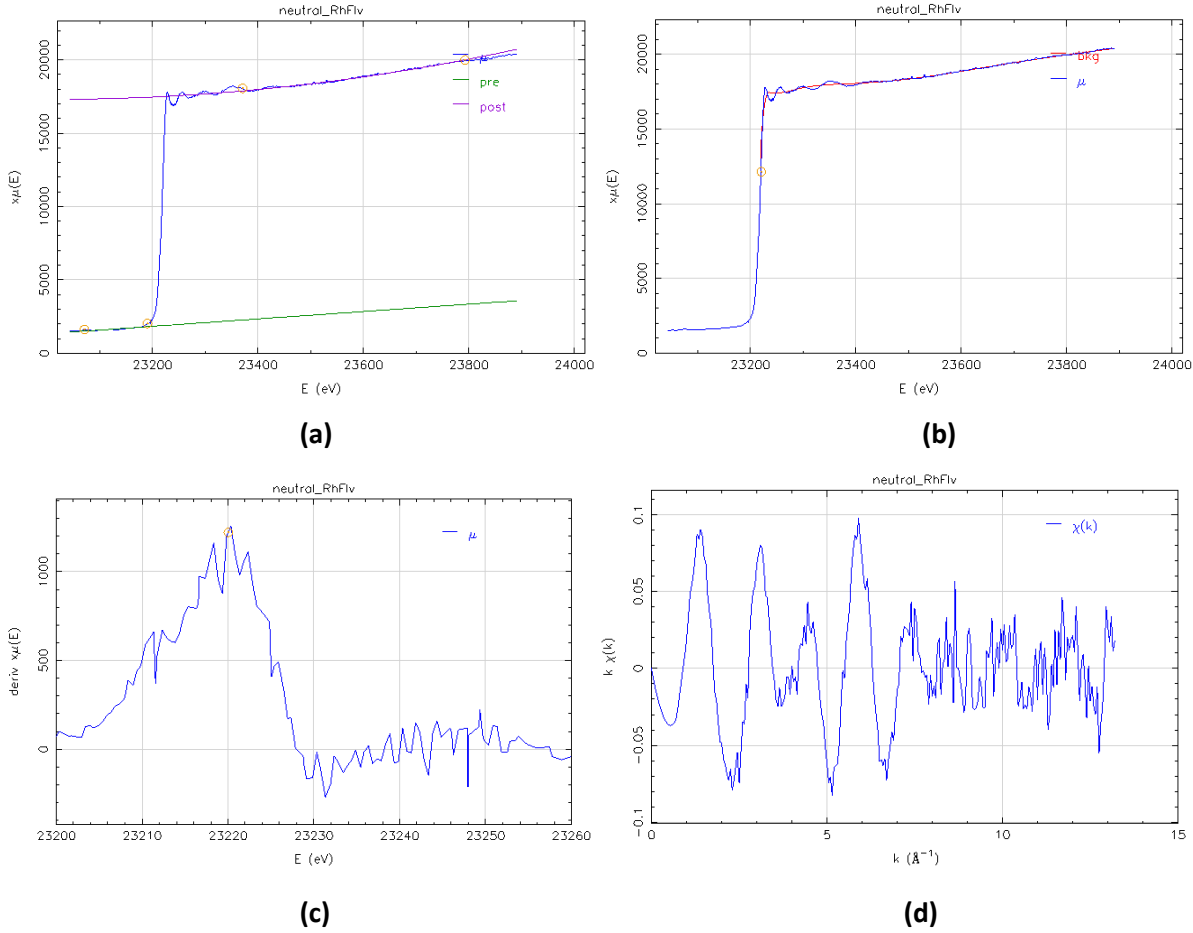


Figure 3.5: The different steps of data processing with ATHENA. (a) the pre- and post-edge lines, (b) Background subtraction, (c) First derivative of $\mu(E)$, (d) Data plotting in k-space.

The data are input to the program which defines a background line from which the $\chi(k)$ signal will be extracted (see Figure 3.5.b). It is then necessary to define accurately the threshold energy value E_0 . ATHENA determines E_0 automatically as the data are imported by finding the first peak of the first derivative of the $\mu_0(E)$ spectrum (see Figure 3.5.c) or with the nearest zero-crossing of the second derivative (not shown here). Alternatively, it can also be set manually to the tabulated atomic value, or to any other arbitrary value chosen by the user. The determination of E_0 is crucial

since it determines the origin of the k scale, and any mistake on the threshold energy would lead to errors in interatomic distances. Figure 3.5.d shows the EXAFS spectra $k\chi(k) = f(k)$ for which the background has been subtracted and only the oscillations caused by the backscattering waves from neighbouring atom on the absorbing atom remains. The ATHENA background function is based upon a Fourier transform based theory and uses the AUTOBK algorithm:²⁷ broadly speaking, the background is the part of the $\mu(E)$ data containing low frequency Fourier components and therefore the remaining higher-frequency Fourier components represent the data.

Data are presented as background removed and normalised by subtracting the curvature of the regression of the quadratic polynomial and the difference between the post-edge and pre-edge polynomial beyond the edge.

The $k\chi(k)$ function (shown in Figure 3.5.(d)) is then Fourier transformed to $\chi(R)$, showing peaks at distances related to the atomic neighbours of the absorbing atom. Data are now ready to be fitted with the ARTEMIS software.

3.4.2 Data fitting

The second step in EXAFS analysis is to perform fits on the data.

As established earlier, the modern EXAFS equation at the K-edge under the single-scattering approximation is written:

$$\chi(k) = -S_0^2(k) \sum_i \frac{N_i^*}{kR_i^2} |f_i(\pi)| e^{-2k^2\sigma_i^2} e^{-2R_i/\lambda_i(k)} \sin[2kR_i + 2\delta_1(k) + \phi_i(k)]$$

This equation contains two different types of information: (a) the parameters solely related to the structure, $[R_i, N_i, \sigma_i^2]$, and (b) the parameters related to chemical nature of the absorbing atom and of the scattering atoms, $[\delta_1, \arg(f_i(\pi)), |f_i(\pi)|, \phi_i(k)]$. In ARTEMIS, a dataset is considered as a

sum of one or several scattering paths by FEFF's multiple scattering path expansion.^{3,13,25,26} Therefore, the EXAFS equation is evaluated for each path included in the fit and the following terms must be specified R_i , S_0^2 , N_i , σ_i^2 , and E_0 . After a FEFF run, the importance of each path (single or multiple-scattering) is estimated and ARTEMIS plots each individual contribution of each path in k -space and R -space.

The Artemis program includes an interface with the ATOMS program²⁸ that allows to read crystallographic data in the form of a CIF file, for example,²⁹ and those data are then converted into a FEFF input file. Once the fit is finished, ARTEMIS gives its fitting statistics, including the R -factor, the reduced χ^2 , and the correlations between all fitting parameters.

The ATHENA and ARTEMIS software package thus meets all requirements for XAS data analysis.

3.5 Synchrotron Radiation sources

3.5.1 History of synchrotron radiation development.

Synchrotron radiation is the light emitted by charged particles, such as electrons or positrons, that are accelerated up to relativistic speed, i.e. approaching the speed of light, c , in curved paths in a magnetic field. The basic principle relies on Maxwell's theory of electromagnetic radiation which, in 1873, permitted the calculation of all quantities related to the emitted electromagnetic field.

The history of synchrotron radiation can be traced back to the end of the nineteenth century with the works of Liénard,³⁰ Wiechert³¹ and Schott³² on the emission from a charged accelerated particle. Liénard identified that when electrons rotate in a circle, they should radiate energy, and he thus established the formula for the rate of radiation from the centripetal acceleration of an electron. Then, Schott and Wiechert significantly detailed the classical theory of radiation from accelerated relativistic electrons. It was shown that any charged particle emits when it is accelerated: if this

particle is subject to a sudden deceleration (in X-ray tubes), this is called the Bremsstrahlung radiation, but if it is subject to the centripetal acceleration of a magnetic field, the particle emits an electromagnetic radiation called synchrotron radiation.

The first visual observation came at the General Electric Research Laboratory in Schenectady, New York, in 1947, where Pollock *et al.*³³ built a 70 MeV electron synchrotron to test the idea of phase stability in accelerators (for details the reader can refer to the publications of Kulipanov *et al.*³⁴ and Hartman³⁵). Their consecutive work initiated the investigation of the spectral distribution and polarisation properties of the radiation, including the major publication by Schwinger³⁶ in 1949.

In 1963, establishment of SURF (Synchrotron Ultraviolet Radiation Facility) began the first generation of synchrotron radiation facilities where Madden and Codling³⁷ tested the 180 MeV NBS facility (National Bureau of Standards) as a continuum light source for absorption spectroscopy in the ultraviolet region. The term first generation refers to the early work carried out on high-energy physics machines where instrumentation such as monochromators, mirrors and detectors were developed for experimental beamlines. The SR research was for a long time considered as parasitic on the high energy physics experiments and this was therefore limiting SR applications and the use of its full potential.

While the number of synchrotron radiation facilities was growing, the next major advance arose with the development of storage rings, where, by definition, the energy of the particles and the stability of their trajectory is maintained constant. This initiated a high demand for design of storage ring but at that time, the first generation of storage rings had lower intensity, stability and brightness and running times than what was required.

The Synchrotron Radiation Source (SRS) at the Daresbury Laboratory in the UK was the first of the resulting second generation of sources and operations started in 1981. This new generation of

facilities were designed to serve as dedicated SR sources. Higher intensity and brightness are the major differences with the first-generation predecessor, specificities of the radiation emitted by bending magnets. In a storage ring, the key function of bending magnets is to maintain the beam in a stable and closed orbit. The wide spectrum provided by bending magnets permits facile tuning over a broad range of wavelength. In addition, insertion devices such as wigglers and undulators were placed in specifically designed straight sections of the storage ring between two bending magnets and designed so that no displacement or deflection of the beam occurs. Wigglers and undulators consist of arrays of magnetic pairs of alternating orientation so that the produced magnetic field has alternating polarity when electrons are passing through the device. The alternating vertical field generated by those magnets force the electron to move in an oscillatory horizontal motion, the plane of the circulating beam. Because the conic light emitted at each bend overlaps, the emitted light is far more intense than at the exit of a bending magnet. The primary difference between wigglers and undulators is that the former has a broader radiation spectrum, whereas the latter emits over a narrow wavelength bandwidth, thus creating a high spatial and spectral brightness (tuneable). Whilst a wiggler has only few periods and the magnetic field is strong, undulators have many periods and a weaker field. The brightness of the undulator is much larger than that of the wiggler.

The idea of a new generation of storage rings with a still lower emittance and long straight sections for insertion devices would permit achieving even higher brightness and with it a considerable degree of spatial coherence. This was achieved by choosing the electron energy to be sufficiently high so that undulators could deliver high-brightness radiation at shorter wavelength ($< 1 \text{ \AA}$). This has led to the third generation of facilities and the European Synchrotron Radiation Facility (ESRF) in Grenoble was the first of the third generation hard x-ray sources to operate. The number of insertion device of undulator type was chosen to be much larger than what was available at second-

generation sources, and x-ray undulators were therefore the primary source of the third generation facilities.

Rings now in construction and development include Free Electron Lasers (FELs) and Energy Recovering Linacs (ERLs). Both could produce very rapid x-ray pulses for facilitating investigations on an extremely rapid timescale by producing ultrashort pulses of ca. 10 fs or lower. FELs can produce bigger pulses than ERLs, with the ability of spatial and temporal coherence, but at a far lower repetition rate.

Inside the synchrotron facility

The general structure presented in Figure 3.6 reflects the basic operation of a synchrotron facility. Electrons are emitted by the electron gun and are then accelerated by two successive accelerators.

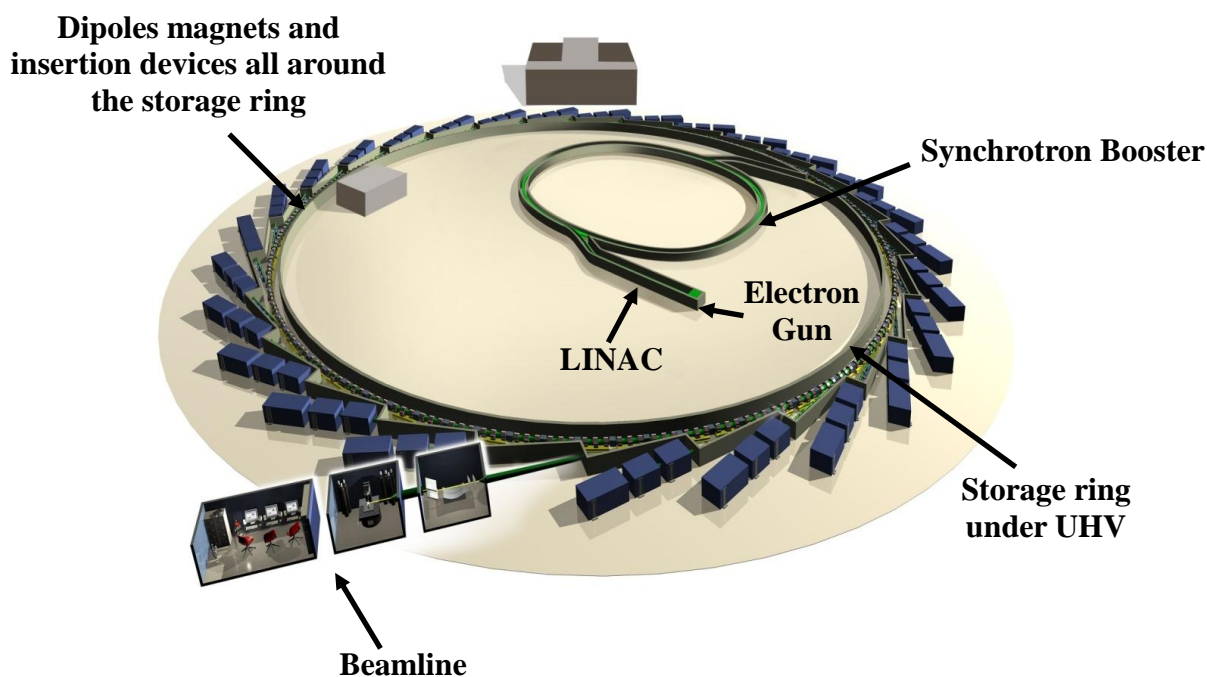


Figure 3.6: Schematic of the configuration of a synchrotron radiation source consisting of a Linear Accelerator (LINAC), a Synchrotron booster, a storage ring kept under ultra-high-vacuum, dipole magnets and insertion devices and beamlines.

Firstly, a linear accelerator (LINAC) accelerates the electrons to close to the speed of light. Secondly, they enter the circular accelerator called the booster Synchrotron where they pass through a series of electric fields which alternate as the electrons pass through; the electrons thus always see a positive field ahead and accelerate towards it. The electrons are injected into the storage ring that is kept under ultra-high vacuum (ca. 10^{-12} mbar). The storage ring (it is actually a polygon) is an assembly of several straight tubes with bending magnets at each of the vertices of the polygon. The dipole magnets are used to bend and control the path of the electrons as they travel around the ring. Electrons that solely pass through a bending magnet produce synchrotron light used for infrared and ultraviolet experiments and as less intense sources of x-rays.

Detection modes

The principle of X-ray absorption permits the use of different detection schemes to record the EXAFS signal. In particular, spectra may be obtained by measuring the intensity of the beam before it hits the sample I_0 and either the intensity of the transmitted beam, I_t , or the fluorescence signal, I_f . The simplest detection mode for EXAFS measurements is the transmission mode where the measurement of I_0 and I_t are generally carried out via the use of two ionisation chambers that are positioned along the beam axis directly in front of and behind the sample of interest.

However, the use of transmission mode is not suitable for every system: the concentration of the sample is not always high and it is not always obtainable, especially in electrochemical studies, or simply by technical issues such as the design of the cell used or specific mounting of the cell. In that case, an alternative detection scheme is required.

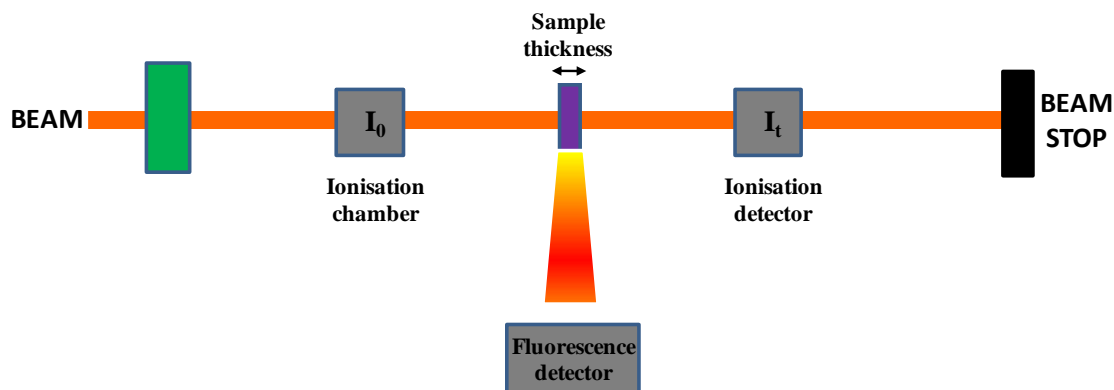


Figure 3.7: Schematic of the layout of an EXAFS experimental set-up. I_0 is measured by an ionisation chamber and the transmitted beam is measured either by transmission (I_t), by the ionisation detector, or by fluorescence, (I_f), with a fluorescence detector.

In the case of more dilute samples, detection in fluorescence is preferable. During the experiment, the sample is generally placed at 45° , at midway between the incoming beam and the detector, in order to optimise the solid angle acceptance for the fluorescence detector. In addition, this specific angle permits the attenuation of self-absorption in EXAFS spectra.³⁸ However, when the concentration of the sample is high, the sample should be positioned at 90° , towards the incident beam, in order to reduce the intensity of fluorescence and thus avoid saturation of the detector. There are several types of fluorescence detector, such as multi-element Ge detector, photoelectric diodes, or “Lytle” detectors.

3.5.2 Description of experimental stations used in this thesis

Three experimental stations, at three different synchrotrons, were used in this study and a brief description of each is presented here.

The Synchrotron Radiation Source (SRS)

The Synchrotron Radiation Source at the Daresbury Laboratory is a second generation source. It is a 2 GeV storage ring and operates with circulating currents in the range 150 to 250 mA. In order to maintain the high beam current, there were typically two beam injections daily into the storage ring.

Station 16.5

SRS Station 16.5 was built for XAS on ultra-dilute systems in the spectral range of 7 to 40 keV, using as a source a 6 Tesla wavelength wiggler. A 1.2 m uncoated plane mirror is used to achieve vertical collimation and harmonic rejection of the beam. The latter is followed by a water-cooled double crystal Si (220) monochromator. For energies up to 26 keV, horizontal focusing is available on the station. If required, a post-monochromator plane mirror is in place for vertical focussing of the beam on the sample.

The beamline is equipped with a high count-rate fluorescence 30-element Ge detector. Count rates of 350 kHz per channel at 8 keV to 150 kHz per channel at 35 keV are obtained without introducing loss of linearity.

The Swiss Light Source (SLS)

The Swiss Light Source at the Paul Scherrer Institut is a third-generation synchrotron light source. It is a 2.4 GeV electron storage ring and, under multi-bunch operation, storage ring currents are typically up to 400 mA.

Station X10DA-SuperXAS

SuperXAS is a dedicated beamline to X-ray Absorption spectroscopy in the applied sciences. It is a super-bending magnet based beamline with a magnetic field of 2.9 T and permits measurements in

the range of 4.5 keV to 35 keV. The SuperXAS station is equipped with a double crystal monochromator, consisting of two water-cooled sets of silicon crystals, Si(111) and Si(311). The beam is reflected from a Rh/Pt-coated vertically focusing mirror before the monochromator and from a Rh/Pt-coated torroidal focusing mirror after the monochromator for harmonic rejection. The flux is of the order of 1×10^{12} ph s⁻¹ and the spot size on the sample can vary from $100 \times 100 \mu\text{m}^2$ to $5 \times 0.5 \text{ mm}^2$.

A solid-state, 13-element Ge detector with fast digital amplifier is used for fluorescence experiments with a resolution of 250 eV FWHM for Mn- K_α at 100 kcps.

Diamond Light Source

Diamond Light Source is located at the Harwell Science and Innovation Campus, Oxfordshire, and is a third generation source. This opened in 2007 and is intended to host 32 beamlines by 2017. It is a 3 GeV electron storage ring which operates at circulating currents of up to 300 mA at present.

Station B18-Core EXAFS

Station B18 is a general purpose XAS beamline, built on a bending magnet that allows a wide operating energy range of 2 to 35 keV. A fixed-exit double crystal monochromator that hosts two directly water-cooled flat crystals sets, Si(111) and Si(311) cut, is used for energy selection (interchangeable in-vacuum). It is designed to carry out both conventional EXAFS and Quick EXAFS (QEXAFS) measurements. A vertically collimating Si mirror is placed before the monochromator and is coated with Cr and Pt stripes and allows covering the whole energy range. The monochromator is followed by a flat cylindrically bent focussing mirror that is doubly coated (Pt and Cr) to focus the two beam branches horizontally and vertically onto the sample. In the experimental hutch, a pair of harmonic rejection mirrors is found and can be positioned in the

optical path when operating below 11 keV. The flux delivered is of the order of 5×10^{11} ph s⁻¹ and the typical spot size is 250 μm in the vertical direction by 200 μm in the horizontal one.

The fluorescence detector array comprises 9 element Ge detector and is cooled by a cryostat with a typical energy resolution of 170 eV at a count rate of 200 kcps per element.

Additional detection techniques include a 4 element silicon detector for fluorescence studies of soft X-ray energies, ionisation chambers for transmission experiments and a detector for wide angle X-ray scattering measurements.

References

1. Gurman, S. J.; Binsted, N.; Ross, I. A Rapid, Exact Curved-Wave Theory for Exafs Calculations. *J. Phys. C Solid State* **1984**, *17* (1), 143-151.
2. Gurman, S. J. The Small-Atom Approximation in Exafs and Surface Exafs. *J. Phys C Solid State* **1988**, *21* (19), 3699-3717.
3. Rehr, J. J.; Albers, R. C. Scattering-Matrix Formulation of Curved-Wave Multiple-Scattering Theory - Application to X-Ray-Absorption Fine-Structure. *Phys. Rev. B* **1990**, *41* (12), 8139-8149.
4. Fricke, H. The K-characteristic absorption frequencies for the chemical elements magnesium to chromium. *Phys. Rev.* **1920**, *16* (3), 202-215.
5. Hertz, G. Absorption limits of the L-series. *Z. Phys.* **1920**, *3*, 19-25.
6. Kronig, R. D. *Z. Phys.* **1931**, *70*, 317.
7. Kronig, R. D. *Z. Phys.* **1932**, *75*, 468.
8. Stern, E. A. Theory of Extended X-Ray-Absorption Fine-Structure. *Phys. Rev. B* **1974**, *10* (8), 3027-3037.
9. Lytle, F. W.; Sayers, D. E.; Stern, E. A. Extended X-Ray-Absorption Fine-Structure Technique .2. Experimental Practice and Selected Results. *Phys. Rev. B* **1975**, *11* (12), 4825-4835.
10. Stern, E. A.; Sayers, D. E.; Lytle, F. W. Extended X-Ray-Absorption Fine-Structure Technique .3. Determination of Physical Parameters. *Phys. Rev. B* **1975**, *11* (12), 4836-4846.

11. Filipponi, A.; DiCicco, A.; Natoli, C. R. X-ray-absorption spectroscopy and n-body distribution functions in condensed matter .1. Theory. *Phys. Rev. B* **1995**, *52* (21), 15122-15134.
12. Rehr, J. J.; Albers, R. C.; Zabinsky, S. I. High-Order Multiple-Scattering Calculations of X-Ray-Absorption Fine-Structure. *Phys. Rev. Lett.* **1992**, *69* (23), 3397-3400.
13. Zabinsky, S. I.; Rehr, J. J.; Ankudinov, A.; Albers, R. C.; Eller, M. J. Multiple-Scattering Calculations of X-Ray-Absorption Spectra. *Phys. Rev. B* **1995**, *52* (4), 2995-3009.
14. Rehr, J. J.; Albers, R. C. Theoretical approaches to x-ray absorption fine structure. *Rev. Mod. Phys.* **2000**, *72* (3), 621-654.
15. Kincaid, B. M.; Eisenberger, P. Synchrotron Radiation Studies of K-Edge Photoabsorption Spectra of Kr, Br₂, and GeCl₄ - Comparison of Theory and Experiment. *Phys. Rev. Lett.* **1975**, *34* (22), 1361-1364.
16. Winick, H.; Bienenstock, A. Synchrotron Radiation Research. *Annu. Rev. Nucl. Part. S.* **1978**, *28*, 33-113.
17. Lindau, I.; Winick, H. Synchrotron Radiation Research - Recent Developments. *J. Vac. Sci. Technol.* **1978**, *15* (3), 977-983.
18. Batterman, B. W.; Ashcroft, N. W. Chess - New Synchrotron Radiation Facility at Cornell. *Science* **1979**, *206* (4415), 157-161.
19. Rehr, J. J.; Stern, E. A.; Martin, R. L.; Davidson, E. R. Extended X-Ray-Absorption Fine-Structure Amplitudes - Wavefunction Relaxation and Chemical Effects. *Phys. Rev. B* **1978**, *17* (2), 560-565.

20. Chou, S. H.; Rehr, J. J.; Stern, E. A.; Davidson, E. R. Abinitio Calculation of Extended X-Ray-Absorption Fine-Structure in Br-2. *Phys. Rev. B* **1987**, *35* (6), 2604-2614.
21. Stern, E. A.; Heald, S. M.; Bunker, B. Amplitude of the Extended-X-Ray-Absorption Fine-Structure in Bromine Molecules. *Phys. Rev. Lett.* **1979**, *42* (20), 1372-1375.
22. Bunker, G. Application of the Ratio Method of Exafs Analysis to Disordered-Systems. *Nucl. Instrum. Methods* **1983**, *207* (3), 437-444.
23. Teo, B. K. *EXAFS: Basic Principles and Data Analysis*; Springer-Verlag Ed., **1986**.
24. Teo, B. K. Novel Method for Angle Determinations by Exafs Via A New Multiple-Scattering Formalism. *J. Am. Chem. Soc.* **1981**, *103* (14), 3990-4001.
25. Ravel, B.; Newville, M. Athena, Artemis, Hephaestus: Data Analysis for X-Ray Absorption Spectroscopy Using Ifeffit. *J. Synchrotron Radiat.* **2005**, *12*, 537-541.
26. Ravel, B.; Newville, M. ATHENA and ARTEMIS: Interactive graphical data analysis using IFEFFIT. *Phys. Scripta* **2005**, *T115*, 1007-1010.
27. Newville, M.; Livins, P.; Yacoby, Y.; Rehr, J. J.; Stern, E. A. Near-Edge X-Ray-Absorption Fine-Structure of Pb - A Comparison of Theory and Experiment. *Phys. Rev. B* **1993**, *47* (21), 14126-14131.
28. Ravel, B. ATOMS: crystallography for the X-ray absorption spectroscopist. *J. Synchrotron Radiat.* **2001**, *8*, 314-316.
29. Hall, S. R.; Allen, F. H.; Brown, I. D. The Crystallographic Information File (Cif) - A New Standard Archive File for Crystallography. *Acta Crystallogr. A* **1991**, *47*, 655-685.
30. Liénard, A. *L'Éclairage Élec.* **1898**, *16*, 5.

31. Wiechert, E. *Arch. Neerl.* **1900**, 549.
32. Schott, G. A. *Electromagnetic radiation* **1912**, 109.
33. Elder, F. R.; Gurewitsch, A. M.; Langmuir, R. V.; Pollock, H. C. Radiation from Electrons in a Synchrotron. *Phys.Rev.* **1947**, *71* (11), 829-830.
34. Kulipanov, G. N.; Skrinsky, A. N. Early work on Synchrotron Radiation. *Synchrotron Radiat. News* **1988**, *3*, 32.
35. Hartman, P. L. Early Experimental Work on Synchrotron Radiation. *Synchrotron Radiat. News* **1988**, *4*, 28.
36. Schwinger, J. On the Classical Radiation of Accelerated Electrons. *Phys. Rev.* **1949**, *75* (12), 1912-1925.
37. Madden, R. P.; Codling, K. New Autoionizing Atomic Energy Levels in He, Ne, and Ar. *Phys. Rev. Lett.* **1963**, *10* (12), 516-518.
38. Troger, L.; Arvanitis, D.; Baberschke, K.; Michaelis, H.; Grimm, U.; Zschech, E. Full Correction of the Self-Absorption in Soft-Fluorescence Extended X-Ray-Absorption Fine-Structure. *Phys. Rev. B* **1992**, *46* (6), 3283-3289.

*Chapter 4: Low temperature studies of
Ruthenocene*

4.1 Introduction

Whilst there have been many published studies on the application of XAS to electrochemistry, the vast majority have concerned the structure of the electrode material or its surface. There have been very few published studies of species in solution generated by redox processes at electrodes which is the domain of electroanalysis. This is due to the experimental challenge involved: the concentration of electrochemical intermediates is low except in the vicinity of the electrode, species of interest exist only for a small period of time close to the electrode and the solution is a mixture of reactants, intermediates and products. The advent of 3rd generation synchrotron sources and improved detection methods has made application of XAS to electroanalysis feasible.

During recent years this research group has been developing XAS techniques for the study of electrochemical intermediates. Initial work focused attention upon the use of energy dispersive XAS to study transient processes. Whilst successful for the study of electrochemical desorption, beam damage hindered study of organometallic species in non-aqueous solution. Hence attention turned to the use of electrochemical flow systems, the outcome of which will be described in chapter 6.

Whilst most electrochemical intermediates are transient in nature, there are some electrochemical systems in which the products cannot be isolated but are nonetheless stable for long periods of time. Such systems are amenable to study by in situ electrolysis combined with XAS and are the subject of this chapter.

4.2 Systems under study

Following from the work successfully carried out previously within the group of studying complexes of elements with edges at a lower energy range, such as iron¹, the idea here is to extend the studies made so far to important electrocatalytic elements such as ruthenium or rhodium.

Because of the challenge of the project, a simple system is needed to test and to develop the methodology. In addition, the system has to be of interest for the electrochemistry community.

An ideal system would be one that provides an EC mechanism in which structural changes between the intermediate and reactant or product are significant. Among those reactions, attention could be, for instance, centred on dimerisation or isomerisation.

4.2.1 The electrochemical behaviour of Ruthenocene

As a starting point, ruthenocene RuCp_2 ($\text{Cp} = \eta^5\text{-C}_5\text{H}_5$) was selected for study because it is a simple, readily available material whose electrochemistry is still not fully understood, despite many years effort.

The first major paper on the electrochemistry of ruthenocene was published by Page and Wilkinson² in 1952 where they reported the oxidation of ruthenocene as being a reversible one electron process at a mercury electrode. They asserted that they isolated a yellow crystalline solid as being the ruthenicinium cation $[\text{RuCp}_2]^+$ as a perchlorate salt. However, it was only 20 years later that Hendrick *et al.*³ showed that the product of the electrochemical oxidation of RuCp_2 at a Hg pool electrode was in fact the mercury-bridged complex

$[(\text{Cp})_2\text{Ru} - \text{Hg} - \text{Ru}(\text{Cp})_2][\text{NaClO}_4]_2$. Facile oxidation of mercury to Hg (I) makes it inadequate as an electrode material for investigations on oxidation processes. The development of solid electrodes then allowed more systematic studies of anodic processes.^{4,5}

Thus, a number of papers on the oxidation of RuCp_2 at a Pt electrode in non-aqueous media, namely acetonitrile and traditional supporting electrolyte anions such as $[\text{ClO}_4]^-$, $[\text{BF}_4]^-$, or $[\text{PF}_6]^-$ reported that the oxidation of ruthenocene is an irreversible two-electron process.⁶⁻¹⁰ For instance, among these publications, the first important one was published in 1959 where the three students, namely Kuwana, Bublitz and Hoh, of the Adams group, described the electrochemical oxidation of ferrocene and ruthenocene.⁵ Chronopotentiometric measurements of the three metal cyclopentadienyl compounds of the group VIII, ferrocene, ruthenocene and osmocene indicated different value of the chronopotentiometric constant, which depends on the diffusion coefficient and the number of electrons transferred per molecule. The structures of the three complexes being similar, they nevertheless obtained for ruthenocene twice the value of that found for ferrocene or osmocene. This observation strongly suggested a two-electron oxidation for ruthenocene.¹⁰

The breakthrough for those investigations appeared when Mann *et al.*¹¹ became interested in developing non coordinating solvent/electrolyte systems, after investigating¹² the electrochemistry of $[\text{CpFe}(\text{CO})_2]_2$ (and the related $[\text{Cp}^*\text{Fe}(\text{CO})_2]_2$). In this paper,¹² they showed, in particular, that during the oxidation process of $[\text{CpFe}(\text{CO})_2]_2$ the resulting cationic product $[\text{CpFe}(\text{CO})_2]_2^+$ is highly sensitive to nucleophilic attack by the solvent/electrolyte conditions, and is therefore susceptible to rapid, ligand-induced disproportionation reactions. The same year, Mann and coworkers¹¹ published their first results with tetrabutylammonium tetrakis[3.5-bis(trifluoromethyl)phenyl]borate,^{13,14} $[\text{NBu}_4][\text{BARF}_{24}]$, where it is stated that the

oxidation of ruthenocene is a simple, one electron process. These findings therefore implied that the use of traditional anions (TAs) had a dramatic effect on the oxidation process of RuCp_2 , where they are likely to have strong nucleophilic activity towards the radical cation. A more detailed review on weakly coordinating anions (WCAs) is found in section 4.2.2.

Later, the Geiger group became interested in the electrochemical behaviour of ruthenocene¹⁵ by observing that its oxidation displayed decreased electrochemical reversibility at reduced temperatures and, additionally, as the concentration increases in a medium containing CH_2Cl_2 and $[\text{NBu}_4][\text{B}(\text{C}_6\text{F}_5)_4]^-$ as a supporting electrolyte. They showed that in a solution of low donor strength solvents such as dichloromethane or benzotrifluorotoluene, and weak nucleophilicity electrolyte anions, such as tetrakis(perfluoroaryl)borate $[\text{B}(\text{C}_6\text{F}_5)_4]^-$ (TFAB) or $[\text{B}(\text{C}_6\text{H}_3(\text{CF}_3)_2)_4]^-$ (BArF_{24}), the oxidation of RuCp_2 gives the 17-electron $[\text{RuCp}_2]^+$ cation in equilibrium with the dominant dimer dication $[(\text{RuCp}_2)_2]^{2+}$ ($\mathbf{2}^{2+}$).

Depending on several parameters such as temperature, analyte concentration, supporting electrolyte anion and scan rate, the peak potential of the electrochemically irreversible product wave varies. For instance, at 243 K, the dimer seems to be stable but when the anion is TFAB, the dimer precipitates. By using the $[\text{B}(\text{C}_6\text{H}_3(\text{CF}_3)_2)_4]^-$ anion, no precipitation is detected. In addition, the increase of the substrate concentration tends to favour the detection of the wave for $[(\text{RuCp}_2)_2]^{2+}$ and to disadvantage the reversibility of $[\text{RuCp}_2]^{0/+}$. Reduction of the secondary product is seen to principally regenerate ruthenocene. They reported that other unidentified products were produced in the electrolysis, which is dominant at ambient temperature. In a more recent paper,¹⁶ Geiger *et al.* identified those electrolysis products as being $\text{Ru} - \text{Ru}$ ($[\text{Ru}_2\text{Cp}_4]^{2+}$), $\text{Ru} - (\sigma)\text{C}$ ($[\text{Ru}_2\text{Cp}_2(\sigma:\eta^5 - \text{C}_5\text{H}_4)_2]^{2+}$), and $\text{Ru} - \text{H}$

([RuC₁₀H₁₁]⁺) containing complexes, offering therefore an explanation of the complex oxidative behaviour of ruthenocene.

4.2.2 The importance of the background salt

The previous review on the oxidative electrochemical process of ruthenocene has highlighted the crucial role that the use of weakly coordinating anions played and, more generally, how crucial is the choice of the medium in an electrochemistry experiment.

The basic role of the supporting electrolyte is to provide the means by which current can pass through an otherwise highly resistive medium, in order to control the diffusion of an electroactive species. The oxidative behaviour of organometallic compounds is generally studied in low polarity halocarbon solvents such as dichloromethane; however, their low dielectric constant enhances ion association and these solvents therefore provide inadequate media for effective dissociation of traditional electrolytes. The strength of the solute-solvent interactions will affect the cell resistance and mass transport but interferes as well with the run of an electrochemical reaction. An adequate combination between the solvent and the salt would minimize the uncompensated iR drop and, therefore, potential control.¹⁷ Therefore, by comparing the conductivity and ion-pairing properties with the TAs and WCAs, LeSuer *et al.*¹⁸ showed that [B(C₆H₃(CF₃)₂)₄]⁻ and [B(C₆F₅)₄]⁻ anions are more appropriate for low polarity solvents. The sharing of negative charges in the fluoro- or CF₃-substituted tetraphenylborate ions compared to the charge distribution in the traditional anion family could explain those findings; their use increases the conductivity of the medium and therefore decreases ohmic effects.

In addition, the stability of an electrogenerated cation radical has been shown to be enhanced by the use of the WCA anions from both kinetics and thermodynamics perspectives. On a kinetic matter, anodic processes of transition metal complexes produce cationic products that are subject to nucleophilic attack by the traditional family of electrolyte anions. In 1988, Beck and Sunkel¹⁹ originally drew attention on this matter but Mann *et al.* were the first to report,¹¹ in 1991, electrochemistry studies in a WCA-based media. Of concern in this study, and as shown in the previous section, the oxidation of RuCp₂ is a reversible one-electron process under these conditions, in contrast to the two-electron process previously reported with the so-called traditional anions (see section 4.2.2). From a thermodynamic point of view, the effect of ion-pairing on $E_{1/2}$ potentials is naturally amplified in lower-polarity solvents with more strongly coordinating anions and the kinetic stability of an electrogenerated radical is widely increased. This has been the object of a number of studies in the Geiger group and has permitted identification of dimers or unique dimer radicals.^{15,16,20-23} To conclude, the most attractive properties of this third generation of anions are found in their low nucleophilicity and the generally increased solubility of their salts in lower polarity solvents.

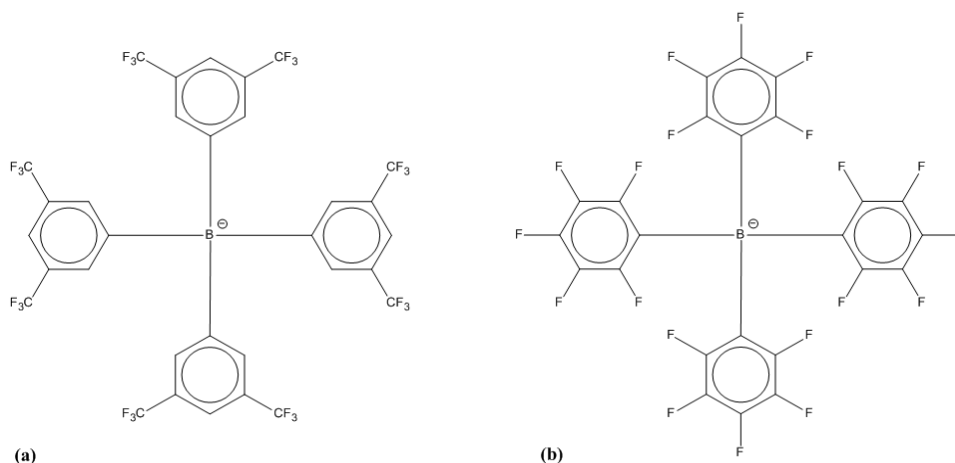


Figure 4.1: (a) Tetrakis[3,5-bis(trifluoromethyl)phenyl] borate anion $[\text{B}(\text{C}_6\text{H}_3(\text{CF}_3)_2)_4]^-$ and (b) Tetrakis(perfluoroaryl)borate anion $[\text{B}(\text{C}_6\text{F}_5)_4]^-$.

Neither electrolyte is commercially available, and the synthesis has to be carried out from compounds $\text{Li}[\text{B}(\text{C}_6\text{F}_5)_4]$, and $\text{Na}[\text{B}(\text{C}_6\text{H}_3(\text{CF}_3)_2)_4]$ that are not cheap. The supporting electrolytes used throughout this project were either synthesised in our laboratory, or provided by our collaborator Prof. William Geiger from the University of Vermont.

4.2.3 Typical electrochemistry of RuCp_2

Electrical testing of the redox behaviour of ruthenocene was carried out initially in a 5-Neck ground glass joints cell (ESA Analytical Ltd), using a standard three-electrode configuration. Electrochemical control was maintained via an Autolab PGSTAT 12 potentiostat. This section reports on the cyclic voltammetry of RuCp_2 (**1**) in benzotrifluorotoluene (BTF) and 0.05 M $[\text{NBu}_4][\text{B}(\text{C}_6\text{F}_5)_4]$. A solution of 0.22 mM RuCp_2 (99%, Acros Organics) in BTF/ 0.05 M was initially prepared and purged for 30 min with argon prior to CV measurements. The mass needed to reach the different concentrations of analyte presented below was added at different

time intervals with same purging procedure before scans. Figures 4.2 and 4.3 show the cyclic voltammograms of 0.22 mM, 0.52 mM, 1.3 mM, and of 5.2 mM of RuCp₂, respectively. The scan for 5.2 mM RuCp₂ is presented separately for convenience of plotting the other CVs on the same scale.

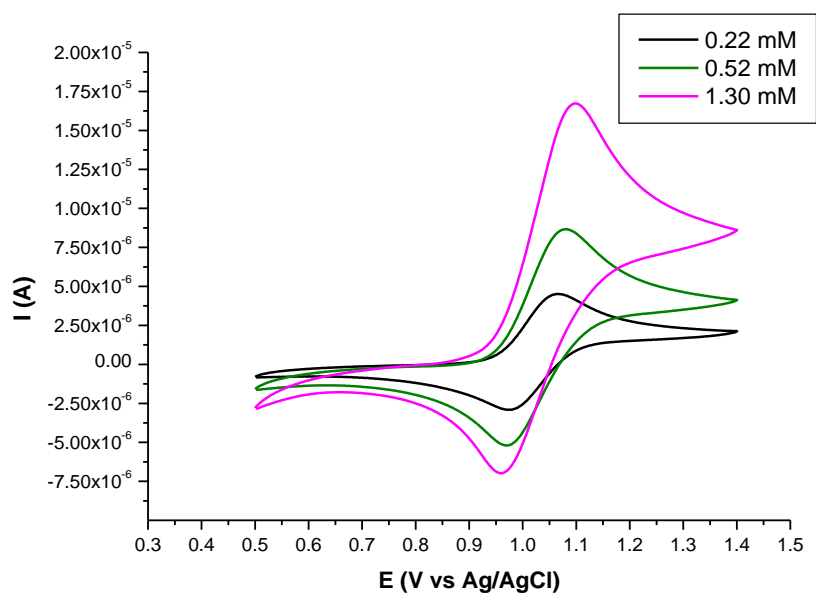


Figure 4.2: Cyclic Voltammograms of 0.22 mM, 0.52 mM, 1.30 mM of **1** in BTF/ 0.05 M [NBu₄][B(C₆F₅)₄] at 1 mm glassy carbon electrode at 0.1 V s⁻¹, 298 K.

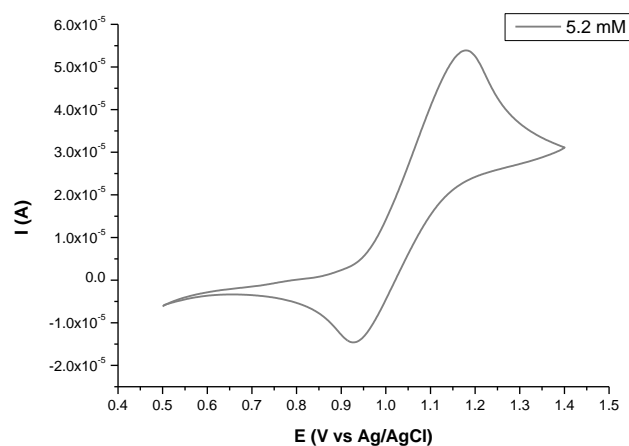


Figure 4.3: Cyclic Voltammogram of 5.2 mM of **1** in BTF/ 0.05 M [NBu₄][B(C₆F₅)₄] at 1 mm glassy carbon electrode at 0.1 V s⁻¹, 298 K.

At room temperature, in a BTF solution of [NBu₄][B(C₆F₅)₄], ruthenocene exhibits a quasi-reversible 1e⁻ oxidation. Previous published studies^{11,15} were carried out in dichloromethane (see section 4.2.3). Nevertheless, by comparing the reversibility of other metallocenes (NiCp₂, CoCp₂) in BTF, Ohrenberg and Geiger²⁴ concluded that the behaviour of ruthenocene mimicked the behaviour observed in CH₂Cl₂.

For the analysis of voltammetric responses, characteristic parameters of the half-wave potentials $E_{1/2}$, peak-to-peak separation ΔE_p , and peak current ratio $i_{p,a}/i_{p,c}$ have been calculated and summarised in Table 4.1.

RuCp ₂	0.22 mM	0.52 mM	1.30 mM	5.20 mM
E_{pa} (mV)	1065	1081	1099	1178
E_{pc} (mV)	974	970	960	929
i_{pa} (μ A)	4.51	8.67	16.73	53.89
i_{pc} (μ A)	-2.91	-5.2	-6.98	-14.61
$i_{pa/2}$ (μ A)	2.26	4.33	8.35	26.95
$i_{pc/2}$ (μ A)	-1.45	-2.6	-3.49	-7.31
$E_{pa/2}$ (mV)	998	1005	1016	1051
$E_{pc/2}$ (mV)	1033	1029	1016	989
ΔE_p (mV)	91	111	139	249
$E_{1/2}$ (mV)	1020	1026	1029	1054
$ i_{pa}/i_{pc} $	1.55	1.67	2.40	3.69

Table 4.1: Experimental parameters for anodic and cathodic process for various concentrations of **1** in BTF/ 0.05 M [NBu₄][B(C₆F₅)₄] at 1 mm glassy carbon electrode at 0.1 V s⁻¹, 298 K.

Examination of these diagnostic parameters shows that increasing the concentration of RuCp₂ tends to diminish electrochemical reversibility. The peak separation between the anodic and the cathodic peak potentials for a concentration of 5.2 mM is more than three times the value of ΔE_p for a concentration of 0.22 mM. The same observation can be made for the current peak ratio. As mentioned in section 4.2.1, this is consistent with the work of Geiger *et al.* who

reported the first experimental evidence¹⁵ that the bis(ruthenocenium) dication $[\text{RuCp}_2]_2^{2+}$ plays a role in the redox process of $[\text{RuCp}_2]^{0/+}$.

Figure 4.4 shows the effect of decreasing the temperature. It can be seen that the wave loses its reversibility and that a new cathodic product wave appears at a more negative potential, ca. 580 mV vs. Ag/AgCl. The shape of this wave is broad and electrochemically irreversible. This effect is accentuated at higher concentration of RuCp_2 .

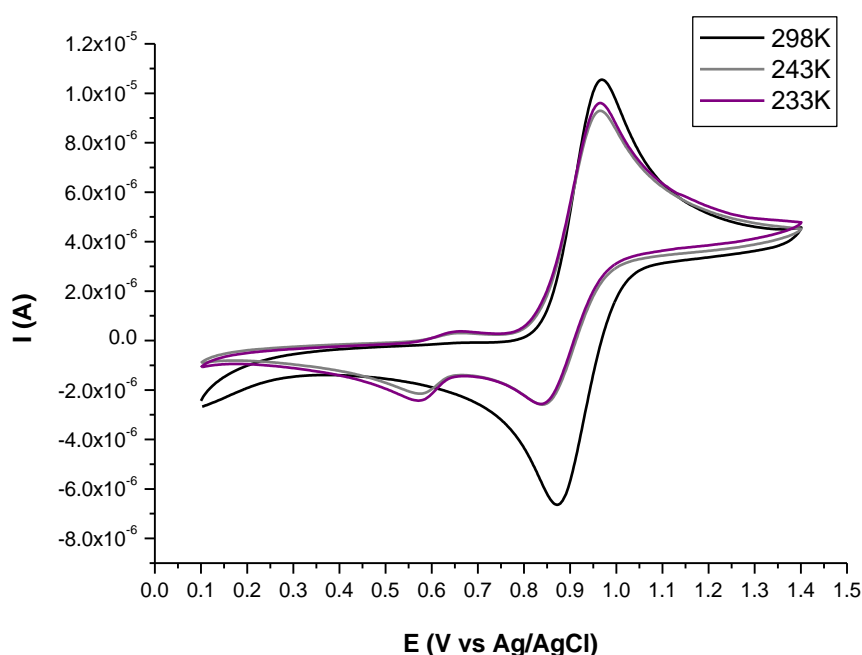
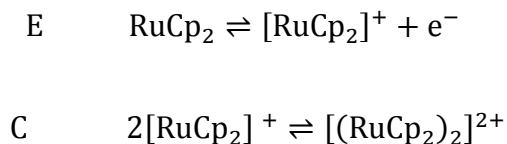


Figure 4.4: Cyclic Voltammograms of 1.30 mM of **1** in BTF/ 0.025 M $[\text{NBu}_4][\text{B}(\text{C}_6\text{F}_5)_4]$ at 1 mm glassy carbon electrode at 298 K, 243 K, and 233 K, 0.1 V s^{-1} .

From these observations, the oxidation of ruthenocene is assigned as an EC_{dim} mechanism where the electron transfer is followed by the dimerisation of $[\text{RuCp}_2]^+$ to give the dimer dication $[(\text{RuCp}_2)_2]^{2+}$. At elevated temperatures, the dimerisation process is fast and reversible on the CV time scale.

The voltammetry is consistent with the EC mechanism where E represents a heterogeneous single electron transfer and C the homogeneous chemical reaction.



4.3 Designs of X-ray spectroelectrochemical cells

4.3.1 Introduction

The objective of spectroelectrochemical cells is to permit spectroscopic and electrochemical investigations to be carried out simultaneously upon a system. In practice the technical demands of the two techniques are frequently found to be in conflict and compromises have to be made. Understanding these is the key to ensuring that insight gained from both techniques can be fruitfully combined.

4.3.2 The solvent and its compatibility with the penetration of X-rays

The solvent must satisfy a number of criteria. In this project, organometallic compounds are of particular interest and the choice of solvent must suit both electrochemical studies and XAS investigations. Physicochemical properties such as Lewis acid-base strength, protic character, polarity, dielectric constant, donor properties and also spectroscopic properties have all to be considered. Whereas the electrochemical behaviour of RuCp_2 has been most frequently studied in CH_2Cl_2 , this solvent is nevertheless an important constraint from a XAS point of view, because of the penetration depth of X-rays. At the Ru K-edge (22117.2 eV),

for CH_2Cl_2 , transmission is much smaller than for BTF (see Figure 4.5) and hence, CH_2Cl_2 is not suitable for EXAFS measurements [22 keV – 23 keV]. An alternative solvent is required.

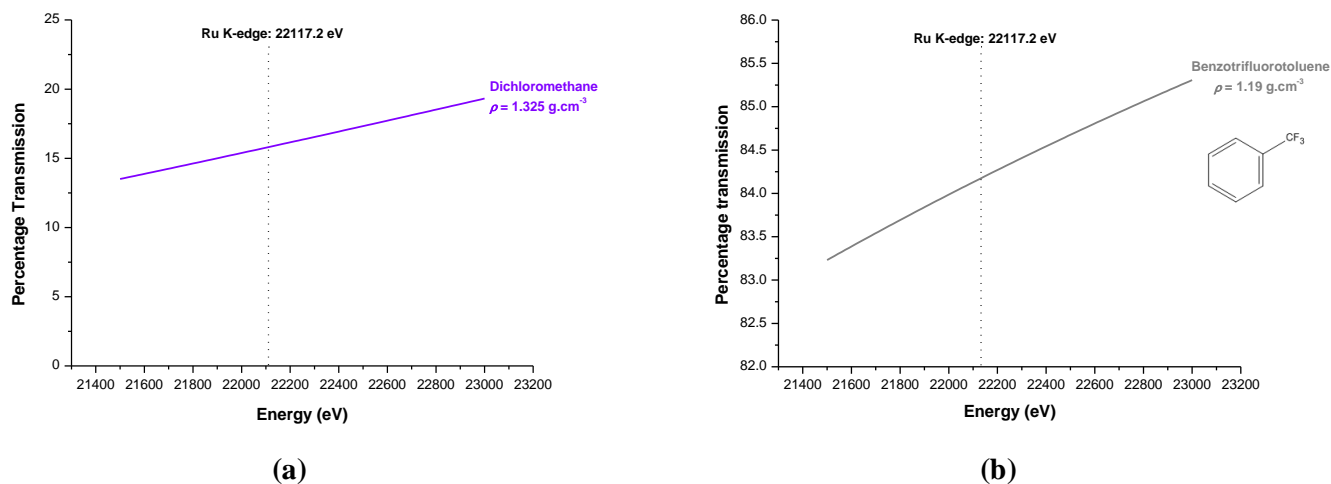


Figure 4.5: X-ray transmission through 3 mm of dichloromethane (a) and benzotrifluorotoluene (b) over a range of energies incorporating the Ru K-edge.

As described in section 4.2.1, under appropriate conditions, the electrochemical oxidation of ruthenocene gives the dimeric dication $[(\text{RuCp}_2)_2]^{2+}$, which is subject to nucleophilic attack and thus is not stable in good Lewis base solvents. A solvent that does not contain donor electron pairs is required. Moreover, the protic character of a solvent must be considered. Since electrochemical intermediates interact with protons, aprotic solvents are generally preferred.

Ohrenberg and Geiger²⁴ have reported benzotrifluorotoluene, $\text{C}_6\text{H}_5\text{CF}_3$, as an attractive alternative to CH_2Cl_2 . These solvents share common properties since they have similar dielectric constant ($\epsilon_{\text{C}_6\text{H}_5\text{CF}_3} = 9.2$ and $\epsilon_{\text{CH}_2\text{Cl}_2} = 8.9$) and close solvent polarity parameters.

In addition, the absence of nucleophilic functional groups in BTF makes it a good candidate to be used in the generation of organometallic cation radicals. This criterion can be considered as the non-coordinating power.

As shown in Figure 4.5, BTF also suits perfectly our requirements from the XAS standpoint.

4.3.3 Spectroelectrochemical cell 1

4.3.3.a Introduction

The design requirements

To carry out a successful *in situ* spectroelectrochemical experiment, several criteria have to be taken into account: the electrochemical requirements, the spectroscopic constraints and, finally, the practicalities of operating the cell at a synchrotron. In contrast with the more commonly used spectroscopic techniques such as UV/vis or IR spectroscopy, designing a spectroelectrochemical cell for XAS measurements presents additional challenges that are developed below.

As regards the first requirement cited above, the cell must use the standard three-electrode configuration, in order to have suitable electrochemical behaviour. Primarily, the cell should have satisfactorily good electrical properties: the iR_s drop should be low, and several criteria for the electrodes have to be considered. That is to say, a well-defined working electrode surface with uniform current density and potential distribution, a stable reference electrode to allow accurate potential control and, finally, an inert counter electrode that is separated from the WE so that reactions, and thus product generated at the CE, will not affect what takes place at the working electrode. In addition, the CE should have a sufficiently high surface area in order to obtain efficient current detection. As a final point, the potentiostat system should

possess enough output voltage and output current in order to operate, without signal distortion, current transient and potential steps.

Electrolytic efficiency was an additional consideration in designing these cells. The efficiency is largely determined by the ratio of the area of the working electrode to the volume of the solution to be electrolysed. Reticulated Vitreous Carbon (RVC) was chosen for the WE and the CE because of its composition, structure, and electrochemical properties (see below for expanded properties of RVC). Electrochemical equilibrium is reported to be achieved rapidly, with rapid electrolysis of the solution in the immediate vicinity of the electrode²⁵. Due to the free void volume of RVC, ca. 90 – 97%, depending on the porosity grade, most of the solution is contained inside the electrode. Therefore, there exists a short average diffusional path to the electrode surface.

Often conflicting with the electrochemical criteria, the spectroscopic requirements include firstly transparency to X-rays from the cell window and any other parts of the cell that are in the X-ray beam. This restricts the range of materials available to a few polymers and ceramics. The most commonly used materials for in situ spectroelectrochemical cell are, in general, polyimide (Kapton®), polyethylene (Mylar®) and polymethylmethacrylate (Perspex®). All of the XAS studies presented in this work have been carried out at hard edges (Ru K edge: 22117 eV and Rh K edge: 23220 eV). At such high energies, attenuation of the beam by the cell window material should not be a problem. Secondly, but not least, XAS spectroscopy criteria include as well a choice of material that is cheap, readily available, robust, and inert. The material of choice should, in addition, be easily machined to the tolerances required for accurate positioning and alignment of the sample. Besides, to ensure precise positioning of the cell in the X-ray beam, cell mounting plates are required.

In addition, the cell has to be constructed from robust and chemically inert material suitable for repetitive use. In the context of valuable synchrotron beamtime, the cell components should be easy to assemble, disassemble, clean and re-assemble. Finally, construction of a leak-tight cell became a major challenge in this project because of the temperature range required, from 298 K to 243 K.

An accurate description of the cells designed and employed for this work is presented here.

The starting point

The first cell designed for this project is based upon the work of Best *et al.*²⁶ (see Figure 4.6), who designed a continuous-flow electrolysis cell that permits transfer of the solution from the working electrode to a separate EXAFS cell.

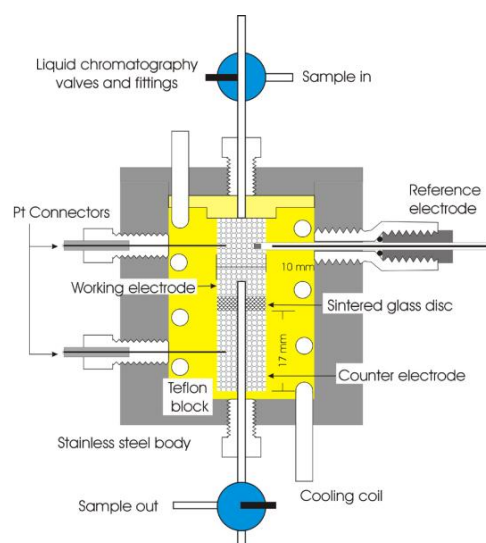


Figure 4.6: Cross-sectional view of the continuous flow electro-synthesis cell designed by Best *et al.*²⁶

For several reasons we were motivated to design an integrated cell but with physically separated compartments for XAS and electrolysis. There are two advantages for such a

configuration. On one hand, the time to transfer the electrolysed solution to the EXAFS compartment is minimised and on the other hand, the temperature can be maintained uniformly from the time the reactants are injected to the cell to the time that products are analysed. In his version, Best froze the electrolyte by immersion of the XAFS cell into liquid nitrogen, which trapped unstable product species. Then data were collected at low temperatures in order to reduce beam damage.²⁶⁻²⁸ This strategy is successful for moderately stable products, but more difficult for very reactive species, or those where a dynamic equilibrium exists amongst various products. Therefore, as a second modification, we opted for cooling the entire assembly by a thermoelectric device.

4.3.3.b Description of spectroelectrochemical cell 1

The electrolysis cell was machined from a block of a PTFE (well known for its chemical inertness) inside which a 10 mm diameter cylinder was bored and closed with a PTFE cap via screw fittings. It should be now noted that when screwing down, the thread has the tendency to be stripped off and care should be taken. To solve this issue, metallic inserts could be used but the presence of the solvent around these could lead to an electrical short circuit. Ports were drilled for the electrodes, and also for the solution inlet and outlet.

The working and the counter electrodes were two 6 mm thick disks machined from a Reticulated Vitreous Carbon (RVC) block (100 pores per inch, ppi). RVC was obtained from ERG Inc. (Oakland, CA) and is available in various porosities (5 to 100 ppi), thus allowing the control of the surface area-to-volume ratio of any electrode. This sponge-like form of glassy carbon has a high free void volume (up to 97%) and a correspondingly high surface area (up to 66 cm²/cm³, for the 100 ppi matrix). The open-pore structure allows easy machining into the desired geometric shape. It was first utilised as an electrode material in

1977 by Norvell and Mamantov who built an Optically Transparent Electrode (OTE) with an RVC electrode²⁵. Since then, because RVC combines the electrochemical properties of non-porous glassy carbon with many hydrodynamic and structural advantages, several in situ electrochemical cells, using RVC as an electrode material, have been published to study transition metal and biological complexes. For our study, RVC was chosen for both the WE and the CE because of its composition, structure and electrochemical properties. The continuous rigid structure results in high electrical conductivity throughout the material matrix. The reference electrode is Ag/AgCl (Cypress Systems). Electrical contact was achieved by placing platinum wires (Goodfellow) on the top surface of each RVC electrode. The CE and the WE were separated by a sintered glass disk (porosity 2). In order to minimize the volume of the electrolysis cell, three carbon paper disks (1 mm thick) were used, in addition to a PTFE cylindric block at the top. A schematic of the internal composition of the electrolysis compartment is presented in Figure 4.7.

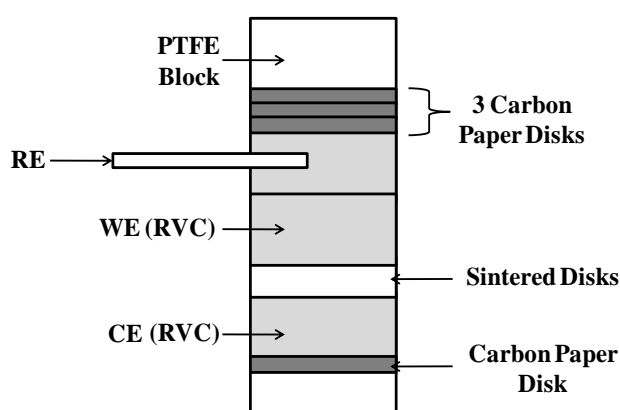


Figure 4.7: Cross sectional view of the spectroelectrochemical cell 1 in a brass housing.

The EXAFS compartment consisted of a raised section on the side of the PTFE block 10 mm in length and 2 mm wide. It was surrounded by a polypropylene window to give a rectangular channel through which the solution flowed (see Figure 4.8) The cell housing comprised a brass box (72.5×54×42 mm) and an aluminium plate with 8 threaded holes to ensure even compression of the polypropylene against the PTFE block. A Kalrez[®] o-ring was used to seal the EXAFS compartment while a second was used to seal the electrolysis cell. The use of Kalrez[®] o-rings rather than Viton o-rings provides the most reliable leak-tight elastomers seals, even though much more expensive. The use of aggressive solvents results in swelling of the rubber and therefore does not assure suitable sealing.

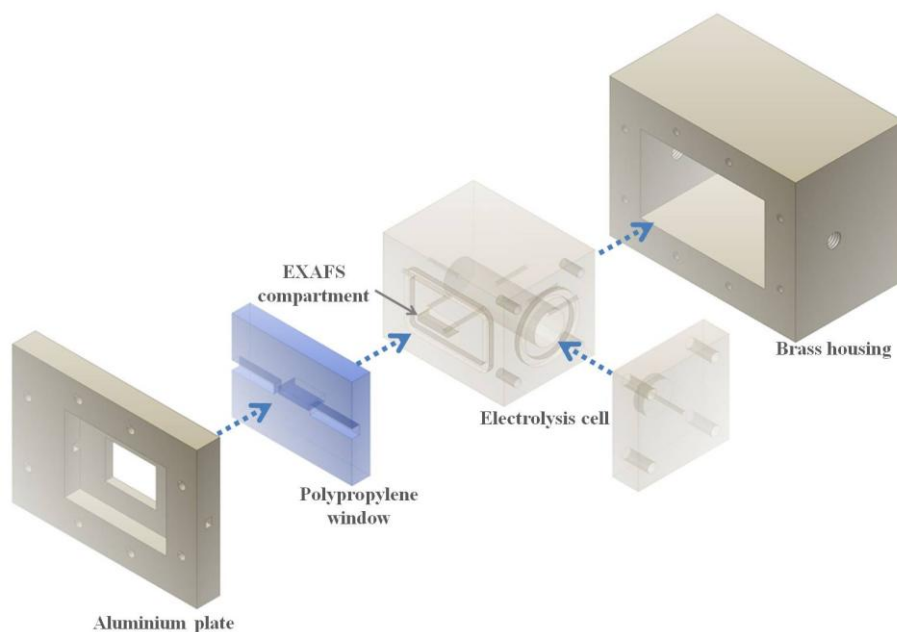


Figure 4.8: Schematic of the 3D view of the spectroelectrochemical cell 1.

The cell was filled as follows: nitrogen-purged background electrolyte-solvent solution was added to the counter electrode compartment of the electrolysis cell to saturate both RVC

disks. Sample solution was then injected to the working electrode compartment. Electrolysed solution was transferred from the electrolysis cell to the EXAFS compartment through a 1 mm diameter hole. Having flowed along the 10 mm length channel, the solution exited the cell by the outlet port.

With practice, the assembly of the cell was completed within 30 min. After the cell has been used for EXAFS measurements, it would be easily disassembled by removing all the screws and taking out all the RVC discs. All the cell components were cleaned by ultra-sonicating in propan-2-ol (or isopropyl alcohol, IPA) for 20 minutes twice, with thorough rinsing with IPA in between and then dried under vacuum. No replacement components were needed, except if damage had been caused during the manipulation of the RVC disks.

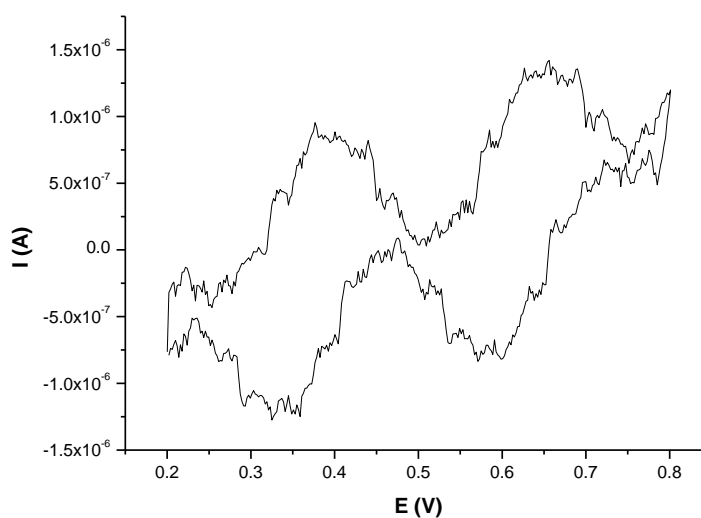
4.3.3.c Description of the cooling system

In order to carry out EXAFS investigations of the behaviour of ruthenocene at low temperature, the sample had to be cooled down. For this purpose, Peltier coolers were used. For Peltier coolers to work efficiently, the heat generated must be dissipated. This was carried out using a copper plate in which chilled water was circulated. Two thermoelectric coolers were attached to the cooled copper plate using thermal paste. A second copper plate was placed above the Peltier coolers for mounting the spectroelectrochemical cell. In addition, for insulation, the cell was mounted in a die-cast box (230×200×180 mm) filled with polystyrene foam. Temperature control was performed using a PR-59 Peltier control module (supplier: Supercool) and a constant voltage-current power supply.

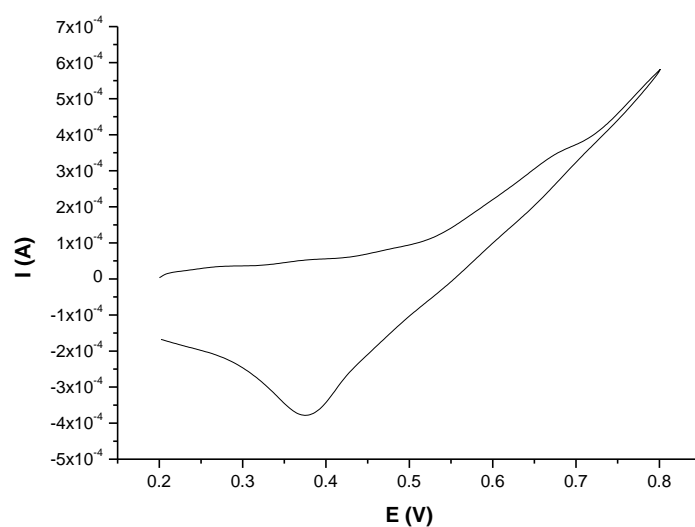
4.3.3.d Electrochemistry trials with Ferrocene

Prior to any beamtime, trials in the laboratory were performed using the ferrocene/ferrocenium couple. The electrochemical behaviour of this complex is well understood, and is stable, reversible and reproducible. In addition, for inorganic electrochemistry it is recommended as the internal standard by the IUPAC.

From an electrochemical standpoint, our cell appeared similar to that published by Best's. That is to say that position and geometry of the electrodes were identical. However, this first spectroelectrochemical cell behaved in a very unexpected manner. Figure 4.10 (a) and (b) shows typical cyclic voltammograms that were recorded.



(a)



(b)

Figure 4.9: Typical Cyclic Voltammograms ((a) and (b)) of 5 mM of FeCp₂ in MeCN/ 0.1M [NBu₄][PF₆] in the cell 1 at 0.05 V s⁻¹, 298 K.

On Figure 4.9 (a) one can observe that no significant electrical response was obtained and therefore no electrochemical control could be achieved. After some thought, we hypothesised that this behaviour could be attributed to the presence of the metal casing affecting the response.

Therefore, we decided to test the cell without the Brass housing, having only, from the cell on the bench, the PTFE electrolysis cell component. Figure 4.9 (b) then showed us that the cell was essentially acting as a curious resistor. Finally, this behaviour was attributed to the fact that the RVC was actually shielding the RE and the CE.

Based on those understandings, the internal configuration of the electrolysis cell was modified. A schematic of the internal composition of the new layout of the electrolysis compartment in Figure 4.10 and its cross sectional view in a brass housing is presented in Figure 4.11.

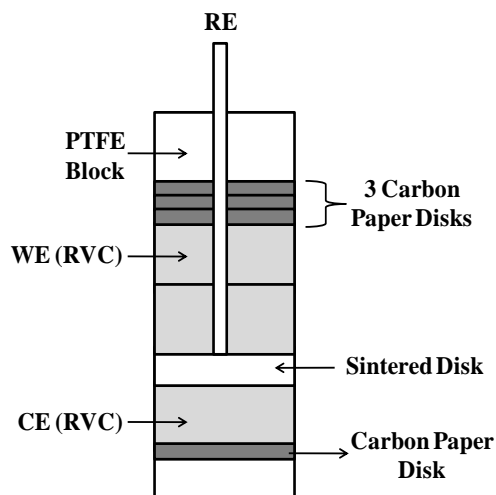


Figure 4.10: Schematic drawing of the internal configuration of the revised layout of the electrolysis compartment.

It can be seen that the principal difference between the two configurations lies in the position of the reference electrode with respect to the working electrode. In the second version, the reference electrode is positioned at the surface of the RVC WE disc facing the CE. In this way the potential experienced by the RE is not shielded by the WE.

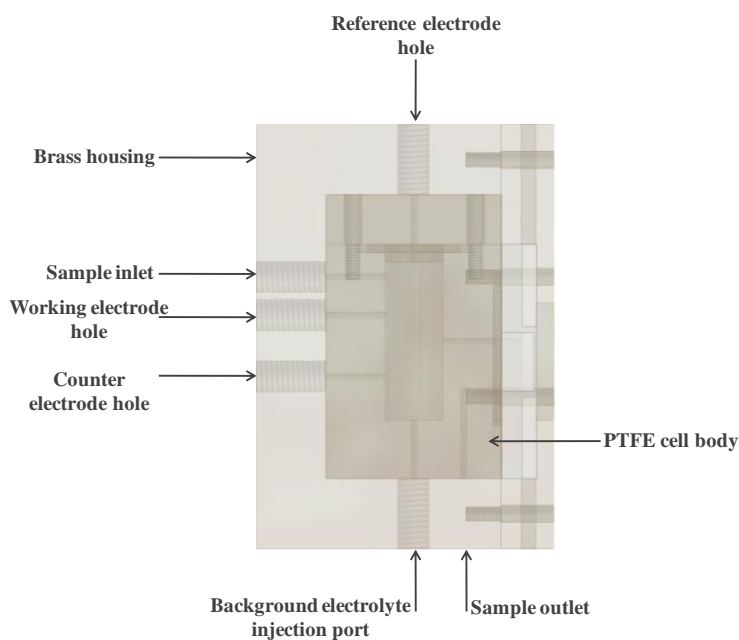


Figure 4.11: Cross sectional view of the new spectroelectrochemical cell 1 in a brass housing.

Electrochemical testing was repeated and a typical cyclic voltammogram of 5 mM of ferrocene and 0.1M [NBu₄][PF₆] in dry as well as purged acetonitrile obtained with the modified version of the spectroelectrochemical cell 1 is shown in Figure 4.12.

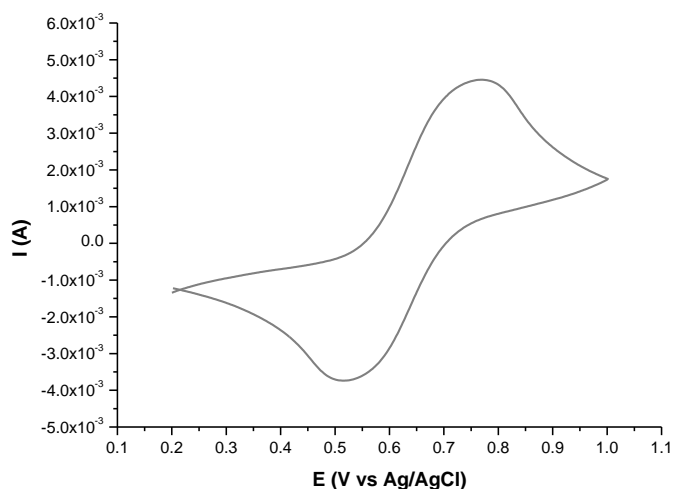


Figure 4.12: Cyclic Voltammogram of 5 mM of FeCp₂ in MeCN/ 0.1M [NBu₄][PF₆] in the cell 1 at 0.05 V s⁻¹, 298 K.

The CV clearly resembles the CV that would be obtained in a conventional three electrode electrochemical cell. However, the scan highlighted two additional features. First, the slope of the scan gives an obvious sign of an iR drop that exists across the cell, due to the solution resistance whose major effects are typically a shift in peak potential and a high oxidation/reduction peak separation. Secondly, these experimental conditions give rise to a smooth-shaped peak rather than the traditional peak-shaped voltammogram. This is attributed to the complex diffusion behaviour within the RVC and we are not able to model this.

4.4 Experiments at the SRS

XAS data presented in this chapter were collected on station 16.5 of the Synchrotron Radiation Source at the Daresbury Laboratory.

4.4.1 Cell alignment

As described in section 4.3.3.b, the EXAFS compartment consists of a 2 mm high and 2 mm wide channel. Consequently, it is necessary to align the X-ray beam with the central axis of the XAS compartment prior to data collection. On station 16.5, the beam dimensions fully focused are 1 mm (vertical) by 2.5 mm (horizontal).

The cell was aligned first in the vertical direction. Because of problems with data storage, alignment has to be done in transmission mode, and then fine tuned manually in fluorescence detection mode. The sample was scanned in the z-axis. Figure 4.13 shows a plot of the transmitted photon flux during a vertical scan:

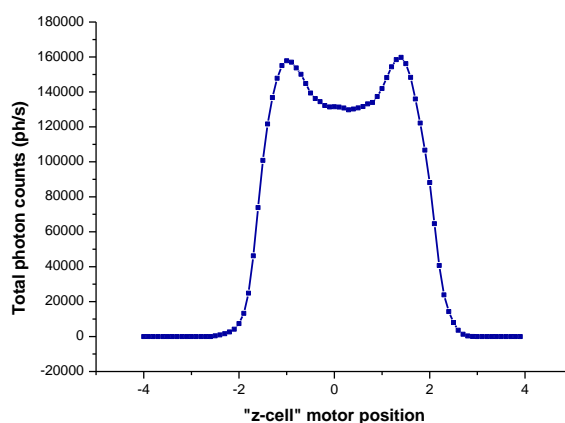


Figure 4.13: vertical alignment scan of the cell channel through the x-ray beam to determine the position of the channel centre. The cell was filled with 5 mM of **1**, 0.025 M $[\text{NPr}_4][\text{B}(\text{C}_6\text{H}_3(\text{CF}_3)_2)_4]$, no flow, open circuit, 298 K.

It can be observed that the beam is masked by the aluminium housing of the channel at each end of the scan. By moving the cell to the z -position of the middle point of the FWHM, the x-ray beam will be in the centre of the channel.

However, the shape of this scan was not expected. The presence of two peaks suggests that the transmission of X-rays through the electrolyte solution is less than through the polypropylene (PP) housing. This is confirmed by calculations shown by Figure 4.14.

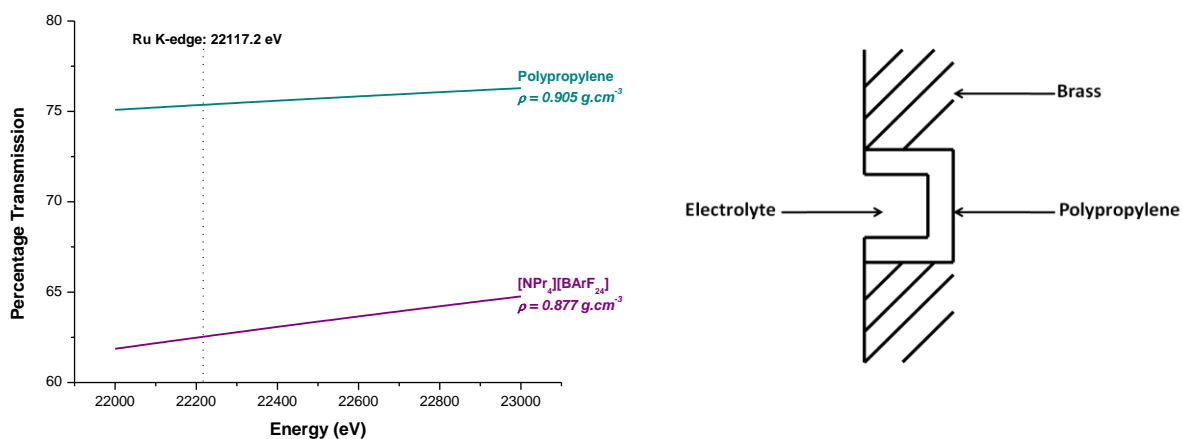


Figure 4.14: X-ray transmission through 10 mm of polypropylene and $[\text{NPr}_4][\text{BARF}_{24}]$ electrolytic salt over a range of energies incorporating the Ru K-edge (on the left) and schematic of a cross section of the surrounding of the channel path in the spectroelectrochemical cell 1 (on the right).

The next step is to ensure that the X-ray beam lies in the correct horizontal position. For this, the sample is scanned in the x-axis, giving data shown in Figure 4.15. The shape of the scan reflects the sagittal focusing, the beam being less uniform in the horizontal plane. The optimum position was taken to be the point of maximum transmission.

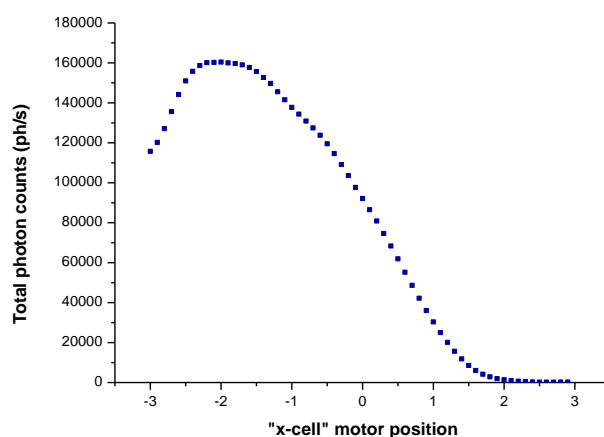


Figure 4.15: Horizontal alignment scan of the cell channel through the X-ray beam to determine the position of the channel centre. The cell was filled with 5 mM of **1**, 0.025 M $[\text{NPr}_4][\text{B}(\text{C}_6\text{H}_3(\text{CF}_3)_2)_4]$, no flow, open circuit, 298 K.

After aligning the cell using the transmitted X-ray flux, the X-ray fluorescence signal was optimized by making small horizontal adjustments of position.

4.4.2 Electrochemistry of ruthenocene in spectroelectrochemical cell 1.

A solution of 5 mM of RuCp_2 , 0.025 M $[\text{NBu}_4][\text{B}(\text{C}_6\text{H}_3(\text{CF}_3)_2)_4]$ in BTF was purged with nitrogen. Before connecting the syringe pump to the cell inlet, 0.5 mL of solution was injected into the cell. As shown in Figure 4.16, a linear sweep voltammogram at a sweep rate of 10 mV s^{-1} was recorded to set the potential of the cell to $E_{\text{appl}}=1.4 \text{ V}$. The current response reaches its maximum value of $1.09 \times 10^{-3} \text{ A}$ at $E_{\text{appl}}=1.35 \text{ V}$. In addition, a straight line can be seen on the scan, due to the fact that the voltage of the counter electrode is reaching the limit. The practical consequence of this observation was that the maximum applied voltage was 1.35 V vs. Ag/AgCl. This is a consequence of the lower conductivity of BTF compared with acetonitrile. MeCN being a considerably more polar solvent ($\epsilon_{\text{MeCN}} = 36$, $\epsilon_{\text{BTF}} = 9.2$), ionic

association constants (K_A) are low. This is due to the fact that the high polarity of acetonitrile minimises the electrostatic effect and the conductivity of its solutions is governed predominantly by ionic mobility. Besides, in the case of high-polarity solvents in general, the large size of the large anions such as $[\text{BArF}_{24}]^-$ and $[\text{TFAB}]^-$ is a disadvantage over traditional anions such as $[\text{BF}_4]^-$ or $[\text{PF}_6]^-$ regarding the conductivity and ohmic drop.^{5,15,18} Table 4.2 shows an illustration of those statements where the limiting ionic conductivity (λ°) is compared between the traditional anions $[\text{PF}_6]^-$ and $[\text{BF}_4]^-$, and the weakly coordinating anion $[\text{TFAB}]^-$ in 3 different solvents, namely dichloromethane, benzonitrile and acetonitrile.

λ° ($\Omega^{-1}\text{cm}^2\text{mol}^{-1}$)	$[\text{PF}_6]$	$[\text{BF}_4]$	$[\text{TFAB}]$
BTF	22.3	46.5	35.3
MeCN	104	<i>n/a</i>	55
DCM	64.1	75.1	42.1

Table 4.2: Limiting Ionic Conductivities of $[\text{PF}_6]$, $[\text{BF}_4]$, and $[\text{TFAB}]$ salts in different media. The values were taken from the studies of LeSuer *et al.*¹⁸

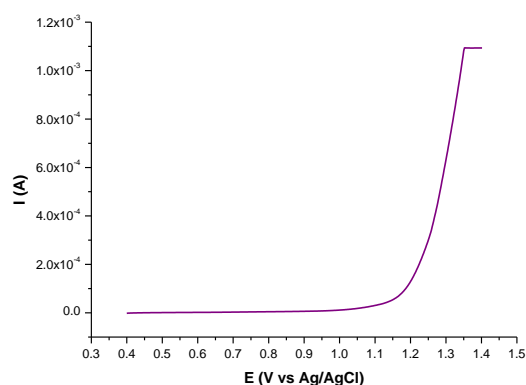


Figure 4.16: Linear Sweep Voltammogram of 5 mM of RuCp₂ in BTf / 0.025 M [NPr₄][B(C₆H₃(CF₃)₂)₄] at 298 K before anodic electrolysis, 10 mV s⁻¹.

With a flow rate of 100 $\mu\text{L} \cdot \text{h}^{-1}$, the potential was held at 1.4 V for 8 hours to allow sufficient time for EXAFS data collection. The purpose of this was to maximise electrolysis of the solution using chronoamperometry. The cell potential was then stepped between values at which the neutral species should be present and oxidised to the [RuCp₂]⁺ cation. For a 100% conversion, the expected current would be equal to reach 2% of its initial value, that is to say ca. 2×10^{-5} A, which is far from what can be observed on the chronoamperogram. The electrolysis conversion is thus expected to be very low. Figure 4.17 shows the recorded current within 8 hours of data collection time, at a constant potential of 1.4 V. In addition, it can be seen that at ca. 18000 seconds the currents dropped which indicated the passivation at the electrode. EXAFS data was then collected during the oxidation and the reduction process.

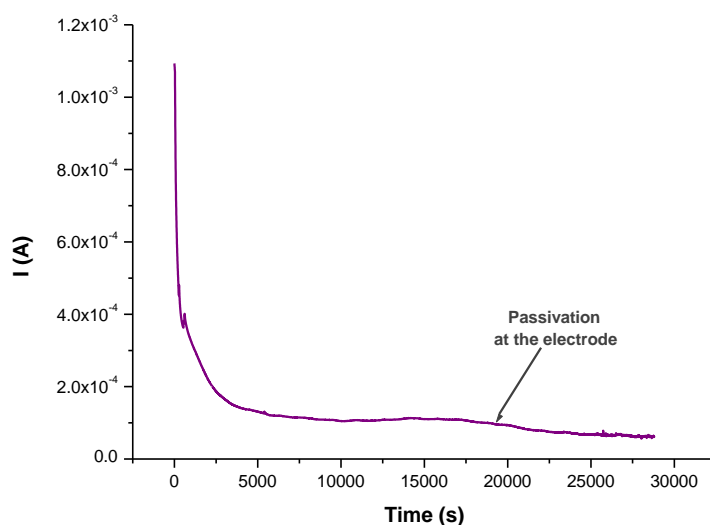


Figure 4.17: Chronoamperogram of 5 mM of RuCp₂ in BTF/0.025 M [NPr₄][B(C₆H₃(CF₃)₂)₄] at 298 K during anodic electrolysis at $E_{appl} = 1.4$ V.

Following XAS data collection, a reverse linear sweep voltammogram was then recorded over the potential interval of 1.4 V to 0.4 V, as shown in Figure 4.18.

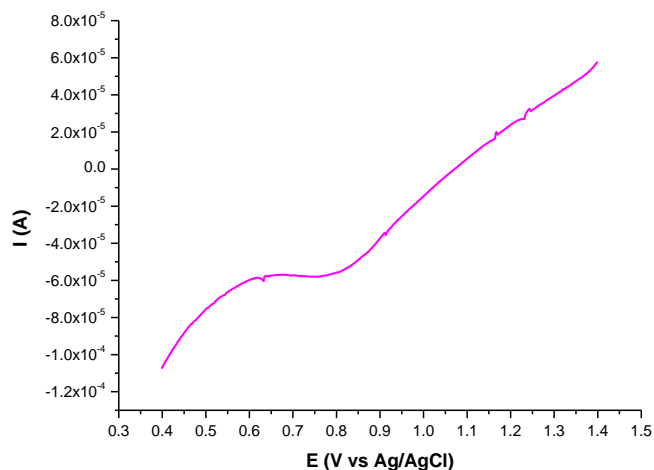


Figure 4.18: Linear Sweep Voltammogram of 5 mM of RuCp₂ in BTF/0.025 M [NPr₄][B(C₆H₃(CF₃)₂)₄] at 298 K after anodic electrolysis, 10 mV s⁻¹.

This shows that whilst the electrode retains some activity, the fraction of conversion from the neutral species to the electrolysed species within the cell is very small.

The electrolysis configuration of this spectroelectrochemical cell did not provide the expected efficiency from Best's publication.²⁶

4.4.3 EXAFS measurements.

As previously discussed, the crystallographic structure of the end point of the ruthenocene oxidation reaction is unknown. The published molecular geometry³⁰ of the neutral species is reproduced in Figure 4.19 and the expected backscatterers of the outgoing photoelectron have been labelled. However, the dimer dication 2^{2+} has defied crystallisation so far.

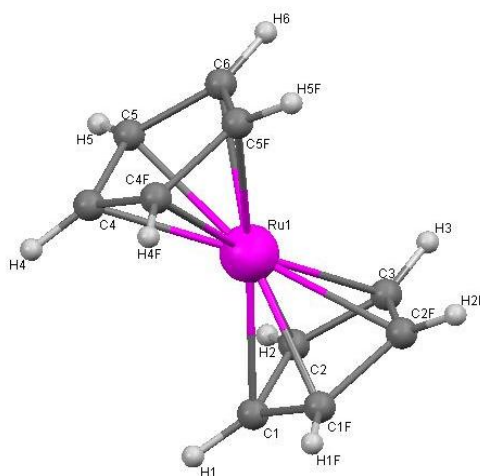


Figure 4.19: Molecular geometry³⁰ of ruthenocene showing labelling scheme used for atomic backscatterers.

The bond distances in ruthenocene are given in Table 4.3. Ruthenocene crystallizes in the orthorhombic space group *Pnma* and the distances given below are averaged over chemically equivalent crystallographic observations.

	Distance R (Å)
Ru ₁ -C	2.1842 (6)
C-C	1.4299 (9)
C-H	1.080

Table 4.3: Bond distances³⁰ with the central atom Ru₁, and the neighbouring atoms.

These distances have been used to set up reference models in ARTEMIS, yielding theoretical EXAFS data for the ruthenocene structure against which experimental data can be compared.

During this beamtime at station 16.5 at the Daresbury SRS, four series of scans were collected for this study: the first series concerns the reference compound while the following three were carried out by applying an oxidative potential, with the aim of generating the dimer dication and thus determining its structure.

Reference scan. Open circuit conditions

A series of 10 scans of a reference solution of 5 mM RuCp₂/0.05 M [NBu₄][B(C₆F₅)₄] in dry BTF in the spectroelectrochemical cell 1 were taken, at room temperature. The electrochemical cell was not under potential control and the flow was set to 200 μl h⁻¹. The cell was mounted on a stage plate and the fluorescence detector was positioned at 100 mm distance from the cell polypropylene window. The beam size was 2 x 2 mm, and the flux 1x10¹⁰ photons s⁻¹. Each scan took ca. 45 min to record and measurements thus lasted ca. seven hours.

When opening the box to disassemble the cell after EXAFS measurements, a strong smell of the solvent suggested the presence of a leak. Through the cell window it was possible to

detect that oxidation had occurred, due to the pink colouring of the channel. However, estimate of the volume in the waste bottle accounted for the presence of 2.7 ml of solution while the initial volume prepared for measurements was ca. 3 ml. Therefore whilst leakage occurred, the conditions were not critical.

Figure 4.20 below shows the sum of the XAS data collected during both open circuit conditions and electrochemical oxidation. The normalised data does not show any difference in the sample whether it is or not subject to the application of a positive potential.

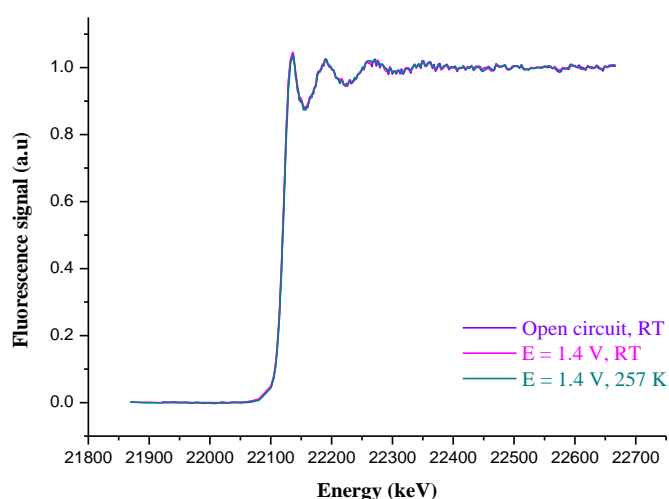


Figure 4.20: Comparison of experimental EXAFS for 5 mM of RuCp_2 in 0.025 M $[\text{NPr}_4][\text{B}(\text{C}_6\text{H}_3\text{CF}_3)_2)_4]$ at open circuit and room temperature conditions (violet line), at an applied potential of $E_{\text{appl}} = 1.4$ V and room temperature conditions (magenta line) and at an applied potential of $E_{\text{appl}} = 1.4$ V and 257 K conditions.

The k^2 weighted EXAFS from each spectrum are also shown in Figure 4.21. Again, no difference can be observed between the three data. Given the large structural variation between ruthenocene and its dimer dication, this data suggests that it is the same structure that is seen throughout, regardless the potential applied.

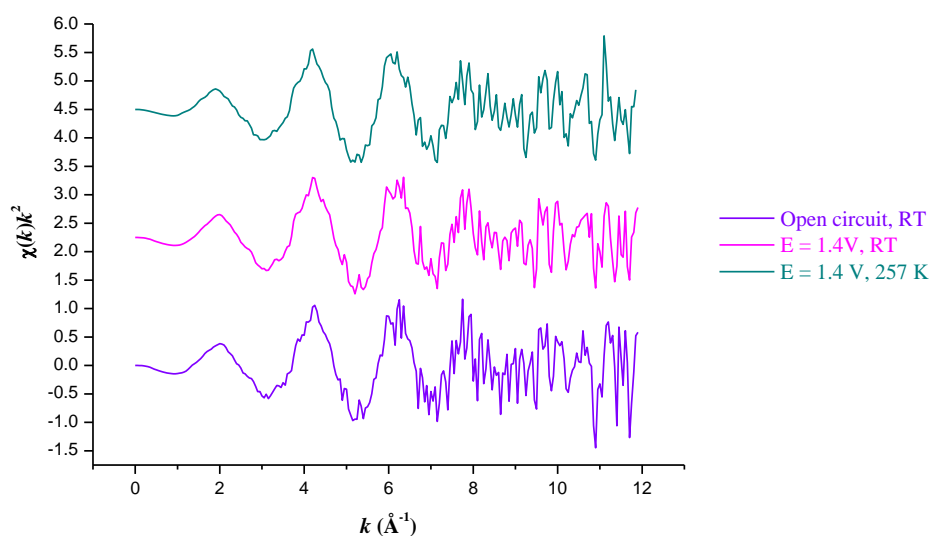


Figure 4.21: k^2 weighted XAS amplitudes for spectroelectrochemical cell measurements upon ruthenocene undertaken in cell 1.

The noise level in the data is obviously very high. It is thus questionable whether the oscillations above 10 \AA^{-1} or so should be included in the fit.

Figure 4.22 shows the structure of RuCp_2 along with the parameters used in the Artemis software for the fits.

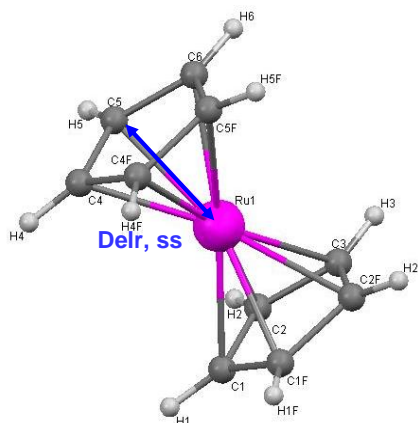


Figure 4.22: Molecular geometry³⁰ of RuCp_2 showing the labelling scheme for atomic backscatterers and the fitting parameters used in the Artemis software.

For the purpose of carrying out XAS calculations, different fitting parameters have been defined as follows: “Delr” characterises the change in the Ru-C bond length compared to that of the referenced crystal structure. All the carbon atoms within the Cp ring are assumed to be at the same distance from the Ru atom. For reasons of simplicity a single Debye-Waller factor “ss” was defined for all the carbon atoms in the first shell, and ssMs for all multiple-scattering path from first and second shell atoms. To finish, the “ S_0^2 ” parameter was used to calculate the passive electron reduction factor, and the “ E_0 ” was utilised to determine the energy shift of the edge value.

As a starting point for fitting the XAS data obtained here, all parameters were set to be fixed to a chosen value: As regards the Debye-Waller factors ss, and ssMs, they have all been attributed the value of 0.01, which can be considered as a realistic guess. At last, the variation of the energy shift E_0 was set to 0 and S_0^2 was defined as equal to 1. Figure 4.23 shows the results of this simulation with the solution at open circuit conditions (fit 1).

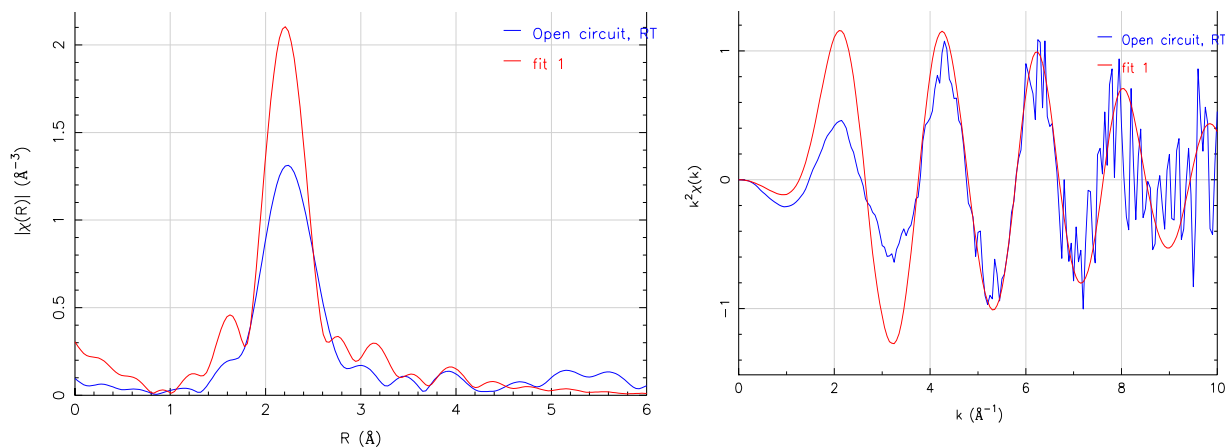


Figure 4.23: Comparison of the experimental data and the simulation (fit1) based upon the crystal structure performed as described above: in R -space (on the left) and in k -space (on the right).

The resultant R -factor value obtained of 0.21 is quite high, and the reduced χ^2 is equal to 8.48.

Subsequently, an optimisation was carried out using the fitting parameters defined in Figure 4.22. The resulting overall fit is shown in Figure 4.24, and plotted against the previous simulation (fit 2) as well as the experimental data.

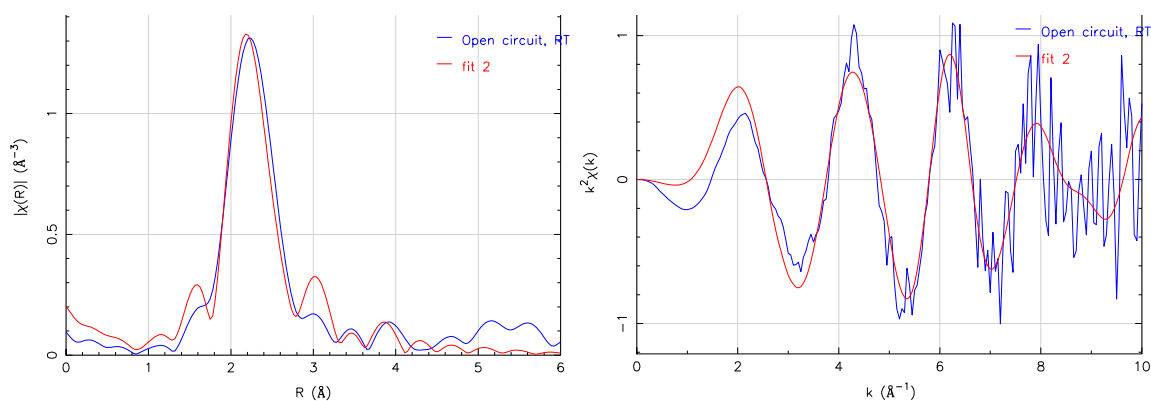


Figure 4.24: Comparison of the experimental data and the simulation (fit2) with optimised parameters as described above: in R -space (on the left) and in k -space (on the right).

Table 4.4 below shows the optimised parameters obtained for fit 2.

Parameter	Optimised value	uncertainty
S_0^2	0.620	+/- 0.4343800
E_0	-2.778	+/- 1.515
ss	0.00274	+/- 0.0012
ssMs	0.010	+/- 0.0047
Delr	-0.0144 Å	+/- 0.0032

Table 4.4: Optimised parameters for ruthenocene.

Thus the change in Ru-C bond length compared with the published structure is equal to -0.0144 Å.

Subsequently, a simulation was performed over the data of the electrolysed species at $E_{\text{appl}}=1.4$ V carried out at 257 K. The result of this fit (fit 3) is show in Figure 4.25 below.

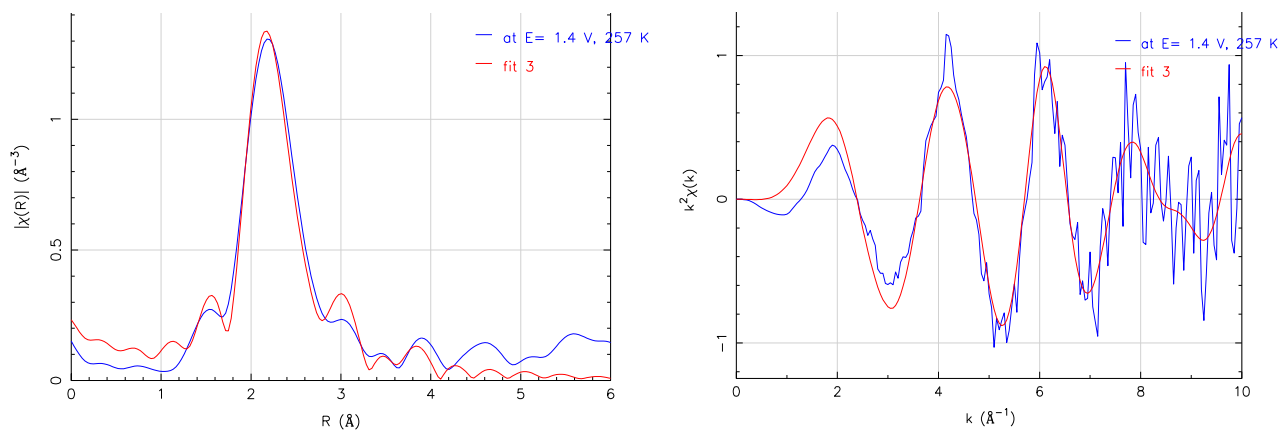


Figure 4.25: Comparison of the experimental data and the simulation (fit3) with optimised parameters as described above: in R -space (on the left) and in k -space (on the right).

Table 4.5 below shows the optimised parameters obtained for fit 3.

Parameter	Optimised value	uncertainty
S_0^2	0.697	+/- 0.089
E_0	-5.93	+/- 1.36
ss	0.0033	+/- 0.0015
ssMs	0.011	+/- 0.0018
Delr	-0.011 Å	+/- 0.0024

Table 4.5: XAS fitting parameters for ruthenocene electrolysed at 1.4 V.

Following electrolysis, the shift in Ru-C bond length compared with the published structure is equal to -0.011 Å. The change in fitted bond length induced by electrolysis is statistically insignificant.

The *R*-factor, which is essentially the fractional misfit, reached a value of 0.0095, and the value of the reduced χ^2 is equal to 0.84.

From the fitting process, it was determined that the central peak arises from the scattering by the five carbons in the η^5 -C₅H₅ ring and the position of this peak corresponds to the distance between the Ru atom and the centroid of the Cp ring.

From these simulations, it is obvious that the main species in solution in neutral ruthenocene regardless the application of an oxidative potential.

4.4.4 Problems at low temperature measurements

The cell is designed to permit careful control of the sample temperature. However, its use at low temperature highlighted an obvious need to change the material used for construction. At 243 K, it was discovered that the cell started to leak catastrophically because of the different

coefficients of thermal expansion. Analysis of the materials properties of the cell components indicates that PTFE was not a good choice of cell material.

For a temperature change, ΔT , the change in the linear dimension can be written as:

$$\frac{\Delta L}{L} = \alpha_L \Delta T$$

Where α_L is the linear thermal coefficient of expansion.

Over the temperature range required for this experiment, the length change of the cell components would be as shown in Table 4.6 below:

Material	Thermal expansion coefficient $\alpha_L/10^{-6}$	Length change ΔL
PTFE	136	340 μm
BRASS	12	38 μm
PEEK	25	50 μm

Table 4.6: Thermal expansion coefficient values for different material with their consequently changes in length.

PTFE was chosen because of its suitability for general electrochemistry, but the thermal properties were obviously not well considered. As it was described in section 4.3.3.c and on Figure 4.8, the PTFE electrolysis cell is held together by pressure from the brass end plates. At 243 K, the difference in thermal contraction of the 2 components is 302 μm , as shown in Table 4.4. This is too large a gap to be sealed by the o-ring. Thus, it seems obvious from the

values presented in the table that PEEK is much better matched to brass. Furthermore, the solvents finally chosen for this project are chemically compatible with PEEK.

4.4.5 Conclusions on Spectroelectrochemical Cell 1

Following analysis of the data, two surprising and rather unwelcome features were found.

The first is that the quality of the data is not as high as we would have expected for Station 16.5. Analysis of the noise in the data led us to conclude that the size of the channel through which the X-ray beam passed was too close in size to the beam size on Station 16.5. Dynamic sagittal focusing works exceedingly well on 16.5, but during servoing small beam movements are induced. Unless the tails of the beam profile are completely contained in the sample, beam movements will induce fluctuations in the fluorescence intensity that cannot be removed by normalisation.

The second problem is a purely electrochemical one. It is common practice to use reticulated vitreous carbon as the electrode in these high throughput electrolysis cells since its surface area is thought to lead to rapid and complete electrolysis. However, the electrolysis is far less rapid than would be expected from the pore size and typical diffusion constants. The cause of this is the electrical shielding within the body of the porous electrode. The direct consequence of this in these experiments was that the fraction of the dimer produced was insufficient to detect with the quality of the data obtained.

The problems encountered thus have independent solutions: as regards the data quality, it seemed obvious that an improved cell had to be constructed with a larger window and flow channel. In addition, another electrode configuration and geometry appeared necessary in order to ensure that the electrolytic efficiency and the time resolution would be optimised.

Moreover, the improved version of the spectroelectrochemical cell 1 aimed to reduce the sample volume, to increase reliability and sample throuput and included a UV/vis spectrometer to give an independent estimate of sample composition.

4.5 Spectroelectrochemical cell 2.

4.5.1 Introduction

Two of the problems encountered with our the spectroelectrochemical cell 1 were straightforward to solve: construction of a new cell with a larger window and flow channel, and a change of materials for low temperature electrochemistry.

Because the concern of the study is to detect reaction intermediates, electrolytic efficiency is a priority. This is the same concern for electrochemical detection in HPLC; there is an extensive literature on electrochemical detection for HPLC, where speed and efficiency are of paramount importance. It seemed sensible to use this knowledge to ensure that the electrolytic efficiency and the time resolution can be optimised. The most popular electrochemical detectors have been based on the amperometric conversion of analyte in a cross-flow thin-layer cell³¹. It is obvious that the percentage of conversion will depend on the mass transport efficiency of the cell, i.e. the flow rate, the electrode area, and the channel thickness.

Moreover, because the investigation concerns the electrochemical behaviour in non-aqueous solvents, special care in the design has to be taken regarding the iR drop. In those conditions, poor conductivity can lead to serious ohmic problems. The optimum positioning of the electrodes is to place the working electrode opposite to the counter electrode in order to have a uniform potential at each point across the surface of the WE, and the charge will therefore pass perpendicular to it. In addition, placing a porous material between both WE and CE

avoids contamination between the two compartments. In the present case, we opted for Porous Vycor[®] glass, Corning 7930.

4.5.2 Cell description

A general assembly drawing of the electrolysis cell is given in Figure 4.24. The body of the electrolysis cell consists of two PEEK blocks ($70 \times 45 \times 16$ mm), held together by aluminium clamping plates and six M5 screws. The working and counter electrode compartments were milled from each of the blocks. These electrodes were sheets of glassy carbon or reticulated vitreous carbon that were cut to the dimensions to fit the two cavities ($40 \times 10 \times 3$ mm). One of the PEEK blocks had an additional cavity (see Figure 4.26, on the right) in order to make space for the separation frit that was Porous Vycor[®] glass (Corning) ($50 \times 20 \times 2$ mm). The reference electrode was Ag/AgCl (Cypress). Ports were drilled to fit the RE into the cell and to achieve electrical contact by placing platinum wires behind the GC or RVC electrodes, as well as for the solution inlet. The electroactive species was constrained here in a layer of 100 μm thickness. A sectional drawing of the electrolysis cell showing the relative position of the electrodes when assembled is given in Figure 4.27.

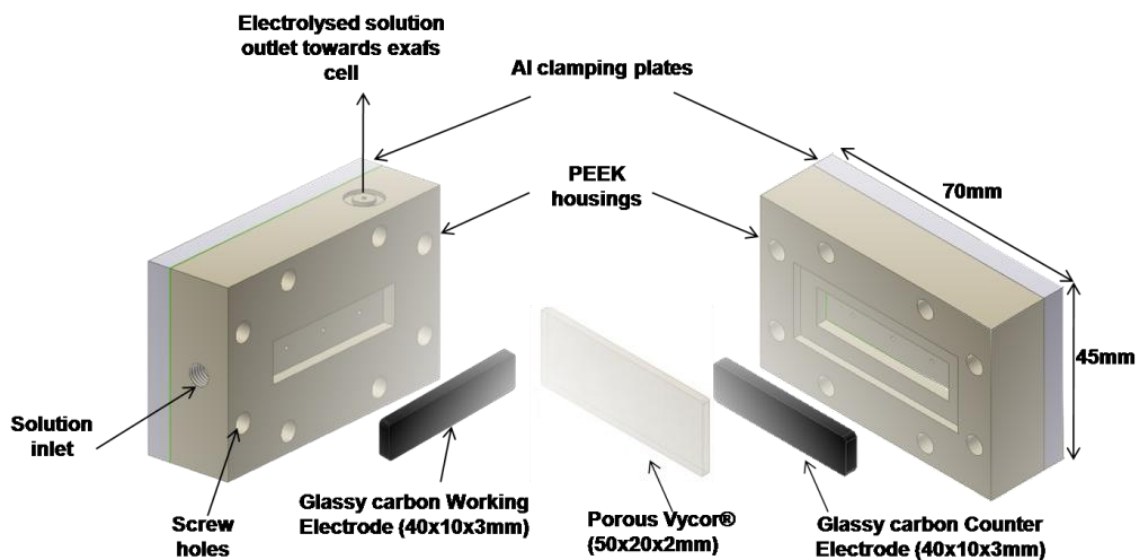


Figure 4.26: Internal composition of the electrolysis compartment of the spectroelectrochemical cell 2.

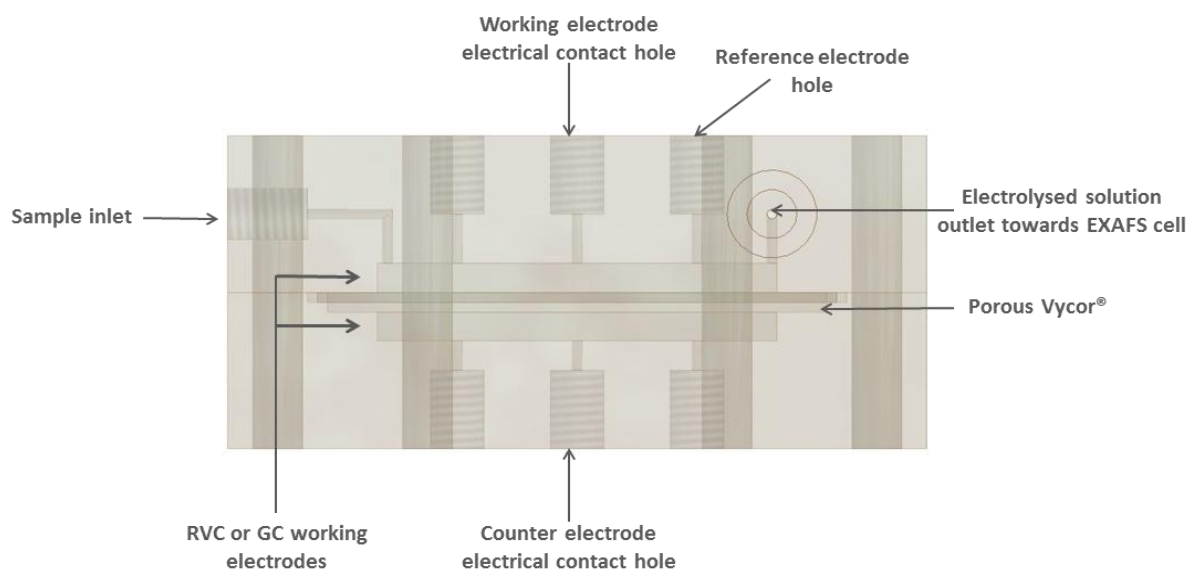


Figure 4.27: Top view of the assembly of the electrolysis compartment of the spectroelectrochemical cell 2.

The EXAFS compartment consisted of a raised section on the side of a PEEK block that was surrounded by a polypropylene window to give a rectangular channel of 10 mm length and 4 mm width through which the solution flows. The latter dimension corresponds to twice the value of the width of the spectroelectrochemical cell 1 since, as mentioned before, this is one of the changes needed for improvement.

The cell was made leaktight via the presence of three Kalrez[®] o-ring seals. One of them was used to seal the two blocks of PEEK of the electrolysis cell, the second was used for a leaktight connection between the PEEK EXAFS compartment and the electrolysis cell and, finally, the third o-ring was meant to ensure sealing between the polypropylene window and the EXAFS block.

As shown in Figure 4.28, the entire cell was clamped together using an aluminium gasket, an aluminium plate and the brass housing that contained the whole electrolysis cell (82 × 51 × 51 mm). Fluid and electrical connections were passed through ports on the outside of both PEEK frames using flanged Omnifit (Omnifit) PTFE tubing and screw fittings.

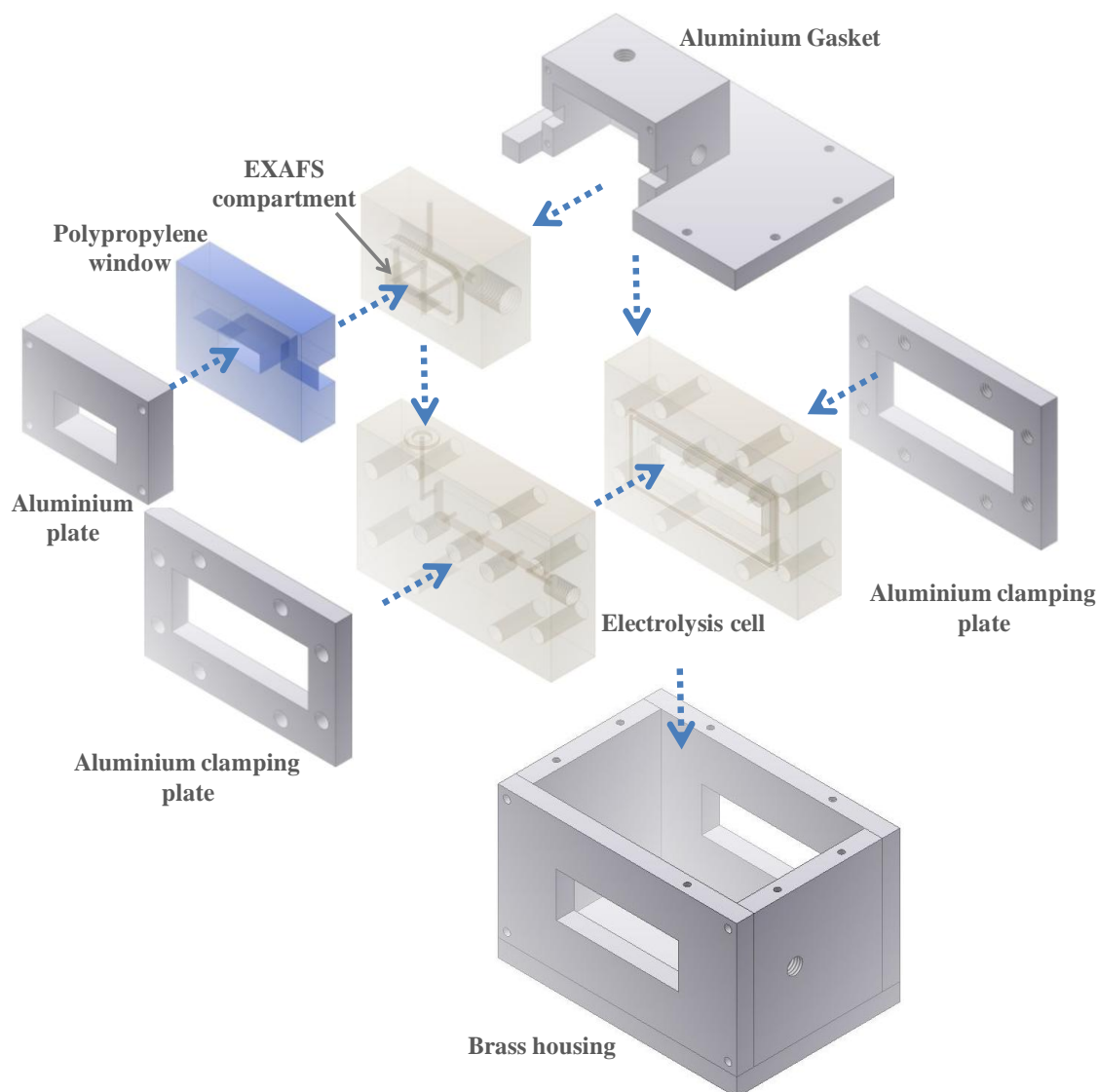


Figure 4.28: Schematic of the 3D view of the spectroelectrochemical cell 2.

In addition to being an integrated XAS/electrolysis cell, this second cell has a supplementary feature: two optic fibres were attached on the PEEK EXAFS block (see Figure 4.29) in order to make in-situ optical absorption measurements. This permits the detection of reaction intermediates and quantifies the electrochemical yield.

The fibres were 600 μm core diameter Premium-grade Optical Fiber, and were connected to a Miniature Fibre Optic Spectrometer (USB4000, Ocean Optics), tuned to a wavelength range of 200 – 850 nm, using a deuterium tungsten halogen Light Source (D-2000 with integrated shutter, Ocean Optics). UV Fused Silica Windows (5 mm diameter) were placed on each side between the flowing solution and the optical fibres.

The cooling system used for this cell was the same used as for the first cell, as described in section 4.3.3.c of this chapter.

The cell was initially filled with degassed electrolyte-solvent solution through the CE compartment. Sample solution was then injected into the WE compartment. Then, the flowing solution was transferred to the EXAFS compartment through a 1 mm diameter hole. Having flowed along the 10 mm channel, the solution was continuing its way to the UV/vis pathlength. The sample finally exited the cell by the outlet port. Figure 4.29 shows the itinerary of the sample solution from its exits from the electrolysis compartment to the exits of the spectroscopic compartment.

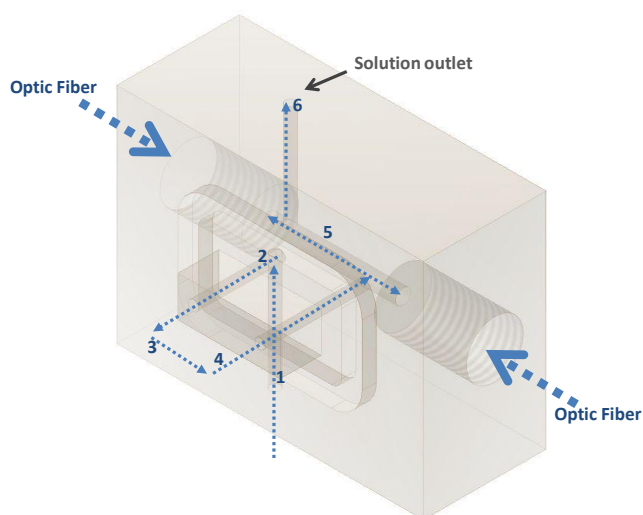


Figure 4.29: Schematic of the spectroscopic compartment including the EXAFS channel and the UV/vis pathlength.

All of the cell components were cleaned by ultra-sonicating in IPA, twice, for 30 min, and then dried under vacuum, except for the porous Vycor®. The latter was soaked in hydrogen peroxide for 1 hour and rinsed thoroughly with water and finally argon-flushed to dry. No replacement components were needed, except if damage had been caused during the manipulation of RVC or Porous Vycor® sheets. With practice, the cell could be assembled in approximately 30 minutes.

4.5.3 Electrochemical evaluation of cell 2

Electrochemical trials were carried out, as before, using a solution of 5 mM ferrocene in acetonitrile, and glassy carbon as working and counter electrodes. The resulting cyclic voltammogram shown in Figure 4.30 below displays comparatively little distortion due to iR potential drop, and confirms that the electrolysis cell has good potential control.

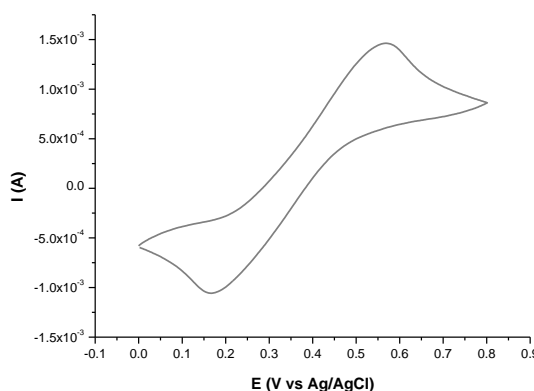


Figure 4.30: Cyclic Voltammograms of 5 mM of FeCp_2 in $\text{MeCN}/0.1 \text{ M } [\text{NBu}_4][\text{PF}_6]$ in the cell 2 constituted of GC working and counter electrodes at 0.1 V s^{-1} , 298 K.

For comparison, a similar voltammogram was recorded in which the working and counter electrodes were reticulated vitreous carbon (RVC). As shown in Figure 4.31, the peak current, when using RVC, is ca. 25 times higher than that using glassy carbon electrodes; this is not

surprising given the increased surface area and electrolyte volume of the RVC compared with GC electrodes. Both configurations give satisfactory electrochemical behaviour.

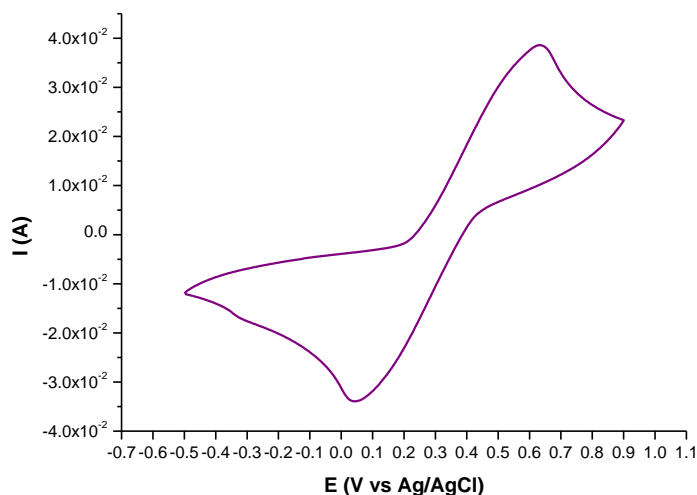


Figure 4.31: Cyclic Voltammogram of 5 mM of FeCp_2 in MeCN/0.1 M $[\text{NBu}_4][\text{PF}_6]$ in the cell 2 constituted of RVC working and counter electrodes at 0.1 V s^{-1} , 298 K.

4.5.4 On line UV/vis analysis

Provision for on line UV/Vis analysis is included in Cell 2 because this technique can provide an independent and potentially more reliable method of measuring the electrochemical yield than coulometry. The feasibility of this approach was tested by online UV/vis measurement of the oxidation of ferrocene. Not only is the electrochemistry reliable but there is also a strong colour change in the visible absorption spectrum upon oxidation. A typical sequence of UV/vis absorption spectra are shown below in Figure 4.32, under flow conditions. It can be seen in Figure 4.32 that over the period of the experiment the electrochemical yield could be quantified by measurements of the integrated areas in the well separated absorption bands. This was an encouraging start in offline experiments.

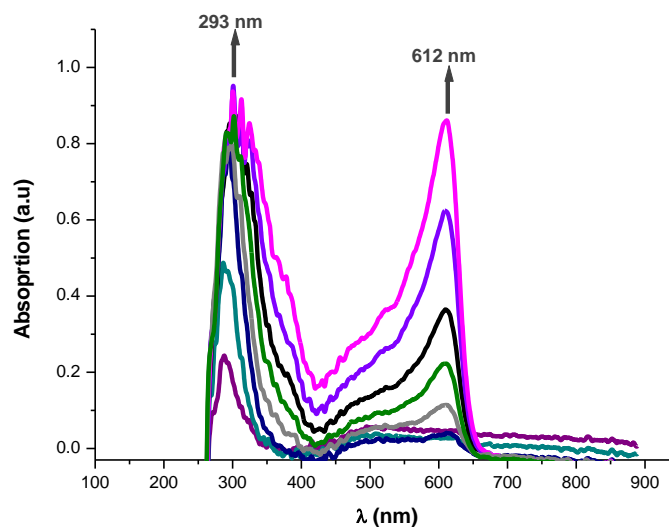


Figure 4.32: A sequence of UV/vis spectra taken for FeCp_2 following the start of electrolysis in Cell 2.

In practice it proved impossible to use UV/vis online analysis during XAS measurements due to an unexpected difficulty caused by the appearance of gas bubbles within the cell. These are of little importance for x-ray measurements provided the bubbles are small and stable for the duration of a scan, but light scattering from a single bubble within the optical path of the UV/vis cell is sufficient to destroy all spectra. This was a particular problem with BTF. Gas was purged from the cell at the outset by injecting solvent into various inlet points, but bubbles always reappeared in the course of electrolysis. At first this was thought to be caused by residual air bubbles that somehow became detached over a period of time. This was not the case – the problem was traced to a reduction in the solubility of nitrogen or argon in BTF with decreasing temperatures. Following normal electrochemical practice, all solutions were rigorously deoxygenated by purging with either nitrogen or argon which meant that the electrolyte solutions were saturated with dissolved gas at room temperature. The volumes of gas were sufficient to prevent collection of good XAS data. Degassing the electrolyte by

freeze/pump/thaw cycles made it possible to collect XAS data, as demonstrated below, but at the SRS it was not possible to degas sufficiently to allow reliable operation of UV/vis analysis.

4.5.5 Experiments at the SRS with Cell 2

The second version of the spectroelectrochemical cell gave completely normal x-ray alignment scans that confirmed that the cell aperture was sufficiently larger than the incident x-ray beam and hence these are not shown here.

A solution of 5 mM RuCp₂, 0.025 M [NPr₄][B(C₆H₃(CF₃)₂)₄] was injected into the cell at a flow rate of 0.4 ml h⁻¹ at a stabilised temperature of 258 K reached by the mean of power supply settings of 1.8 A, 10 V. Working and counter electrodes were RVC and solution was flowing for a sufficient long period of time to monitor enough scans to maximise the signal/noise ratio. A total of 13 scans were recorded, at open circuit conditions, and as observed in Figure 4.33, the plotting in *k*-space increased from 12 to 16 Å⁻¹ and is far less noisy than that obtained with spectroelectrochemical cell 1, previously presented in this chapter.

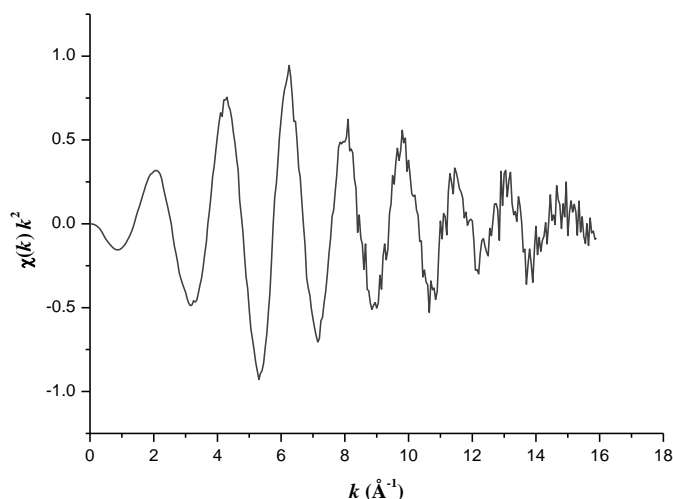


Figure 4.33: k^2 weighted EXAFS of data obtained for 5 mM RuCp₂, 0.025 M [NPr₄][B(C₆H₃(CF₃)₂)₄] under open circuit conditions.

With a flow rate of 200 $\mu\text{l h}^{-1}$, a solution of 5 mM RuCp₂/ 0.025 M [NPr₄][B(C₆H₃(CF₃)₂)₄] was flowing through the cell at a stabilised temperature of 257 K. The potential was held at $E_{\text{appl}} = 1.17$ V during XAS data collection. The chronoamperogram is shown in Figure 4.34. It is expected that the current should drop to a diffusion and flow controlled limit over a period of a few seconds. In figure 4.34, the current drops to a low level and then increases to a plateau. The reason for this behaviour is not known, but could possibly be caused by slow displacement of BTF with which the cell had been initially purged.

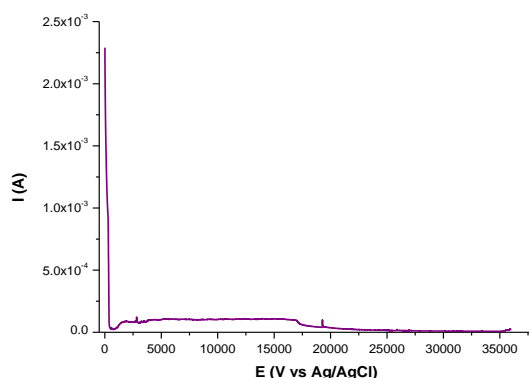


Figure 4.34: Chronoamperogram of 5 mM of RuCp_2 in BTF/0.025 M $[\text{NPr}_4][\text{B}(\text{C}_6\text{H}_3(\text{CF}_3)_2)_4]$ at 258 K during anodic electrolysis at $E_{\text{appl}} = 1.17$ V, with the reticulous vitreous carbon electrodes configuration, collected at Daresbury, station 16.5.

Figure 4.35 shows the normalised XAS data collected during electrolysis and at open circuit conditions. Examination of the normalised spectra shows that upon electrolysis there is an increase in the intensity of the white line. A difference in the XANES region is expected when a loss of electron occurs upon oxidation.

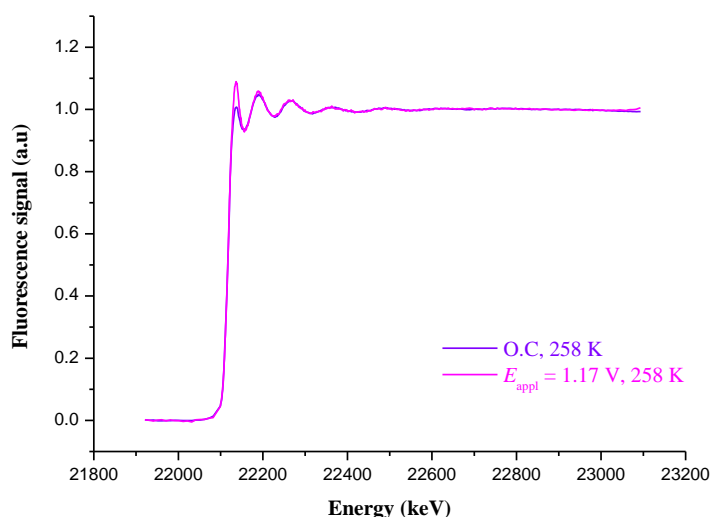


Figure 4.35: Normalised fluorescence spectra of 5 mM RuCp_2 in BTF/0.025 M $[\text{NPr}_4][\text{B}(\text{C}_6\text{H}_3(\text{CF}_3)_2)_4]$ at 258 K, under open circuit (violet line) and under oxidising potential $E_{\text{appl}} = 1.17$ V.

The k^2 weighted EXAFS are also shown in Figure 4.36 but no differences visible by inspection that can be observed between the two data sets.

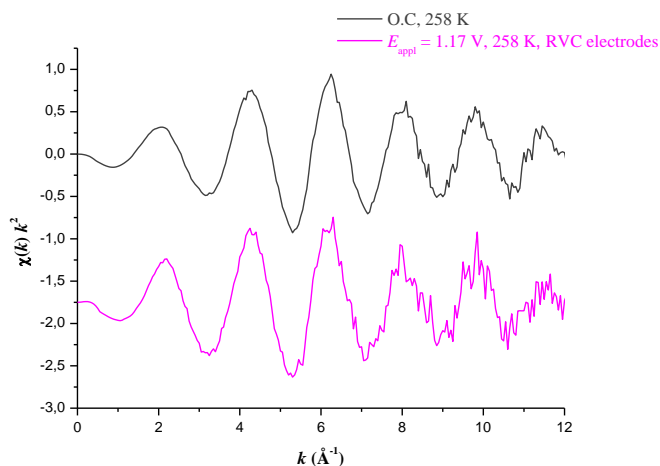


Figure 4.36: k^2 weighted EXAFS of 5 mM RuCp_2 in BTF/0.025M $[\text{NPr}_4][\text{B}(\text{C}_6\text{H}_3(\text{CF}_3)_2)_4]$ at 258K, under open circuit (violet line) and under oxidising potential $E_{\text{appl}} = 1.17$ V.

Both sets of data, at open circuit conditions and under oxidising potential have been fitted and the resulting fits are shown Figure 4.37 and 4.38, respectively.

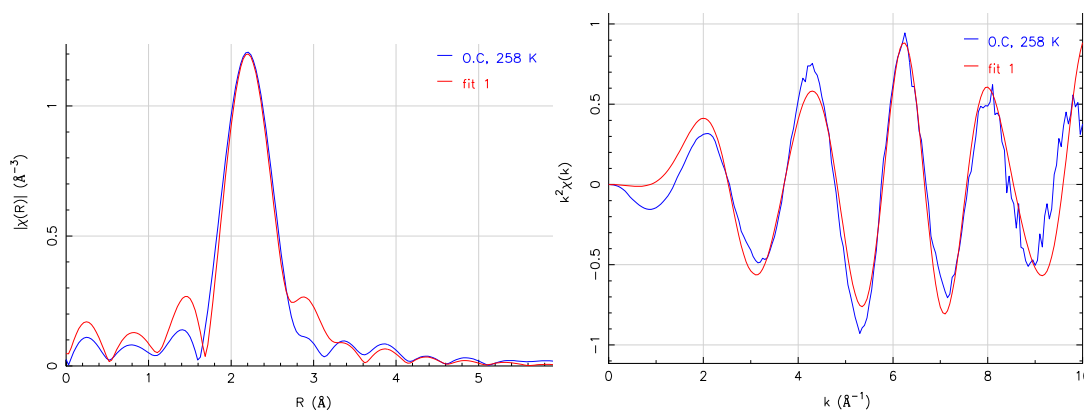


Figure 4.37: XAS amplitudes in real and k space for ruthenocene spectra collected at open circuit at 258 K.

Table 4.7 below shows the optimised parameters obtained for fit 1.

Parameter	Optimised value	uncertainty
S_0^2	0.361	+/- 0.066
E_0	-3.93	+/- 0.96
ss	0.0044	+/- 0.0026
ssMs	0.0148	+/- 0.0062
Delr	-0.0317	+/- 0.0037

Table 4.7: XAS Fitted parameters for ruthenocene collected at open circuit and at 258 K.

The R-factor was equal to 0.027 and the change in the Ru-C bond length compared to that of the published structure was equal to -0.0317.

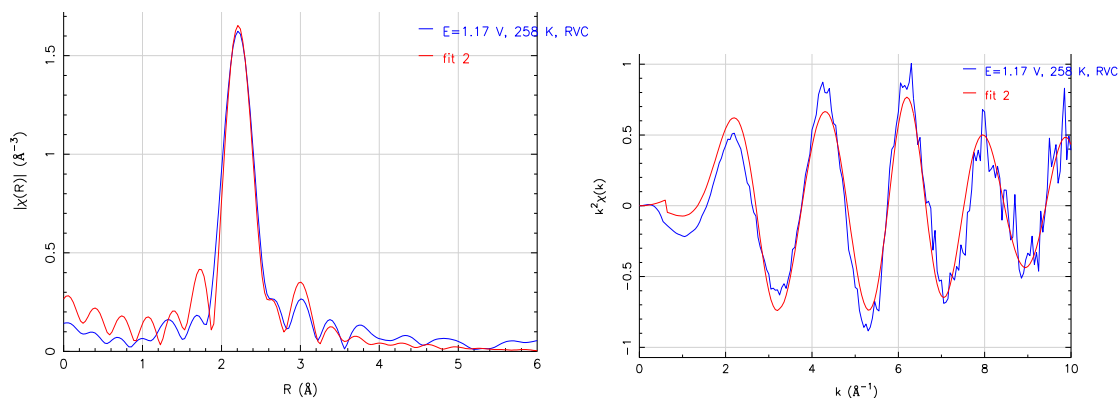


Figure 4.38: XAS amplitudes in real and k space spectra for electrolysed ruthenocene collected at 258 K with the RVC electrodes configuration.

Table 4.8 below shows the optimised parameters obtained for fit 2.

Parameter	Optimised value	uncertainty
S_0^2	0.478	+/- 0.044
E_0	1.45	+/- 0.71
ss	0.0009	+/- 0.001
ssMs	0.008	+/- 0.0035
Delr	0.0080 Å	+/- 0.0001

Table 4.8: XAS Fitted parameters for electrolysed ruthenocene collected at 258 K with the RVC electrodes configuration.

The R-factor reached a value of 0.031 and the reduced χ^2 is equal to 11.37. The change in the Ru-C bond length compared with the published structure is equal to 0.0080 Å which, with experimental error is identical to the published value. The value of the Rh-C bond length obtained using Cell 2 is better than that gained from Cell 1 which reflects the better quality of XAS data obtained in the improved cell.

Following these two data series collected, we decided to change electrode material from RVC to GC, and to further decrease temperature in order to favour the detection of the expected dimer dication. $\mathbf{1}_2^{2+}$. To generate the electrolysed species, the potential was held at $E_{appl} = 1.1$ V and the corresponding chronoamperogram obtained is displayed in Figure 4.39:

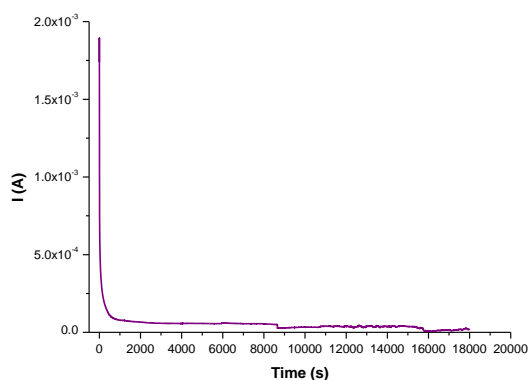


Figure 4.39: Chronoamperogram of 5 mM of RuCp_2 in BTF/0.025M $[\text{NPr}_4][\text{B}(\text{C}_6\text{H}_3(\text{CF}_3)_2)_4]$ at 249 K during anodic electrolysis at $E_{\text{appl}} = 1.1$ V, with the glassy carbon electrodes configuration, collected at Daresbury, station 16.5.

It can be seen that the chronoamperogram displays the expected form, thus strengthening suspicions that the curious behaviour in Figure 4.34 is a feature of RVC electrodes. Comparison of the three sets of experiments described above is illustrated in Figure 4.40, which shows the normalised XAS data, and the k^2 weighted EXAFS signal from each spectrum.

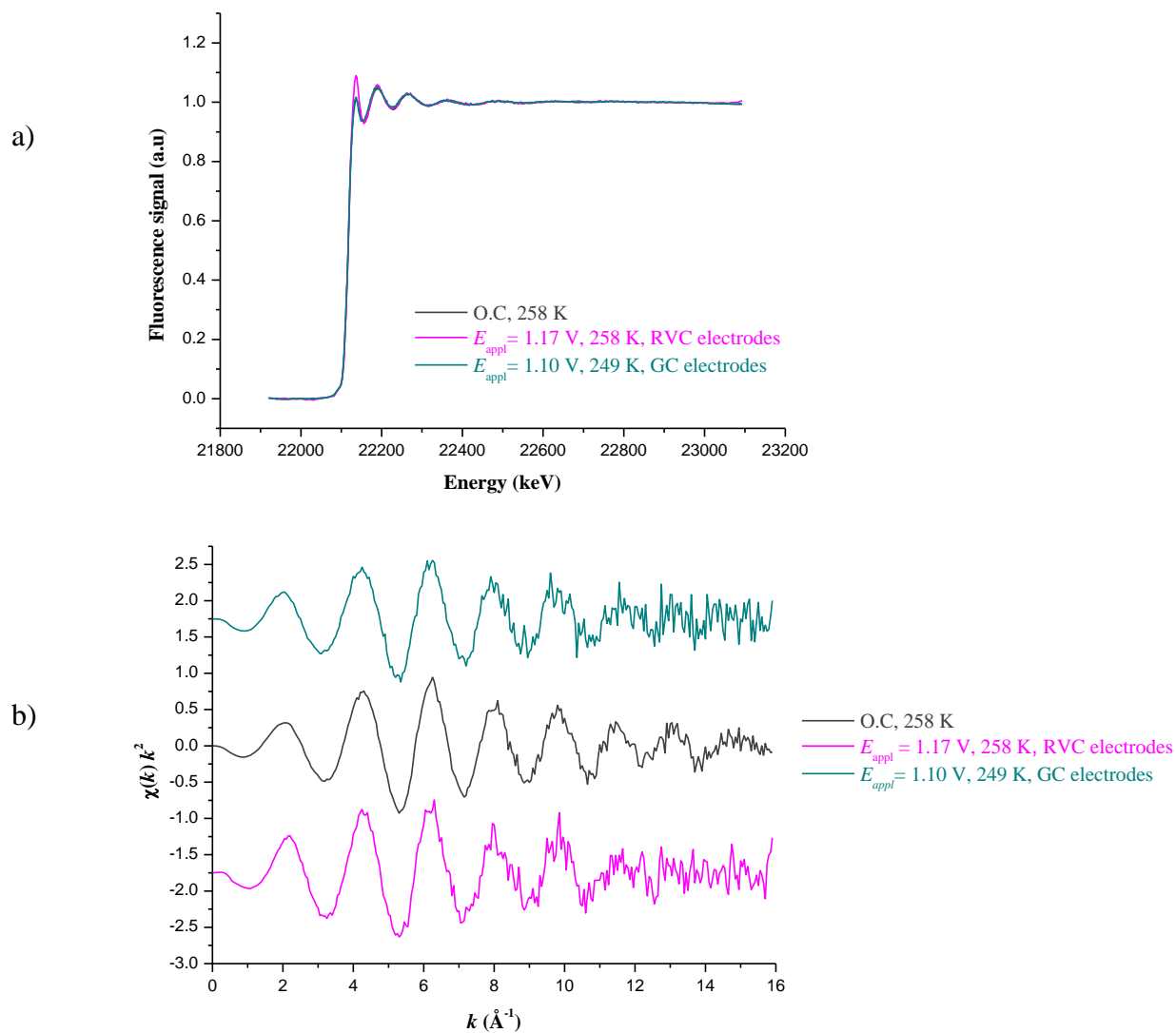


Figure 4.40: A summary of XAS data collected with Cell 2 for ruthenocene a) normalised raw data, b) XAS amplitudes.

The data obtained with the GC electrodes under an oxidising potential of $E_{\text{appl}} = 1.10 \text{ V}$ have thus been fitted and the resulting fit (fit 3) is shown Figure 4.41.

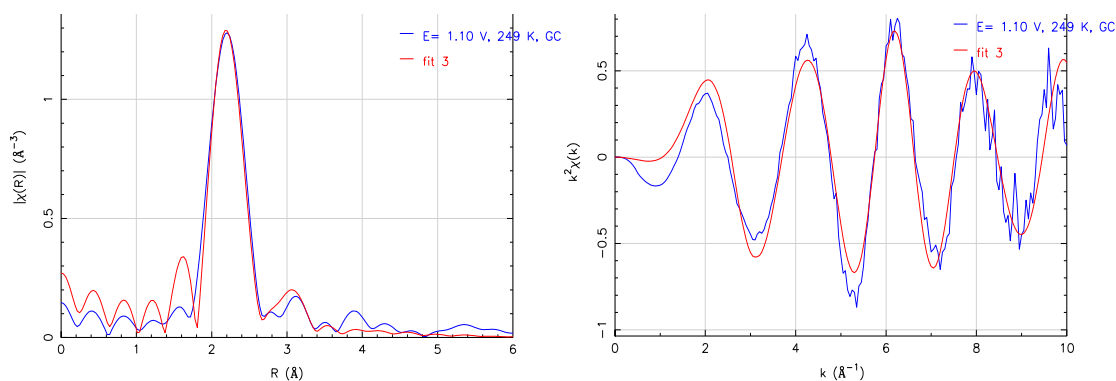


Figure 4.41: XAS amplitudes in real and k space spectra for electrolysed ruthenocene collected at 258 K with the glassy carbon electrodes configuration.

Table 4.9 below shows the optimised parameters obtained for fit 3

Parameter	Optimised value	uncertainty
S_0^2	0.383	+/- 0.046
E_0	-1.75	+/- 0.93
ss	0.0026	+/- 0.0019
ssMs	0.011	+/- 0.0038
DelScale	-0.0033	+/- 0.0038

Table 4.9: XAS Fitted parameters for electrolysed ruthenocene collected at 258 K with the GC electrodes configuration.

Despite the improved electrochemical behaviour of the cells for the spectra shown in Figures 4.35 and 4.36 the change in Ru-C bond length compared with the published structure is only equal to -0.00717\AA which is not a statistically significant change.

However examination of the normalised spectra does show that upon electrolysis there is a small but reproducible increase in the intensity of the white line. This is compatible with a small decrease in the effective d-orbital occupancy of ruthenocene. At the same time there are

very little obvious differences between the XAS amplitudes for the different scans. This is confirmed by fitting the data as described above. At first sight this might seem to indicate that little oxidation of ruthenocene had taken place which is at variance with the electrolysis conversion calculated from the limiting current. Because of the shape of the chronoamperogram for the RVC electrode it is somewhat difficult to define a limiting current, but for the experiment with glassy carbon, the conversion rate is greater than 70 %, as shown in Table 4.10 below:

	Limiting current I_{lim}	Electrolysis conversion
Reticulated Vitreous Carbon	?	?
Glassy Carbon	19.4 μ A	71.4 %

Table 4.10: Electrochemical conversion for electrolysis of ruthenocene with RVC and glassy carbon electrodes.

Substantial conversion of ruthenocene was also confirmed by an obvious colour change visible through the translucent XAS cell upon disassembly at low temperatures. Thus we are compelled to conclude that the chemical conversion is very substantial but also that this produces little changes in the XAS spectra. The most likely interpretation for the striking lack of difference is due to the fact the positive charge of the cation and the cation dimer is delocalised on the cyclopentadienyl rings, and thus there is very little charge transfer to the Ru atom. There are two consequences of this hypothesis. Firstly, the Ru-C bond length would not be expected to change very much. Secondly, with the quality of the data obtained in these experiments, the Fourier transform gives significant data only as far as the first shell. The Ru-Ru bond is a weak bond and would be expected to have a large Debye Waller factor. The backscattering amplitude of any single Ru-Ru bond would be small in comparison with the

ten Ru-C bonds in each molecule of ruthenocene. It is thus perhaps not surprising, even if a little disappointing that the Ru-Ru bond could not be detected in these measurements.

4.5.6 Conclusion:

We have reported here the development of a cell for combined XAS/ electrochemistry/ UV-vis spectroscopy. The obstacles encountered showed that care should be taken of electric fields in the design of electrochemical cells. In particular, when using reticulous vitreous carbon, one should ensure that the gains hoped for in terms of increased surface area are not defeated by diffusion and potential shielding.

Moreover, we have shown the feasibility of UV/vis online analysis in XAS spectroelectrochemistry.

Data have been collected on the low temperature electrochemistry of ruthenocene. The structure changes upon oxidation are small and at the limit of detection in these measurements.

References

1. Wiltshire, R.J.K.; Smila-Castro, O.; Connelly, N.G.; Matthews, S.M.; Fisher, A.C.; Rayment, T. Channel-Flow Cell for X-ray Absorption Spectroelectrochemistry. *J. Phys. Chem. C* **2009**, *113* (1), 308-315.
2. Page, J. A.; Wilkinson, G. The Polarographic Chemistry of Ferrocene, Ruthenocene and the Metal Hydrocarbon Ions. *J. Am. Chem. Soc.* **1952**, *74* (23), 6149-6150.
3. Hendrick, D. N.; Gray, H. B.; Sohn, Y. S.; Morrison, W. H. Characterization of Electrochemical Oxidation Product of Ruthenocene at A Mercury Anode. *Inorg. Chem.* **1972**, *11* (4), 808-811.
4. Adam, R. N. *Electrochemistry at solid electrodes*; Marcel Dekker Inc: 1969.
5. Geiger, W. E. Organometallic electrochemistry: Origins, development, and future. *Organometallics* **2007**, *26* (24), 5738-5765.
6. Bublitz, D. E.; Hoh, G.; Kuwana, T. Chronopotentiometric Oxidation of Ferrocene, Ruthenocene, Osmocene, and Some of Their Derivatives at A Platinum Electrode. *Chem. Ind-London* **1959**, (20), 635-636.
7. Kuwana, T.; Bublitz, D. E.; Hoh, G. Chronopotentiometric Studies on the Oxidation of Ferrocene, Ruthenocene, Osmocene and Some of Their Derivatives. *J. Am. Chem. Soc.* **1960**, *82* (22), 5811-5817.
8. Gubin, S. P.; Smirnova, S. A.; Denisovi, L. I.; Lubovich, A. A. Redox Properties of Cyclopentadienylmetal Compounds .1. Ferrocene, Ruthenocene, Osmocene. *J. Organomet. Chem.* **1971**, *30* (2), 243-255.
9. Denisovi, L. I.; Zakurin, N. V.; Bezrukov, A. A.; Gubin, S. P. Chemical and Electrochemical Oxidation of Metallocenes - Reactions of Metallocenes with Mercury Salts. *J. Organomet. Chem.* **1974**, *81* (2), 207-216.
10. Gale, R. J.; Job, R. Metallocene Electrochemistry .3. Reduction-Oxidation Study of Dicyclopentadienyl Compounds of Ruthenium and Titanium in Lewis Acid-Base Molten-Salts. *Inorg. Chem.* **1981**, *20* (1), 42-45.
11. Hill, M. G.; Lamanna, W. M.; Mann, K. R. Tetrabutylammonium Tetrakis[3,5-Bis(Trifluoromethyl)Phenyl]Borate As A Noncoordinating Electrolyte - Reversible 1e- Oxidations of Ruthenocene, Osmocene, and $\text{Rh}_2(\text{Tm}_4)^{42+}$ ($\text{Tm}_4 = 2,5\text{-Diisocyano-2,5-Dimethylhexane}$). *Inorg. Chem.* **1991**, *30* (25), 4687-4690.

12. Bullock, J. P.; Palazotto, M. C.; Mann, K. R. Electrochemistry and Infrared Spectroelectrochemistry of $[(\eta^5\text{-C}_5\text{R}_5)\text{Fe}(\text{CO})_2]_2$ (R = H, Me) - Generation and Characterization of $[(\eta^5\text{-C}_5\text{R}_5)\text{Fe}(\text{CO})_2]_2$ (PF₆) Complexes. *Inorg. Chem.* **1991**, *30* (6), 1284-1293.
13. Brookhart, M.; Volte Jr., A. F.; DeSimone, J. M.; Lamanna, W. M. *Polym. Prepr.* **1991**, *32*, 461.
14. Nishida, H.; Takada, N.; Yoshimura, M.; Sonoda, T.; Kobayashi, H. Tetrakis[3,5-Bis(Trifluoromethyl)Phenyl]Borate - Highly Lipophilic Stable Anionic Agent for Solvent-Extraction of Cations. *B. Chem. Soc. Jpn* **1984**, *57* (9), 2600-2604.
15. Trupia, S.; Nafady, A.; Geiger, W. E. Electrochemical preparation of the bis(ruthenocenium) dication. *Inorg. Chem.* **2003**, *42* (18), 5480-5482.
16. Swarts, J. C.; Nafady, A.; Roudebush, J. H.; Trupia, S.; Geiger, W. E. One-Electron Oxidation of Ruthenocene: Reactions of the Ruthenocenium Ion in Gentle Electrolyte Media. *Inorg. Chem.* **2009**, *48* (5), 2156-2165.
17. Sawyer, D. T.; Sobkowiak, A.; Roberts, J. L. *Electrochemistry for Chemists*; Second Edition ed.; Wiley-Interscience: **1995**.
18. LeSuer, R. J.; Buttolph, C.; Geiger, W. E. Comparison of the conductivity properties of the tetrabutylammonium salt of tetrakis(pentafluorophenyl)borate anion with those of traditional supporting electrolyte anions in nonaqueous solvents. *Anal. Chem.* **2004**, *76* (21), 6395-6401.
19. Beck, W.; Sunkel, K. Metal-Complexes of Weakly Coordinating Anions - Precursors of Strong Cationic Organometallic Lewis-Acids. *Chem. Rev.* **1988**, *88* (7), 1405-1421.
20. Camire, N.; Nafady, A.; Geiger, W. E. Characterization and reactions of previously elusive 17-electron cations: Electrochemical oxidations of $(\text{C}_6\text{H}_6)\text{Cr}(\text{CO})_3$ and $(\text{C}_5\text{H}_5)\text{Co}(\text{CO})_2$ in the presence of $[\text{B}(\text{C}_6\text{F}_5)_4]^-$. *J. Am. Chem. Soc.* **2002**, *124* (25), 7260-7261.
21. Nafady, A.; Costa, P. J.; Calhorda, M. J.; Geiger, W. E. Electrochemical oxidation of $\text{CoCp}(\text{CO})_2$: Radical-substrate reaction of a 17 e⁻/18 e⁻ pair and production of a unique dimer radical. *J. Am. Chem. Soc.* **2006**, *128* (51), 16587-16599.
22. Chong, D. S.; Nafady, A.; Costa, P. J.; Calhorda, M. J.; Geiger, W. E. Anodic preparation of $[\text{Re}_2\text{Cp}_2(\text{CO})_6]^{2+}$: A dimeric dication that provides the powerful one-electron oxidant $[\text{ReCp}(\text{CO})(3)](+)$. *J. Am. Chem. Soc.* **2005**, *127* (45), 15676-15677.

23. Chong, D.; Laws, D. R.; Nafady, A.; Costa, P. J.; Rheingold, A. L.; Calhorda, M. J.; Geiger, W. E. $[\text{Re}(\eta^5\text{-C}_5\text{H}_5)(\text{CO})_3]^+$ family of 17-electron compounds: Monomer/dimer equilibria and other reactions. *J. Am. Chem. Soc.* **2008**, *130* (8), 2692-2703.
24. Ohrenberg, C.; Geiger, W. E. Electrochemistry in benzotrifluoride: Redox studies in a "noncoordinating" solvent capable of bridging the organic and fluorous phases. *Inorg. Chem.* **2000**, *39* (13), 2948-2950.
25. Norvell, V. E.; Mamantov, G. Optically Transparent Vitreous Carbon Electrode. *Anal. Chem.* **1977**, *49* (9), 1470-1472.
26. Bondin, M. I.; Foran, G.; Best, S. P. Electrosynthesis cell for X-ray absorption fine structure measurement: Reduction of air-sensitive iron-sulfur compounds. *Aust. J. Chem.* **2001**, *54* (11), 705-709.
27. Cheah, M. H.; Borg, S. J.; Bondin, M. I.; Best, S. P. Electrocatalytic proton reduction by phosphido-bridged diiron carbonyl compounds: Distant relations to the H-cluster? *Inorg. Chem.* **2004**, *43* (18), 5635-5644.
28. Borg, S. J.; Behrsing, T.; Best, S. P.; Razavet, M.; Liu, X. M.; Pickett, C. J. Electron transfer at a dithiolate-bridged diiron assembly: Electrocatalytic hydrogen evolution. *J. Am. Chem. Soc.* **2004**, *126* (51), 16988-16999.
29. Bondin, M. I.; Borg, S. J.; Cheah, M. H.; Foran, G.; Best, S. P. Integration of EXAFS, spectroscopic, and DFT techniques for elucidation of the structure of reactive diiron compounds. *Aust. J. Chem.* **2006**, *59* (4), 263-272.
30. Borissova, A.O.; Antipin, M.Y.; Perekalin, D.S.; Lyssenko, K.A. Crucial role of Ru dot center dot H interactions in the crystal packing of ruthenocene and its derivatives. *CrystEngComm.* **2008**, *10* (7), 827-832.
31. Kissinger, P.T.; Heineman, W.R. Laboratory Techniques in Electroanalytical Chemistry, *Marcel Dekker*, **1996**.

*Chapter 5: Electrochemical behaviour of
 $Cp^*Rh(CO)_2$*

5.1 Introduction

The oxidation of complexes of the type $(\eta^5\text{-C}_5\text{H}_5)\text{Rh}(\text{CO})\text{L}$ (L=PPh₃, PMe₃, or P(OPh)₃) is generally agreed to cause dimerisation at either the metal or through ligands, forming the dication of a fulvane complex, or the metal-metal bonded dication. In 1983, Connelly *et al.*¹ reported an electrochemical study of CpRh(CO)PPh₃ where, upon oxidation, the latter gives the radical cation [CpRh(CO)PPh₃]⁺ which rapidly dimerises to the fulvalene complex [Cp₂Rh₂(CO)₂(PPh₃)₂]²⁺. A few years later, Fonseca *et al.*,² showed that when L=PMe₃ or P(OPh)₃, the bulk electrolysis of the rhodium complex leads to a 17-electron cation radical that dimerises by formation of a rhodium-rhodium bond. As a general tendency, ring-ring coupling through the ligand is favoured due to the presence of larger coulombic repulsion between the two metal centres.

The first electrochemical report of the oxidative behaviour of CpRh(CO)₂ and Cp*Rh(CO)₂ in CH₂Cl₂/ [NBu₄][PF₆] occurred in 1986 by Gennett *et al.*³ Studies were limited due to the poor solubility of the [PF₆]⁻ salt in the low-donor solvent which was needed to avoid solvent attack on the radical cation. They reported that with solid electrodes, the CV scans revealed severe adsorption leading to precipitation, as a salt of traditional electrolyte of the positively charged oxidation product. At a hanging-mercury-drop-electrode a chemically reversible one-electron process was observed, seemingly due to the formation of a mercury-rhodium complex [Hg₂][CpRh(CO)₂].

Recent development of experimental conditions⁴⁻⁶ now permits circumvention of nucleophilic attack upon the metal centre by traditional supporting electrolyte anions such as [PF₆]⁻ or [BF₄]⁻.⁷ In addition, metal carbonyl cations tend to be poorly soluble as salts of the traditional anions in solvents of low-donor strength such as dichloromethane, and oxidation processes were difficult

to investigate. The discovery of weakly coordinating electrolyte anions has provided a solution to these drawbacks.

Taking into account these properties, we report in this chapter the electrochemical behaviour of Cp*Rh(CO)₂ in a medium containing a low donor strength solvent, namely dichloromethane, and weakly coordinating anions such as tetrakis(perfluorophenyl)borate, [B(C₆F₅)₄]⁻ or [TFAB]⁻ and tetrakis[3,5-bis(trifluoromethyl)phenyl]borate or [BArF₂₄]⁻.

This investigation has been carried out in the laboratory of Prof. William Geiger at the University of Vermont, USA.

5.2 Experimental

Experimental procedures were carried out either under nitrogen using a Vacuum Atmospheres drybox or (argon) Schlenk type conditions. Reagent-grade dichloromethane was first distilled from the drying reagent CaH₂ into a round-bottomed storage flask. For electrochemical experiments, an appropriate amount of solvent was transferred into a flask fitted on a vacuum line and frozen in liquid nitrogen. Dichloromethane was then degassed on the vacuum line for fifteen minutes and then warmed up to room temperature. This cycle was repeated three times before vacuum transferring the dichloromethane into a receiving flask. After a final freeze-pump-thaw cycle, the dichloromethane was put in the dry box.

Glassware used for electrochemical experiments was cleaned in aqua regia for at least 12 h, followed by copious rinsing with nanopure water and subsequent drying for at least 12 h in a 120°C oven. The hot glassware was then loaded into the drybox antechamber and allowed to cool under vacuum.

Cp*Rh(CO)₂ and decamethylferrocene were purchased from Strem and used as received.

Electrochemistry measurements were performed using a standard three electrode system in an H-type cell. The working electrode compartment was separated from the counter and reference electrode compartments by two fine E-porosity frits of 10 mm diameter, in order to avoid intermixing. The reference electrode was a AgCl coated Ag wire; the counter electrode was a Pt gauze. Two different types of working electrode were employed: if CV scans were recorded, a 1 mm diameter glassy carbon disc was used (or a 3 mm disc if working at low concentration) and, if bulk electrolysis was performed, a large Pt gauze was used. The glassy carbon working electrode was preliminarily polished on a polishing cloth with 1 micron and 0.25 micron diamond paste (Buehler), followed by rinsing with distilled water and drying in vacuo.

The supporting electrolyte, either [NBu₄][B(C₆F₅)₄] (= [TBA][TFAB]) or [NEt₄][B(C₆H₃(CF₃)₂)₄] (= [TEA][BArF₂₄]), was first added in the three different compartments and the analyte, Cp*Rh(CO)₂ (**1**, Cp* = η⁵-C₅Me₅), was subsequently introduced into the working electrode compartment.

All potentials presented in this chapter are referenced to the ferrocene/ferrocenium couple: decamethylferrocene was used as an internal standard and the experimentally measured potential was converted to the ferrocene potential by adding -0.61 V, which is the E_{1/2} of decamethylferrocene vs. FeCp₂^{0/+} measured in CH₂Cl₂/0.05 M [NBu₄][B(C₆F₅)₄] in the laboratory.⁸

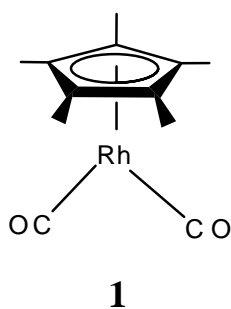
Cyclic voltammetry, chronoamperometry, linear sweep voltammetry and differential pulse voltammetry experiments were all carried out using a PARC 273A potentiostat.

In situ IR spectroelectrochemistry was performed using an ATI-Mattson Infinity Series FTIR spectrometer interfaced to a computer employing Winfirst software at a resolution of 4 cm⁻¹. In

situ IR spectra were recorded using a mid-IR fibre optic dip probe⁹ (Remspec, Inc) with a standard H-type electrolysis cell under argon.

NMR data were acquired on a Bruker ARX-500 NMR spectrometer. Typically, CD₂Cl₂ was used as the solvent to record ¹H-NMR spectra.

5.3 Voltammetry studies of Cp*Rh(CO)₂ at 298 K



An electrochemical investigation was undertaken of Cp*Rh(CO)₂ to discover evidence for dimer formation upon oxidation and if so to discover the conditions under which it took place. This work is a prerequisite for any subsequent spectroscopic or structural studies.

CV scans of **1** in CH₂Cl₂/0.05 M [NBu₄][B(C₆F₅)₄] have been performed over a substrate concentration range of 0.23 mM to 5 mM.

Figure 5.1 to Figure 5.3 on the following pages summarise cyclic voltammograms of **1** for 1, 2, and 3 mM in CH₂Cl₂/ 0.05 M [NBu₄][B(C₆F₅)₄] at 298 K and the corresponding experimental parameters are reported in Tables 5.1, 5.2 and 5.3, respectively.

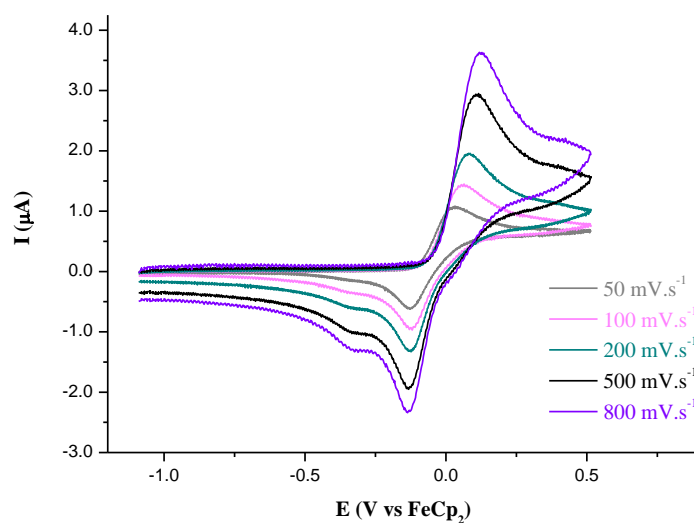


Figure 5.1: Cyclic Voltammograms of 1 mM of **1** in CH₂Cl₂/0.05 M [NBu₄][TFAB] at 1 mm glassy carbon electrode at various scan rates, 298 K.

Scan rate ν (mV s ⁻¹)	E_{pa} (V)	E_{pc} (V)	i_{pa} (μ A)	i_{pc} (μ A)	ΔE_p (mV)	i_{pc}/i_{pa}
50	0.03	-0.126	1.08	-1.14	156	0.95
100	0.064	-0.12	1.45	-1.41	184	0.97
200	0.08	-0.124	1.96	-1.73	204	0.88
500	0.116	-0.132	2.95	-2.29	248	0.78
800	0.118	-0.136	3.63	-2.67	254	0.74

Table 5.1: Experimental parameters for anodic and cathodic process for 1 mM of **1** in CH₂Cl₂/0.05 M [NBu₄][TFAB] at 1 mm glassy carbon electrode at various scan rates, 298 K.

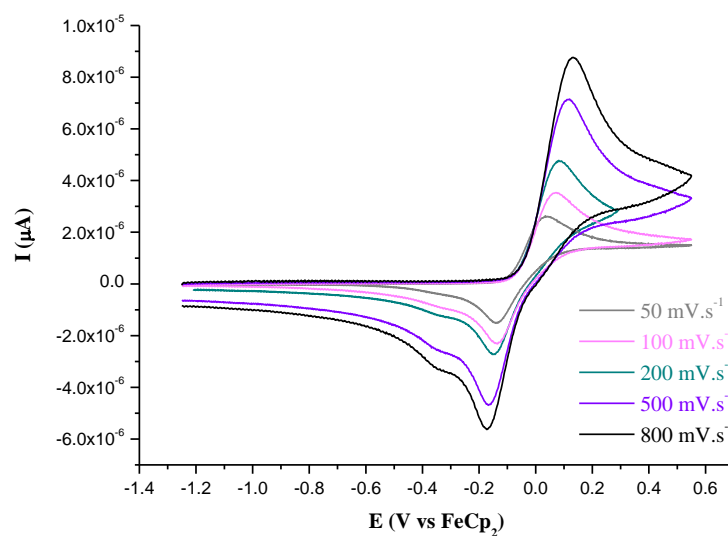


Figure 5.2: Cyclic Voltammograms of 2 mM of **1** in CH₂Cl₂/0.05 M [NBu₄][TFAB] at 1 mm glassy carbon electrode at various scan rates, 298 K.

Scan rate ν (mV s ⁻¹)	E_{pa} (V)	E_{pc} (V)	i_{pa} (μ A)	i_{pc} (μ A)	ΔE_p (mV)
50	0.034	-0.14	2.64	-2.79	173
100	0.07	-0.136	3.53	-3.44	206
200	0.082	-0.144	4.78	-3.27	226
500	0.12	-0.168	7.15	-5.93	288
800	0.13	-0.172	8.76	-7.09	302

Table 5.2: Experimental parameters for anodic process for 2 mM of **1** in CH₂Cl₂/0.05 M [NBu₄][TFAB] at 1 mm glassy carbon electrode at various scan rates, 298 K.

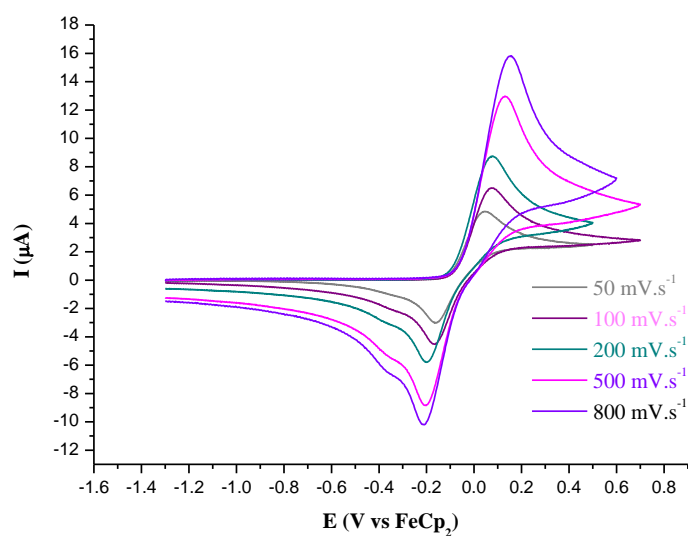


Figure 5.3: Cyclic Voltammograms of 3 mM of **1** in CH₂Cl₂/0.05 M [NBu₄][TFAB] at 1 mm glassy carbon electrode at various scan rates, 298 K.

Scan rate ν (mV s ⁻¹)	E_{pa} (V)	E_{pc} (V)	i_{pa} (μ A)	i_{pc} (μ A)	ΔE_p
50	0.046	-0.164	4.85	-5.0	210
100	0.074	-0.164	6.51	-6.47	238
200	0.08	-0.2	8.75	-7.84	280
500	0.13	-0.2	13.0	-11.31	330
800	0.15	-0.21	15.81	-12.97	360

Table 5.3: Experimental parameters for anodic process for 3 mM of **1** in CH₂Cl₂/0.05 M [NBu₄][TFAB] at 1 mm glassy carbon electrode at various scan rates, 298 K.

As a general observation, the anodic peak current shifts to a more positive potential as the scan rate is increased. The separation between the anodic and cathodic peaks ΔE_p is very high in all cases investigated, which is typical of an irreversible heterogeneous electron process.

The $i_{pa}/\nu^{1/2}$ ratios over the whole sweep range investigated are tabulated in Table 5.4. The decreasing values of this ratio as a function of increasing scan rate are consistent with the behaviour of a diffusion-controlled system undergoing either slow electron transfer or being subject to increasing ohmic errors.

Scan rate ν (mV s ⁻¹)	50	100	200	500	800
$i_{pa}/\nu^{1/2}$ (1 mM)	4.8	4.6	4.4	4.2	4.0
$i_{pa}/\nu^{1/2}$ (2 mM)	11.8	11.2	10.7	10.1	9.8
$i_{pa}/\nu^{1/2}$ (3 mM)	21.7	20.6	19.6	18.4	17.7

Table 5.4: Calculated value of the $i_{pa}/\nu^{1/2}$ ratio for concentrations of **1** for 1, 2, and 3 mM at different scan rates.

Figure 5.4 below shows a comparison of the CV scans of **1** at 200 mV s⁻¹ for the three different concentrations investigated here. It is noticeable that the peak separation increases with concentration, most likely due to increasing ohmic errors. Corresponding ΔE_p values are presented in Table 5.5.

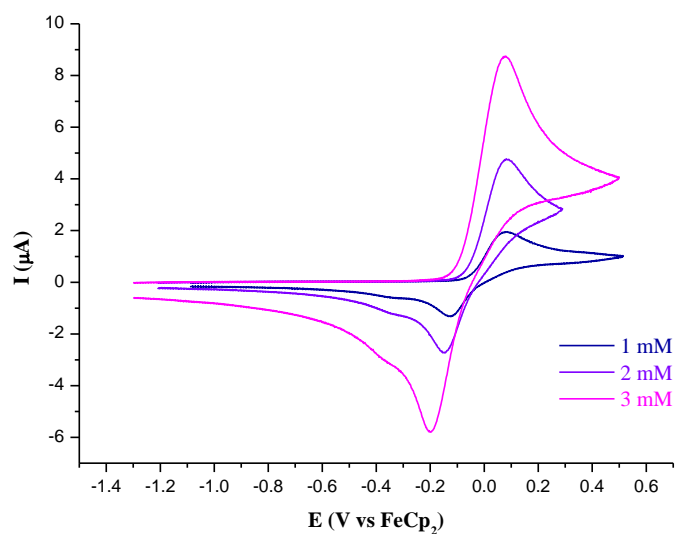


Figure 5.4: Cyclic Voltammograms of 1, 2, and 3 mM of **1** in CH₂Cl₂/0.05 M [NBu₄][TFAB] at 1 mm glassy carbon electrode at 200 mV s⁻¹, 298 K.

	1 mM	2 mM	3 mM
$\Delta E_p / \text{mV}$	204	226	280

Table 5.5: ΔE_p values for the different concentrations 1, 2, and 3 mM of **1**.

The breadth of the anodic wave at half intensity δE_p is another useful diagnostic parameter. With increasing concentration, and for a scan rate of 200 mV s⁻¹, one can note the augmentation of δE_p from 77 mV for 1 mM to 100 mV for 3 mM. The theoretical value for a fast and reversible one-electron transfer is 30 mV. The fact that the measured values are much higher is consistent with a slow electron transfer reaction.

[Cp*Rh(CO) ₂]	$\delta E_p = E_{pa} - E_{pa/2}$	$E_{pa} - E_{1/2}$
1 mM	77	41
2 mM	83	41
3 mM	100	30

Table 5.6: δE_p and $(E_{pa} - E_{1/2})$ values for the different concentrations 1, 2, and 3 mM of **1**.

A second cathodic wave was noticeable in all CVs presented so far and since it seemed to be more pronounced when the concentration was lower, we decided to carry out the studies at a much lower concentration of 0.23 mM. Because this concentration is low, the size of the oxidation and reduction features were comparable to the capacitive charging current. For that reason in order to reduce the significance of the charging currents, these experiments were carried out using a 3 mm diameter glassy carbon electrode. The results are shown in Figure 5.5.

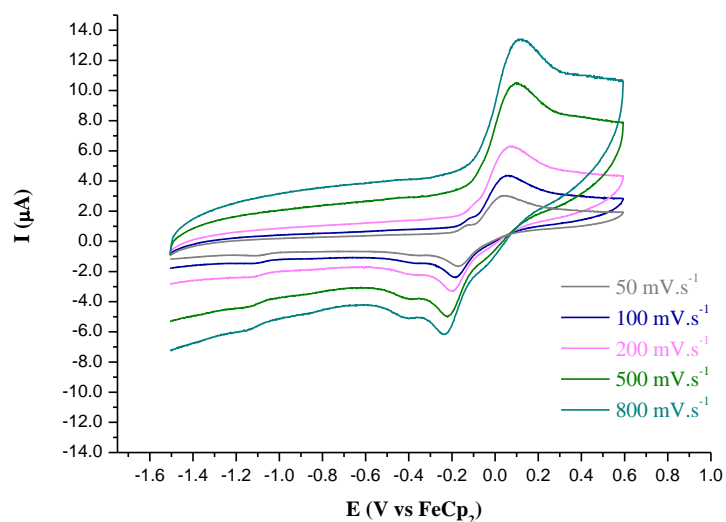


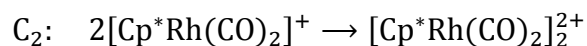
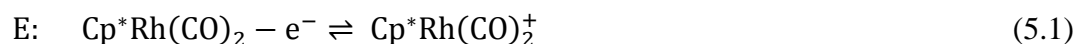
Figure 5.5: Cyclic Voltammograms of 0.23 mM of **1** in CH₂Cl₂/0.05 M [NBu₄][TFAB] at 3 mm glassy carbon electrode at various scan rates, 298 K.

After comparing the data in Figure 5.5 with that for higher concentrations it was found that the ratio of the two cathodic peaks remained quasi-constant. However, in the event of generating a dimer dication from the oxidation of Cp*Rh(CO)₂, a diminution of intensity of the second peak should be observed at lower concentrations and, conversely, an increase of the same peak at higher concentration. For thermodynamic reasons, the dimer should be less favoured at lower concentrations. Therefore, this observation removes the possibility of the extra cathodic wave arising from either [Cp*Rh(CO)₂]⁺ or the dimer dication.

5.4 Conclusion for studies at 298 K

From the results obtained here, it can be concluded that the anodic wave cannot be assigned to a quasi-Nernstian and chemically reversible system, as expected for a **1/1**⁺ process. These data are thus consistent with an electron-transfer process complicated by some sort of follow-up chemical reaction of **1**⁺.

We therefore propose that Cp*Rh(CO)₂ undergoes a one-electron oxidation followed by dimerisation, that is to say an EC mechanism where the electron transfer step is followed by dimerisation, as shown in equation 5.1:



However it is not possible to prove it directly since it would mean to achieve a concentration low enough to limit the reaction to the monomer **1**⁺ process. (The presence of a background charging current throughout the experiment restricts the detection limit to an insufficiently low concentration).

Therefore, there are several pieces of evidences behind a dimerisation mechanism. Firstly, as noticed earlier, the positions and shape of the peaks do not match a quasi-reversible one electron process, with a reasonably fast electron transfer. Thus a follow-up reaction of $\mathbf{1}^+$ is implied.

Moreover, from an EC mechanism followed by dimerisation, two possibilities have then to be considered: a Radical-Radical (R-R) coupling or a Radical-Substrate (R-S) coupling, as illustrated in equation (5.3) and (5.4, 5.5) respectively, within the context of a neutral to cation one-electron process (equation 5.2). However, voltammetric studies performed here do not allow us to distinguish the two mechanisms.



The thermodynamic instability of $\mathbf{1}^+$ affects the reduction of the dimer dication, making it a two electron irreversible process.

The CV scans observed are qualitatively identical in both cases, in that R-S and R-R mechanism both show a single-anodic wave followed by a two-electron cathodic wave.

5.5 Voltammetry studies of Cp*Rh(CO)₂ at low temperature

Previous studies^{8,10-12} on organometallic compounds have shown that dimerization is favoured at low temperatures. Therefore, voltammetry studies and exhaustive bulk electrolysis were carried out at 283 K, 273 K, 253 K and at 243 K, influencing the solubility of the obtained product. A

series of experiments in the concentration range 2 to 6.5 mM has been carried out using $[\text{NBu}_4][\text{TFAB}]$ and $[\text{NEt}_4][\text{BARF}_{24}]$ as electrolytes.

The results of this electrochemical investigation are shown in the Figures and Tables on the following pages (Figures 5.6 – 5.8 and Tables 5.7 – 5.9).

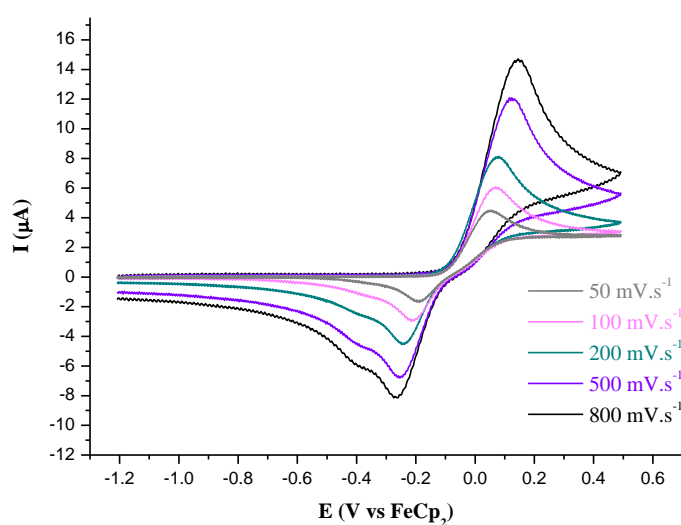


Figure 5.6: Cyclic Voltammograms of 3 mM of **1** in $\text{CH}_2\text{Cl}_2/0.05 \text{ M } [\text{NEt}_4][\text{BARF}_{24}]$ at 1 mm glassy carbon electrode at various scan rates, 273 K.

Scan rate ν (mV s^{-1})	E_{pa} (V)	E_{pc} (V)	i_{pa} (μA)	i_{pc} (μA)	ΔE_p (mV)
50	0.05	-0.188	4.51	-4.31	238
100	0.07	-0.216	6.08	-5.3	286
200	0.08	-0.248	8.14	-6.76	328
500	0.116	-0.254	12.1	-8.88	370
800	0.144	-0.274	14.7	-10.11	418

Table 5.7: Experimental parameters for anodic process for 3 mM of **1** in $\text{CH}_2\text{Cl}_2/0.05 \text{ M}$ $[\text{NEt}_4][\text{BArF}_{24}]$ at 1 mm glassy carbon electrode at various scan rates, 273 K.

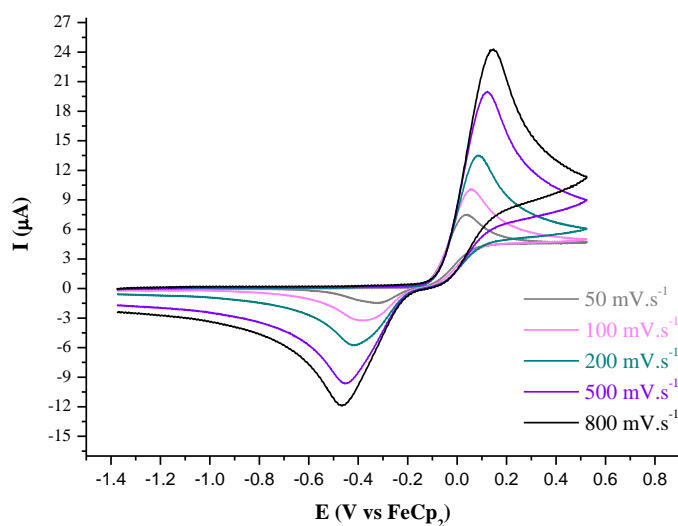


Figure 5.7: Cyclic Voltammograms of 6.5 mM of **1** in $\text{CH}_2\text{Cl}_2/0.05 \text{ M}$ $[\text{NEt}_4][\text{BArF}_{24}]$ at 1 mm glassy carbon electrode at various scan rates, 273 K.

Scan rate ν (mV s^{-1})	E_{pa} (V)	E_{pc} (V)	i_{pa} (μA)	i_{pc} (μA)	ΔE_p (mV)
50	0.036	-0.32	7.51	-5.72	356
100	0.052	-0.384	10.1	-7.25	436
200	0.08	-0.414	13.5	-8.96	494
500	0.122	-0.454	20	-11.78	576
800	0.146	-0.464	24.3	-13.8	610

Table 5.8: Experimental parameters for anodic process for 6.5 mM of **1** in $\text{CH}_2\text{Cl}_2/0.05 \text{ M}$ $[\text{NEt}_4][\text{BArF}_{24}]$ at 1 mm glassy carbon electrode at various scan rates, 273 K.

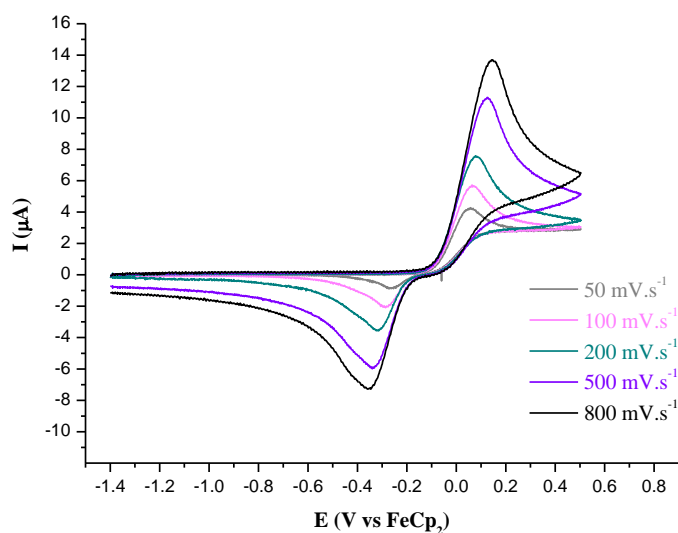


Figure 5.8: Cyclic Voltammograms of 3 mM of **1** in $\text{CH}_2\text{Cl}_2/0.05 \text{ M}$ $[\text{NBu}_4][\text{TFAB}]$ at 1 mm glassy carbon electrode at various scan rates, 253 K.

Scan rate ν (mV s ⁻¹)	E_{pa} (V)	E_{pc} (V)	i_{pa} (μ A)	i_{pc} (μ A)	ΔE_p (mV)
50	0.058	-0.272	4.28	-3.55	330
100	0.064	-0.286	5.27	-4.63	350
200	0.08	-0.314	7.57	-5.65	394
500	0.124	-0.34	11.3	-7.63	464
800	0.142	-0.346	13.7	-8.59	488

Table 5.9: Experimental parameters for anodic process for 3 mM of **1** in CH₂Cl₂/0.05 M [NBu₄][TFAB] at 1 mm glassy carbon electrode at various scan rates, 253 K.

For the studies at room temperature, the shift of the anodic peak follows the increase in the scan rate. When comparing CVs obtained for the same concentration of 3 mM (Figure 5.6 and Figure 5.7) and at different temperature (273 K and 253 K, respectively), one can observe that as the temperature decreases, peak separation is increasing as well. It is important to note that the last comment concerns experiments with two different electrolytes. The exhaustive electrolysis studies presented in the next section (section 5.6) should allow more accuracy in the latter statement. The system loses reversibility and the reaction is thus favoured in the direction of dimerisation. When comparing the two studies presented in Figure 5.6 and Figure 5.7, where the electrolyte medium was for both cases [NEt₄][BArF₂₄], and at a similar temperature of 273 K, an augmentation of the concentration reveals an increase of the peak separation and thus a loss in reversibility. Reversibility is therefore dependent on scan rate, temperature and concentration.

5.6 Exhaustive Electrolysis

Bulk oxidations of solutions were carried out over a substrate concentration range of 2 mM to 6.5 mM of Cp*Rh(CO)₂ in CH₂Cl₂/0.05 M [NBu₄][TFAB] or [NEt₄][BArF₂₄] in a temperature interval of 283 K to 243 K. The potentials applied varied from $E_{appl} = 0.23$ to 0.34 V and gave a color change from a yellow solution to a bright red-orange solution. In some cases, back electrolysis was performed to regenerate **1**, whether or not the product of bulk oxidation was subsequently isolated.

Details of each study are gathered in Table 5.10, including concentrations studied with their respective temperatures, masses of analyte used $m_{Cp^*Rh(CO)_2}$, volumes of DCM utilised, electrolytes employed, potential applied E_{appl} , experimental charge passed Q_{exp} , calculated charge passed for one electron transfer process Q_{calc} , the percentage of conversion calculated from the ratio Q_{exp}/Q_{calc} , the percentage of conversion calculated from the current height of the linear sweep voltammograms.

Thus, both Coulomb counts and determination of current heights of linear sweep voltammograms (LSV) were employed in order to calculate the percentages of conversion of the neutral species to the electrolysis product after bulk oxidation and of electrolysed material regenerated to the starting material from bulk reduction.

[Cp*Rh(CO)₂]						
Parameters	0.23 mM	2 mM	3 mM	3 mM	5 mM	6.5 mM
m_{Cp*Rh(CO)₂}	5*10 ⁻⁴	1.05*10 ⁻²	6*10 ⁻³	6*10 ⁻³	1*10 ⁻²	1.3*10 ⁻²
Vol. in W.E compartment	7.5	25	6.8	6.8	6.8	6.8
Electrolyte	[TBA][TFAB]	[TBA][TFAB]	[TBA][TFAB]	[TEA][BARF ₂₄]	[TBA][TFAB]	[TEA][BARF ₂₄]
T° (K)	298	283	253	273	243	273
E_{appl} Oxidation (V vs FeCp₂)	0.23	0.25	0.34	0.28	0.23	0.27
Q_{exp} (mC)	125	2473	1730	1704	2821	3858
Q_{calc} (mC)	164	3456	1920	1968	3281	4260
E_{appl} Reduction (V vs FeCp₂)	-0.46	-0.61	-0.46	X	X	X
Q_{exp} (mC)	77.6	1865	1620	X	X	X
conversion Q_{exp} / Q_{calc} from Bulk Oxidation	76	72	90	87	86	84
Yield from current height	31	37	47	48	X	X
conversion Q_{exp} / Q_{calc} from Bulk Reduction	62	75	94	X	X	X
Conversion from Current height	50	60	88	X	X	X

Table 5.10: Experimental parameters for anodic process of **1** in CH₂Cl₂/0.05 M [NBu₄][TFAB] or [NEt₄][BARF₂₄] at a Pt gauze working electrode at various concentrations and temperatures.

Firstly, the linear sweep voltammograms of the four first experiments tabulated in Table 5 are presented in the following pages, in Figure 5.9 to Figure 5.12.

Bulk electrolysis of 0.23 mM of $\text{Cp}^*\text{Rh}(\text{CO})_2$ at 298 K

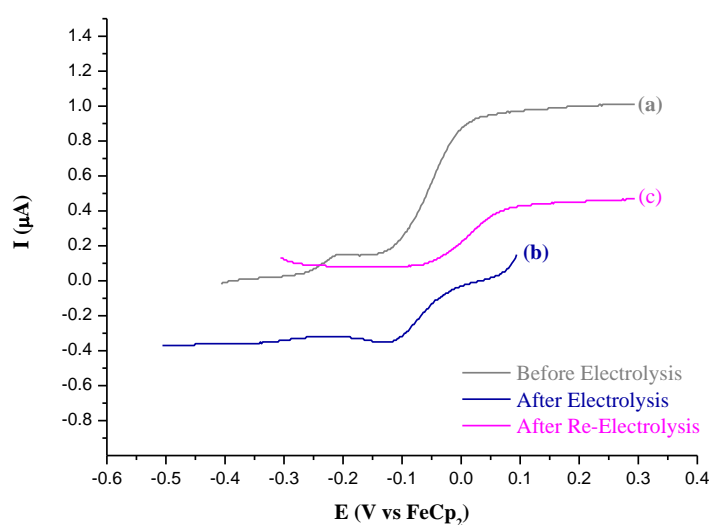


Figure 5.9: Linear Sweep Voltammograms obtained during electrolysis experiments of 0.23 mM $\text{Cp}^*\text{Rh}(\text{CO})_2$ in $\text{CH}_2\text{Cl}_2/0.05$ M $[\text{NBu}_4][\text{B}(\text{C}_6\text{F}_5)_4]$ at 298 K, 3 mm glassy carbon electrode, 3 mV s^{-1} (a) initial solution, (b) after anodic electrolysis at $E_{\text{appl}} = 0.23$ V, (c) after cathodic re-electrolysis at $E_{\text{appl}} = -0.46$ V.

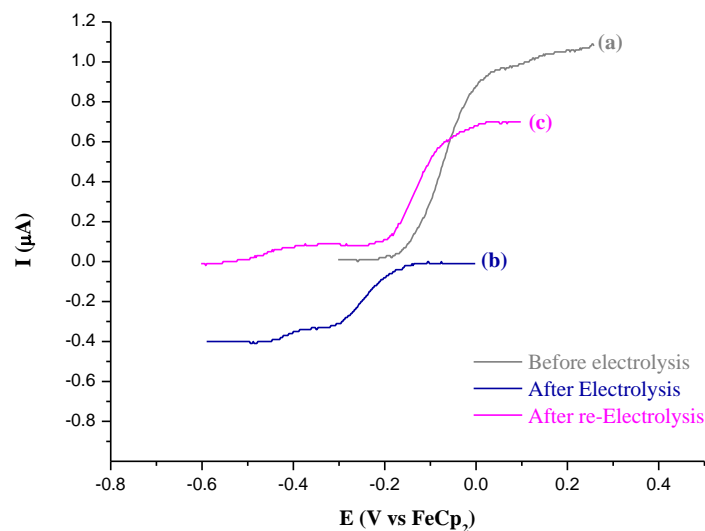
Bulk electrolysis of 2 mM of Cp*Rh(CO)₂ at 283 K

Figure 5.10: Linear Sweep Voltammograms obtained during electrolysis experiments of 2 mM Cp*Rh(CO)₂ in CH₂Cl₂/0.05 M [NBu₄][B(C₆F₅)₄] at 283 K, 1 mm glassy carbon electrode, 3 mV s⁻¹ (a) initial solution, (b) after anodic electrolysis at $E_{appl} = 0.25$ V, (c) after cathodic re-electrolysis at $E_{appl} = -0.61$ V.

Bulk electrolysis of 3 mM of 1 at 253 K

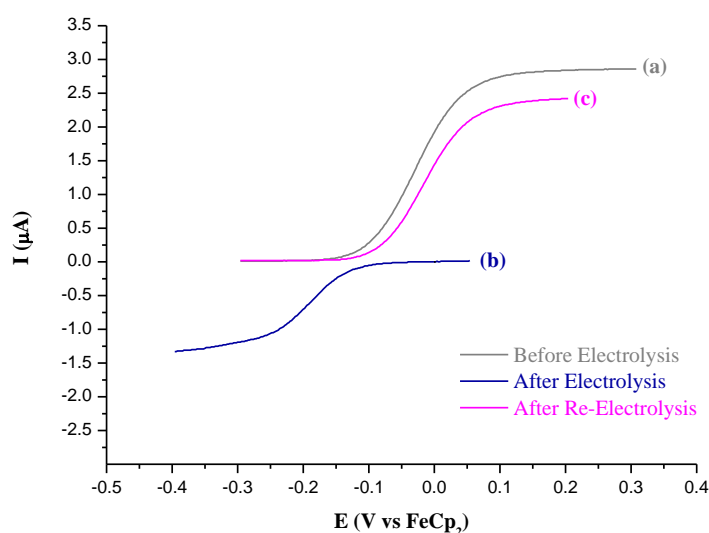


Figure 5.11: Linear Sweep Voltammograms obtained during electrolysis experiments of 3 mM Cp*Rh(CO)₂ in CH₂Cl₂/0.05 M [NBu₄][B(C₆F₅)₄] at 253 K, 1 mm glassy carbon electrode, 3 mV s⁻¹ (a) initial solution, (b) after anodic electrolysis at $E_{appl} = 0.34$ V, (c) after cathodic re-electrolysis at $E_{appl} = -0.46$ V.

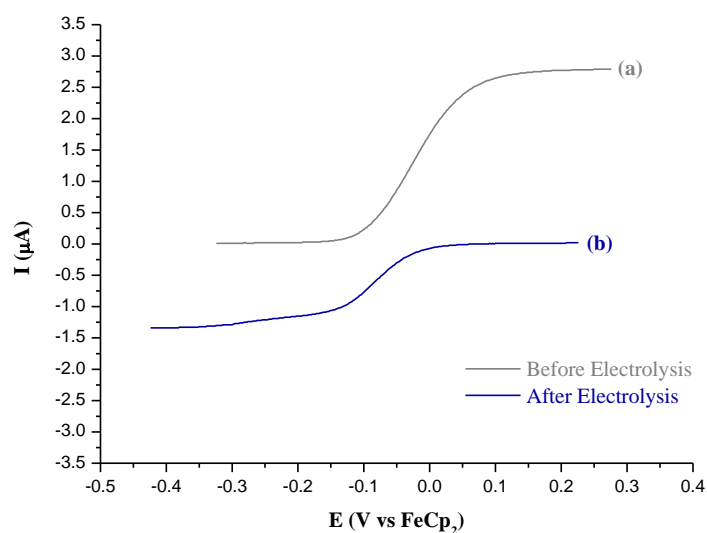
Bulk electrolysis of 3 mM of Cp^{*}Rh(CO)₂ at 273 K, 0.05 M [NEt₄][BArF₂₄]

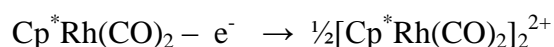
Figure 5.12: Linear Sweep Voltammograms obtained during electrolysis experiments of 3 mM Cp^{*}Rh(CO)₂ in CH₂Cl₂/0.05 M [NEt₄][BArF₂₄] at 273 K, 1 mm glassy carbon electrode, 3 mV s⁻¹ (a) initial solution, (b) after anodic electrolysis at $E_{appl} = 0.28$ V.

The calculated charge passed suggests, in the case of a one-electron transfer process, a variation of 72 to 90 %, depending on conditions of the experiment. The highest conversion is found for a solution of 3 mM of **1** in CH₂Cl₂/ 0.05 M [TBA][TFAB] at 253 K. As a general trend, the parameter that seems to influence the most the outcome of the conversion is found to be the temperature. The lower the temperature, the more complete is conversion. Data taken at room temperature indicates the poorest conversion yield obtained among all investigations reported here. As observed earlier, in the voltammetry studies at low temperatures section (section 5.5), when the electrolyte medium was [NEt₄][BArF₂₄], and the temperature was 273 K, an augmentation of the concentration reveals an increase of the percentage of conversion. The data obtained are in agreement with the earlier voltammetry studies where it is sensible to state that the formation of the dimer is favoured at low temperature and high concentration.

In addition, one can observe for example on Figure 5.11 that with appropriate conditions, the oxidation of **1** may generate only a small amount of side product and that therefore, **1** can be regenerated in good yield after back-reduction of the electrolysis product.

It is important to note that the calculated conversion from the current height from the linear sweep voltammogram recorded after bulk oxidation extends from 31 to 50 %, which are much lower values than the one reported from the calculated conversion from the charged passed during the chronoamperometry measurements. This feature can be attributed to the influence of the diffusion coefficient since the peak height is square-root dependent on the diffusion coefficient of the species in solution. Therefore, all data obtained so far strongly suggest that the major product of the anodic oxidation of **1** is the dimer dication.

That is, the primary oxidation reaction is



And the reverse cathodic reaction is :



Moreover, cyclic voltammograms of the oxidised species have been recorded, as well as the corresponding square-wave voltammograms. CVs after bulk oxidation of 0.23 mM of **1** (Figure 5.13), after bulk oxidation of 3 mM of **1** in CH₂Cl₂/ 0.05 M [NBu₄][TFAB] (Figure 5.16) are displayed, along with the corresponding square-wave voltammograms (Figure 5.14), and the Differential-Pulse voltammogram (Figure 5.15) after exhaustive electrolysis of 0.23 mM of **1**.

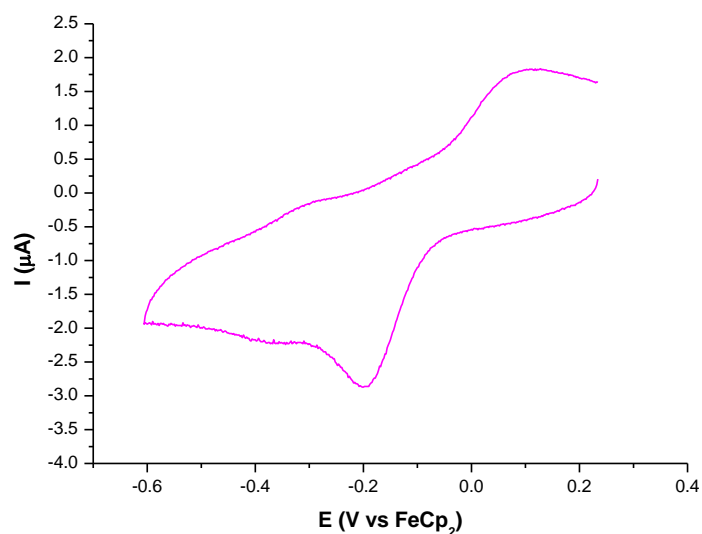


Figure 5.13: Cyclic voltammogram after bulk oxidation of 0.23 mM of **1** in $\text{CH}_2\text{Cl}_2/0.05$ M $[\text{NBu}_4][\text{TFAB}]$ at 3 mm glassy carbon electrode at 200 mV s^{-1} , 298 K.

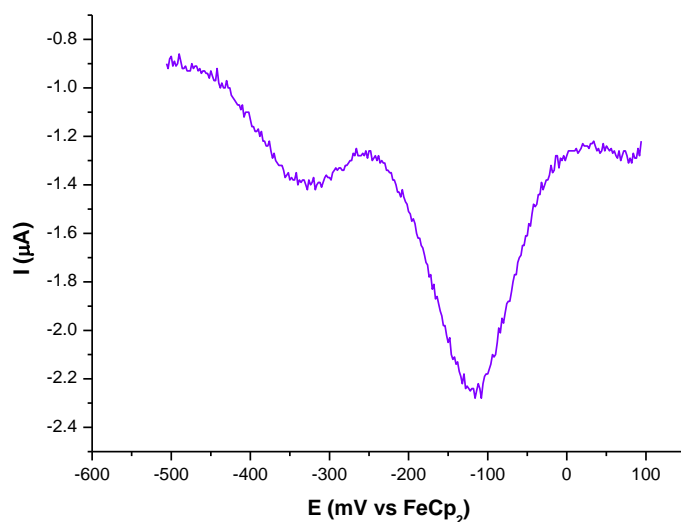


Figure 5.14: Square-wave voltammogram after bulk oxidation of 0.23 mM of **1** in $\text{CH}_2\text{Cl}_2/0.05$ M $[\text{NBu}_4][\text{TFAB}]$ at 3 mm glassy carbon electrode at 10 mV s^{-1} , 298 K

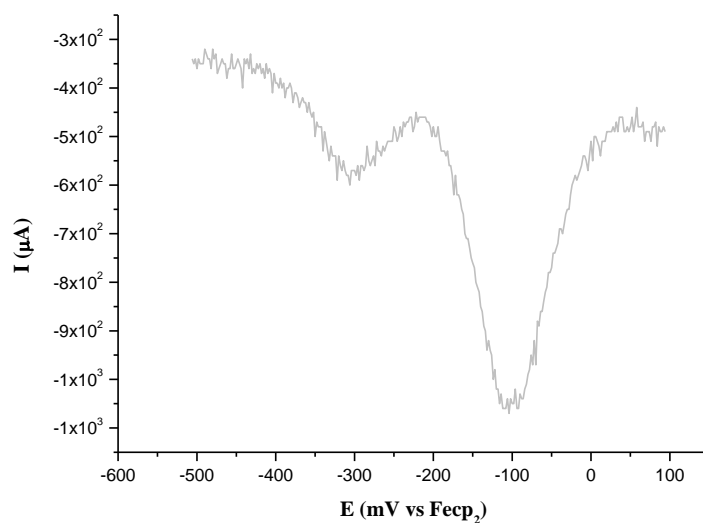


Figure 5.15: Differential-Pulse Voltammetry after bulk oxidation of 0.23 mM of **1** in CH₂Cl₂/0.05 M [NBu₄][TFAB] at 1mm glassy carbon electrode at 10 mV s⁻¹, 298 K.

Figures 5.14 and 5.15 highlight the fact that the major product of the electrolysis, the dimer dication, is firstly reduced to **1**⁺ (first wave) and then back to the neutral species **1**. It is also clear that there is a secondary reduction at about -0.3 V vs. ferrocene. After the back bulk cathodic reduction, this wave was no longer present.

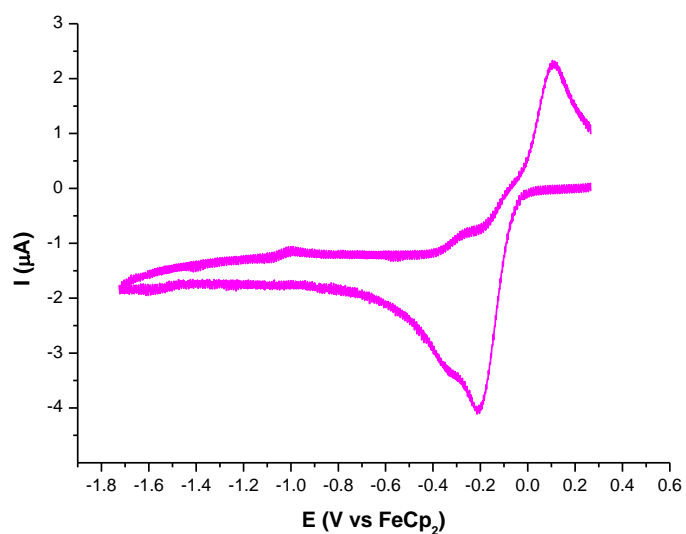


Figure 5.16: Cyclic Voltammogram after bulk oxidation of 3 mM of **1** in $CH_2Cl_2/0.05$ M $[NBu_4][BARF_{24}]$ at 1 mm glassy carbon electrode at various scan rates, 273 K.

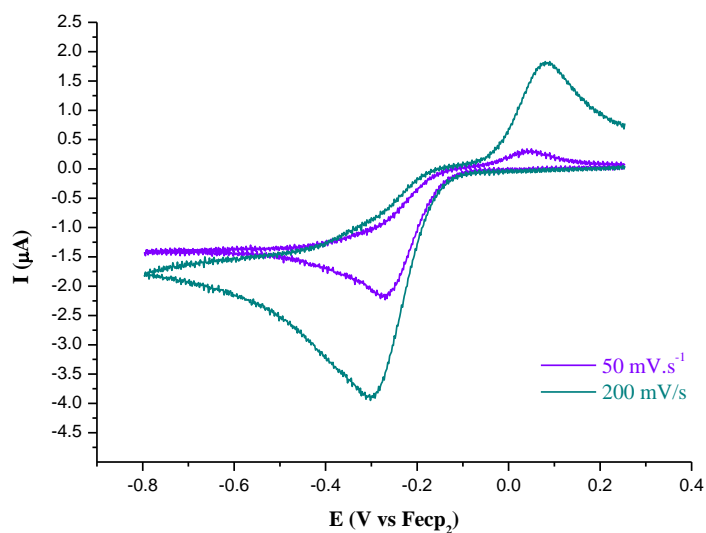


Figure 5.17: Cyclic Voltammograms after bulk oxidation of 3 mM of **1** in $CH_2Cl_2/0.05$ M $[NBu_4][TFAB]$, at $E_{appl} = 0.34$ V, at 1 mm glassy carbon electrode at various scan rates, 253 K.

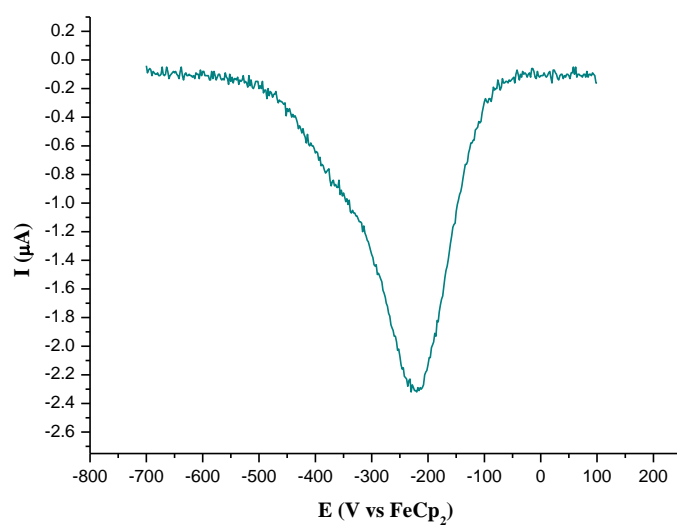


Figure 5.18: Square-wave voltammogram after bulk oxidation of 3 mM of **1** in $\text{CH}_2\text{Cl}_2/0.05 \text{ M}$ $[\text{NBu}_4][\text{TFAB}]$ at 1 mm glassy carbon electrode at 10 mV s^{-1} , 253 K.

5.7 In situ Spectroelectrochemistry

As mentioned earlier, IR spectra of the electrolysis product were obtained via a fibre-optic *in-situ* spectroscopy dip probe, using a standard electrolysis H-type cell. The spectrum of the electrolysed solution was monitored as the oxidation proceeded. Exhaustive electrolysis containing 2 mM of Cp*Rh(CO)₂ in CH₂Cl₂/0.05 M [NBu₄][B(C₆F₅)₄] and $E_{\text{appl}} = 0.25$ V gave a colour change from a yellow solution to a bright red-orange solution at 283 K. Bulk oxidation was performed with a platinum gauze working electrode. In order to monitor the process, electrolysis was intermittently halted at different Coulomb counts of charge passed and IR spectra and cyclic voltammograms were recorded. The analysis took 2 to 3 min and was performed until the electrolysis current was less than 2% of the initial value.

Figure 5.19 displays the recorded *in-situ* IR spectrum of the carbonyl-range (spectra were recorded from 1700 to 2200 cm⁻¹) at regular time intervals from the starting material in solution through the complete electrolysis. The neutral solution, displayed in black, shows two absorption bands appearing at 2017 and 1950 cm⁻¹; the former band has a slightly higher intensity. As the electrolysis proceeded, the two bands for **1** started to decrease in intensity and a single product peak began to appear at 2077 cm⁻¹ from after 10 % of the oxidative process was completed (see Figure 5.19). It was expected that the spectra would show two ν_{CO} bands corresponding to the two CO ligands attached to the metal. The presence of a single band would thus suggest the loss of a carbonyl ligand but this is unlikely since the starting material was regenerated, as shown in Figure 5.19.

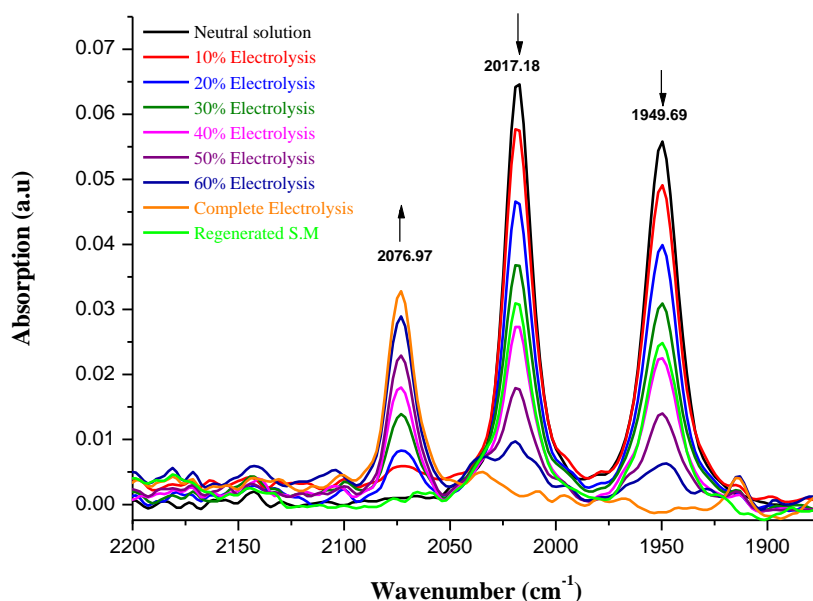


Figure 5.19: *In situ* spectroelectrochemistry of 2 mM of **1** in $CH_2Cl_2/0.05$ M $[NBu_4][B(C_6F_5)_4]$ recorded during bulk electrolysis at $E_{appl} = 0.25$ V, at 283 K.

Whereas it is not shown on Figure 5.19, it is important to note that spectra in the bridging carbonyl region were blank and only one terminal carbonyl vibration is found for the oxidation product of **1**. Bulk cathodic electrolysis at $E_{appl} = 0.61$ V of the oxidised solution yielded the starting material **1** in about 86 % yield, as determined by coulometry (though the current height of LSV suggests 48 %, for unknown reasons).

The presence of a single peak was confirmed by *ex-situ* solution phase IR where the solution was transferred from the dry box to the instrument, and also by solid state IR (see Figure 5.20).

The isolation of the product of bulk electrolysis of $Cp^*Rh(CO)_2$ was carried out at two different concentrations, in two distinct electrolyte environments.

When the electrolyte was $[TBA][TFAB]$, a bright red/orange precipitate formed at 243 K, which was filtered off, but no precipitation occurred at 253 K, 273 K, and 298 K.

When the electrolyte was [TEA][BArF₂₄], the same red/orange precipitate was formed but at a slightly higher temperature of 273 K. The IR features were consistent with the data obtained with [TBA][TFAB] electrolyte.

Figure 5.20 displays the IR spectra recorded neat on an FT-IR spectrometer of the precipitated product resulting from the bulk oxidation of a solution of 5 mM of **1**, 0.05 M [TBA][TFAB] at 243 K. As for the *in-situ* measurement, a single band is observed at 2072 cm⁻¹ in this spectrum in the carbonyl range, which is consistent with the data obtained previously. However, one can notice that the band has a distinct shoulder at higher frequencies, and so it is possible to hypothesise the presence of two overlapping carbonyl bands. However there is also noise in the spectrum which might equally well account for this observation).

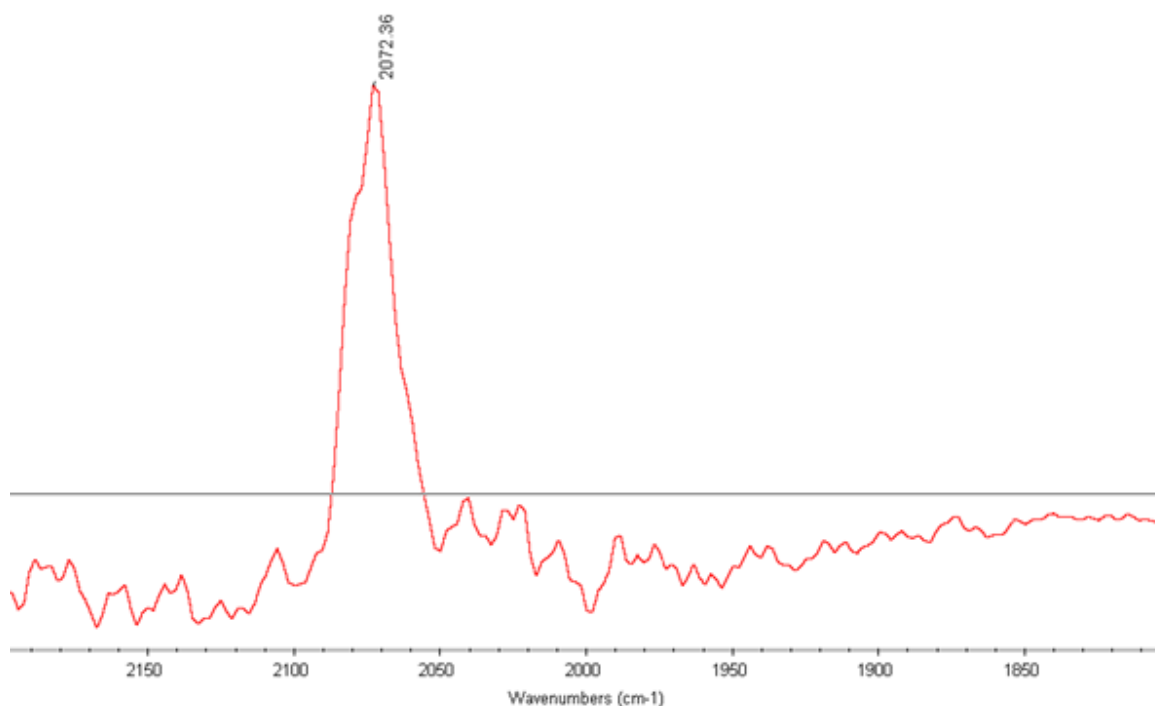


Figure 5.20: Solid State IR of precipitated product from bulk electrolysis of 5 mM **1** in CH₂Cl₂/0.05 M [TBA][TFAB] at 243 K, $E_{appl} = 0.21$ V.

A solution-phase IR spectrum was recorded after the electrolysis of a solution of 3 mM of **1**/0.05 M [TEA][BArF₂₄] at 273 K and is shown in Figure 5.21. The sample product was removed from the solution and transferred to a suitable cell for IR investigation in an oxygen free environment.

It can be seen that in the solution-phase IR spectra, the carbonyl band is narrow and there is no evidence for a splitting of this band. Thus, we are led to conclude that the product of electrolysis displays a single carbonyl band.

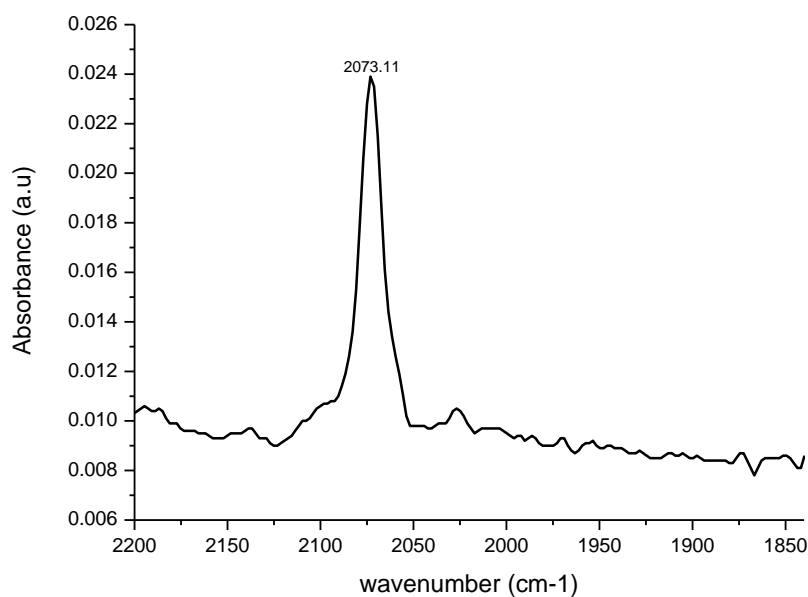


Figure 5.21: Solution phase IR of precipitated product from the bulk electrolysis of 3 mM of **1** in CH₂Cl₂/0.05 M [NEt₄][BArF₂₄] at 273 K.

5.8 NMR Spectroscopy

Both the starting material and the electrolysis product have been characterised by NMR spectroscopy (¹H). Figure 5.22 presents the ¹H-NMR spectrum of the starting material Cp*Rh(CO)₂, **1**, in ²d-dichloromethane, showing a singlet at 2.04 ppm that can be assigned to the methyl groups arising from the cyclopentadienyl ligand.

The ¹H-NMR spectra shown in Figure 5.23 was recorded following anodic electrolysis of a solution of 3 mM of **1** in CH₂Cl₂/0.05 M [TEA][BArF₂₄] at 273 K. The precipitated product was dissolved in ²d-CD₂Cl₂. The two singlets visible at 7.57 ppm and 7.72 ppm are assigned to the aromatic rings of the counter anion, BArF₂₄, of the electrolyte. The peak that is displaced upfield ($\delta = 7.57$ ppm) is attributed to the equivalent H_a and H_b protons (see Figure 5.23) due to their closest proximity to the electronegative boron central atom, whereas the peak at 7.72 ppm is assigned to the H_c proton. In addition, the singlet at 2.12 ppm belongs to the methyl group of the Cp* ligand. By comparison with the ¹H-NMR spectrum of the starting material, a downfield chemical shift of the singlet of the methyl group of the Cp* ligand in the product is observed, which is of the order of 0.09 ppm. This feature is a direct consequence of the oxidative process, and a result of the metal centre oxidation which becomes more shielded.

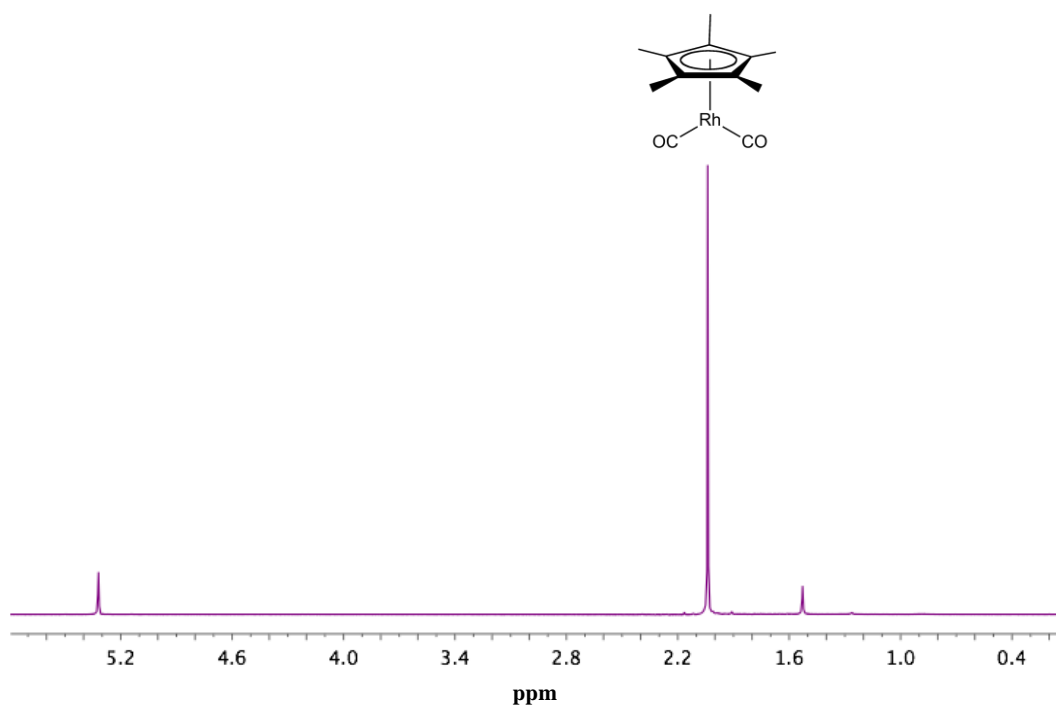


Figure 5.22: ¹H-NMR (500 MHz) spectrum of Cp*Rh(CO)₂ in CD₂Cl₂.

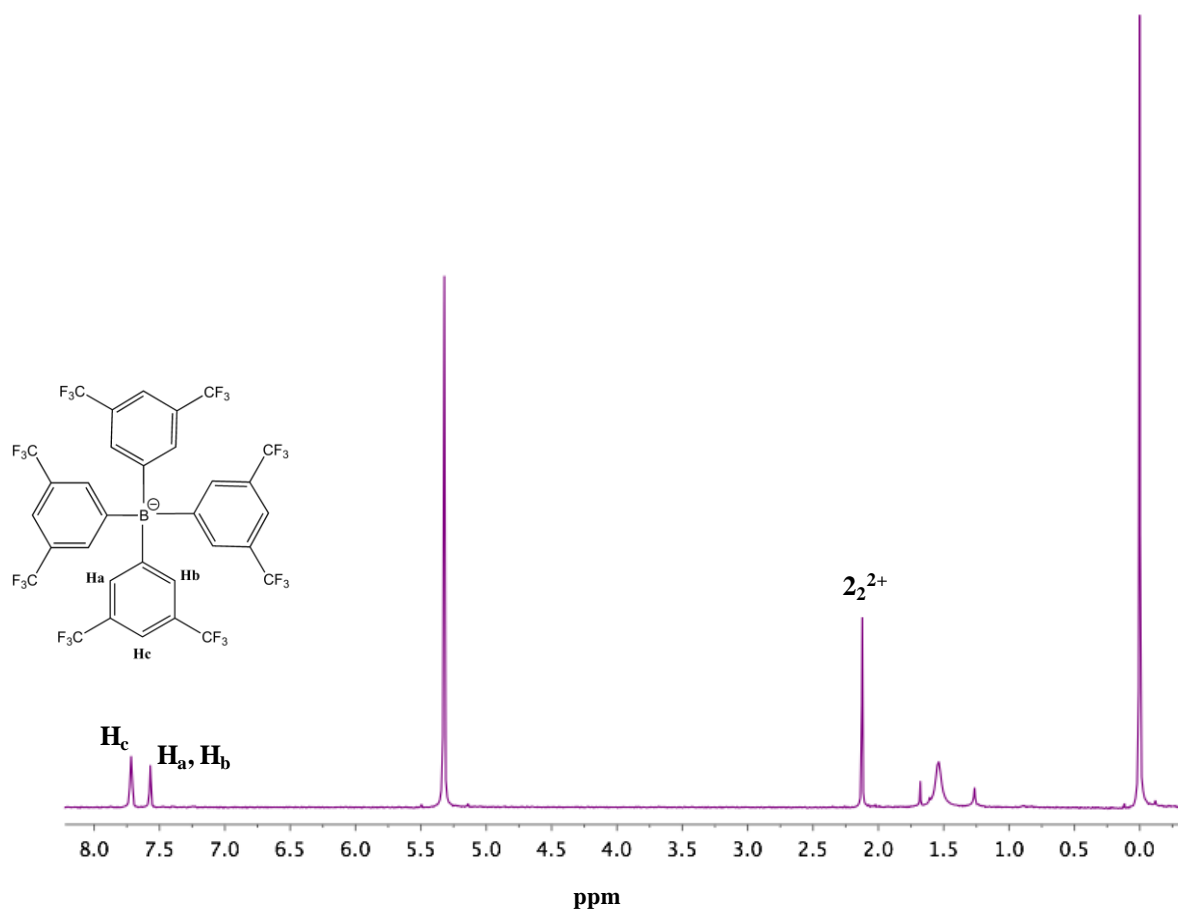


Figure 5.23: ¹H-NMR (500 MHz) spectrum of electrolysis product of 3 mM of Cp*Rh(CO)₂/0.05 M [TEA][BARF₂₄], in CD₂Cl₂.

The ¹H-NMR spectrum shown in Figure 5.24 was recorded after anodic electrolysis of a solution of 6.5 mM of **1** in CH₂Cl₂/0.05 M [TEA][BArF₂₄] at 273 K. The precipitated product was dissolved in ²d-CD₂Cl₂. The two singlets at 7.57 ppm and 7.72 ppm are assigned to the aromatic rings of the counter anion, BArF₂₄, of the electrolyte. In addition, the singlet at 2.13 ppm belongs to the methyl group of the Cp^{*} ligand. As before, a downfield chemical shift of ca. 0.10 ppm is observed for the singlet of the methyl group of the Cp^{*} ligand following oxidation.

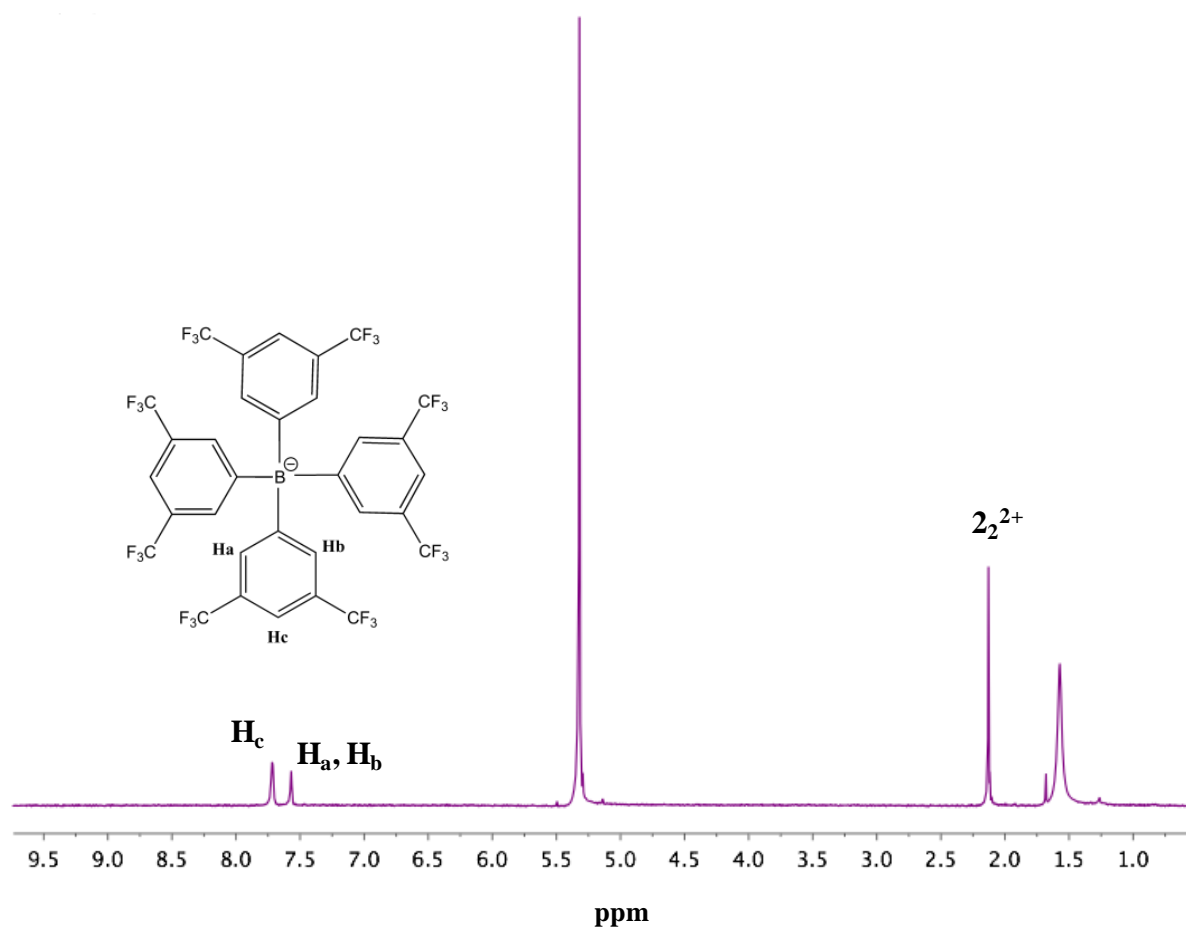


Figure 5.24: ¹H-NMR (500 MHz) spectrum of electrolysis product of a solution of 6.5 mM of Cp^{*}Rh(CO)₂/0.05 M [TEA][BArF₂₄], in CD₂Cl₂.

5.9 Conclusions

The electrochemical studies carried out on Cp*Rh(CO)₂ give insight into reaction mechanisms but cannot bring information on the structural changes occurring in the molecule under study.

IR spectroscopy has been coupled to electrochemistry, showing that the electrolysis product is not likely to possess a bridging carbonyl (to be confirmed), but only terminal carbonyls.

NMR spectra indicate a shift between the neutral species and the electrolysis product, indicating that the latter could potentially be the dimer dication.

However, none of these methods could provide structural characterisation of the generated species.

X-ray absorption spectroscopy is well suited to this task. X-ray Absorption spectroscopy (XAS) gives quantitative information about the local structures of materials such as the number and types of atoms coordinated to the metal, their bond lengths and angles, as well as being an electronic probe of vacant states of absorbing atoms. Cp*Rh(CO)₂ has been one of our studied materials during experiments at the Swiss Light Source and at Diamond Light Source. However, these experiments happened to be more challenging than expected. Cp*Rh(CO)₂ is indeed a very air sensitive material. There have been two trials for its study at two different beamtime. During the first one, although we used gas tight syringes to manipulate the compound, this was not sufficient to maintain the rhodium compound stable: it turned from light orange colour to black in 2 min time. During the second beamtime, we decided to use a glove box in addition to the gas tight syringes but the outcomes were identical. Therefore, we have not been able to obtain any EXAFS spectra in order to show in this thesis the completion of the interesting and promising study demonstrated in this chapter.

References

1. Connelly, N. G.; Lucy, A. R.; Payne, J. D.; Galas, A. M. R.; Geiger, W. E. Reduction Oxidation Properties of Organotransition-Metal Complexes .17. the Reaction of [Rh(CO)(PPh₃)(η-C₅H₅)] with One-Electron Oxidants - Fulvalene Complex and Silver Adduct Formation, and the X-Ray Crystal-Structure of [Ag(Rh(CO)(PPh₃)(η-C₅H₅))₂][PF₆].C₆H₅Me. *J. Chem. Soc. Dalton* **1983**, (9), 1879-1885.
2. Fonseca, E.; Geiger, W. E.; Bitterwolf, T. E.; Rheingold, A. L. Dimerization of A 17-Electron Cation Radical by Formation of A Rhodium Rhodium Bond. *Organometallics* **1988**, 7 (2), 567-568.
3. Gennett, T.; Grzeszczyk, E.; Jefferson, A.; Sidur, K. M. Unusual Oxidative Behavior of (η⁵-C₅R₅)M(CO)₂ R=H, CH₃-M=Rh,Co) Complexes at Mercury and Platinum-Electrodes. *Inorg Chem.* **1987**, 26 (12), 1856-1860.
4. Barriere, F.; Lesuer, R. J.; Geiger, W. E. Electrochemical advances using fluoroarylborate anion supporting electrolytes. *TMEC* **2004**, 413-444.
5. Hill, M. G.; Lamanna, W. M.; Mann, K. R. Tetrabutylammonium Tetrakis [3,5-Bis(Trifluoromethyl)Phenyl]Borate As a Noncoordinating Electrolyte - Reversible 1e-Oxidations of Ruthenocene, Osmocene, and Rh₂(Tm₄)⁴²⁺ (Tm₄=2,5-Diisocyano-2,5-Dimethylhexane). *Inorg. Chem.* **1991**, 30 (25), 4687-4690.
6. Lesuer, R. J.; Buttolph, C.; Geiger, W. E. Comparison of the conductivity properties of the tetrabutylammonium salt of tetrakis(pentafluorophenyl)borate anion with those of traditional supporting electrolyte anions in nonaqueous solvents. *Anal. Chem.* **2004**, 76 (21), 6395-6401.
7. Camire, N.; Nafady, A.; Geiger, W. E. Characterization and reactions of previously elusive 17-electron cations: Electrochemical oxidations of (C₆H₆)Cr(CO)₃ and (C₅H₅)Co(CO)₂ in the presence of [B(C₆F₅)₄]⁻. *J. Am. Chem. Soc.* **2002**, 124 (25), 7260-7261.
8. Nafady, A.; Costa, P. J.; Calhorda, M. J.; Geiger, W. E. Electrochemical oxidation of CoCp(CO)₂: Radical-substrate reaction of a 17 e⁻/18 e⁻ pair and production of a unique dimer radical. *J. Am. Chem. Soc.* **2006**, 128 (51), 16587-16599.

9. Shaw, M. J.; Geiger, W. E. A new approach to infrared spectroelectrochemistry using a fiber-optic probe: Application to organometallic redox chemistry. *Organometallics* **1996**, *15* (1), 13-15.
10. Chong, D.; Laws, D. R.; Nafady, A.; Costa, P. J.; Rheingold, A. L.; Calhorda, M. J.; Geiger, W. E. [Re(η^5 -C₅H₅)(CO)₃]⁺ family of 17-electron compounds: Monomer/dimer equilibria and other reactions. *J. Am. Chem. Soc.* **2008**, *130* (8), 2692-2703.
11. Swarts, J. C.; Nafady, A.; Roudebush, J. H.; Trupia, S.; Geiger, W. E. One-Electron Oxidation of Ruthenocene: Reactions of the Ruthenocenium Ion in Gentle Electrolyte Media. *Inorg. Chem.* **2009**, *48* (5), 2156-2165.
12. Trupia, S.; Nafady, A.; Geiger, W. E. Electrochemical preparation of the bis(ruthenocenium) dication. *Inorg. Chem.* **2003**, *42* (18), 5480-5482.

*Chapter 6: Development of a
microdispenser for XAS*

6.1 Introduction

The experimental challenge in studying electrochemical intermediates arises because they are formed at or close to an electrode surface and may react to form products before diffusing into the bulk of the solution. In addition, intermediates will be present usually for only a short period of time and possibly only at low concentrations. The challenge is thus to create intermediates in sufficient concentration and then to study them before they can react or diffuse away.

One strategy that we have explored is to use a channel-flow electrochemical cell where damaged material flows immediately to waste and a microfocussed X-ray beam is used to probe intermediates generated at the electrode within the flowing electrolyte.¹ The benefit of using a highly focussed beam is that it allows smaller distances of approach. This permits solution with the highest concentration of intermediates to be probed with the additional benefit that the timescale of the experiment is reduced and intermediates with short life times can be detected. However, despite the use of a flowing system, the organometallics under investigation are subject to beam damage, a problem exacerbated by highly focussed beams; whilst most materials flow away from the beam, a small fraction deposits and accumulates on the windows and the electrode, within the path of the beam. This contamination ruins the XAS measurements.

An alternative strategy was to stabilise intermediates by combining a variable temperature cell with XAS, in order to investigate transient species where the temperature dependence of the chemistry is important. We designed two integrated continuous flow electrolysis and EXAFS cells whose geometry permitted operation in both transmission and fluorescence. These were the object of the investigations demonstrated in Chapter 4. Both designs presented were

suitable for intermediates with longer life times so that micro-focussed beams were not required.

Another strategy is to freeze the electrolytes to trap unstable product species where rapid bulk electrolysis is followed by freeze-quenching to prevent decay; this approach has been utilised for both ESR and XAS studies.²⁻⁴ The principal advantage is that only modest focussing is required, reducing the drawbacks caused by beam damage. In addition, data quality can be improved with samples at liquid nitrogen temperatures. However, in the approach used by Best *et al.*,³⁻⁶ the time resolution was limited by the rate at which material can be electrolysed and transferred from the electrolysis cell and quenched.

In this chapter, we describe a strategy that overcomes all the limitations cited above. We present a rapid freeze quench system that traps short-lived intermediates on a millisecond timescale. This corresponds to several orders of magnitude improvement over what has previously been achieved.

In recent years, there has been a dramatic advancement in the handling of low volume samples. This has emerged from developments in micro fabrication and inkjet technologies.⁷ Most research applications of inkjet technology have started by adapting readily available inkjet cartridges found in printers. These are not suitable for use in electrochemistry because the commonly available devices have a single filling point and the only exit is via the jet nozzle.

In order to study electrochemical intermediates it is necessary to control the time that elapses between preparation of the intermediate and deposition via the inkjet nozzle; this necessitates a flow through configuration. There are few of this type of microdispenser that are

commercially available and, after an extensive search, the dispenser produced by Picology AB⁸ was selected for investigation. The properties of the microdispenser are described below.

6.2 Understanding the microdispenser

The cross-section of the flow-through dispenser utilised in this study is shown in Figure 6.1. It consists of a rectangular channel through which the solution flows. A piezoceramic plate is positioned in the channel wall and, as a voltage is applied, the plate contracts and bends due to the silicon structure that is attached to it. This generates a pressure wave in the flow channel and a droplet of solution is ejected.

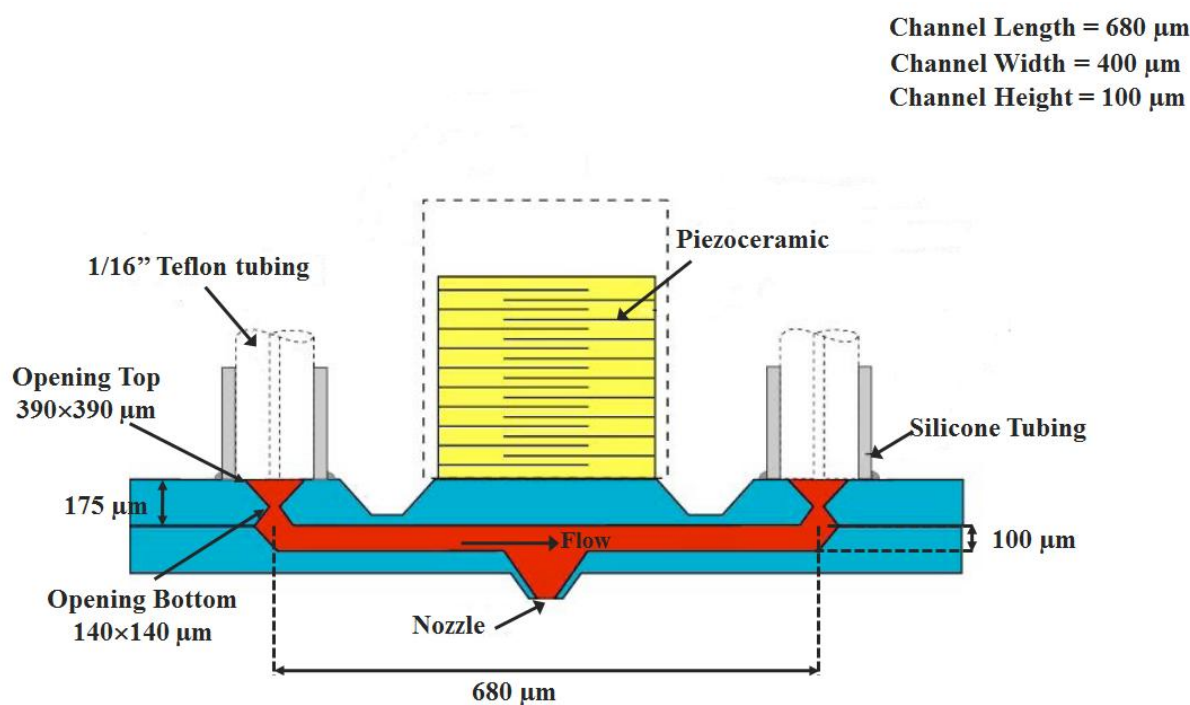


Figure 6.1: Cross section of the flow-through microdispenser.

The pulse voltage needed for droplet generation is dependent on solvent parameters such as surface tension and viscosity. The microdispenser is fabricated in silicon and silicone rubber

tubes with inner diameter matched to 1/16" tubes are attached to the inlet and outlet. A pyramid-shaped nozzle projects out from the silicon surface by 70 μm . This is the most fragile component of the dispenser, it should not be rubbed or touched with hard material.

To ensure stable generation of droplets, it is important to prevent air bubbles entering the dispenser during the filling and during the experiment. For example, when using acetonitrile throughout our investigations, we noted that, because it is a very volatile solvent, it evaporates almost immediately once the dispenser is stopped. Hence, evaporation from the nozzle created bubbles in the channel and the dispenser stopped working. There is then a high risk of damaging the device.

6.2.1 The control box parameters

The piezoelectric actuator is driven via a pulse function generator control box that is furnished with the microdispenser.

The output of the controller is a series of voltage pulses of defined shape, amplitude, and duration: the pulse length, the pulse period, the pulse amplitude, the number of pulses or bursts (depending on which mode of the two is chosen), the burst frequency, and finally the supply voltage. A typical plot of the output voltage versus time is given below in Figure 6.2.

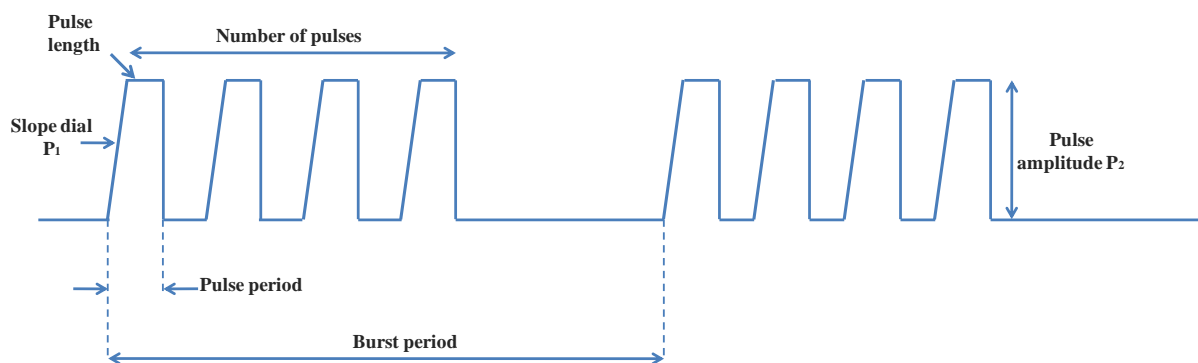


Figure 6.2: Typical plot of the output voltage versus time.

The controller allows all the parameters given in the figure above to be specified via the settings presented in Table 6.1.

1	Pulse length (time from the start of the pulse until the pulse begins to level off)	10 - 1000 μ s
2	Pulse frequency (sets the frequency of the pulses applied to the dispenser. It must not be higher than allowed by the pulse length, otherwise the output is undetermined) which may destroy the drive electronics.	0.1 - 10000 Hz
3	Number of pulses / burst in burst mode (sets the number of pulses of each burst in Burst mode. The frequency of the pulses is determined by the settings in (2)).	0 - 10000 st.
4	Burst frequency (sets the repetition frequency of the bursts in Burst mode)	0.01 – 1000 Hz
5	Supply voltage (determines maximum pulse amplitude)	< 30 V

Table 6.1: Parameters to be set for operating the flow-through microdispenser.

Moreover, two additional parameters have to be set for each experimental conditions: the voltage settings of the Slope dial (P1) and Amplitude dial (P2). The slope adjusts the rise time for the leading edge of the pulse (a higher voltage means a shorter rise time) and the

amplitude sets the pulse amplitude or height. The values may be adjusted while running the dispenser. The optimal values differ between different dispensers and are dependent on the solvent used, depending upon the surface tension and viscosity.

The controller allows the key operating parameters to be adjusted and stored for future experiments. A picture of the control box is shown in Figure 6.3.



Figure 6.3: Picture of the control box of the flow-through microdispenser.

6.2.2 The first tests

Droplets formation

The first tests carried out with the flow-through microdispenser were purely qualitative. The main aim was to gain familiarity with its operation, but most importantly to be able to understand how solution flows, how the jet is spraying and mainly what are the characteristics of the dispensed droplets. As shown in Figure 6.4, the dispenser was mounted horizontally and an aluminium target plate was aligned to it and displaced at increasing distances, in order

to observe the formation of droplets. A short length of 1/16'' PTFE tubing was attached to the outlet of the dispenser and the inlet which was connected to a syringe pump.

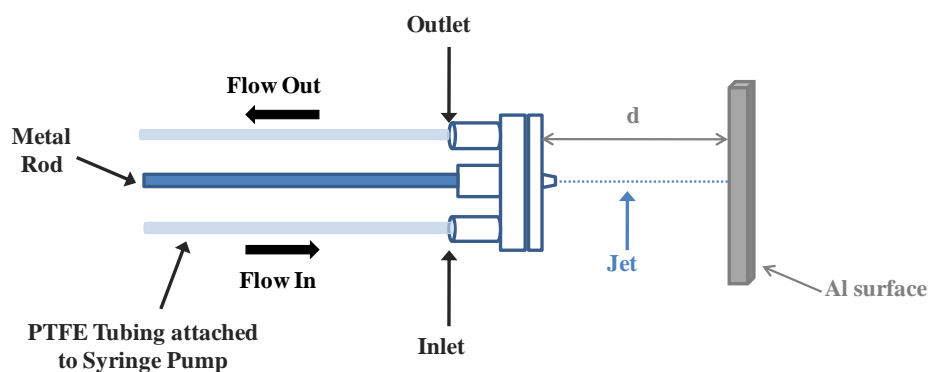


Figure 6.4: Schematic of the set-up for the understanding of the droplets formation.

The length of the outlet tube is an important parameter: it has to be as short as possible because the dispenser is very sensitive to pressure. Wide-bore outlet tubing is preferable since this reduces the fluctuations in pressure caused by surface tension during the formation of droplets at the end of the tube.

It was observed that the limit for range of flight for successful droplets of water formed is ca. 20 mm. However, it could be noted that the jet was very sensitive to air drafts in the laboratory, which could potentially be an issue regarding the convection around the cold finger in the XAS chamber (see later).

With an exit tube 20 cm long and when increasing the flow rate up to 5 ml h^{-1} , the operation remained unaffected. Higher flow rates are supposedly possible particularly with shorter tubing and a wider bore exit tube. However, the flow rate limit varies for different electrolyte/solvent solutions; we observed that, when using MeCN, droplets were successfully

formed over a distance of ca. 15 mm with a flow rate of 2 ml h⁻¹. Above this latter value, MeCN flooded the nozzle. As regards BTF, the limiting value was found to be ca. 3 ml h⁻¹.

Size of droplets

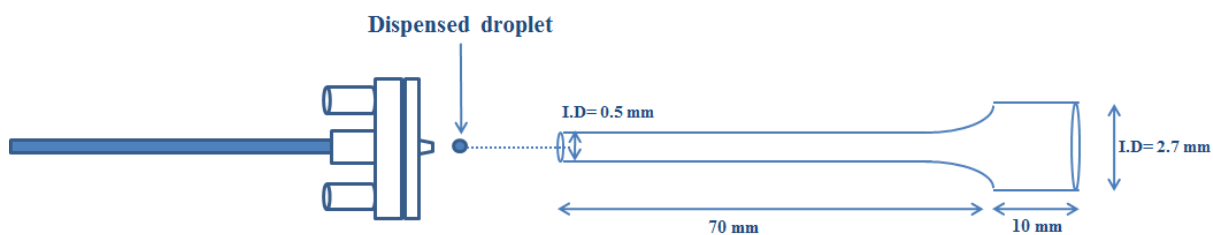


Figure 6.5: Schematic of the set-up for the determination of the size of the formed droplets.

The size of the droplets was characterised using a precision 0.5 mm internal diameter capillary tube.⁹ The dispenser was filled with water and the capillary tube was positioned over the microdispenser nozzle, as shown in Figure 6.5. Alignment was performed under a microscope.

The procedure was as follows: with a flow rate of 1 ml h⁻¹ and a dispensing frequency of 50 Hz, a pulse slope of ca. 6 V, an amplitude of ca. 12 V, and a pulse length of 100 μ s, the volume of the capillary tube filled was measured as a function of time. The results obtained are summarised in Table 6.2.

Time (min)	Distance (mm)	Volume filled in the capillary (mm³)	Calculated Volume of a droplet (pl)	Calculated diameter of droplets (μm)
3	7.9	1.55	172	69
6	15.8	3.10	172	69
9	21.7	4.26	158	67

Table 6.2: Experimental parameters for the determination of the volume and the size of the dispensed droplets.

The volume of a droplet was determined from the following data: the volume filled in the capillary, the pulse frequency and the elapsed time. Then the diameter of the droplet was determined by trivial calculation.

The pulse voltage needed to generate droplets depends on solvent parameters such as surface tension and viscosity: lower surface tension should mean lower voltage and higher viscosity means higher voltage. In order to gain an understanding of the parameters, we ensured that that droplet generation was as effective with the two other solvents used in this study, namely acetonitrile and benzotrifluorotoluene, as it was with water.

6.3 Electrochemical characterisation of the microdispenser

6.3.1 Cell Design

The electrochemical cells were constructed from miniature tee barb connectors (Dionex, P/N 30538) that are used in HPLC applications, and sealed with epoxy resin (Bondmaster, Double Bubble). A schematic diagram of a typical electrode configuration is shown in Figure 6.6.

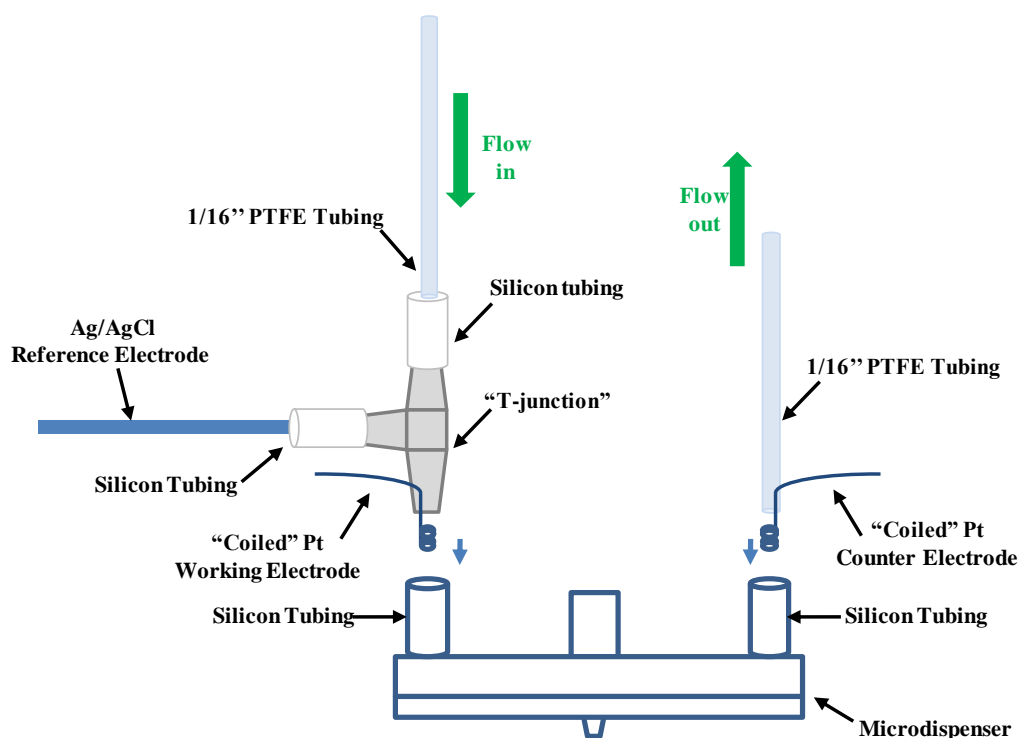


Figure 6.6: Schematic of the set-up of the electrochemical cell with the microdispenser.

Cleaning procedure

Cleaning of the microdispenser was achieved by first sucking out the remaining electrolyte solution and then, by flowing IPA through for an hour at a flow rate of 2 ml h^{-1} . The nozzle was gently cleaned on the outside by using the corner of a soft tissue; care was taken to never push the tissue against the nozzle with a finger. In addition, it was important to ensure that the

dispenser was emptied completely and that no liquid was left inside the nozzle; surface tension could keep the liquid in the nozzle. This was achieved by sucking air through the dispenser from the outlet to the inlet. The outlet was briefly closed so that air was sucked backwards through the nozzle to remove any liquid remaining.

6.3.2 Preliminary electrochemistry: FeCp₂ in MeCN

This reliable system was used to acquire an understanding of the device for inorganic electrochemistry in non-aqueous solvents. As mentioned in the previous chapter, ferrocene is a readily available and cheap compound which makes it ideal for our investigations. Electrochemical control was maintained via an Autolab PGSTAT 10 potentiostat. Solution flow was achieved by means of a syringe pump (Harvard Apparatus) fitted with a 5 ml gastight syringe with a PTFE luer lock (Aldrich).

As a first attempt, a cyclic voltammetry study was carried out for 2.3 mM FeCp₂ in 0.1 M [NEt₄][BF₄] in argon-purged anhydrous acetonitrile. The standard procedure to fill the dispenser was initially to flow solution at 5 ml h⁻¹ with a gas tight 5 ml glass syringe until the solution approached the device inlet (in order to save time), then the flow was reduced to the desired rate for dispensing, here 1 ml hr⁻¹. Glass syringes are better suited to the microdispenser than disposable syringes, because the flow is much steadier and thus sudden flow peaks that may appear from the latter are avoided. Figure 6.7 shows the resulting cyclic voltammogram at various scan rates, for a flow rate of 1 ml h⁻¹. It can be seen immediately that the current has a maximum value of ca. 60 μA, which is reached for scan rates greater than 5 mV s⁻¹.

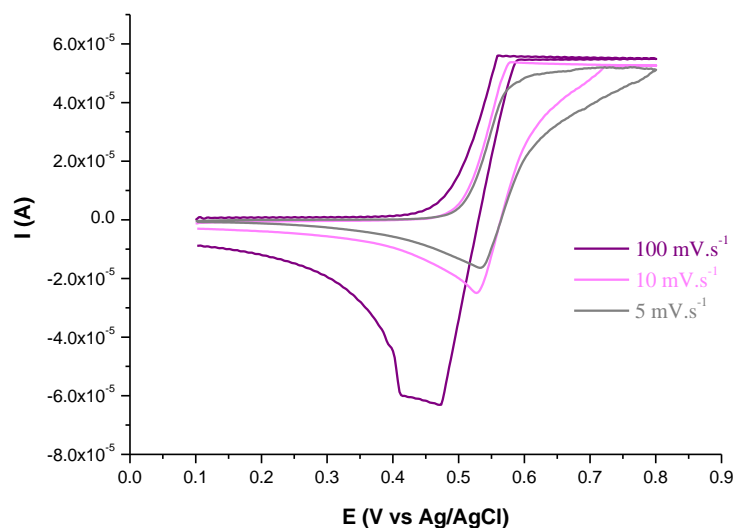


Figure 6.7: Cyclic voltammograms of 2.3 mM FeCp₂ in MeCN/ 0.1 M [NEt₄][BF₄] with a flow rate of 1 ml h⁻¹, dispenser on, at various scan rates.

In order to check if the flow is the source of disruption in the electrochemical behaviour, scans were recorded when no solution was flowing, i.e at static conditions (see Figure 6.8).

The same behaviour is observed but the maximum scan rate is now 10 mV s⁻¹.

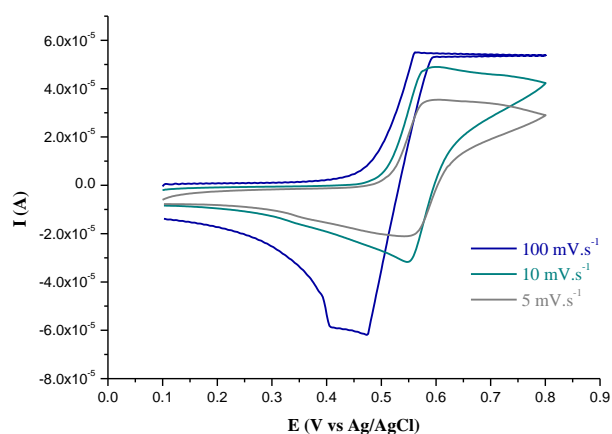


Figure 6.8: Cyclic voltammograms of 2.3 mM of FeCp₂ in MeCN/ 0.1 M [NEt₄][BF₄] without flow, dispenser on, at various scan rates.

It may be seen that, under flow conditions, it is just possible to maintain electrochemical control over the whole voltage range but control was lost for sweep rates greater than 5 mV s^{-1} . Besides, we tried switching the potentiostat in use to an Autolab PGSTAT 12 which has a larger compliance voltage and, surprisingly, no improvement was noted. Actually, electrochemical control was even slightly worse.

These figures show an obvious limitation of the compliance voltage caused by an excessive iR potential drop between the WE and the CE. To overcome this problem, it is necessary to lower the current across the cell or decrease the magnitude of the resistance across the microchannel. This may be achieved in a variety of ways. We explored different strategies: firstly, to increase the conductivity of the solution by using a higher concentration of the background electrolyte. Secondly, to reduce the concentration of the redox species. Thirdly, shrinking the size of the working electrode would reduce the double-layer capacitance C_d proportionally but only at the expense of reducing the electrolysis conversion, the prime objective.

6.3.3 Improving potential control: Reducing the concentration of FeCp_2 .

Figure 6.9 shows cyclic voltammograms for 0.5 mM ferrocene in MeCN carried out for a wide range of scan rates; it can be seen that for this concentration full potentiostatic control is achieved under all circumstances. This is encouraging but 0.5 mM is a low concentration from an XAS standpoint. This is less than ideal.

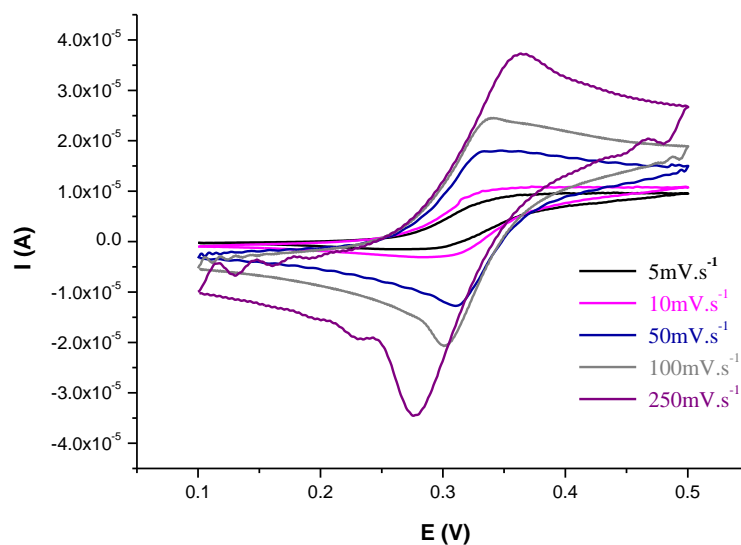


Figure 6.9: Cyclic voltammograms of 0.5 mM of FeCp_2 in $\text{MeCN}/0.1 \text{ M } [\text{NET}_4][\text{BF}_4]$ with a flow rate of 1 ml h^{-1} , dispenser off, at various scan rates.

Figure 6.10 shows the effect of changing the concentration upon electrochemical behaviour at a fixed scan rate of 100 mV s^{-1} . It can be seen that potentiostatic control is lost for concentrations much greater than 0.5 mM .

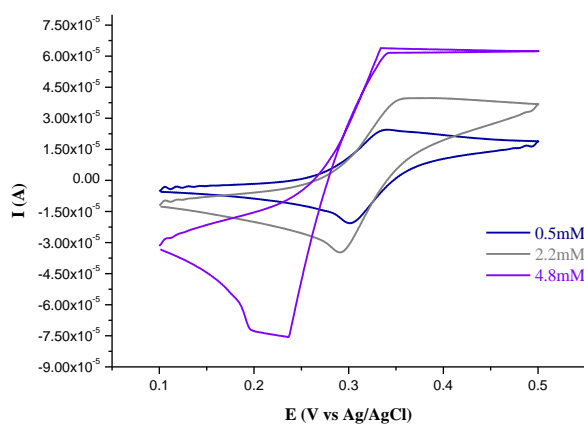


Figure 6.10: Cyclic voltammograms of FeCp_2 at various concentrations in $\text{MeCN}/0.1 \text{ M } [\text{NET}_4][\text{BF}_4]$, with a flow rate of 1 ml h^{-1} , dispenser off, at 100 mV s^{-1} .

6.3.4 Improving potential control: Increasing the concentration of background electrolyte

The previous section has highlighted the loss of potential control observed at scan rates greater than 10 mV s^{-1} for a concentration of 5 mM of FeCp_2 . In terms of EXAFS studies, the latter concentration is towards the lower concentration limit. The following experiment tested whether or not an increase of the concentration of background electrolyte would improve potential control.

Three different concentrations of $[\text{NEt}_4][\text{BF}_4]$ were tested: 0.05 M , 0.1 M , and 0.2 M , in a solution of 2.5 mM of FeCp_2 . The CVs recorded are shown in Figure 6.11.

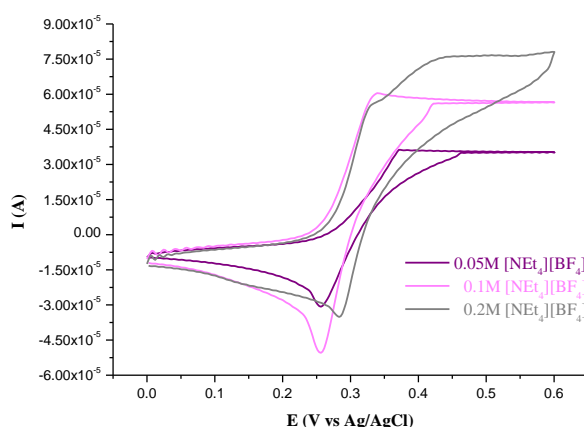


Figure 6.11: Cyclic voltammograms of 2.5 mM of FeCp_2 in MeCN, with a flow rate of 1 ml h^{-1} , dispenser off, at 100 mV s^{-1} , for increasing concentrations of $[\text{NEt}_4][\text{BF}_4]$.

For both 0.05 M and 0.1 M background concentrations, potential overload was observed, with a current plateau at 35 and $60 \text{ }\mu\text{A}$, respectively. However, at 0.2 M of $[\text{NEt}_4][\text{BF}_4]$, the voltage was no longer overloading and the current maximum was at $74 \text{ }\mu\text{A}$, but the shape of the CV remained distorted. Nevertheless, it appeared quite rapidly during the experiment that crystallisation was occurring on and around the nozzle exit. This stopped the droplet ejection

and thus, the dispenser stopped working. The crystals could be dissolved and removed with IPA but this indicated that we were reaching the limit in terms of operation.

These previous experimental tests did not give a conclusive solution; therefore the electrode configuration was reconsidered.

The initial configuration was changed three ways as illustrated in Figure 6.12. Based on the experience in Chapter 4, the coiled Pt WE was replaced with a straight wire to reduce the risk that the WE shields the RE from the applied potential for the CE. The RE was replaced by a Pt pseudo-reference in order to minimise the distance between the WE and RE. These changes were tested separately and together.

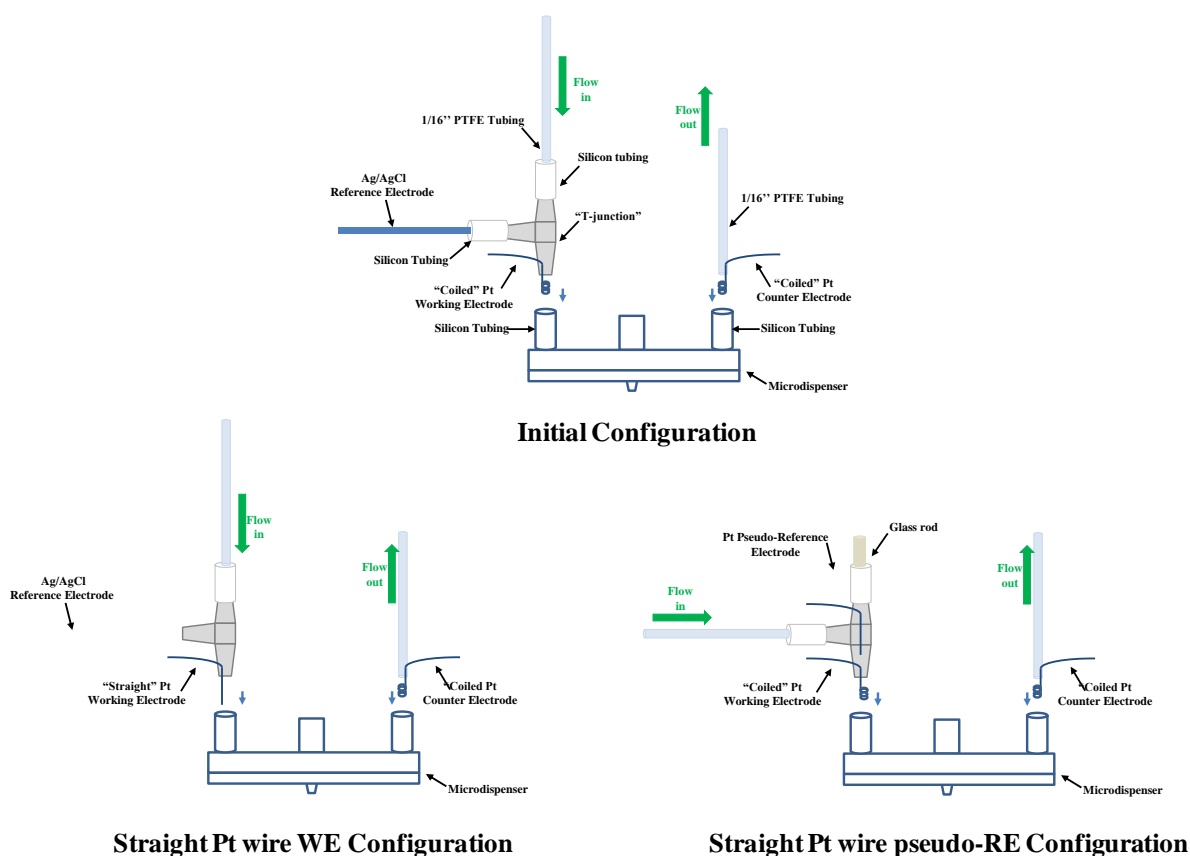


Figure 6.12: Schematic diagrams showing modifications of the initial electrolysis cell configuration.

Replacing the Ag/AgCl reference electrode with a pseudo-reference electrode was not successful: the overload detected in the previous investigations remained a problem. However, when the WE was a straight wire of Pt, good electrochemical behaviour was observed as shown in Figure 6.13 for cyclic voltammograms of 1.02 mM FeCp₂/0.1 M [NEt₄][BF₄] in MeCN at various scan rates.

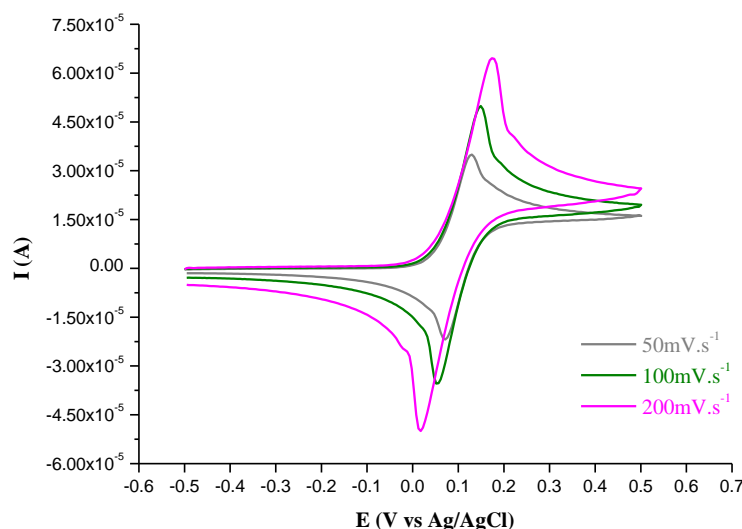


Figure 6.13: Cyclic voltammograms of 1.02 mM FeCp₂, 0.1 M [NEt₄][BF₄] in MeCN.

However, this good behaviour was at the expense of the electrolysis conversion. The electrochemical behaviour is clearly very sensitive to the shape of the WE and its position within the cell. By experiment, we observed that by increasing the number of loops and folding the loops together, we could in fact obtain high conversion yield and maintain electrochemical control. Figure 6.14 shows typical chronoamperometric measurements for the optimum geometry for electrolysis in MeCN. The resulting conversion rates are tabulated in Table 6.3.

Flow Rate (ml h ⁻¹)	I _{limiting} (μA)	Moles s ⁻¹	Conversion (%)
0.25	6.5	7.08×10 ⁻¹¹	96
0.5	11.3	14.2×10 ⁻¹¹	83
1	17.3	2.84×10 ⁻¹⁰	63
2	25.2	5.67×10 ⁻¹⁰	46
0.25	6.0	7.08×10 ⁻¹¹	88

Table 6.3: Experimental results from chronoampero-measurements of 1.02 mM FeCp₂, 0.1 M [NEt₄][BF₄] in MeCN, at different flow rates.

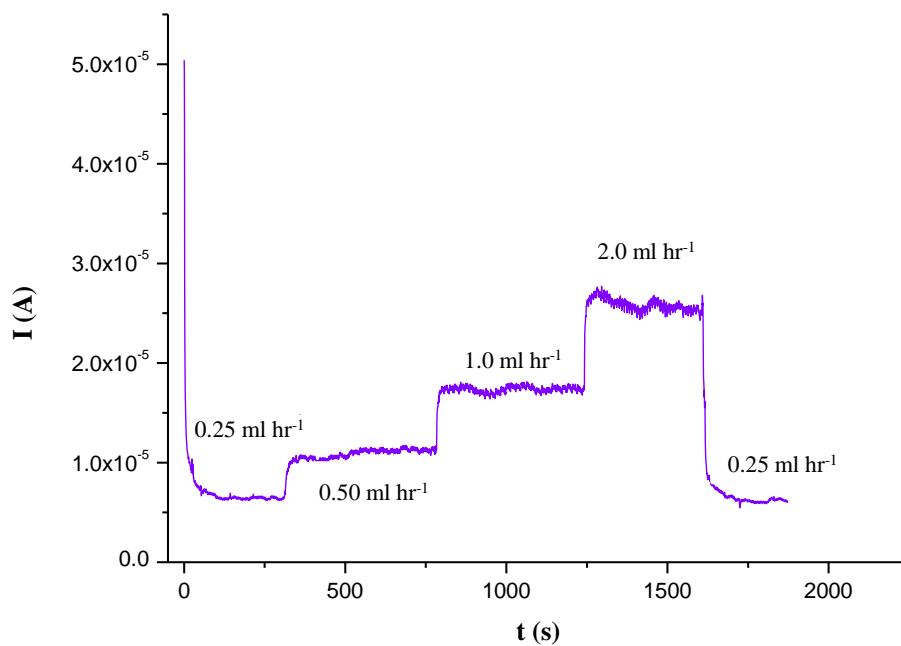


Figure 6.14: Limiting currents for 1.02 mM FeCp₂, 0.1 M [NEt₄][BF₄] in MeCN, at different flow rates.

3.5. Cell design modifications for use with BTF

The electrode geometry that was found to be successful for electrolysis in acetonitrile could not be made to function correctly when the solvent was changed to BTF. This is not surprising because the conductivity of electrolytes in BTF is significantly lower than those in ACN. This is illustrated by the cyclic voltammogram of FeCp_2 in BTF shown in Figure 6.15 below.

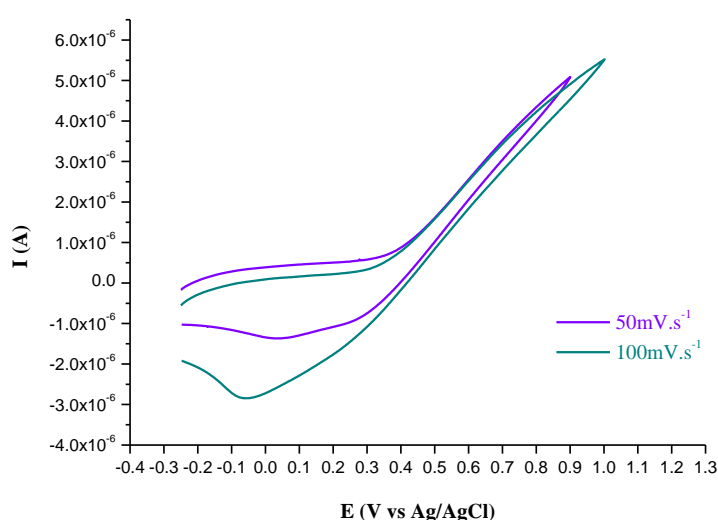


Figure 6.15: Cyclic voltammograms of 3.5 mM of FeCp_2 / 0.1 M $[\text{NEt}_4][\text{BF}_4]$ in MeCN, at different scan rates.

The principal problem associated with the design of the electrochemical cell used earlier is the high resistance of the electrolyte between the WE and CE. This is made worse by the small internal cross section of the microdispenser, but this feature is necessary to minimise the time between electrolysis and deposition onto the cold substrate. With BTF-based electrolytes it proved impossible to increase the conductivity of the solution sufficiently to maintain electrochemical control over the desired range of potentials.

It was therefore necessary to place all electrodes on the inlet side of the microdispenser so that the solution resistance between the counter and working electrodes, R_C , could be minimised by shortening the distance between the electrodes. The first idea, shown schematically in Figure 6.15, was to position the coiled Pt CE within the inlet tube and instead of using the Ag/AgCl RE in the side arm of the tee connector a fine PTFE tube would be inserted to act as a Luggin electrode. The objective of this was to reduce the effect of the iR drop upon the voltage sensed by the reference electrode. The WE was placed, as before, as close as possible to the inlet to the microdispenser.

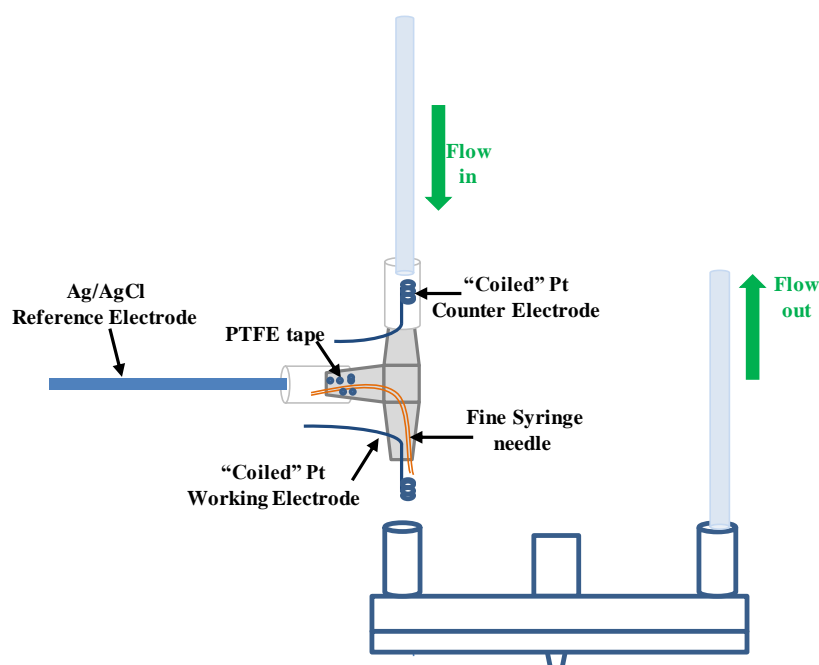


Figure 6.15: Proposed electrode configuration 2.

However, in practice this configuration proved impractical since the Luggin electrode was very difficult to insert correctly and interfered with the correct positioning of the WE.

To summarise, the desirable features were as follows: the WE has to be as close as possible to the dispenser nozzle, the RE should be as close as possible to the WE and, finally, the CE should be close to the WE in order to lower the solution resistance. However, the CE should not be in the direct flow, to avoid contamination from electrolysis at the CE. By the means of an additional connector, here a Y junction, it was possible to achieve all the desired features. The resulting cell configuration is shown in Figure 6.16.

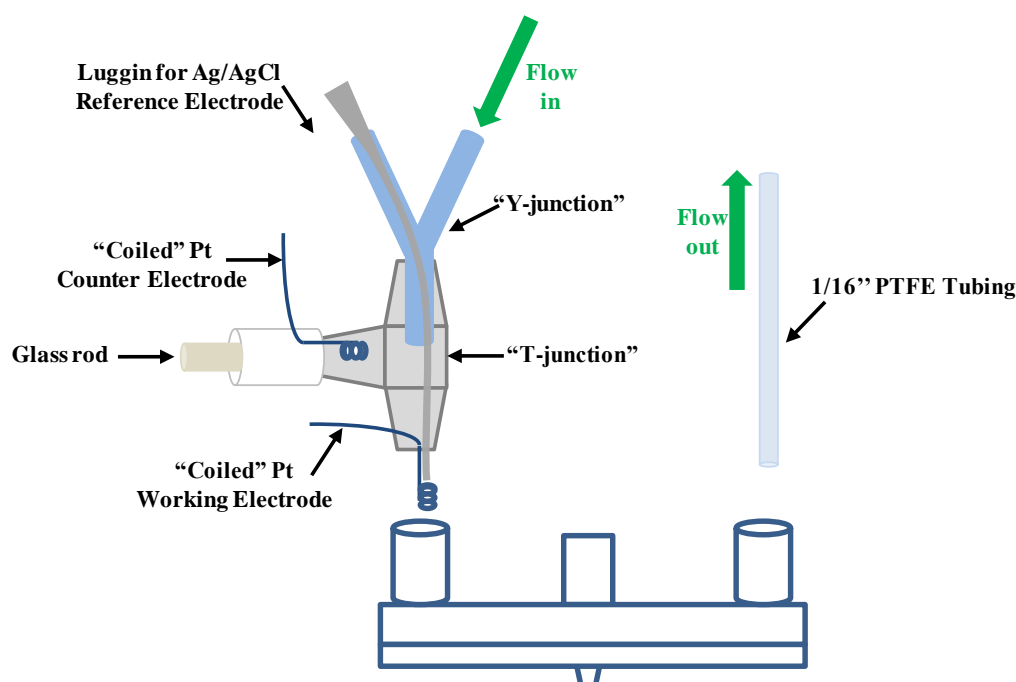


Figure 6.16: Revised electrode geometry for electrolysis of solutions in BTF.

It can be seen that the use of the ‘Y’ tube allows a Luggin electrode to be inserted into the electrolyte near the WE and the side arm of the tee connector is then freed up for use by the CE where there is no direct flow of electrolyte over the CE. BTF causes another experimental challenge in that it softens the silicone tubing connectors such that they ceased to be self supporting. A simple lightweight support was constructed from aluminium sheet to maintain all of the cell components in place.

6.4 The cryostat

The cryostat was designed and constructed by Dr. Richard Wiltshire. The description given below is sufficient to give an understanding of the equipment.

The overall objective of the experiment was to deposit droplets of solution evenly upon a cold target and then to carry out XAS measurements on the frozen sample. Deposition took place at 1 bar under nitrogen, followed by evacuation of the sample chamber for XAS investigations. The sample was mounted on a cold finger that could be rotated to face either the deposition system or both the incoming beam and fluorescence windows. Figure 6.17 gives a schematic of the two experimental set-up configurations: for deposition and for XAS measurements.

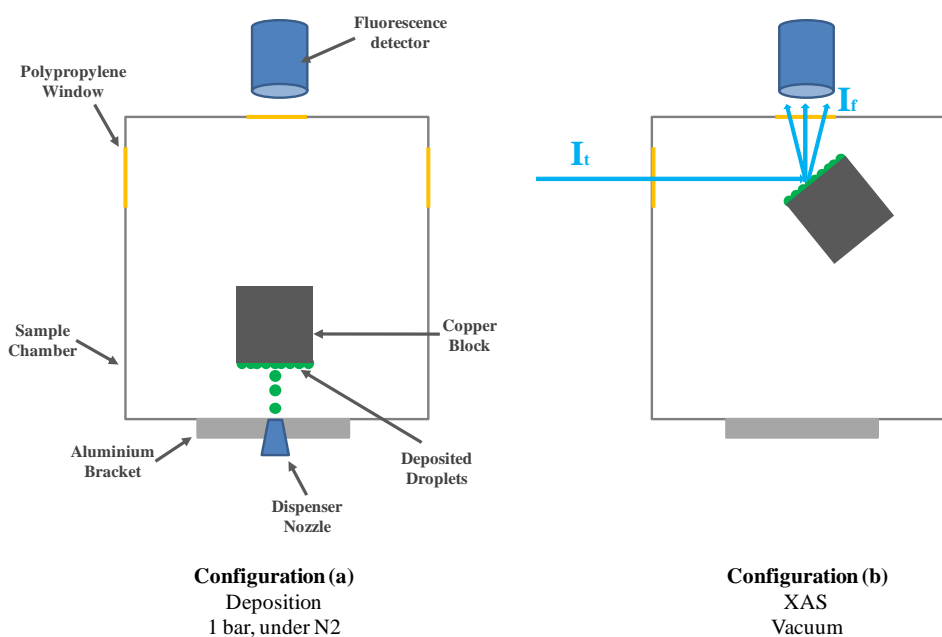


Figure 6.17: Sketches of the configuration for deposition (left) and for XAS measurements configuration (right).

Two versions of the cryostat were built but, for simplicity, only the second and final version will be described in detail. In the pilot study of the project, the chamber design relied on a manual control of the dispenser; deposition occurred at a fixed position and the upper part of the cryostat was rotated manually to spread out the sample on the substrate. However, to achieve reproducible and uniform coverage of the target, a motorised x-y stage was required. Figure 6.18 shows a general assembly drawing of the cryostat and cold finger (the liquid nitrogen dewar is omitted for clarity).

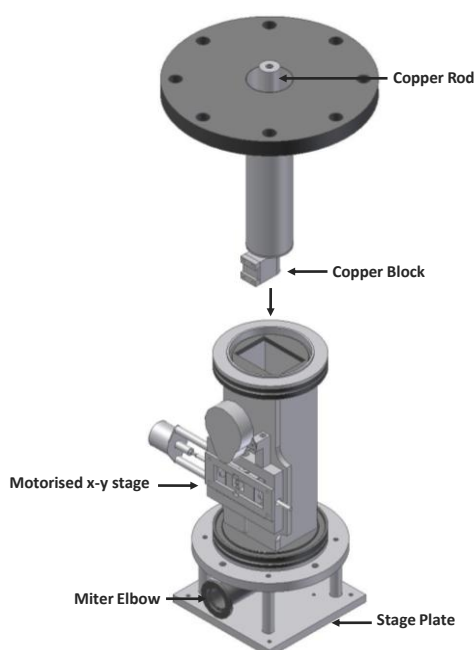


Figure 6.18: Schematic drawing of the cryostat.

The cold finger consists of a copper rod to which a copper block is attached and that was used as the target holder. Two Al centring o-ring seals were placed at the base and at the top of the chamber to achieve vacuum sealing. An elbow was welded at the base of the chamber in order to achieve connection to the vacuum pump.

The motorised x-y stage

A detailed sketch of the computer-controlled translation stage is shown in Figure 6.19. A linear actuator provides motion along the horizontal axis and a rotating cam is used for the vertical motion.

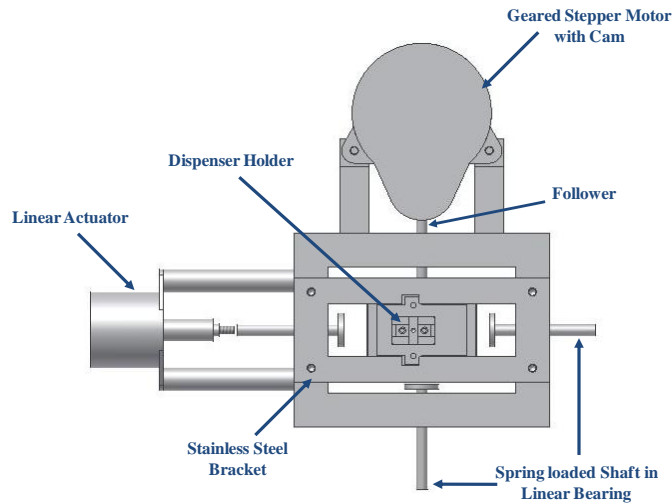


Figure 6.19: Schematic of the design for the motorised x-y stage.

A program was written to control the translation stage in order to provide even coverage over a defined area of the substrate. The distance travelled in the x direction was 6 mm and was less than 1 mm in the y direction. The translation step in the y direction corresponds to the calculated diameter of a droplet (see section 6.2.2 above). The deposition pattern followed by the stage is illustrated in Figure 6.20.

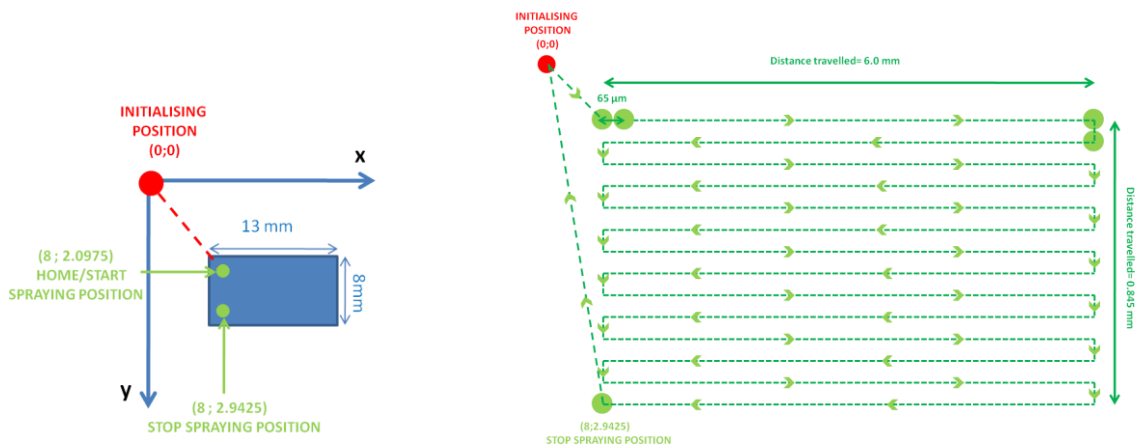


Figure 6.20: Pattern of the deposition procedure via the motorised x-y stage program.

6.5 Optimisation of deposition parameters

6.5.1 Cooling of the chamber

The droplets were quenched by spraying onto a liquid nitrogen-cooled target. To ensure a freeze/quench environment, the cold finger was connected to a polystyrene dewar via a doubled copper braid that was attached to a ca. 5 cm diameter copper block. The latter was a push-fit into the polystyrene bucket, thus assuring that all connections were leak tight. The temperature of the target surface was monitored via a type K insulated thermocouple. The set-up is shown in Figure 6.21.

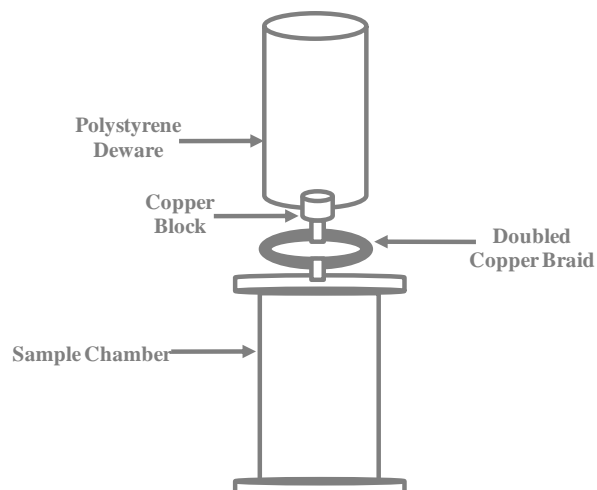


Figure 6.21: Schematic of the cooling set-up.

Approximately 30 minutes were required to evacuate the sample chamber to an appropriate vacuum pressure of ca. 5×10^{-6} mbar and, following addition of liquid nitrogen to the dewar, a temperature of ca. -115°C was reached in ca. 45 minutes.

6.5.2 The operation procedure

The generated droplets are both air and moisture sensitive so it is important that the dispensing procedure is carried out in a carefully controlled environment. To achieve this, the experimental set-up was such as the sample chamber was connected to both a vacuum pump and a high purity nitrogen supply, as shown in Figure 6.22.

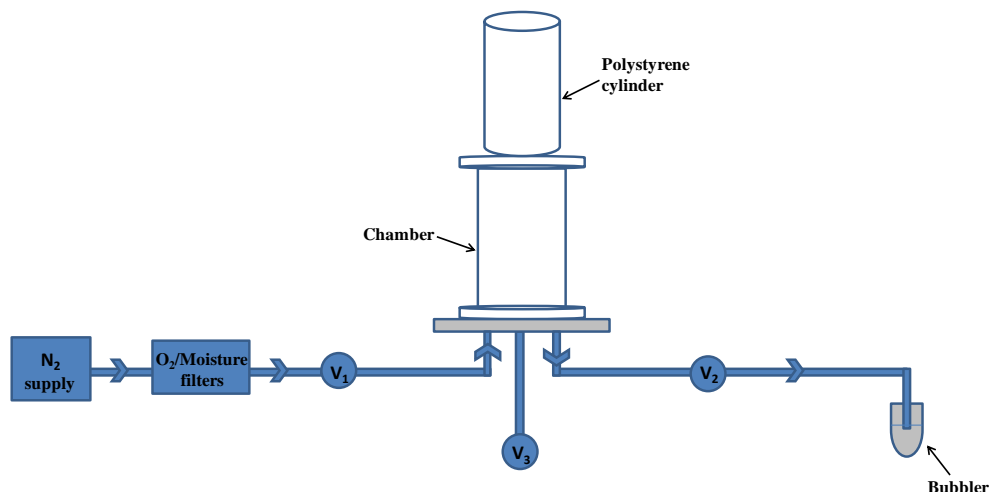


Figure 6.22: Schematic drawing of the gas and vacuum connections to the microdispenser/cryostat.

At first, the chamber was pumped down (V_1 and V_2 are closed, V_3 is open). It was considered worthwhile to flush the chamber with dry gas (by closing V_3 and pumping it down a number of times (ca. three times) at the start, in order to purge the system of oxygen and moisture.

The polystyrene dewar was first filled with liquid nitrogen when the chamber was under vacuum. The advantages of this procedure were to ensure removal of all oxygen and to accelerate the cooling of the sample by reduction of convection losses.

When the chamber reached an appropriate temperature suitable for quenching the solution, the electrolysed material was prepared to be dispensed on the silicon target. The chamber was brought to atmospheric pressure with pure nitrogen gas. A flow regulator was used to control the nitrogen flow to ensure that the XAS windows were not blown away by excess of nitrogen pressure. A bubbler was used to give an estimation of the flow.

After deposition, the cold finger was rotated by 45°, and the clamp screws were tightened. The chamber was sealed (V_1 and V_2 are now closed) and pumped down again (V_3 is open) for the remainder of the time of the experiment. As soon as the pressure reached ca. 10^{-6} mbar, XAS data were collected.

6.5.3 Choice of target material

Optimisation of number of parameters has been discussed so far. By means of cell design modification, the electrochemical behaviour of ferrocene has been adjusted to both acetonitrile and benzonitrile conditions. From a technical standpoint, liquid nitrogen cooling proved to be reliable and once stable, dispenser operation continued so for the whole deposition period. In addition, the use of a computer-controlled x-y stage permits the deposition of a uniform array of frozen droplets. However, the pilot study at the SLS highlighted a technical problem that prevented us from obtaining fully usable XAS data at the first attempt: the choice of the target material.

In order to ensure rapid quenching, the deposition target had to have high thermal conductivity. For that reason, all measurements that are presented here were carried out in fluorescence mode and the obvious first choice of target substrate was copper. However, the pilot study of this work highlighted a drawback in the experimental set-up: the EXAFS signal happened to be masked by the diffraction of this material. Figure 6.23 shows a background scan of the copper target with the fluorescence counts for the 13 detector elements as a function of energy. It can be seen that in many of the channels there is a broad peak above 7.4 keV and that furthermore, the position of the peak is different for each channel. This is a characteristic of diffraction from a polycrystalline sample.

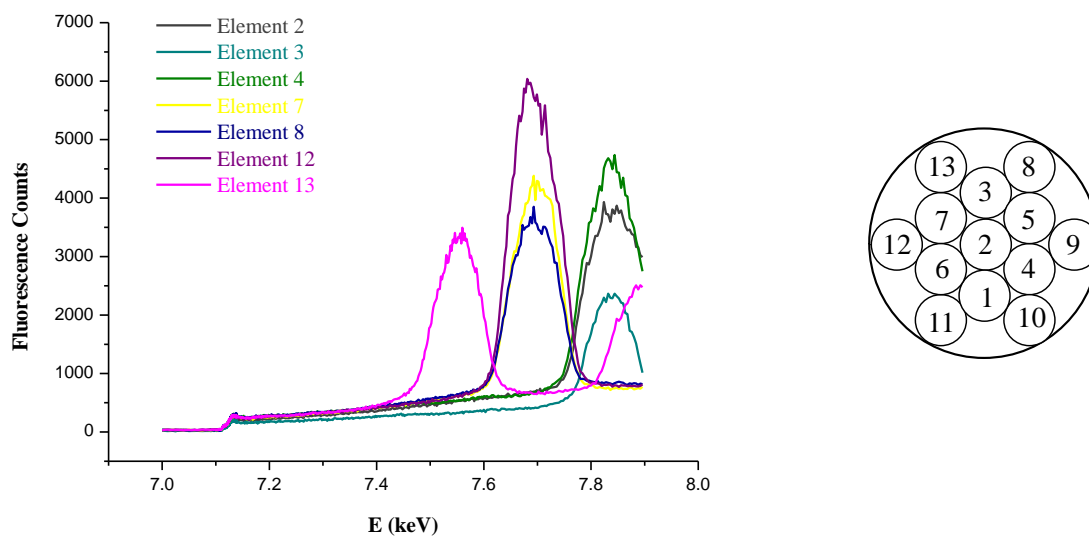


Figure 6.23: Fluorescence background from a clean copper substrate.

Only 5 of the 13-elements of the germanium detector provided usable data, even after varying both the distance between the target and the detector and the angle of the target regarding the detector.

A silicon crystal was then utilised as deposition substrate, cut to the dimensions (13x8 mm) of the copper block of the cold finger. It gave a very low background for the fluorescence spectra and allowed us to use data from every active channel in the detector.

6.6 Spectroelectrochemical characterisation of the microdispenser

6.6.1 Choice of systems for study

The following two systems were selected for study: $\text{CpRh}(\text{CO})\text{PPh}_3$ and $\text{Cp}^*\text{Rh}(\text{CO})_2$. For details on the latter, see Chapter 5. As regards $\text{CpRh}(\text{CO})\text{PPh}_3$; it was selected because, upon oxidation, a stable fulvalene dication is formed and the structure of both species is known.^{10,11}

This species made it possible to study a well known electrochemical reaction to test the experimental protocol.

In addition, because the compound is not commercially available and because it was not possible to get it from our collaborators, $\text{CpRh}(\text{CO})\text{PPh}_3$ had to be synthesised in our laboratory. The following section thus presents the synthesis of $\text{CpRh}(\text{CO})\text{PPh}_3$.

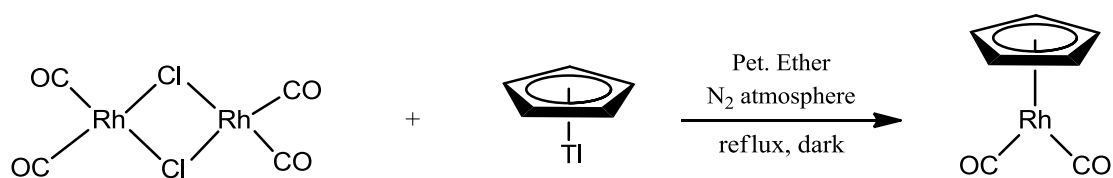
6.6.2 Synthesis of $\text{CpRh}(\text{CO})\text{PPh}_3$

6.6.2.1 General experimental

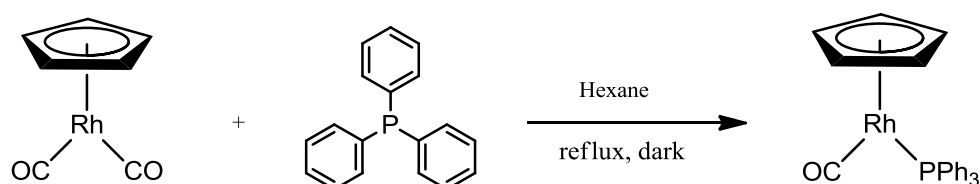
^1H , ^{13}C and ^{31}P NMR data were recorded on a Bruker AV300 or a Bruker AV400 spectrometer. Spectra were recorded in CD_2Cl_2 referenced to residual CH_2Cl_2 (^1H , 5.33 ppm; ^{13}C , 53.8 ppm; ^{31}P was referenced to an internal standard of H_3PO_4 set at 0 ppm). Chemical shifts (δ) are reported in ppm and coupling constants (J) are reported in Hz. The following abbreviations are used to describe multiplicity; d-doublet, q-quartet, m-multiplet. All coupling constants are reported as observed and averaged. Mass spectra were recorded on a LCT spectrometer utilising electrospray ionisation (recorded in the positive mode) with a methanol mobile phase, and are reported as (m/z (%)). IR spectra were recorded neat on a Perkin Elmer 1600 series FT-IR spectrometer. Analytical TLC was carried out on Merck 60 F245 aluminium-backed silica gel plates. Short wave UV (245 nm) was used to visualise components. Compounds were purified by flash column chromatography using Merck silica gel 60.

Hexane was distilled from sodium.

All other reagents and solvents were purchased from Sigma-Aldrich or Fisher Scientific and were used as received. All reactions in non-aqueous solvents were carried out under argon in oven-dried glassware.

6.6.2.2 Step 1: Preparation of CpRh(CO)₂Scheme 1: Synthesis of CpRh(CO)₂

The complex was prepared according to the procedure described by Knight and Mays.¹² A reaction mixture containing [Rh(CO)₂Cl]₂ (500 mg, 1.286 mmol) and thallium(I) cyclopentadienyl (1.09 g, 4.05 mmol) in petroleum ether (b.p 30°C-40°C; 29.2 mL) was continually stirred in a dry round-bottomed flask and heated at reflux for 24 h. The reaction was monitored by IR spectroscopy. The mixture was allowed to cool to room temperature and filtered to give an orange solution. The latter was concentrated under reduced pressure and purified by column chromatography to give the title compound (187.5 mg, 38%). ν_{\max} (neat)/cm⁻¹ 2032 (CO), 1957 (CO).

6.6.2.3 Step 2: Preparation of CpRh(CO)PPh₃Scheme 2: Synthesis of CpRh(CO)PPh₃

$\text{CpRh}(\text{CO})\text{PPh}_3$ was prepared and isolated according a published modification of the procedure described by Schuster-Woldan *et al.*¹³

A reaction mixture containing $\text{CpRh}(\text{CO})_2$ (187.5 mg, 0.84 mmol) and PPh_3 (210 mg, 1.07 mmol) in degassed hexane (30 mL) was refluxed for 12 h in the dark. The solution was allowed to cool to room temperature and 7.5 mL of solvent was removed. Bright orange crystals were obtained and separated from the solution. The crystals were collected by suction filtration, and washed several times with hexane (3×5 mL), and dried. The resulting product obtained was $\text{RhCp}(\text{CO})\text{PPh}_3$ (108.6 mg, 58%). R_f 0.59 (hexane) ; ν_{max} (neat)/ cm^{-1} 1933; δ_{H} (300 MHz; CD_2Cl_2), 7.50-7.58 (m, 12 H), 7.77-7.68 (m, 8 H); δ_{C} (100 MHz; CD_2Cl_2), 128.4 (d, J 10.3, CH), 130.2 (CH), 134.0 (d, J 12.6, CH), 137.5 (d, J 47.0, C), 195.3 (q, J 63.4-23.5, C); δ_{P} (121 MHz; CD_2Cl_2) 27.3; m/z (ESI) 481.0 $[\text{M}+\text{Na}]^+$.

6.7 XAS studies with a microdispenser system

6.7.1 $\text{CpRh}(\text{CO})\text{PPh}_3$

As previously discussed, both the structure of $\text{CpRh}(\text{CO})\text{PPh}_3$ and the cis-dication fulvalene are already known.^{10,11} The published molecular structures of both species are represented in Figure 6.24.

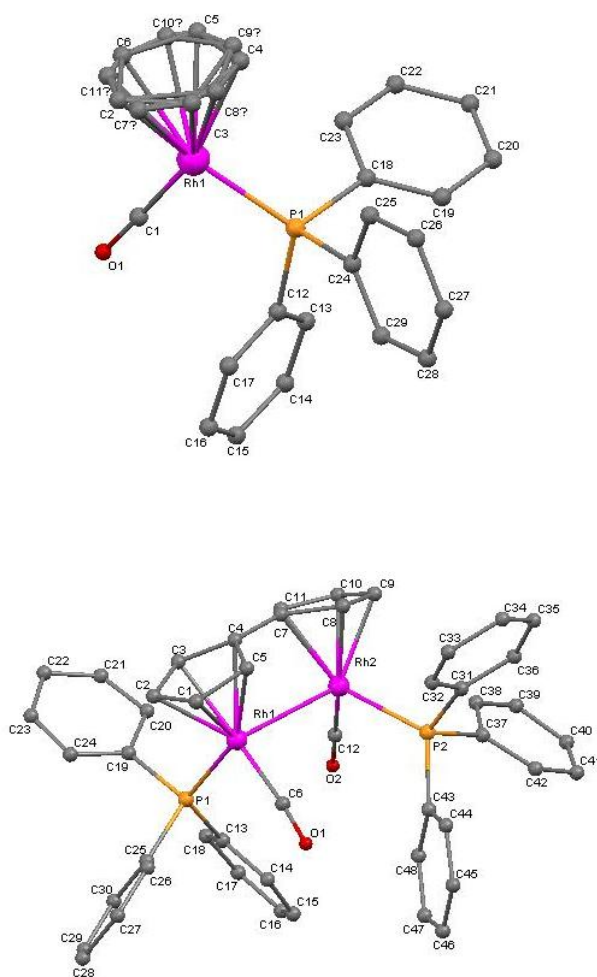


Figure 6.24: Molecular geometry of $\text{CpRh}(\text{CO})\text{PPh}_3$ (top) and of the cis-Dication (bottom), showing the labelling scheme used for atomic backscatterers^{10,11}. Hydrogen atoms have been omitted for clarity.

The bond distances from the central atom Rh_1 atoms for both compounds are given in Table 6.3. $\text{CpRh}(\text{CO})\text{PPh}_3$ crystallizes in a triclinic system and the cis-dication in the orthorhombic system. The distances given are averaged, when appropriate, over chemically equivalent crystallographic observations.

RhCpCOPPh₃		Cis-dication Fulvalene	
	Distance r (Å)		Distance r (Å)
		Rh ₁ -Rh ₂	2.930
Rh ₁ -C ₁	1.808	Rh-C(O)	1.821
Rh ₁ -P	2.2445	Rh-P	2.322
Rh ₁ -C (Cp ring)	2.282	Rh-C (Cp ring)	2.225
C ₁ -O	1.158	C-O	1.161
Rh ₁ -----O	2.966	Rh-----O	2.982

Table 6.3: Bond distances from the central atom Rh₁ to the nearest neighbours.

The distances in Table 6.3 were used to set up reference models in Artemis, yielding theoretical EXAFS for each of the structures against which experimental data can be compared and fitted. XAS data presented in this chapter were all collected on station SuperXAS at the Swiss Light Source.

Electrochemistry was carried out in acetonitrile at 298 K at a concentration of 3.15 mM using [NEt₄][BF₄] background electrolyte. The potential was held at $E_{\text{appl}} = 0.6$ V vs. Ag/AgCl during deposition of enough material on the substrate. The microdispenser gave a stable response over a period of more than 15 minutes, as shown in Figure 6.25. This was sufficient time for the deposition. The amount of conversion from the neutral species to the electrolysis product was determined as equal to 80 %.

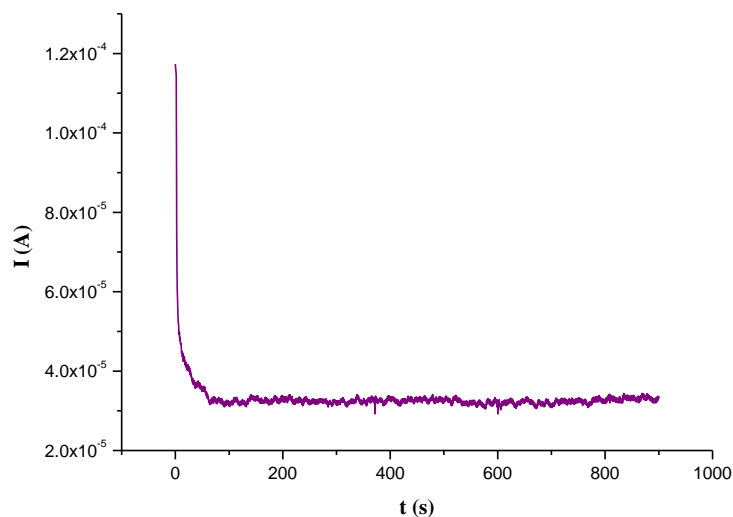


Figure 6.25: Chronoamperogram of 3.15 mM of $\text{CpRh}(\text{CO})\text{PPh}_3$ in $\text{MeCN}/0.1 \text{ M}$ $[\text{NEt}_4][\text{BF}_4]$ at 298 K during anodic electrolysis at $E_{\text{appl}} = 0.6 \text{ V}$ vs. Ag/AgCl

Figures 6.26 to 6.28 show a comparison of the XAS data collected at the SLS on the starting material deposited at open circuit, and that for material dispensed at a potential of $E_{\text{appl}} = 0.6 \text{ V}$ vs. Ag/AgCl . Inspection of the normalised spectrum in Figure 6.27 shows that upon oxidation the intensity of the white line increases. This is a natural consequence of a decrease in the d orbital occupancy upon oxidation. There are also clearly visible differences in the k^2 weighted EXAFS amplitude shown in Figure 6.27.

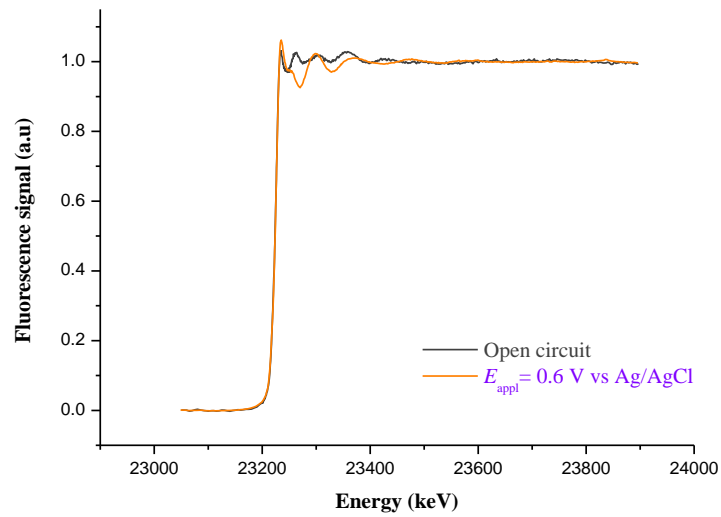


Figure 6.26: Comparison of the normalised spectra for CpRh(CO)PPh_3 deposited at open circuit and at an applied potential of $E_{\text{appl}} = 0.6 \text{ V vs. Ag/AgCl}$.

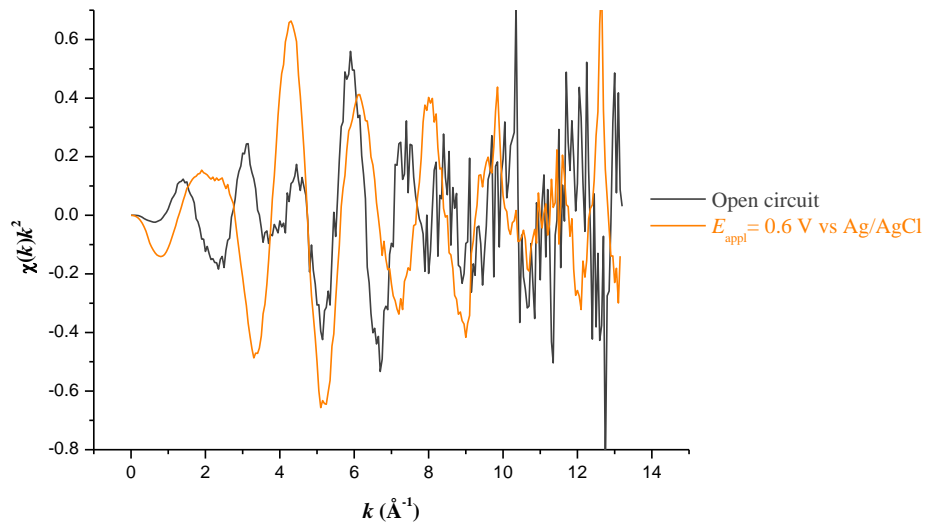


Figure 6.27: k^2 weighted of the EXAFS signal for CpRh(CO)PPh_3 deposited at open circuit and at an applied potential of $E_{\text{appl}} = 0.6 \text{ V vs. Ag/AgCl}$.

Finally, it can be seen that there is a marked difference between the neutral and oxidised species in the real-space Fourier transform of the EXAFS amplitudes. These data confirm the successful operation of the combined microdispenser / electrolysis cell.

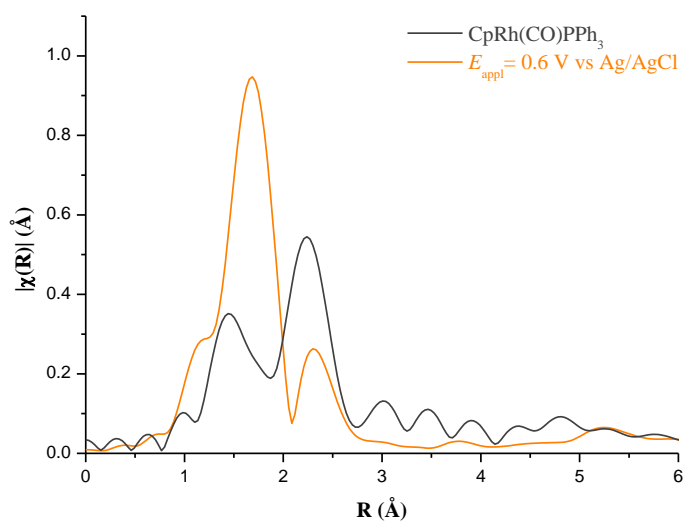


Figure 6.28: Plot in R -space of the Fourier transformed EXAFS signal for $\text{CpRh}(\text{CO})\text{PPh}_3$ deposited at open circuit and at an applied potential of $E_{\text{appl}} = 0.6 \text{ V vs. Ag/AgCl}$.

In the following section the different stages of the fitting procedure is described for the dataset obtained at the SLS. Firstly XAS amplitudes were extracted from the raw data according to the procedures described in Chapter 3 (section 3.4). Figure 6.29 shows the structure of $\text{CpRh}(\text{CO})\text{PPh}_3$ along with the parameters used in the Artemis software for the fits. The purpose of the fitting parameters shown in the figure will be explained later in this section.

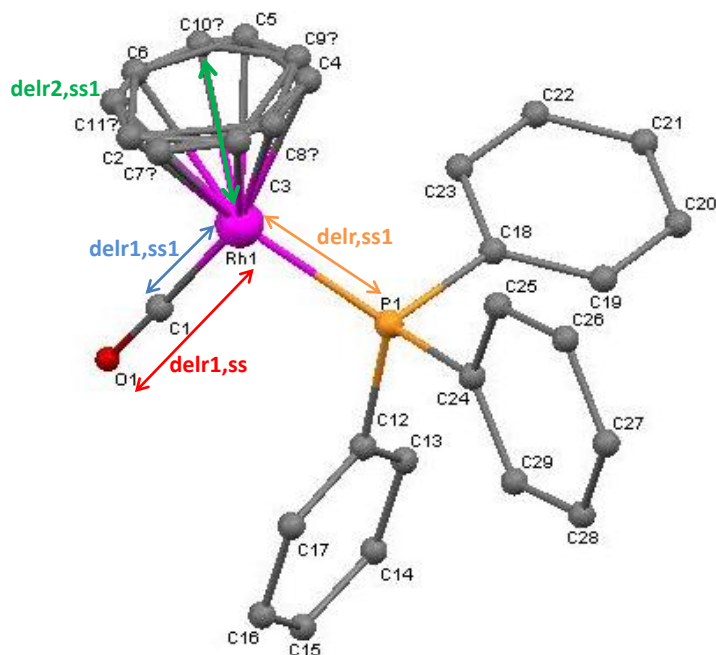


Figure 6.29: Molecular geometry¹⁰ of $\text{CpRh}(\text{CO})\text{PPh}_3$ showing the labelling scheme for atomic backscatterers and the fitting parameters used in the Artemis software.

It can be seen from the figure 6.29 that there is a large number of different scattering atoms within the first and second shell around the Rh atom. For example within the first shell, the carbon atom C1, the phosphorous atom P1 and all the carbon atoms from the Cp ring must be considered. For the purpose of carrying out XAS calculations, different fitting parameters have been defined as follows: “*delr*” characterises the change in the Rh-P bond length compared to that of the referenced crystal structure. Similarly “*delr1*” refers to the change of the Rh-C (from carbonyl group) bond length and finally “*delr2*” refers to the Rh-C (from the Cp ring) bond length. All the carbon atoms within the Cp ring are assumed to be at the same distance from the Rh atom. For reasons of simplicity a single Debye-Waller factor “*ss1*” was defined for all the atoms in the first shell, “*ss*” for all the single-scattering path regarding backscatterers from the second shell and finally, *ssMs* for all multiple-scattering path from first and second shell atoms. To finish, the “ S_0^2 ” parameter was used to calculate the passive

electron reduction factor, and the “ E_0 ” was utilised to determine the energy shift of the edge value.

As a starting point for fitting the XAS data obtained here, all parameters were set to be fixed to a chosen value: As regards the Debye-Waller factors ss , $ss1$ and $ssMs$, they have all been attributed the value of 0.003, which can be considered as a realistic guess. Finally, the variation of the energy shift E_0 was set to 0 and S_0^2 was defined as equal to 1. Figure 6.30 shows the results of this simulation (fit 1).

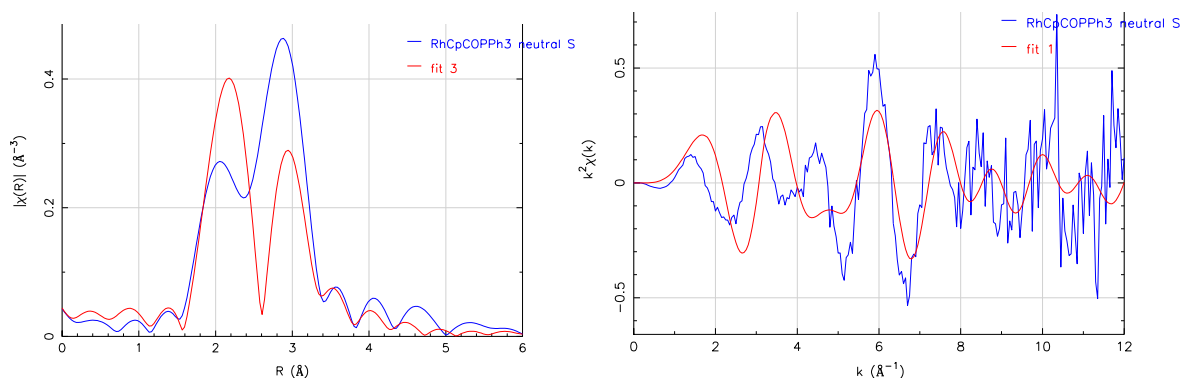


Figure 6.30: Comparison of the experimental data and the simulation based upon the crystal structure performed as described above: in R -space (on the left) and in k -space (on the right).

The resultant R -factor value obtained of 1.28 is very high, and the reduced χ^2 is equal to 86.65. Despite the fact that our compound is not a crystal and is in a of a frozen electrolyte matrix, it should nevertheless be possible to be fitted against the known crystal structure and the fit seems rather poor. However, as seen previously, there is a large number of scattering atoms and it is not a simple molecule.

Subsequently, an optimisation was carried out using all the fitting parameters defined in Figure 6.29. The resulting overall fit is shown in Figure 6.31, and plotted against the previous simulation as well as the experimental data.

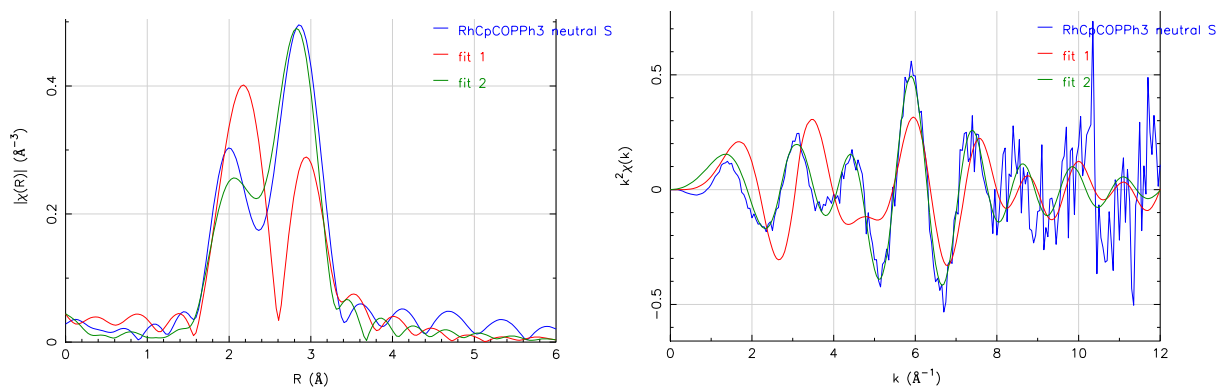


Figure 6.31: Comparison of the experimental data and two simulations in R -space (on the left) and in k -space (on the right). In green, the fit is based upon the crystal structure and as shown in Figure 6.31. In red, the fit was obtained after optimisation of all the parameters used in the Artemis software.

Following fitting, the R -factor has here decreased to a value of 0.027 and the reduced χ^2 to 6.32, which shows a very substantial improvement. However since the number of variables is large and the structure is complex, a deeper understanding of the result of this fit was sought by consideration of the contribution of individual paths. Figure 6.32 shows the contribution of every single-scattering path within the first shell, in R and k space.

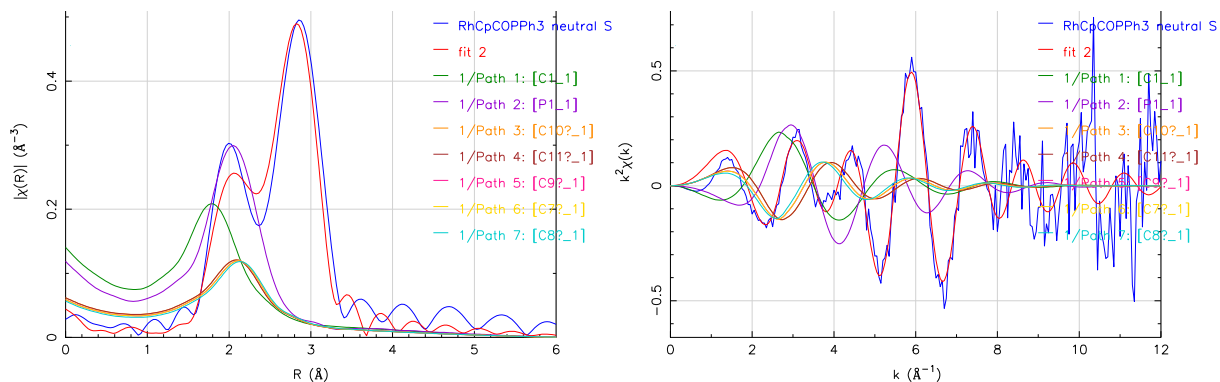


Figure 6.32: Contributions of every single-scattering paths within the first shell in R -space (on the left) and k -space (on the right).

The plot in R -space shows, as stated above that many atoms contribute to first peak occurring at ca. 2\AA . This has a number of consequences. Firstly it would not have been sensible to fit individual Debye-Waller factors for the back-scattering atoms because D-W factors for individual atoms would be highly correlated. The values of the different D-W factors optimised after fitting are summarised below:

$$ss = 0.0079, ssI = 0.014, ssMs = 0.0077$$

In addition, as it can be seen from Figure 6.32 that the phase factors of the P atom and the C atoms from the Cp ring are different and effectively cause the amplitudes to cancel each other out over the whole k range, which is an additional obstacle to the fitting procedure.

Another feature was highlighted during the fitting procedure, that is the importance of the oxygen scattering atom. Figure 6.33 below shows its contribution for both single and multiple scattering:

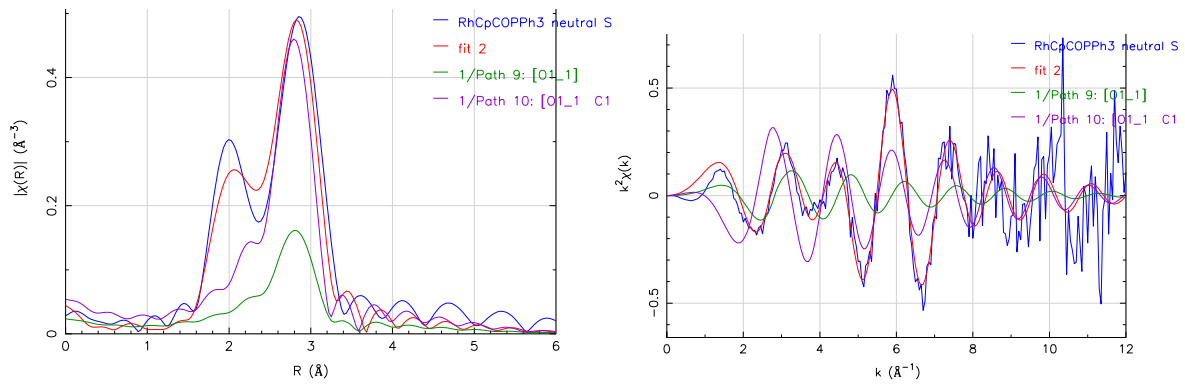


Figure 6.33: contribution of the single and multiple scattering paths from the oxygen atom in R -space (on the left) and k -space (on the right).

Figure 6.33 shows that the oxygen atom is the main contributor to the second peak occurring at ca 2.9 Å when it is implicated in both single and multiple scattering paths. Furthermore when the sum of all of the contributions of multiple scattering paths are plotted in Figure 6.34 below, and one can observe that both the oxygen atom and the sum of all multiple scattering paths sum up together in the same region.

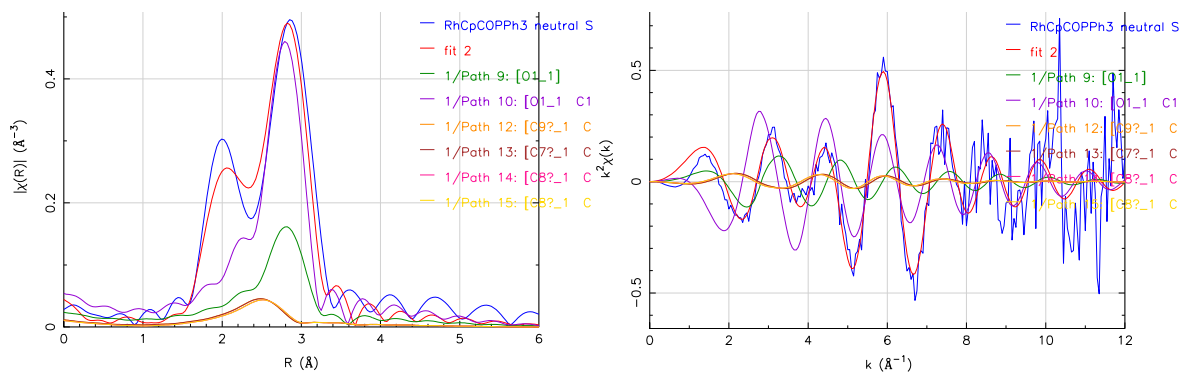


Figure 6.34: Contributions of all multiple scattering paths plotted in R -space (on the left) and k -space (on the right).

Therefore in conclusion, this is a challenging system to study via XAS because there is a large number of scatterers at similar distances in addition to the fact that there is a strong multiple scattering.

As a final check if the fit was significant, the imaginary part of R -space was plotted to gather information on the phase of each of the contribution. In Figure 6.35 below, one can observe a comparison of the imaginary parts of both the fit of the first shell only and the imaginary part of the fit considering the first and the second shell including both single and multiple scattering paths.

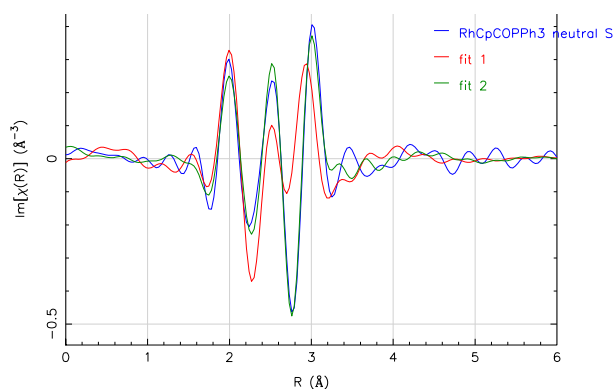


Figure 6.35: In Red, imaginary part of the R -space of the fit when only the first shell is considered. In green, imaginary part of the R -space of the fit when both the first and second shell are considered. The experimental data is represented in blue.

Thus, Figure 6.35 shows a good agreement between the last fit and the experimental data and allows us to confirm that considering only the first shell is not appropriate and that the second shell as well as multiple scattering have to be taken into account. We can therefore conclude that the fit obtained is reasonable.

Finally, Table 6.4 presents all the fitted parameters with their optimised value. During the fitting, the number of fitted parameters did not exceed the number of statistically allowable parameters.

Parameter	Optimised value	uncertainty
S_0^2	1.55	+/- 0.4343800
E_0	-7.83	+/- 1.33
ss	0.0079	+/- 0.014
ss1	0.014	+/- 0.0030
ssMs	0.0077	+/- 0.0028900
Delr	-0.0294310	+/- 0.0117220
Delr1	-0.0068540	+/- 0.0046730
Delr2	-0.0279200	+/- 0.0066200

Table 6.4: Fitted parameters with their optimised values along with their uncertainty for the molecular structure of $\text{CpRh}(\text{CO})\text{PPh}_3$.

The large value of the energy shift is due to the experimental conditions at the time. The scans were taken with no previous calibration with a Rh foil and therefore a shift in the raw data could be observed of +6.5 eV.

In the Artemis software, *delr*, *delr1*, and *delr2* are defined as being the value assigned proportionally to the atom path length and is equal to $\text{delscale}(1,2) \cdot \text{reff}$. *Reff* is a reserved variable which always refers to the atom generated absorber-scatterer distance (or half the total path length for multiple-scattering paths). The values found for bond distances are therefore presented in Table 6.5, along with those relative to the known crystal structure.

RhCpCOPPh ₃ (crystal)		RhCpCOPPh ₃ (experimental)	
	Distance r (Å)		Distance r (Å)
Rh ₁ -C ₁	1.808	Rh ₁ -C ₁	1.796
Rh ₁ -P	2.2445	Rh ₁ -P	2.310
Rh ₁ -C (Cp ring)	2.282	Rh ₁ -C (Cp ring)	2.218
C ₁ -O	1.158	C ₁ -O	1.158
Rh ₁ -----O	2.966	Rh ₁ -----O	2.954

Table 6.5: comparison of bond distances from the central atom Rh₁ to the nearest neighbours for both the crystal structure¹⁰ and the fitted experimental data.

Despite the modest quality of the data, there is still a good agreement between the experimental data and the theoretical model that shows that the complex CpRh(CO)PPh₃ is in solution.

It has been shown earlier in Figure 6.28 that there was a marked difference between the neutral and oxidised species in the real space Fourier transform of the EXAFS amplitudes. The data upon oxidation of a 3.15 mM solution of CpRh(CO)PPh₃ will now be analysed. Figure 6.36 shows the structure¹¹ of the dication along with the parameters used in the Artemis software for the fits.

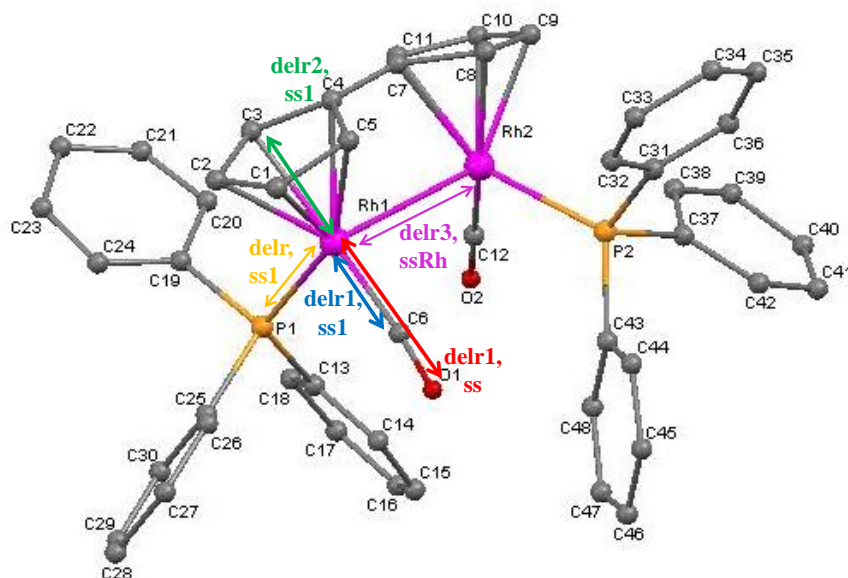


Figure 6.36: Molecular geometry of the Cis-dication Fulvalene¹¹ showing the labelling scheme for atomic backscatterers and the fitting parameters used in the Artemis software.

For the purpose of carrying out XAS calculations, different fitting parameters have been defined as follows: “*delr*” refers to the change of the Rh-P bond length. Similarly, “*delr1*” characterises the change in the Rh-C (from the carbonyl group) bond length, “*delr2*” refers to the Rh-C (from the Cp ring) bond length, and finally, “*delr3*” is associated to the Rh-Rh bond distance. All the carbon atoms within the Cp ring are assumed to be at the same distance from the Rh atom, since this distance is averaged. As regards the Debye-Waller parameter, “*ss1*” was defined for all the atoms in the first shell, “*ss*” for all the single-scattering paths regarding backscatterers from the second shell, “*ssMs*” for all multiple-scattering paths from the first and second shell and finally, “*ssRh*” was defined independently for the scattering paths regarding the second rhodium atom. To finish, the “ S_0^2 ” parameter was utilised to calculate the passive electron reduction factor and the “ E_0 ” parameter was used to determine the energy shift of the edge value.

As for the fit of the neutral species in the previous section, the EXAFS spectrum for the electrolysed species have been calculated using the distances derived from the known crystal structure and this was used as the starting point for fitting the XAS data obtained here. Therefore, all the Debye-Waller factors ss , ssl , $ssMs$, and $ssRh$ have all been attributed the value of 0.003. In addition, the variation in the energy shift E_0 was set to 0 and S_0^2 was defined as equal to 1. Figure 6.37 shows the results of this fit. Taking into account the quality of the data, the fitting process was performed over a k -space range of 2 to 11 \AA^{-1} and over a R -space range of 1 to 3.9 \AA .

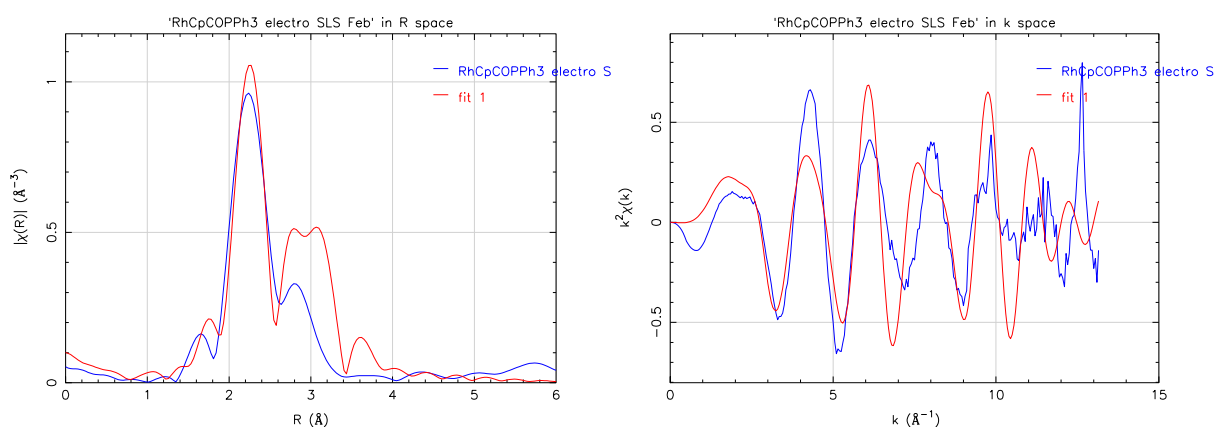


Figure 6.37: Comparison of the experimental data and the simulation based upon the crystal structure performed as described above: in R -space (on the left) and in k -space (on the right).

The value obtained for the resultant R -factor of 0.388 is quite high, and the reduced χ^2 is equal to 624.61. Since the fit seems rather poor and the following section will now show the improvements that can be brought to it. Therefore, an optimisation was carried out using all the fitting parameters defined earlier and mentioned in Figure 6.36. The resulting overall fit

(fit 2) is shown in Figure 6.38, and plotted against the experimental data of the electrolysed species.

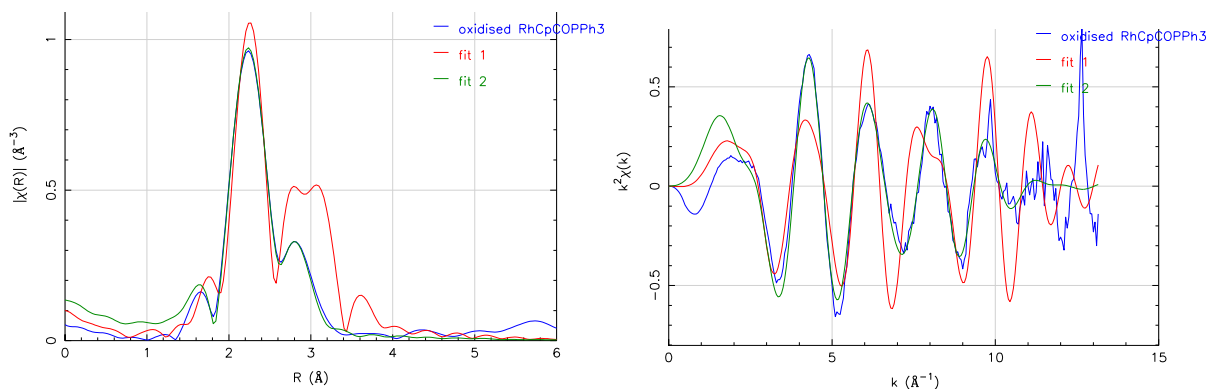


Figure 6.38: comparison of the experimental and theoretical Cis-dication Fulvalene $\text{Rh}_2(\text{CO})_2(\text{PPh}_3)_2(\eta^5\text{-}\eta^5\text{-C}_{10}\text{H}_8)$ Fourier transform (on the left) and k^2 weighted (on the right) EXAFS signals.

The resultant fitting displays a value of the R -factor down to 0.00365 and a reduced χ^2 of 14.53, which shows a significant improvement, as well as a very suitable fit of the data. For a better understanding of this result, the contribution of individual paths were analysed. Figure 6.39 shows the contributions of single scattering paths within the first shell.

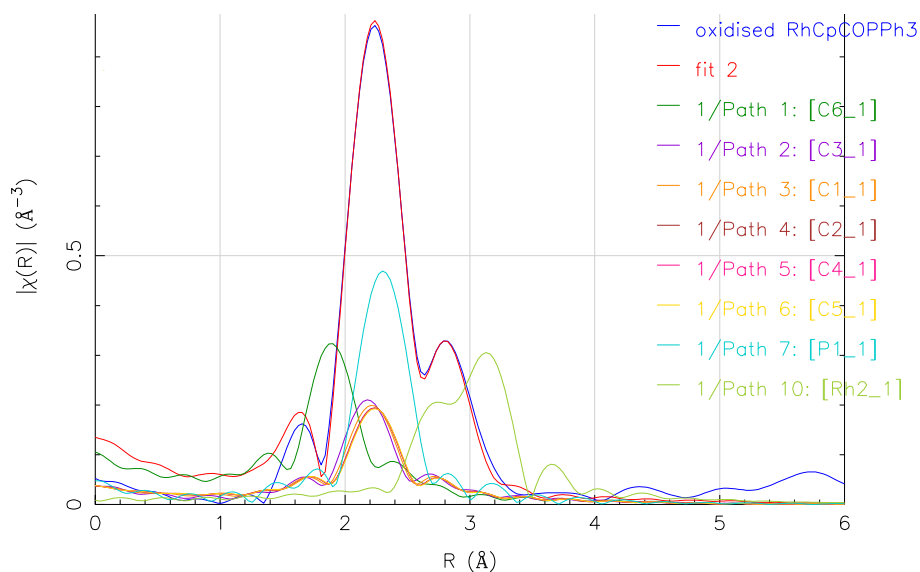


Figure 6.39: Plot in R -space of the experimental data, the optimised fit, and contributions of single scattering paths within the first shell.

One can observe that because several atoms contribute to the peak at ca. 2.2 Å, it was important to set the same Debye-Waller factor for the atoms belonging to the first shell in order to avoid highly correlated variables.

In addition, the importance that the oxygen atom brings a large contribution to the second peak occurring at ca 2.8 Å when it is implicated in both single and multiple scattering paths as it can be seen in Figure 6.40.

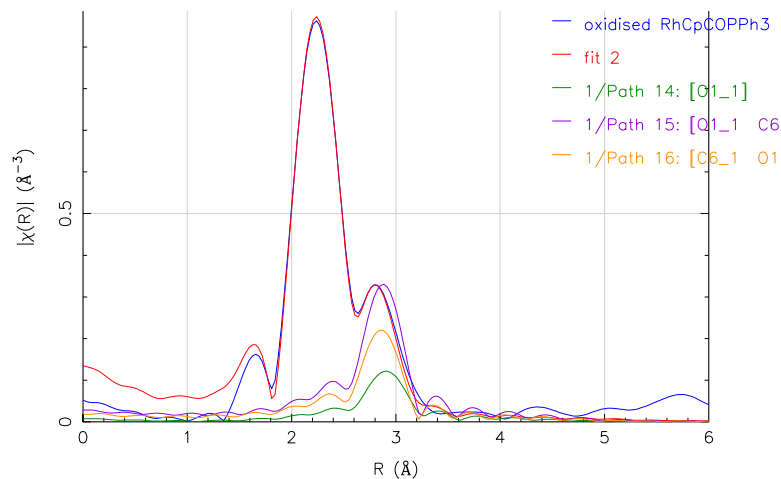


Figure 6.40: Plot in R -space of the experimental data, the optimised fit, and the contribution of the backscattering oxygen atom for single and multiple scattering paths.

Furthermore when the sum of some of the contributions of multiple scattering paths (for clarity) are plotted in Figures 6.42 below, and one can observe that both the oxygen atom and the sum of the multiple scattering paths both from the oxygen atom and the carbon atoms from the Cp ring, sum up together in the same region.

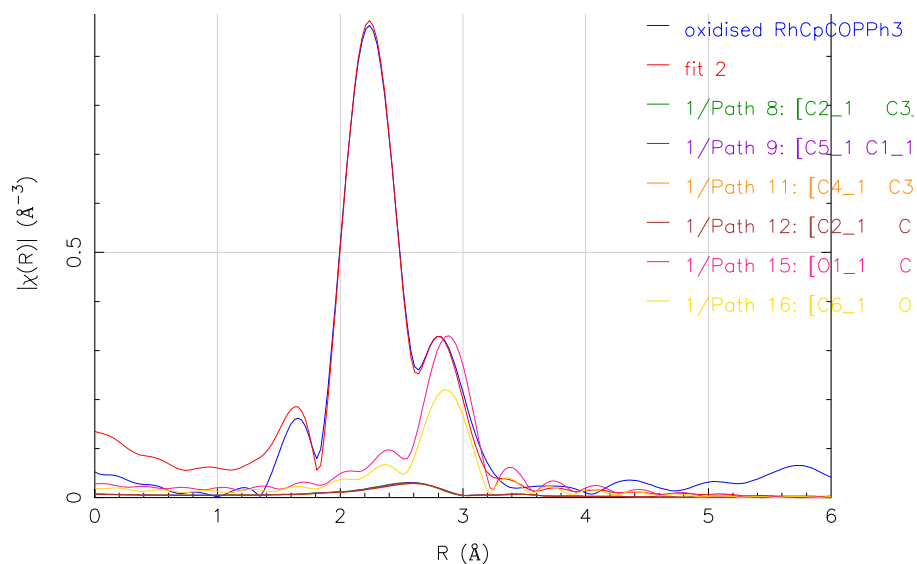


Figure 6.42: Plot in R -space of the experimental data, the optimised fit, and the contribution of the backscattering oxygen atom for single and multiple scattering paths.

Finally, Table 6.6 presents all the fitted parameters with their optimised value. During the fitting, the number of fitted parameters did not exceed the number of statistically allowable parameters.

Parameter	Optimised value	uncertainty
S_0^2	2.14	+/- 0.61
E_0	-4.01	+/- 2.28
ss	0.018	+/- 0.016
ss1	0.010	+/- 0.002
ssMs	0.014	+/- 0.006
ssRh	0.013	+/- 0.0024
Delr	-0.036	+/- 0.009
Delr1	-0.016	+/- 0.006
Delr2	-0.019	+/- 0.009
Delr3	-0.16	+/- 0.009

Table 6.6: Fitted parameters with their optimised values along with their uncertainty for the molecular structure of $\text{CpRh}(\text{CO})\text{PPh}_3$.

The large value of the energy shift is due to the experimental conditions at the time. The scans were taken with no previous calibration with a Rh foil and therefore a shift in the raw data could be observed of +4.5 eV.

From Table 6.6, one can observe that all Debye-Waller factors obtained are quite high. This is expected since according to the electrochemical data presented earlier, the conversion of starting material to product is ca. 80% and there is therefore a mixture of species in the experimental sample.

However there are very close similarities between the structures of the starting material and product. The only significant change of bond connectivity being the formation of a Rh-Rh bond. Thus apart from the presence of a Rh-Rh neighbour it can be expected that the values

found for bond distances in the first and second shell excluding the Rh-Rh bond should be similar to that for the pure dication in its crystalline form. The comparison of bond length for the electrochemical product and the structure derived from crystal data is presented in Table 6.7.

Cis-dication Fulvalene (crystal)		Cis-dication Fulvalene (experimental)	
	Distance r (Å)		Distance r (Å)
Rh-Rh	2.930	Rh-Rh	2.762
Rh-C(O)	1.821	Rh ₁ -C(O)	1.805
Rh-P	2.322	Rh-P	2.286
Rh ₁ -C (Cp ring)	2.225	Rh ₁ -C (Cp ring)	2.198
C ₁ -O	1.161	C ₁ -O	1.158
Rh ₁ -----O	2.982	Rh ₁ -----O	2.963

Table 6.7: comparison of bond distances from the central atom Rh₁ to the nearest neighbours for both the crystal structure¹¹ and the fitted experimental data.

In view of the modest quality of data that could be obtained in these pilot experiments it is encouraging that the structural data derived from XAS matches that expected from the electrochemical yield and compares well with the reference compound¹¹. The good agreement between the experimental data and the theoretical model of the dication suggests that, upon oxidation, the fulvalene metal-metal bonded dication has been formed. Although the formation of a single Rh-Rh bond in this system produces a change in the XAS spectra that is apparent by visual inspection it is worth noting that, in general, interpretation of XAS spectra for organometallic systems is non-trivial. For this system, it was thus determined that the central and most intense Fourier transform peak occurring at 2.24 Å is a result of scattering by the 5 carbons in the cyclopentadienyl ring and from the phosphorus. The small FT peak at ca.

1.66 Å arises from the scattering from the carbonyl carbon. Finally, the FT peak at ca. 2.82 Å occurs as a consequence of scattering from the second Rh atom, and in addition from single and multiple scattering through the oxygen atom and finally from multiple scattering through the carbonyl group.

6.8 Conclusion

The combination of an electrolysis cell integrated to a microdispenser and a sample chamber has been developed which permits material to be transported very rapidly from the electrode via an ink-jet dispenser to a quenched state. With a typical flow of 2 ml h⁻¹, the time it takes the electrochemically generated species to travel from the working electrode to the dispenser nozzle is approximately 200 ms.

In this chapter, the performance of a method for dispensing and freeze-quenching materials has been demonstrated with XAS data of sufficient quality for structural characterisation.

References

1. Wiltshire, R. J. K.; Smila-Castro, O.; Connelly, N. G.; Matthews, S. M.; Fisher, A. C.; Rayment, T. Channel-Flow Cell for X-ray Absorption Spectroelectrochemistry. *J. Phys. Chem. C* **2009**, *113* (1), 308-315.
2. Ballou, D. P.; Palmer, G. A. Practical Rapid Quenching Instrument for Study of Reaction Mechanisms by Electron-Paramagnetic Resonance Spectroscopy. *Anal. Chem.* **1974**, *46* (9), 1248-1253.
3. Bondin, M. I.; Foran, G.; Best, S. P. Electrosynthesis cell for X-ray absorption fine structure measurement: Reduction of air-sensitive iron-sulfur compounds. *Aust. J. Chem.* **2001**, *54* (11), 705-709.
4. Cheah, M. H.; Borg, S. J.; Bondin, M. I.; Best, S. P. Electrocatalytic proton reduction by phosphido-bridged diiron carbonyl compounds: Distant relations to the H-cluster? *Inorg. Chem.* **2004**, *43* (18), 5635-5644.
5. Bondin, M. I.; Borg, S. J.; Cheah, M. H.; Foran, G.; Best, S. P. Integration of EXAFS, spectroscopic, and DFT techniques for elucidation of the structure of reactive diiron compounds. *Aust. J. Chem.* **2006**, *59* (4), 263-272.
6. Borg, S. J.; Behrsing, T.; Best, S. P.; Razavet, M.; Liu, X. M.; Pickett, C. J. Electron transfer at a dithiolate-bridged diiron assembly: Electrocatalytic hydrogen evolution. *J. Am. Chem. Soc.* **2004**, *126* (51), 16988-16999.
7. Laurell, T.; Wallman, L.; Nilsson, J. Design and development of a silicon microfabricated flow-through dispenser for on-line picolitre sample handling. *J. Micromech. Microeng.* **1999**, *9* (4), 369-376.
8. Picology AB . Okennelev. 7, SE-237 35, Bjarred, Sweden.
9. Capillary Tube Supplies Ltd, <http://www.capillarytubes.co.uk>, **2010**.

10. Choi, M. G.; Brown, T. L. A Molecular Mechanics Model of Ligand Effects .5. Ligand Repulsive Energy Values for Phosphines and Phosphites Bound to CpRh(CO) and the Crystal Structure of CpRh(CO)(PPh₃). *Inorg. Chem.* **1993**, 32 (24), 5603-5610.
11. Freeman, M. J.; Orpen, A. G.; Connelly, N. G.; Manners, I.; Raven, S. J. Stereochemical Consequences of the 2e⁻ Oxidation of A Dirhodium Fulvalene Complex- the X-Ray Crystal Structures of Trans-[Rh₂(CO)₂(PPh₃)₂-(η⁵-η⁵-C₁₀H₈)] and Cis [Rh₂(CO)₂(PPh₃)₂(η⁵-η⁵-C₁₀H₈)] [PF₆]₂. *J. Chem. Soc. Dalton Trans.* **1985**, (11), 2283-2289.
12. Knight, J.; Mays, M. J. New Polynuclear Carbonyl Complexes containing Iron with Cobalt or Rhodium. *J. Chem. Soc. (A)* **1970**, 654.
13. Schuster, H. G.; Basolo, F. Kinetics and Mechanism of Substitution Reactions of π-Cyclopentadienyldicarbonylrhodium. *J. Am. Chem. Soc.* **1966**, 88 (8), 1657-1663.

Chapter 7: Final Conclusions

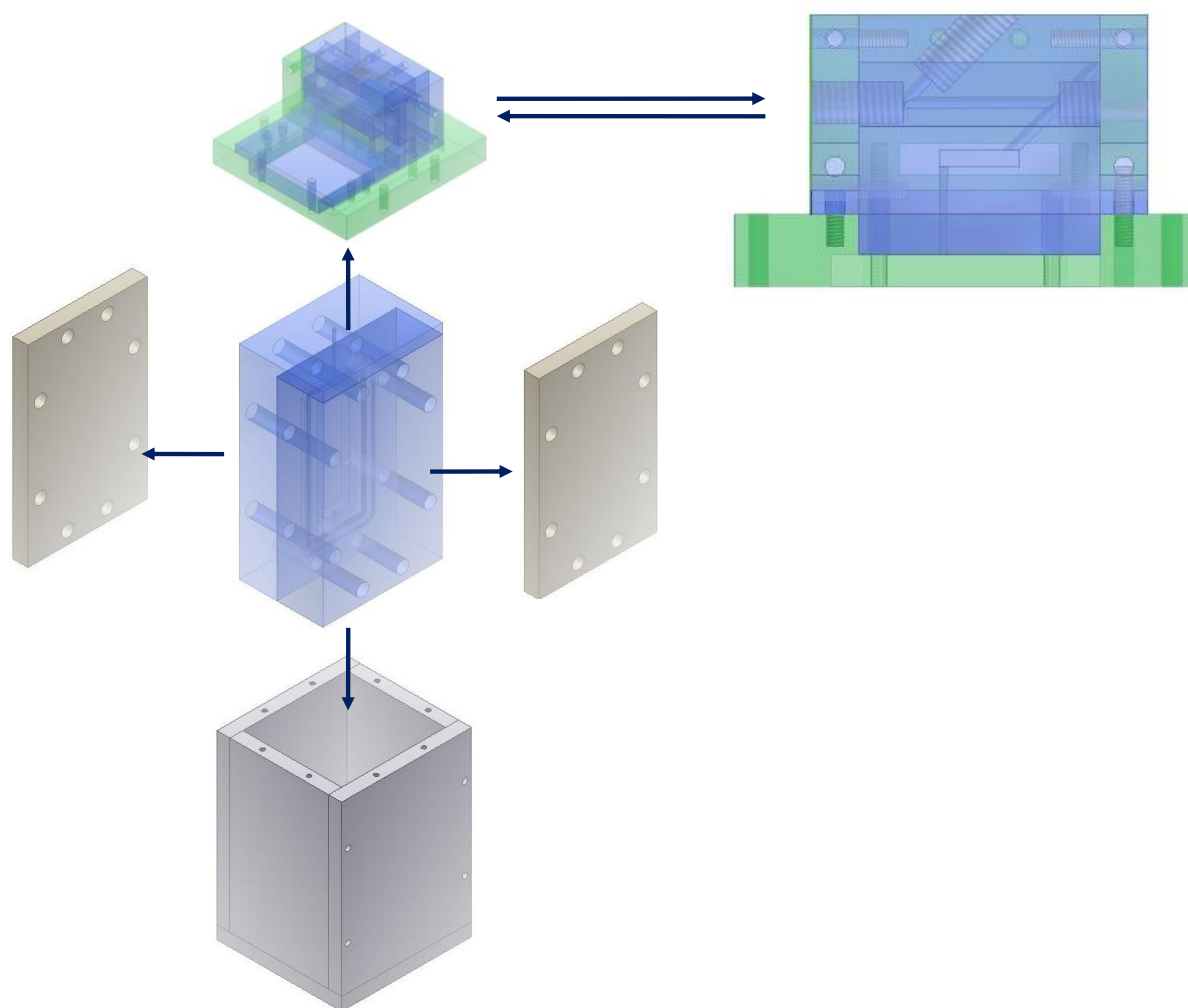
Final conclusions

In the course of this research, significant progress has been achieved in the application of X-ray absorption spectroscopy to the study of electrochemical intermediates.

As shown in Chapter 4, a strategy has been developed for situations where the temperature dependence of the chemistry is important. In that aim, two integrated continuous flow electrolysis cells for XAS have been designed and tested. Integrating the XAS cell with the electrolysis cell reduces the time between the products leaving the electrode and reaching the path of the beam. Temperature control is simplified and contamination is reduced. Because the sample tested is stable (over a few minutes at room temperature) there is no need for a micron sized beam.

However, difficulties have hindered the full potential of the cells built. The obstacles encountered showed that care should be taken of electric fields in the design of electrochemical cells. In particular, when using reticulous vitreous carbon, one should ensure that the gains hoped for in terms of increased surface area are not defeated by diffusion and potential shielding.

To overcome the problems encountered and cited above, a new cell has been designed and is shown in the figure below:



It is a similar design to that of the spectroelectrochemical cell 2 presented in Chapter 4 but differences are found in the direction of the flow in the electrolysis cell and a major change made to the solution flow through the EXAFS/UV/vis compartment. This new configuration should allow high quality electrochemistry and spectroscopic investigations leading to structural characterisation of the studied species.

In chapter 6, a second strategy has been explored: freezing the electrolytes to trap unstable product species. The advantage is that only modest focussing is required, reducing the risk of beam damage. In addition, data quality can be improved with samples at liquid nitrogen temperatures.

One of the limitations of this approach may have been the time resolution due to the rate at which material can be removed from the electrolysis cell and cooled.

It has been here demonstrated that transport of material very rapidly from the electrode to a quenched state has been realised successfully. In addition, both the starting material and the reaction product were identified by XAS.

Thus, the study showed the development of a new method for dispensing and freeze-quenching air-sensitive materials with XAS data of sufficient quality for structural characterisation.

The work presented in this thesis has clearly demonstrated that the application of XAS spectroscopy can bring new insights into electron transfer processes.

Future work on what has been achieved so far should allow fully successful application of XAS spectroscopy to the study of electrochemical intermediates